



LEHIGH  
UNIVERSITY

Library &  
Technology  
Services

The Preserve: Lehigh Library Digital Collections

# An Investigation of Micro and Nanoscale Molding for Biomedical Applications

## Citation

Rajhi, Ali A., and John P. Coulter. *An Investigation of Micro and Nanoscale Molding for Biomedical Applications*. 2019, <https://preserve.lehigh.edu/lehigh-scholarship/graduate-publications-theses-dissertations/theses-dissertations-227>.

Find more at <https://preserve.lehigh.edu/>

*This document is brought to you for free and open access by Lehigh Preserve. It has been accepted for inclusion by an authorized administrator of Lehigh Preserve. For more information, please contact [preserve@lehigh.edu](mailto:preserve@lehigh.edu).*

# **An Investigation of Micro and Nanoscale Molding for Biomedical Applications**

**By**

**Ali A. Rajhi**

Presented to the Graduate and Research Committee

of Lehigh University

in Candidacy for the Degree of

Doctor of Philosophy

in

Mechanical Engineering

Lehigh University

May 2019

Approved and recommended for acceptance as a dissertation in partial fulfillment of the requirements for the degree of Doctor of Philosophy.

---

Date

---

Dissertation Director: Dr. John P. Coulter

---

Accepted Date

Committee Members:

---

Committee Chair: Dr. John P. Coulter

---

Dr. Yaling Liu

---

Dr. Sabrina Jedlicka

---

Dr. Xuanhong Cheng

## ACKNOWLEDGMENTS

This dissertation here represents a lot of work over many years and majorly signifies a relationship with many amazing people I have met during my graduate work here at Lehigh University.

Starting with my family, I really cannot thank you enough for your support and motivation that you provided all these years. Without their support and engorgement, this work would never been possible. An exceptional thanks to my wife and my daughter who showed a wonderful support and were always there for me during these years. Thank you!!

I am really thankful to my advisor Prof. John Coulter, Prof. Sabrina Jedlicka, and all my committee members for guiding me throughout this project. Without your guidance this work would have not been possible.

Also, I am really appreciative to Dr. John Rodgers (Ximedica Design Assurance Engineer) to show me how use the micro-injection molding machine and advices me through this project.

I am also grateful to Ray Filozof who is the nano-electronics lab instructor for his help and guidance in fabricating the silicon molds using photolithography process and deep reactive ion etching.

I am really thankful to Walter Robinson who joined the project as a summer student to help moving the project forward.

I like also to thank Eric Rufe and John Thornton from Bruker corporation for gave me the opportunity to use the new Atomic Force Microscopy (AFM) to characterize my sample and for their guidance.

I am also thankful for Tim Hanvery and Jarred Packard who are ASA CLEAN marketing managers for providing the purging compound to clean our micro-injection molding machine.

Thank you to all the members of the manufacturing science lab from the past and present including Majed Alserheed, Chandresh Thukar, Qi Li, Alaauldeen Duhduh, Khalied Alqosaibi, Hussam Noor, and Peng Gao.

I would like also to thank Brianne Lisk the graduate program manager, Allison Marsteller the graduate coordinator and all my professor and department staff for creating a supportive environment during these years.

This research was funded by National Science Foundation (award number 1543109) under division of industrial innovation and partnerships. I would like to Thank NSF for funding this project and support this research to move it forward.

*“Crystalize your goals. Make a plan for achieving them and set yourself a deadline. Then, with supreme confidence, determination and disregard to obstacles and other people’s criticisms, carry out your plan “*

Paul J. Meyer

## Table of Contents

ACKNOWLEDGMENTS .....	3
ABSTRACT.....	1
CHAPTER 1: INTRODUCTION.....	4
1.1 Micro/Nanostructured Surfaces.....	4
1.1 Problem Description.....	6
1.2 Opportunity .....	6
1.2 Research Motivation and Program Objectives.....	7
1.2.1 Biomedical Cell Culture Development.....	7
1.2.2 Target Application Area .....	9
1.2.3 Research Motivation .....	9
1.2.4 Dissertation Objectives .....	10
1.3 Dissertation Structure.....	10
CHAPTER 2: RELATED SCIENTIFIC DEVELOPMENTS.....	13
2.1 Injection molding at the micro and nanoscale.....	13
2.1.1 Micro Injection Molding Machine and Modification .....	13
2.1.2 Critical Processing Parameters .....	15
2.1.3 Micro-Injection Molding Technology .....	17
2.1.4 Mold Temperature Control Methods .....	18
2.1.1 Applications .....	20
2.2 Tooling Fabrication Methods.....	22
2.2.1 Silicon-Based Tooling .....	22
2.1.5 Aluminum Anodic Oxide (AAO) .....	27
2.1.6 Bulk Metallic Glass Inserts.....	28
2.1.7 Laser Micro-Drilling.....	31
2.1.8 Nickel-phosphorus Plating (NIP).....	32
2.1.9 Sacrificial Tooling .....	34
2.1.10 Soft lithography .....	35
2.1.11 Demolding Agents .....	36

2.2	Polymer Micro Fluidic Flow .....	36
2.2.1	Macro/ Micro interface .....	36
2.2.2	Viscosity .....	38
2.2.3	Wall Slip Velocity.....	39
2.3	Previous Lehigh Research.....	39
2.4	Remaining Scientific Challenges .....	41
2.4.1	Process Parameters Optimization .....	41
2.4.2	Better molds .....	42
2.4.3	Large Surface area .....	42
2.4.4	Parts Demolding.....	42
2.4.5	Inspection/Metrology.....	43
2.5	Objectives in More Details.....	47
CHAPTER 3: Micro/Nanoscale Features for studying Cell Mechanosensing .....		50
3.1	Introduction .....	50
3.1.1	Influence of substrate stiffness on Cells .....	51
3.1.2	Influence of substrate Micro/Nano topography and geometries on Cells....	51
3.1.3	Remaining Challenges .....	53
3.2	Micro/Nano-Pillars Bending Mechanism.....	53
3.1.4	Euler – Bernoulli Approximation .....	53
3.1.5	Accounting for Shear Deformation by including the Timoshenko Beam Approximation Deflection Term .....	55
3.2	Ansys Simulations.....	72
3.3	CONCLUSION .....	74
CHAPTER 4: TOOLING DEVELOPMENT AND TESTING.....		75
4.1	Silicon-based Tooling .....	75
4.1.1	Photolithography.....	75
4.2	Deep Reactive Ion Etching (DRIE) Trails .....	78
4.3	Silicon Mold Assembly.....	81
4.4	BMG Based Mold .....	82
4.4.1	Fabrication of Si Micro Pillars Molds .....	84

4.1.1	Thermoplastic forming of BMG .....	89
4.5	Mold Durability Simulations and Testing.....	113
4.5.1	Demolding Process of Micro molded Structures .....	113
4.5.2	Mold fatigue life analysis.....	122
4.5.3	Experimental validations .....	132
CHAPTER 5:    NUMERICAL ANALYSIS OF MICRO INJECTION MOLDING ..		137
5.1	Introduction .....	137
5.2	Moldflow Theoretical Background .....	137
5.2.1	Mathematical Model .....	137
5.2.2	Governing Equations .....	138
5.2.3	Viscosity model: .....	139
5.2.4	Wall Slip Velocity Model: .....	140
5.3	Target Mechanotransduction Surfaces .....	140
5.4	Materials.....	142
5.4.1	General purpose Polystyrene (GPPS) .....	143
5.4.2	Thermoplastic Polyurethane (TPU) .....	144
5.4.3	Low-Density Polyethylene (LDPE).....	147
5.4.4	High-Density Polyethylene (HDPE).....	148
5.4.5	Cyclic Olefin Copolymer (COC).....	149
5.5	2D Micro Filling Simulations (Molding Window Analysis) .....	151
5.6	3D Micro Filling Simulations .....	154
5.6.1	Analysis Sequences.....	154
5.6.2	Results and Discussions .....	155
5.6.3	Different Molding Material (PS, TPU, LDPE, HDPE) .....	163
5.1.1	Micro Features Simulation (15, 10, 5 um, and flat).....	164
5.1	Sprue Size Change Simulations .....	165
5.7	Discussion and Conclusion .....	167
CHAPTER 6:    EXPERIMENTAL RESULTS AND CHARACTERIZATIONS .....		169
6.1	Micro-Injection Molding Replication .....	169
6.1.1	Polystyrene (PS) Experimental Trails.....	169

6.1.2	Thermoplastic Polyurethane (TPU) Trails.....	178
6.1.3	Low-Density Polyethylene (LDPE).....	190
6.1.4	High-Density Polyethylene (HDPE).....	194
6.1.5	Cyclic Olefin Copolymer (COC).....	199
6.2	Mold Modification .....	202
6.3	Experimental validation .....	204
6.3.1	Atomic Force Microscope (AFM) Characterization.....	205
6.4	Conclusion.....	207
CHAPTER 7: MANUFACTURING COST ANALYSIS .....		209
7.1	Market Size .....	209
7.2	Potential Opportunity .....	210
7.3	Substrates Commercialization Considerations.....	210
7.4	Dimensional analysis.....	211
7.5	Molded Part Cost Analysis.....	213
7.6	Sensitivity Analysis.....	215
CHAPTER 8: CONCLUSION AND FUTURE RECOMMENDATIONS.....		217
8.1	Research Summary.....	217
8.2	Impact of Dissertation Research .....	219
8.3	Future Recommendations.....	221
REFERENCES: .....		224
VITA.....		233

## List of Tables

Table 4-1: Bosch Processing Parameters.....	79
Table 4-2: Etching processing parameters.....	86
Table 4-3: Mechanical properties of Zr-BMG (Provided by Materion Corporation).....	90
Table 4-4: Characteristic temperatures of Zr-BMG found by DSC at a scan rate of 20 C°/min.....	91
Table 4-5: Zr <sub>2</sub> -Cu and Zr-Be <sub>2</sub> XRD patterns.....	97
Table 4-6: Polystyrene young modulus as a function of temperature. ....	120
Table 4-7: Silicon Fatigue life parameters.....	124
Table 4-8: Fatigue life (cycle) for Si molds with 5um diameter, 2.5 depth, and different C2C spacing.....	126
Table 4-9: BMG Fatigue life parameters.....	126
Table 4-10: Fatigue life (cycle) for Zr-BMG molds with 5um diameter, 2.5 depth, and different spacing.....	128
Table 4-11: Fatigue life (cycle) for Si molds with 5um diameter, 2.5 depth, and different spacing. ....	130
Table 4-12: Fatigue life (cycle) for Zr-BMG molds with 5um diameter, 2.5 depth, and different spacing.....	131
Table 5-1: targeted mechanotrasduction surface. ....	141
Table 5-2: Physical and mechanical properties for 666D STYRON.....	143
Table 5-3: Physical and mechanical properties for TPU Texin 985.....	145
Table 5-4: Physical and mechanical properties for LDPE ASI CP 851 .....	147
Table 5-5: Physical and mechanical properties for HDPE Exxon HD-6733.....	148

Table 5-6: Physical and mechanical properties for COC TOPAS 5013S-04 .....	150
Table 5-7: Moldflow recommended molding parameters for 15 um oval micro features using different molding materials. ....	164
Table 5-8: Recommended molding parameters for diffident micro features using PS STYRON 666D.....	165
Table 5-9: Processing parameters provided by Moldflow simulation. ....	167
Table 6-1: Moldflow recommended molding parameters for STYRON 666D.....	170
Table 6-2: Molding parameters for polystyrene (STTRON 666D). ....	176
Table 6-3: Moldflow recommended molding parameters for Texin 985. ....	179
Table 6-4: Moldflow recommended molding parameters for LDPE CP 851.....	191
Table 6-5: Moldflow recommended molding parameters for HDPE HD 6733.....	195
Table 6-6: Moldflow recommended molding parameters for TOPAS 5013S-04.....	199
Table 7-1: Silicon mold insert cost. ....	212
Table 7-2: BMG mold insert cost. ....	213
Table 7-3: Molded part unit cost using Si mold. ....	214
Table 7-4: Molded part unit cost using BMG mold.....	214

## List of Figures

Figure 1-1: Nature based Micro / Nano applications.....	4
Figure 1-2: Micro molded parts .....	5
Figure 1-3: A) Fallopian tube surface. B) SEM of a fertilized human ovum in a fallopian tube (Scale bar 100 um), mag. 1000x. C-D) 96 well plate & Petri dish with micro molded plat.....	8
Figure 2-1: A) Conventional Injection Molding Machine. B) Plasticization unit for $\mu$ IM .....	14
Figure 2-2: (a) Straight drilled cooling channel. (b) Conformal cooling channel .....	18
Figure 2-3: Injection molding cycle time using variotherm passive approach.....	20
Figure 2-4: PDMS microneedles array for drug delivery .....	21
Figure 2-5: The process of LIGA.....	23
Figure 2-6: Positive and Negative Photoresist.....	25
Figure 2-7: A-B) Isotropic and anisotropic etching. C) Alternating process passivation and etching processes during DRIE technique .....	26
Figure 2-8: Schematic drawing of AAO structure prepared by electrochemical anodization of Al .....	28
Figure 2-9: Schematic of a laser cutting machine.....	31
Figure 2-10: 15 um holes laser drilled with a pitch of 30um on metal mold.....	31
Figure 2-11: Effect of annealing on the hardness of Ni–P alloys <sup>10</sup> .....	33
Figure 2-12: SEM micrographs of Ni–P electrodeposits with different P contents. (a) 0% P, (b) 4.64% P, (c) 9.14% P,(d) 15.22% P.....	34
Figure 2-13: PDMS microfluidic chips.....	35

Figure 2-14: illustration of contact angle formed on hydrophobic and hydrophilic surfaces .....	44
Figure 2-15: Advancing and Reseeding contact angle techniques .....	45
Figure 2-16: Schematic of water droplet interfaces for Wenzel model (a) and Cassie- Baxter model (b).....	46
Figure 3-1: Apparent modulus of elasticity (a) pillar aspect ratio and (b) pillars spacing of various diameters. ....	52
Figure 3-2: Schematic of Cantilver Beam deflection .....	54
Figure 3-3: Injection Molded Array of Bending Micro/Nano-Structures due to Force Exerted by Cell. ....	57
Figure 3-4: Orthogonal Array with C2C spacing( $\chi$ ).....	59
Figure 3-5: Effect of shear on the apparent elastic modulus of 5um diameter, 8 um center to center spacing made of TPU with E=12.5 MP .....	60
Figure 3-6: 5 um diameter Cylindrical Polystyrene pillars with 6, 7, 8 um C2C spacing.	61
Figure 3-7: 5um diameter cylindrical pillars with 8 um C2C spacing with different material. ....	62
Figure 3-8: TPU 5um diameter Cylindrical pillars with a different C2C spacing.....	63
Figure 3-9: LDPE 5um diameter Cylindrical pillars with different C2C spacing. ....	63
Figure 3-10: HPDE 5um diameter Cylindrical pillars with different C2C spacing.....	64
Figure 3-11: TPU micro pillars with diameter (D) sensitivity analysis to Apparent Elastic modulus on cells. ....	65
Figure 3-12 TPU 5um micro pillars with height (L) sensitivity analysis to Apparent Elastic modulus on cells. ....	65

Figure 3-13: Oval Cross section with a rotating angle .....	67
Figure 3-14: PS Elliptical pillars with semi-major diameter $a=1 \mu\text{m}$ and different pitch (C2C spacing). .....	68
Figure 3-15: Elliptical pillars with semi-major diameter $a=1 \mu\text{m}$ , $b= 0.5 \mu\text{m}$ and $2 \mu\text{m}$ C2C spacing. ....	69
Figure 3-16: TPU Elliptical pillars with semi-major diameter $a=1 \mu\text{m}$ , $b=0.5 \mu\text{m}$ and different C2C spacing. ....	69
Figure 3-17: LDPE Elliptical pillars with semi-major diameter $a=1 \mu\text{m}$ and different C2C spacing. ....	70
Figure 3-18: TPU micro pillars with semi-major diameter (a) sensitivity analysis to Apparent Elastic modulus on cells.....	71
Figure 3-19: TPU $2 \mu\text{m}$ micro elliptical pillars with height (L) sensitivity analysis to Apparent Elastic modulus on cells.....	72
Figure 3-20: A) Equivalent stress result (MPa). B) Displacement result ( $\mu\text{m}$ ). ....	73
Figure 3-21: Force-displacement plot for $5\mu\text{m}$ diameter post with $10 \mu\text{m}$ height. ....	73
Figure 4-1: a) Photolithography Mask, b) 4 micro-features regions. ....	75
Figure 4-2: Schematic of photolithography process. ....	76
Figure 4-3: Wafer Surface Modification with HMDS.....	77
Figure 4-4: Exposure time effects on features dimensions. ....	77
Figure 4-5: Etch rate curves for Si and $\text{SiO}_2$ wafers. ....	79
Figure 4-6: Silicon molds with different depth.....	80
Figure 4-7: Si Wafer Bonded to Aluminum Mold base with Adhesive. ....	81

Figure 4-8: Bulk metallic insert fabrication using Micro/Nano structured silicon. template. .....	84
Figure 4-9: Photolithography Process.....	85
Figure 4-10: Trail 1 Tapered Si pillars. ....	87
Figure 4-11: Si pillars with 15 um diameter and 15 um height. ....	87
Figure 4-12: O2 Plasma Ashing Machine.....	88
Figure 4-13: Schematic of a time-temperature-transformation (TTT) diagram showing that metallic glass can be formed via (1) direct casting. (2) Thermoplastic forming .....	89
Figure 4-14: DSC curves of Zr-BMG sample with scanning rate of 20 C/min. (A) Zoom of glass transition peak between 300 C° and 400 C°. (B) Crystallization temperature peak.	92
Figure 4-15: XRD scan of Zr-BMG after dicing to 12x12 mm.....	93
Figure 4-16: Vacuum Hot Press Machine with Cooling Rate and Heating Rate Calculated during Experiments. ....	94
Figure 4-17: Schematic of the Graphite Die used in Hot Press Experiments.....	95
Figure 4-18: XRD Scan for Zr-BMG TPF at 450 C° at 458 kg.....	97
Figure 4-19: XRD Scan for Zr-BMG TPF at 350 C° at 75 kg Load. ....	98
Figure 4-20: TPF Zr-BMG sample (A). Zr-BMG with Si mold breakage due to load during cooling (B) red area shows scatter light as a sign of microstructured region. ....	99
Figure 4-21: XRD Scan for Zr-BMG sample that was TPF at 275 C° at 75 Kg Load. ....	99
Figure 4-22: SEM Image of TPF Zr-BMG at the Center of the Sample. ....	100
Figure 4-23: SEM Image of Zr-BMG sample at the Edge.....	100
Figure 4-24: SEM Image of Zr-BMG TPF at 375 C° with 75 Kg Load.....	102
Figure 4-25: SEM Image of Zr-BMG TPF at 375 C° with 75 Kg Load.....	102

Figure 4-26: XRD Scans of TPF Zr-BMG at 275 C° with 75 Kg Load before and after polishing 100 μm of the surface.....	103
Figure 4-27: Zr-BMG sample was TPF at 340C with 75 kg load for 1 min.....	104
Figure 4-28: XRD Scan of TPF Zr-BMG sample at 340 C with 75 Kg load (Si contact area).....	105
Figure 4-29: SEM Image of Zr-BMG TPF at 340C and 75 Kg Load.....	105
Figure 4-30: Zr-BMG TPF at 340C with 250 Kg. ....	106
Figure 4-31: SEM Image of Zr-BMG TPF at 340C and 250 Kg Load.....	107
Figure 4-32: Zr-BMG TPF at 340 C with 3 minutes hold and 150 Kg load.....	108
Figure 4-33: XRD results for micro molded BMG at 340C at 75, and 150 Kg load compared to as received scan. ....	108
Figure 4-34: SEM Image of Zr-BMG TPF at 340 C with 3 Minutes Hold and 150 Kg Load. ....	109
Figure 4-35: Si wafer used in 340 C with 3 minutes hold and 150 Kg Load trail.....	109
Figure 4-36: Zr-BMG mold after KOH dissolving (exposed area). ....	110
Figure 4-37: Zr-BMG mold after KOH dissolving (Si covered area). ....	111
Figure 4-38: Si pillars with 5um diameter and 2.1 um height. ....	112
Figure 4-39: Middle region of Zr-BMG after TPF. ....	112
Figure 4-40: Zr-BMG after TPF towards the edges.....	113
Figure 4-41: Schematic of demolding a single microstructure. ....	114
Figure 4-42: Contact pressure between the microstructure and microcavity .....	115
Figure 4-43: PVT curves of 666D STYRON. ....	116
Figure 4-44: Curve fitting data for Polystyrene 666D STYRON.....	120

Figure 4-45: Demolding force is needed to demold a single microstructure from a circular microcavity with D=5um and H=2um. ....	121
Figure 4-46: Demolding force is needed to demold a single microstructure from an oval microcavity with D=15um and H=15um. ....	121
Figure 4-47: Equivalent stress (Von Mises stress) formed on Si mold 5um circular microcavities with 8um center-to-center (C2C) spacing under P= 4 MPa, T=80 C°. ....	125
Figure 4-48: Si mold number of Cycles before failure for 5um circular microcavities with 8um C2C spacing under P=4MPa, T=80 C°. ....	125
Figure 4-49: Equivalent stress (Von Mises stress) formed on Zr-BMG mold 5um circular microcavities with 8um C2C spacing under P= 4 MPa, T=80 C°. ....	127
Figure 4-50: Zr-BMG mold number of Cycles before failure for 5um circular microcavities with 8um C2C spacing under P=4MPa, T=80 C°. ....	127
Figure 4-51: Equivalent stress (Von Mises stress) formed on Si mold 15um circular microcavities with 18um C2C spacing under P= 4 MPa, T=80 C°. ....	129
Figure 4-52: Si mold number of Cycles before failure for 5um circular microcavities with 8um C2C spacing under P=4MPa, T=80 C°. ....	129
Figure 4-53: Equivalent stress (Von Mises stress) formed on Zr-BMG mold 15um circular microcavities with 18um C2C spacing under P= 4 MPa, T=80 C°. ....	130
Figure 4-54: Zr-BMG mold number of Cycles before failure for 5um circular microcavities with 8um C2C spacing under P=4MPa, T=80 C°. ....	131
Figure 4-55: Molded samples height (μm). ....	133
Figure 4-56: SEM photographs for molded part cycle no.80 at 5 different regions with T <sub>mold</sub> =83 C°. (Scale bar 10 um).....	134

Figure 4-57: A) 5um Si mold after 105 cycles. B) 5um molded part after 105 cycles....	134
Figure 4-58: SEM image of molded part no.25 (15 um Oval).....	135
Figure 4-59: 15 um oval Si mold after 25 cycles.....	136
Figure 5-1: CAD model for molded part. ....	142
Figure 5-2: Polystyrene repeating unit.....	143
Figure 5-3: Cross WLF plot viscosity verses shear rate .....	144
Figure 5-4: Thermoplastic Polyurethane Structure.....	145
Figure 5-5: Cross WLF plot viscosity verses shear rate .....	146
Figure 5-6: TPU Elongation % versus Tensile strength as function of temperature .....	146
Figure 5-7: Polyethylene Polymer .....	147
Figure 5-8: Cross WLF plot viscosity verses shear rate for LDPE ASI CP 851 .....	148
Figure 5-9: Cross WLF plot viscosity verses shear rate for HD-6733 .....	149
Figure 5-10: COC Chemical Structure .....	149
Figure 5-11: Cross WLF plot viscosity verses shear rate for COC TOPAS 5013S-04 ...	150
Figure 5-12: a) CAD model with tetrahedral mesh (3-D) in Moldflow. b) Array of ellipses (5x5) at D=15um and H=15um.....	152
Figure 5-13: Zone (Molding window) result. ....	152
Figure 5-14: Molded Part Replication Quality (%) using STYRON 666D at Different Mold Temperature.....	153
Figure 5-15: Filling simulation results at 50, 85, 95, and 100% of the part filled.....	155
Figure 5-16: Micro-structured region filled at t=0.1408 sec. ....	156
Figure 5-17: Velocity contours at the end of velocity filling stage (tinj=0.1923 sec).....	157

Figure 5-18: Velocity contours at different filling time (0.167, 0.1923, and 0.2095. b) velocity at the injection point.....	157
Figure 5-19: Pressure distribution at V/P switchover (A) and the end of fill (B).....	158
Figure 5-20: Pressure distribution during filling at different locations. ....	159
Figure 5-21: Viscosity distribution at the end of fill.....	159
Figure 5-22: Temperature distribution at flow front.....	160
Figure 5-23: Frozen layer diffraction at end of fill. ....	160
Figure 5-24: Warpage analysis. ....	161
Figure 5-25: Shear stress at micro-cavities walls. ....	162
Figure 5-26: Velocity slip appearance inside the micro cavities. ....	162
Figure 5-27: Cooling Time at different mold temperatures at $T_{melt}=215C$ . ....	163
Figure 5-28: Time to reach ejection temperature A) old Sprue. B) Modified sprue. ....	166
Figure 6-1: Si mold with 5 um diameter and 2.49 um depth. ....	171
Figure 6-2: 5um diameter molded pillars (666D STYRON) with 45 sec cooling time...172	
Figure 6-3: 5um diameter molded pillars (666D STYRON) with 55 sec cooling time...173	
Figure 6-4: 5um diameter molded pillars (666D STYRON) with 65 sec cooling time..173	
Figure 6-5: 5um diameter molded pillars (666D STYRON) with 85 sec cooling time...174	
Figure 6-6: 5um diameter molded pillars (666D STYRON) with 88 sec cooling time...174	
Figure 6-7: 5um diameter with 2.136 um height molded pillars (666D STYRON) with 95 sec cooling time. ....	175
Figure 6-8: SEM image for Si molds tool I&II.....	176
Figure 6-9: PS 10 um diameter with 6 (A), 30 (B) MPa packing pressure.....	177

Figure 6-10: PS molded samples with injection velocity of A) 25, B) 50, C) 100, D) 150 mm/sec (scale bar 25,20,20,20 respectively).....	178
Figure 6-11: Silicon Mold inserts with Oval shapes with 15µm Diameter and 21.5, 8.38 µm depth (Tool I &II (without antistiction coating)). And Cylindrical shapes with 5 µm diameter and 2.49 µm depth (Scale Bar for Tool I, II, and III is 20, 25. 20µm respectively). .....	180
Figure 6-12: 15µm TPU Oval pillars molded at packing pressure of 15 MPa (A), 20 MPa (B), 25MPa (C). .....	181
Figure 6-13:5µm TPU micro pillars A) 15 Sec, B) 60 Sec, C) 88 Sec cooling time.....	183
Figure 6-14: 15 µm TPU Pillars A) 15 Sec B) 88 Sec cooling time.....	184
Figure 6-15: 15 µm TPU oval pillars height demolded after 15, 45, 60, and 88 Sec cooling time. ....	185
Figure 6-16: TPU 15µm micro pillars. A) 15 sec cooling time. B) 45 Sec Cooling time (Scale Bar is 50um).....	186
Figure 6-17: 10 um oval pillars with 10.02 um height. ....	188
Figure 6-18: TPU molded sample with 15um at A) 15 sec, B) 88 sec cooling time. ....	189
Figure 6-19: CAD model of molded part show the 9 regions that SEM were taken.....	190
Figure 6-20: SEM Images of 9 regions of molded sample. ....	190
Figure 6-21: Silicon Mold inserts with Oval shapes with 15µm Diameter and 21.5, 15.03 µm depth (Tool I &II ), 10 µm diameter with 10.02 µm depth (Tool III) and Cylindrical shapes with 5 µm diameter and 2.49 µm depth (Tool IV) (Scale Bar is 20 µm).....	191
Figure 6-22: 15 µm diameter with 21,391 µm height LDPE.....	192
Figure 6-23: 15 µm diameter with 15.09 µm height.....	193

Figure 6-24: 10 $\mu\text{m}$ diameter with 10.031 $\mu\text{m}$ height.....	193
Figure 6-25: 5 $\mu\text{m}$ diameter with 2.434 $\mu\text{m}$ height.....	194
Figure 6-26: 15 $\mu\text{m}$ diameter with 19.833 height with lower packing pressure 15 MPa.	195
Figure 6-27: 15 $\mu\text{m}$ diameter with 21.41 $\mu\text{m}$ height with 33 sec cooling time.....	196
Figure 6-28: 15 $\mu\text{m}$ diameter with 22.56 at 15 sec cooling time .....	196
Figure 6-29: 15 $\mu\text{m}$ diameter with 15.263 $\mu\text{m}$ height. ....	197
Figure 6-30: 10 $\mu\text{m}$ diameter with 10.049 $\mu\text{m}$ height. ....	198
Figure 6-31: 5 $\mu\text{m}$ diameter with 2.389 $\mu\text{m}$ height .....	198
Figure 6-32: 5 $\mu\text{m}$ diameter with 1.808 $\mu\text{m}$ height. ....	200
Figure 6-33: 15 $\mu\text{m}$ diameter with 5.172 $\mu\text{m}$ height. ....	200
Figure 6-34: 5 $\mu\text{m}$ diameter with 2.283 $\mu\text{m}$ height. ....	201
Figure 6-35: 15 $\mu\text{m}$ diameter with 11.325 $\mu\text{m}$ height. ....	201
Figure 6-36: CAD Model for a molded part with sprue size. ....	202
Figure 6-37: Sprue diameter configuration.....	203
Figure 6-38: Nozzle bushing configuration with mold plate (yellow) and molded part (orange).....	204
Figure 6-39: SEM image of Molded pillars with 5 $\mu\text{m}$ diameter.....	205
Figure 6-40: AFM image of molded pillars with 5 $\mu\text{m}$ diameter.....	206
Figure 6-41: Cross sectional measurement of AFM scanned image. ....	206
Figure 7-1: Global microinjection polymer molding revenue share by application.....	209
Figure 7-2: Cost of injection molded unit.....	211
Figure 7-3: Molded part unit cost using Si mold versus mold insert life cycles. ....	215
Figure 7-4: Molded part unit cost using BMG mold versus mold insert life cycles.....	216

## **ABSTRACT**

In the last decade, there has been rapid advancement of micro and nano manufacturing. Microinjection molding is a cost-effective fabrication technique that can fulfill the requirements of many medical applications. Despite the many advancements of microinjection molding, there are several challenges that need to be addressed to improve the replication. One of the most critical challenges for micro molders is the ability to fill a micro mold in a predictable fashion during injection molding. To enhance the replication quality of the parts, particularly those with high aspect ratio micron scale features, it is imperative to gain a scientific understanding of the role of the various processing parameters on micro-cavity filling during injection molding.

The main objective of this research was to develop a micro injection molding strategy to optimize the filling of micro/nano features. That included the design and manufacture an efficient mold that can produce high quality molding features at high replication rates. The intended application was cell culture substrates for different biomedical applications. Specifically, the research was focused on the development of a microstructured surface that would mimic human tissue topography to potentially enhance the cell culture process. The research also aims to develop a processing approach for high volume production of this part with high quality using bio-compatible polymers.

The research also investigated if Si tooling is the proper material/method for this process, mainly due to its brittle nature, and relatively high pressures employed in injection molding. For high volume manufacturing, a long-lasting mold is a key factor in offsetting the high cost of mold cavity micro-fabrication. In this research, the life expectancy of the

Si insert is examined and was experimentally and numerically determined to be inadequate for micro-scale injection molding.

Demolding force for oval and cylindrical micro geometries were calculated and used as input for the mold fatigue simulation. Mold fatigue life simulations were performed to show the effect of cyclic loading under micro injection molding cycles. It was shown that Si molds survive for hundreds of cycles. In the experimental work, Si molds survive only for 105 cycles this implies that there are other factors that needed to be considered such as micro/nano cracks that initiated when fabricating these types of mold.

Bulk metallic glass (BMG) showed a potential mold life for these specific features scale, but it needs a better fabrication technique to transfer the pattern completely into the BMG mold. Microcavities with 5  $\mu\text{m}$  diameter with 2  $\mu\text{m}$  depth were successfully fabricated over a 2x2 mm BMG mold surface.

Silicon (Si) molds with micro-holes were fabricated using ultraviolet lithography followed by deep reactive ion etching (DRIE). Scanning electron microscopy (SEM) was used to validate the targeted dimensional specifications of the fabricated mold cavities. The Si insert then served as the mold cavity for injection molding.

Numerical simulations using Moldflow<sup>®</sup> Insight were done to optimize the filling the microcavities and reduce the trial and error type experimentations. Molding experimentations were found to validate the processing parameters conducted from Moldflow<sup>®</sup> simulation. Injection pressure and packing pressure were increased to a point where the material replicates the microcavities entirely.

A cell sensing model was developed to match the effective elastic modulus of human tissue and used as a tool to design micro and nanoscale surfaces. In this model it

was assumed that the cell culture process will be enhanced if the effective modulus of substrate mimics that of the extra cellular matrix that the particular type of the cell will in contact with in its native environment and the mechanical interaction between the cells and the substrate was determined. The model was derived based on pillar deflection and shear deformation that was expected during cells culturing process. The Euler-Bernoulli and Timoshenko approximations were utilized for the calculations. This model will provide a better method to design pillar arrays prior to cell culturing procedure and significantly improve the ability to study cells developments.

This dissertation outlines my contributions to the advancement of the science and technology related to micro and nano injection molding technology. These contributions include the design and fabrication of micro features over dense area and development of a scientific framework to understand the role of processing parameters on the quality of microinjection molding through numerical simulations and experiments.

## CHAPTER 1: INTRODUCTION

### 1.1 Micro/Nanostructured Surfaces

Surfaces with micro/nano-scale features are ubiquitous in nature. Such surfaces provide unique characteristics such the adhesion of gecko feet, vibrant colors of butterfly wings or the non-wetting behavior of lotus leaves as shown in Figure 1-1. The field of biomimetics focuses on the implementation of these nature-inspired concepts and principals for developing functional materials and devices with characteristic properties that cannot be derived from the material itself. For example, incorporating micro-scale to a surface mimicking lotus leaf could render it hydrophobic allowing water droplet to slide on the surface and remove dust.

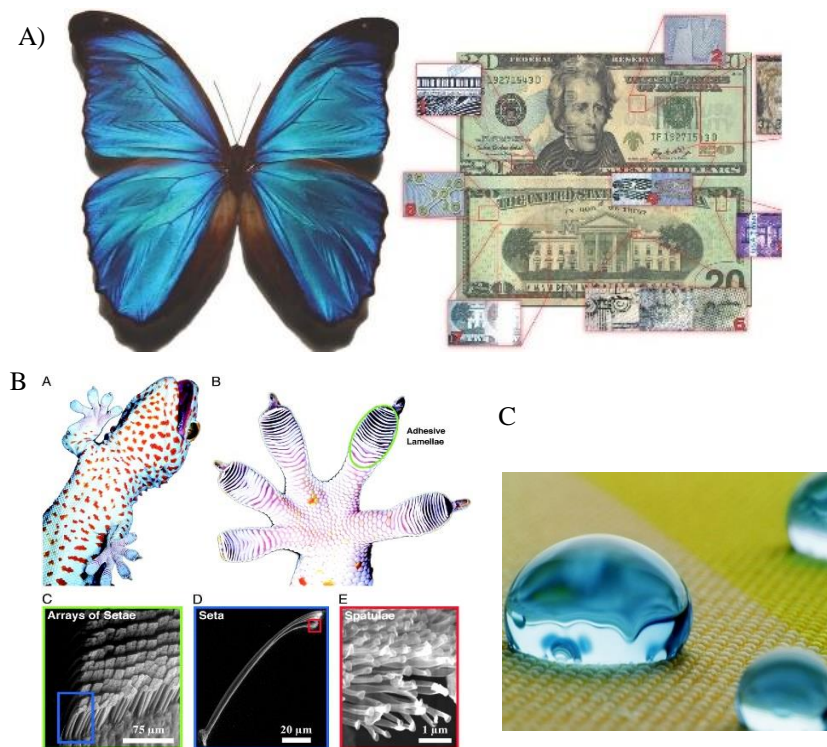


Figure 1-1: Nature based Micro / Nano applications [1–3].

Several manufacturing techniques such as injection molding, hot embossing; ultra violet nanoimprinting lithography have been utilized for manufacturing functional polymer materials with micro/nano-scale features. Among these techniques micro-injection molding is an attractive technique primarily because high precision parts weighing less than 100 mg with a tolerance of less than  $\pm 1 \mu\text{m}$ [4] can be produced economically. Since the first introduction of this manufacturing process in 1872, it has been reinvented and optimized for mass producing plastic parts for a vast array of industries including automotive, aerospace, electronics, medical as well as wide range of consumer products. A few example of micro/nano products can be seen in Figure 1-2.

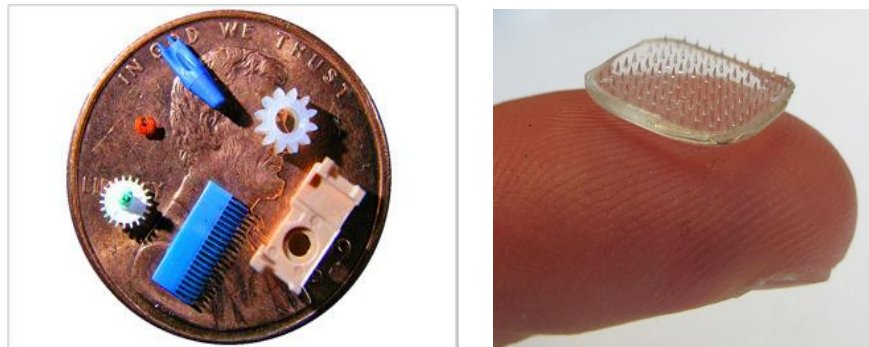


Figure 1-2: Micro molded parts [5,6]

## **1.1 Problem Description**

One of the biggest challenges that face micro molders is the ability to fill a micro mold sufficiently. Finding the optimum processing parameters to ensure a complete filling of a certain micro cavity could lead to a better way to enhance the replications of micro surfaces with high aspect ratio. Silicon-based mold inserts are widely used in micro and nanoscale features replication, but their strength, durability, and heat transfer characteristics are often insufficient for high volume, high-speed molding. Some of these challenges will be investigated in this investigation to overcome some of these issues.

On the other hand, micro molded substrates were used to study the effects of modifying the substrate topography with different shapes and aspect ratio. Substrate stiffness plays an essential role in cells mechanosensing to determine a proper microenvironment during the cell culturing process. It has been found that substrate stiffness and topography have a significant impact on traction forces as well as cell differentiation.

## **1.2 Opportunity**

Microinjection molding is a low-cost process that can fulfill the requirements of microfluidic devices and biological testing applications. It has been shown in the literature that many advancements have been done to overcome certain limitations to advance the process of microinjection molding. In order to satisfy the market needs, this technology needs more investigations on pattern filling accuracy and improved replication rate.

The global market of injection molding is predicted to reach \$278 billion by 2020[7]. The medical market is expected to raise around 50% to hit \$3.5 billion by 2018 [7]. Thus, there is an extensive need for medical micro and nanoscale molded parts to be innovatively designed and made to attain the market needs.

A few companies have modified existing cell culture devices through biological coating (collagen, laminin, and fibronectin), synthetic nanofiber surfaces, and plasma treatment to enhance hydrophobicity, cell performance, and functionality. These advancements require an additional cost to main culture devices, special handling, and storage. Due to previous requirements, these products are not widely commercialized. In this work, a plate with micro/nanostructures that mimic human tissue topography was fabricated through microinjection molding to serve as substrates for cell culturing developments. Consumable micro molded surfaces fabricated were placed on petri-dishes and 96 well plates to study cell behaviors to the surrounding microenvironment and optimize cell culturing growth.

## **1.2 Research Motivation and Program Objectives**

### **1.2.1 Biomedical Cell Culture Development**

In medical applications, the demand for new products is dramatically growing. Cell to substrate interactions have got attention recently in both academic laboratories and industry. Cells interact with chemical and mechanical signals from surrounding microenvironments. While chemical signals have been well studied in the last decade, mechanical cues are also significant to cell growth owing to a surface rigidity and

compatibility. Cells that make tissues are adherent to their surrounding extracellular matrix (ECM). ECM is made up of non-cellular components present with all tissues and organs that provide both physical support and mechanosensing distribution in both directions [8]. Cells explore a cultured substrate via traction forces in order to migrate across their environment, and also mechanically sense the characteristics of the substrate. The stiffness of the substrate plays an essential role in cells mechanosensing. It has been recognized that substrate stiffness has a significant effect on traction forces as well as cell differentiation[9]. Fabrication of substrates with micro and nanopillars have made it possible to estimate cell traction forces through pillar deflection [10].

In this dissertation, polymeric platforms with micro/nanostructures that mimic human tissue topography will be fabricated through microinjection molding to serve as substrates for the cell culture process as shown in Figure 1-3.

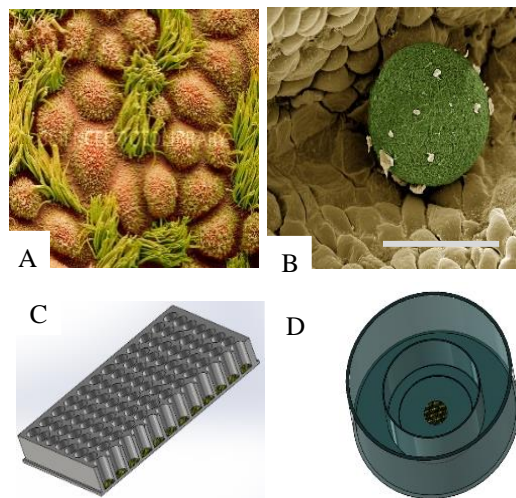


Figure 1-3: A) Fallopian tube surface. B) SEM of a fertilized human ovum in a fallopian tube (Scale bar 100 um), mag. 1000x. C-D) 96 well plate & Petri dish with micro molded plat[39, 40]

### **1.2.2 Target Application Area**

Besides the manufacturing of consumable substrates for the cell culture development applications that are targeted in this investigation, increasing the scientific understanding of microinjection molding processes will increase the demand for new innovated products. Many applications such as micro-electro-mechanical systems (MEMS), automotive and microfluidic devices, surgical devices, pharmaceutical industries will be affected by existing technologies and provide new ideas to be innovated.

### **1.2.3 Research Motivation**

Microinjection molding is considered one of the highest growing markets globally in many areas. In medical applications, the demand of replicating micro surfaces to study the behavior of cell interactions with the replicated substrates is high. The substrate stiffness can be manipulated using spacing of the microstructure and the aspect ratio. In this work, a cell sensing model was developed to predict the effective elastic modulus of human tissue and used as tool to design micro and nanoscale surfaces for laboratory research.

Silicon-based mold inserts are widely used in micro and nanoscale features replication in academic laboratories, but their strength, durability, and heat transfer characteristics are often insufficient for high volume, high-speed molding. In order to replicate these types of features, a proper tooling is needed to achieve higher replication rate. It also requires precise control of the molding process parameters and most necessary to fabricate better molds that can last longer for large production scale to meet the marketing demands.

#### **1.2.4 Dissertation Objectives**

The main objectives of the proposed research program include:

1. Developing a robust micro-injection molding processing strategy to fabricate parts with micro/nano features. That will involve designing, fabricating, and testing micro and nano mold inserts.
2. Evaluating alternative methods to fabricate robust mold inserts with optimal tooling life for high productivity that could replace silicon-based mold inserts.
3. Optimizing injection molding process parameters to achieve high cavity filling with the aid of numerical simulations followed by experimental verification of the simulations.
4. Analytically and experimentally examining mold insert at optimum processing condition to evaluate mold capability and robustness for high volume manufacturing.

#### **1.3 Dissertation Structure**

This dissertation presents the design, fabrication and precise production of a biomedical part with enhanced properties. The biomedical part will mimic human tissue topography and is intended to enhance cell culture process. The aim of the research is to develop a strategy for high volume production of this part with high quality and biocompatibility.

This dissertation consists of eight chapters described as follows.

Chapter 1 presents a brief description of the research topic with potential opportunity for microinjection molding of surfaces with micro/nano features. The overall targeted area and specific research objective are also listed.

Chapter 2 details the research related scientific background to this study, including information on microinjection molding, types of tooling used to replicate features in a microscale and an overview of common challenges of polymer flow behavior in micro and nanoscale. It also provides an overview of the outstanding challenges and describes the research objectives to overcome some of these challenges in details.

Chapter 3 describes a theoretical analysis of micro/nanoscale features for studying cell mechanosensing. This theoretical cell sensing model will allow a proper understanding of pillar deflection and shear occur during cells culturing process based on Euler-Bernoulli and Timoshenko approximations. A cell sensing model is also established to match the effective elastic modulus of human tissue and used as tool to design micro and nanoscale surfaces for laboratory research.

Chapter 4 presents the work performed to fabricate the desired micro features on two distinct substrates.

1. Silicon (Si) based tooling with micro holes were fabricated using photolithography followed by deep reactive ion etching.
2. Bulk metallic glass based tooling was made using Si with micropillars that were thermoplastic formed in a hot press with controlling temperature and pressure to maintain the amorphous structure.

Chapter 5 describes the results of the numerical simulations (using Moldflow<sup>®</sup> Insight) performed to optimize the filling of cylindrical micro-cavities under the

processing conditions. Preliminary processing parameters derived from Moldflow simulation were utilized as input for experimental investigation in chapter 6 for optimal filling of the micro-cavities.

Chapter 6 contains experimental results of replication of the targeted features on different polymeric materials. Samples were primarily characterized using scanning electron microscopy. The focus was to gain insight on the replication rate of the features and repeatability of the molding process.

Chapter 7 provides a financial analysis of molded parts unit costs using both molds discussed in chapter 4 in order to assess the commercial viability of the processing strategy employed in this research.

Chapter 8 presents the conclusion of all the work performed in this research effort and the impact of this work. A few potential strategies to address the outstanding issues are also presented in this chapter.

## **CHAPTER 2: RELATED SCIENTIFIC DEVELOPMENTS**

### **2.1 Injection molding at the micro and nanoscale**

Injection molding is considered one of the fastest growing markets globally in many areas such as MEMS, industrial, medical application and microfluidic devices. Microinjection molding has been around since the 1980s [11]. The microinjection molding process is not typically reducing the scale of the standard injection process. The process requires an intelligent consideration of each step until the final product is ejected from the mold [11]. High-quality mold fabrication is critical for microscale injection molding since once the mold insert is in place, it is expected to produce large quantities of the product with some adjustment for the other parts of the process. However, fabricating of an excellent mold does not always guarantee that a good product will be manufactured. Molding processes have its challenges to highly replicate the mold in such scale.

#### **2.1.1 Micro Injection Molding Machine and Modification**

There are several commercially-available micro-injection molding machines produced by companies such as Sumitomo, Wittman Battnefeld, Fanuc, and others. The microinjection molding machines are different from conventional machines in its capability of small shot sizes down to 9 grams (1/3oz). These machines use a small screw size (down to 14mm diameter) and are capable of very high injection pressures (up to 275MPa). They are also much more capable of controlling and monitoring the fill, pack, and hold cycles than larger conventional presses. The basic functionality and cycle

sequencing of these micro-scale presses are no different from larger conventional presses. They still use a reciprocating screw in a heated barrel to melt and advance the material into the dosing chamber, and they still use a plunging motion from the screw to inject the molten material into the mold, through a sprue and runner system, then into the cavity.

Microinjection machines have a primary distinguishing unit called a plasticization unit (Figure 2-1). This unit can control the shot size, therefore, regulating the degradation of the polymer due to high temperature.

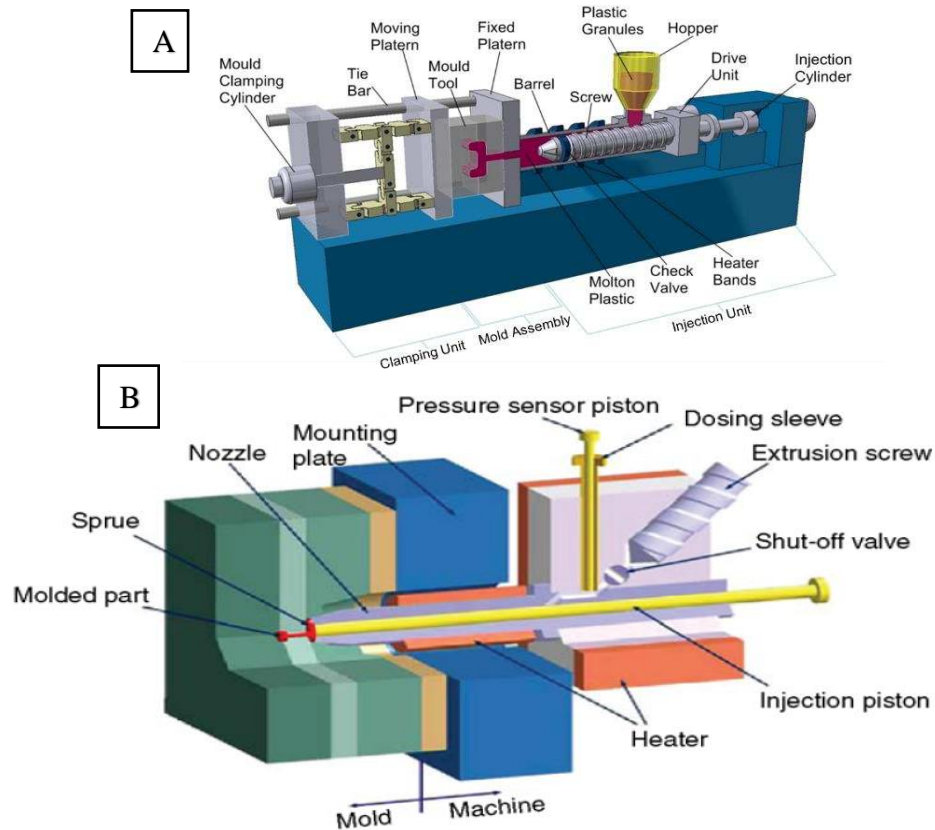


Figure 2-1: A) Conventional Injection Molding Machine. B) Plasticization unit for  $\mu$ IM[12,13]

### 2.1.2 Critical Processing Parameters

Micro-injection molding presses use the same mechanisms for molding as larger traditional presses do. The typical injection mold cycle has the following steps:

- Close the mold;
- Apply clamping pressure to the mold;
- Fill the mold cavity by plunging the screw forward at a programmed speed profile;
- Pack the mold cavity by applying a programmed packing pressure and hold the mold cavity under a programmed pressure until the gate is frozen enough to prevent backflow of the plastic;
- Release the injection pressure and prepare the next dose by retracting the injection unit and spinning the screw to advance the molten plastic to the front of the barrel;
- Hold the part in the mold until it is sufficiently cooled and solidified;
- Open the mold;
- Eject the part;
- Start the next cycle.

Another critical part of the micro-molding process that is not linked to the mold press, mold tool, or the molding material, is the ambient environment in which the molding occurs. Industrial injection molding is not a clean process. Oils, dust, coolants, and foreign objects are common contaminants in an injection molding operation. A typical dust particle is between  $2\mu\text{m}$  and  $10\mu\text{m}$ ; they are larger than many of the features being molded during

microinjection molding. For this reason, microinjection molding should be done in a clean room with High-Efficiency Particulate Air (HEPA) filtered and non-hydraulic mold presses. It is also essential to keep the mold tooling immaculate. Mold cavities with micro features should never be cleaned by wiping them with a cloth because of the abrasive foreign objects that can quickly and inadvertently get trapped within the cloth. Visible scratches on the cavity surface could be larger than the micro-features; once it formed, then the cavity is probably ruined. Raw resin is also a critical factor in micro molding; It has to be stored and conveyed to the machine in a way that prevents contaminants from getting into it. Potential contaminants can be metal shavings or dust and can act as abrasives during the mold cycle and also damage the cavity.

Filling the cavity has always been a challenge in microinjection process. This issue can be solved efficiently in conventional injection machines by controlling the pressure and the speed of the process. Raising the pressure forces the material to flow into the narrow cavities but the freezing layer will resist the flow causing product defects as high stresses and sink marks. Another solution is increasing the injection speed that decreases the viscosity of the polymer melt due to the shear- thinning effect associated with viscoelastic materials thus enhancing the filling process[14]. Other methods have been proposed as increasing the mold temperature to the melt temperature of the polymer to avoid the formation of a frozen layer. Another method is creating a vacuum in the cavity to prevent air bubbles[14]. In a traditional injection molding process, some adjustments have to be done to achieve filling accuracy to produce microscale products. Increasing the runner size is applied when micro scale product is required on a standard injection machine.

### 2.1.3 Micro-Injection Molding Technology

In all plastic manufacturing processes, temperature, pressure, shear rate all greatly influence the physical and mechanical properties of the final part. Micro/nano Injection molding is not different from conventional injection molding regarding parameters that control the replication process, but additional factors are involved to assure complete fill and micro-features sufficient demolding. In a study by Zhang et al., the effects of mold temperature, hold pressure, and injection velocity was related to the quality of the micro-feature replication[15]. A Veeco Optical Profilometer was utilized to measure the height of the micro-features on the part. In their Design of Experiments (DOE), they used the following parameters:

- Mold Temperatures: 60°C, 100°C
- Injection Velocities: 100mm/sec, 250mm/sec
- Hold Pressures: 50Mpa, 70Mpa

The rest of the parameters in the injection cycle remained constant for all of their samples. It is important to note that the melt temperature of the polymer used in the study was 210°C. The thinnest feature on the test specimen was approximately 300nm wide. Their results showed that the parameter with the biggest influence on feature quality was the mold temperature, followed by the injection velocity. The holding pressure had a minor effect. The higher mold temperature was more successful at filling the features because it allowed the polymer to stay molten for a more extended period, therefore increasing its filling time in the feature. The higher velocity decreased the viscosity of the polymer allowing it to flow easier into the microfeatures. As expected, the most significant factors

in successfully filling the mold were directly related to the viscosity of the material, which is controlled by temperature and shear rate. It is also interesting to consider that the high holding pressures were not very effective at “packing” the cavity in the micro features. This is likely due to rapid solidification of the polymer once it touches the cooler mold, caused by the high surface area to volume ratio of the part.

## 2.1.4 Mold Temperature Control Methods

### 2.1.4.1 Conformal cooling

In injection molding, conventional cooling arrangements utilize straight line cooling channels (Figure 2-2). In contrast, the conformal cooling scheme utilizes cooling lines that follow the geometry of the part. Conformal cooling helps to generate a uniform temperature distribution in the molded parts [16]. Conformal cooling channels are used to reduce the cooling time in the injection molding process since cooling time consumes more than 50% of the injection molding cycle time. It was observed that this technique could reduce the cycle time by 20% to 40% [17]. Moreover, it also helps to reduce warping issues in parts. The design of the conformal cooling channels could be done with the help of Autodesk mold flow simulation to ensure the better design of cooling channels.

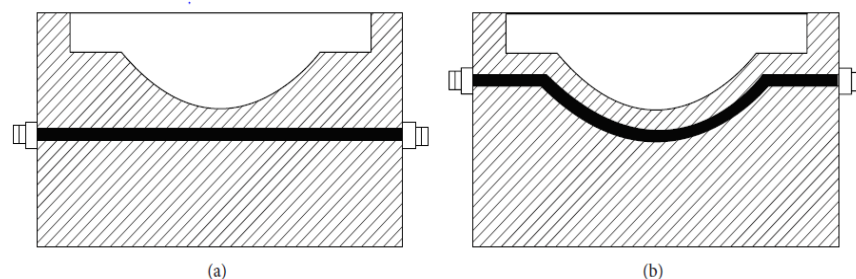


Figure 2-2: (a) Straight drilled cooling channel. (b) Conformal cooling channel [15].

#### 2.1.4.2 Variotherm Heating Systems

The variotherm process involves raising the mold temperature during the filling phase, then quickly cooling it down at the end of the filling. Due to high mold temperatures usually higher than polymer freezing temperature, the frozen layer which generally causes incomplete filling of targeted micro-cavities is reduced or entirely vanishes. The benefits of using variotherm processing include improving the melt flow, reducing the residual stress between the melt flow and mold walls, improving molded parts quality and micro-channels replications. This process is used to reduce cycle time and to solve molding problems such as weld lines, flow marks and sink marks. Variotherm heating can be identified into two categories:

- Passive Heating
- Active Heating

In the passive approach, the cavity wall heats up by the conduction of thermal energy from the injected melt, the water flow for mold cooling is interrupted during this step, An active heating approach utilizes warm fluids or electromagnetic induction coils to heat the molds. Then, an intense cooling phase is applied to cool the mold, resulting in lower cycle time without consuming more energy (Figure 2-3)[18,19]. During active heating, the mold temperature is held to the glass transition temperature which helps achieve higher aspect ratio micro and nano features, and it also works to reduce the amount of distortion on created geometries thus influences the final product quality. While increasing the mold temperature, the chance of creating the frozen layer that usually

initiated at mold walls decreases with higher mold temperatures. In this work, mold base cartridge heaters are designed to control mold temperatures as explained in Chapter 5.

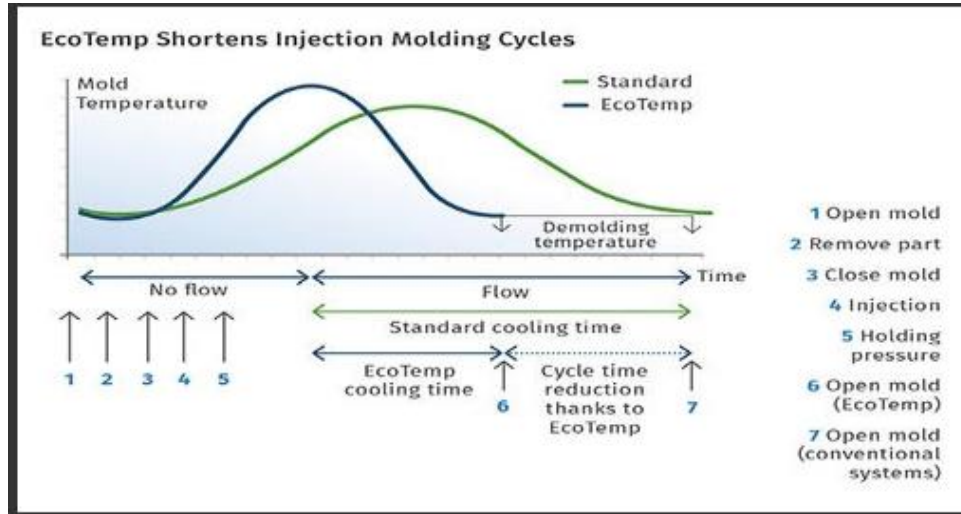


Figure 2-3: Injection molding cycle time using variotherm passive approach [16].

### 2.1.1 Applications

Polymers are attractive materials for various applications such as medical, electronic, commercial, and other applications because of their strength, optical transparency, biodegradability, and biocompatibility. Micro –Electro Mechanical Systems (MEMS) are in size between 20 $\mu$ m and 1mm and are made up of components ranging in size from 1 $\mu$ m to 100 $\mu$ m. They often contain a microprocessor and micro-sensors and are used for micro-scale sensing and analytics such as blood testing devices, accelerometers in automobile airbag sensors, and ink cartridges. Microinjection molding is used to produce the plastic

components used in these systems due to its relatively high production speeds, and high volume capacity.

The biodegradability and biocompatibility of certain polymers such as Polystyrene (PS), Polyethylene (PE), and Polylactic acid (PLA) make them an ideal choice for various applications such as surgical implants, drug delivery, bone fixation. Microinjection molding is a preferred technique for fabricating parts for such applications. An example of an advanced drug delivery system is presented in Figure 2-4. In this application, an array of polymer microneedles is used to inject medication through the skin without reaching the nerves system causing no pain for the patient [20].

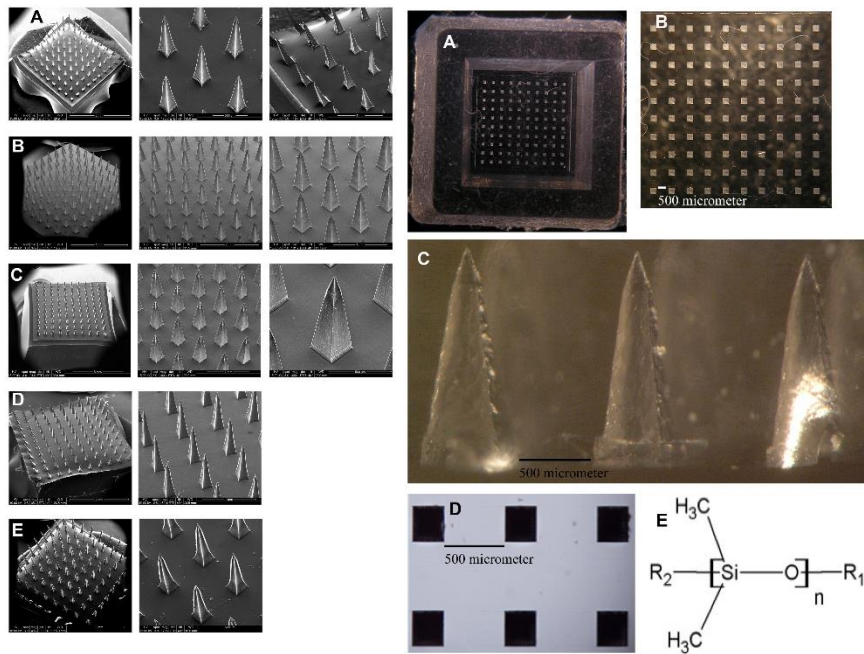


Figure 2-4: PDMS microneedles array for drug delivery [20].

## **2.2 Tooling Fabrication Methods**

Microfabrication is the term that used to describe processes of making micro/nanoscale structures. Micro molded features are intended to interact with cell and microorganisms in the nanoscale. In order to replicate small devices that can diagnose and examine these types of micro or nanoscale organisms, manufacturers have been striving to find a better mold with that precision nanoscale. Conventional tooling turns out to be hard to reach down to this scale with hardened steel tooling due to grain boundary deficiencies[21].

The mold is an essential component where the microfeatures are formed. Several fabrication techniques have been used to make mold inserts as discussed in detail in the following section.

### **2.2.1 Silicon-Based Tooling**

Silicon-based tooling is widely used because of its precise and controlled fabrication procedure for these types of features at this scale. Several techniques exist for the fabrication of silicon toolings.

#### **2.1.4.3 LIGA**

LIGA is a German acronym for lithography, electroplating and polymer replication. The term LIGA was introduced in 1982[22]. It offers high precision tooling fabrication with high aspect ratio features and low wall roughness. The process starts with coating a Si wafer with a conductive material (Au, Cr...) followed by another coating of polymethyl

methacrylate (PMMA) or negative SU-8 resist as shown in Figure 2-5. A positive X-ray mask that has the pattern of the final product is then placed over the coated wafer and exposed to high X-ray or UV radiation forming a PMMA pattern. Next, the electroplating process begins where an electrolytic cell with anode and a cathode are plunged into an electrolytic bath forming the mold insert. LIGA is one of the best micro mold fabrication techniques but is cost prohibitive for many applications. The fabrication cost is high for both the X-ray source (\$250 per hour), and the X-ray mask price varies from (\$12000-\$25000)[22].

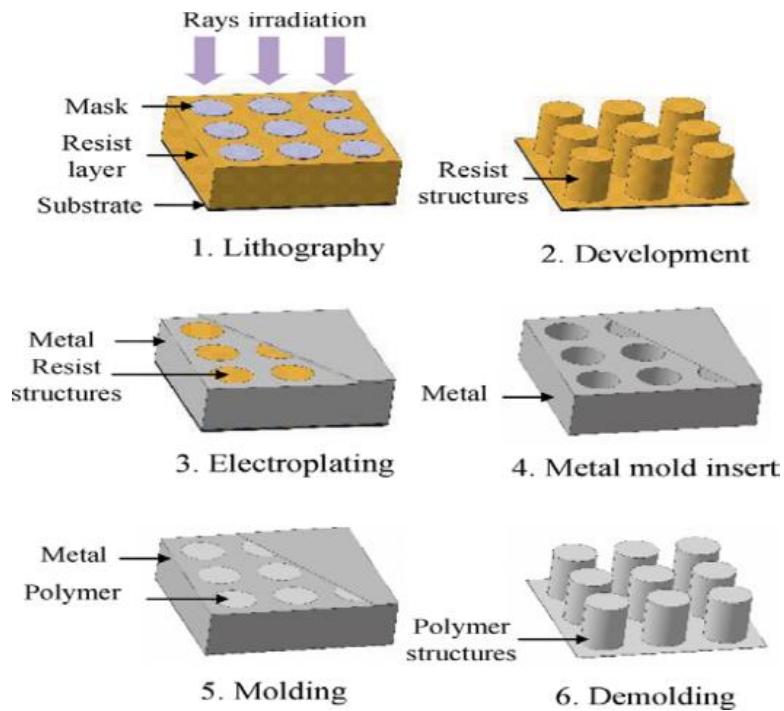


Figure 2-5: The process of LIGA [11]

#### 2.1.4.4 Photolithography

UV lithography is a widely used process for microelectromechanical systems (MEMS) industries and the only technique for scalable patterning mass production [23]. In this process, the patterns are initially created on a mask and transferred to the substrate by utilizing a light source. Ultraviolet (UV), X-ray, e-beam, laser and ion beam commonly used as the light source in the lithography process. Based on the light source used in lithography, the minimum size of features that can be fabricated is determined to be down to 10 nm using e-beam lithography.

The process starts with cleaning silicon wafers to remove contaminants followed by baking at temperatures  $>100\text{C}^\circ$  to remove residual moisture. The silicon wafers are then spin-coated with a photoresist (PR) whose thickness can vary from 500nm to 25000nm [24]. The thickness is controlled by varying the spinning velocity. Patterning resolution is affected by the thickness and uniformity of the PR layer[24]. Thin photoresist produces high pattern resolution, but pinholes might exist in these thin PR layer causing pattern defects. After spin coating, a soft bake for 30 minutes is applied to ensure optimal PR adhesion. Next, the mask is aligned with the wafer and exposed to UV light. The photoresists can be a negative PR or a positive PR. In this process exposed regions become more soluble when a positive PR is used while for a negative PR the exposed regions become harder. Then the wafer is subjected to an organic solvent as a developer. The positive PR exposed areas dissolve and unexposed areas remain while the opposite happens with the negative PR as seen in Figure 2-6. A hard bake at  $180^\circ\text{C}$  for 30 minutes improves

adhesion and residual solution removal. Once the pattern in the mask is transferred to the PR layer, an etching process is needed to transfer it to the wafer.

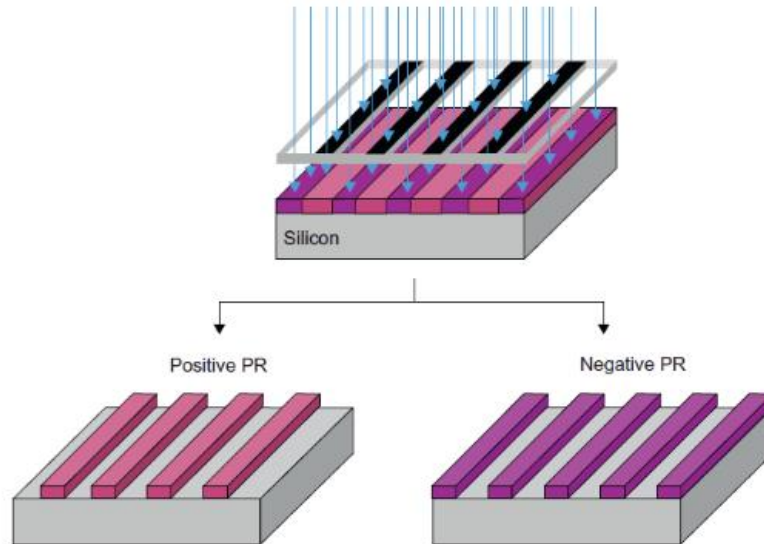


Figure 2-6: Positive and Negative Photoresist [23]

#### 2.1.4.5 Deep Reactive Ion Etching (DRIE)

Deep reactive ion etching (DRIE) is essential for high aspect ratio (HAR) patterning. The Bosch process is currently the most common process for HAR etching in DRIE nanofabrication. This process consists of repeating steps of plasma etching and passivation step (sidewall coating). A typical etching profile in the DRIE process can be isotropic or anisotropic. As shown in Figure 2-7(A), isotropic etching attacks material in all directions while in Figure 2-7(B) anisotropic, etching is substantial in one direction. Isotropic etching is performed using sulfur Hexafluoride ( $\text{SF}_6$ ) plasma which reacts with Si wafer to produce  $\text{SiF}_4$  (gas) that is pumped out of the system. Isotropic etching depth is limited to less than  $1\mu\text{m}$  because of the  $\text{SF}_6$  etch rates. To reach higher depth an

octafluorocyclobutane ( $C_4F_8$ ) polymer coating has to follow before each  $SF_6$  etching step until the required depth is achieved. The result is an anisotropic etch that can have a vertical sidewall with nano scallops of dimensions  $< 50$  nm. The Bosch process has an etching rate range from  $1.3\text{-}3 \mu\text{m}/\text{min}$  [25]. Many factors that affect etching rate including etching gas  $SF_6$  flow rate, duration of the etching process, coating polymer  $C_4F_8$  flow rate, power during etching and passivation, temperature, chamber pressure, and gas combustion during the process[26]. Mask selectivity is also another critical factor in dry etching. While the masking layer can be PR or silicon dioxide ( $SiO_2$ ) or both of them, the etching ratio can increase to 100:1 in  $SiO_2$  case[25].

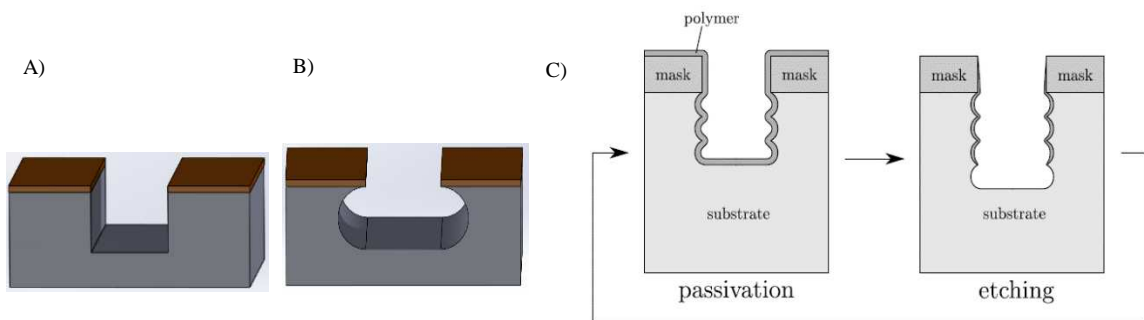


Figure 2-7: A-B) Isotropic and anisotropic etching. C) Alternating process passivation and etching processes during DRIE technique[23].

#### 2.1.4.6 Electron Beam Lithography

Electron Beam lithography (EBL) is used to fabricate small features that conventional lithography is not capable of due to the limitations imposed by the wavelength of light. EBL utilizes electron beam to pattern features down to 10 nm. The pattern is transferred by exposing the resist to electron beam over the substrate with the designed CAD program. EBL uses an electron sensitive resist which softens when exposed to the electron beam and

removed by a developer. After developing, the resist on the substrate is used as a mask for transferring the pattern into the substrate by etching techniques or sacrificed for lift-off patterning[27,28].

### **2.1.5 Aluminum Anodic Oxide (AAO)**

Aluminum Anodic Oxide (AAO) is a nonporous self-ordered structure that produces through an electrochemical anodization process. Nanoporous AAO membranes have shown superior properties improvement in areas including molecular separation, biosensors, energy storage, electronics...etc. The parameters of the AAO structure can be precise by controlling anodization conditions. The pore diameter range can be 10-400 nm, with interpores distance 50-600 nm, and a thickness of 10 nm to 150  $\mu\text{m}$  as presented in Figure 2-8[29,30]. AAO prepared by anodization of aluminum (Al) using an electrolytic cell. Electrolyte type influences the anodization process and dominates the feature size. For example, the pore size of electrolyte as oxalic acid, phosphoric acid, and sulphuric acid respectively will reach 80, 100, 235 nm[29]. AAO structures are produced using two-step anodization. Before starting the process, the Al substrate has an oxide layer formed by the ambient oxygen at the atmosphere should be treated using acetone and then electrochemically polished in a solution of NaOH for 5 minutes then washed in water[31]. Uniform oxide layers will initially form under a constant voltage condition applied. Once this layer has been created, the current density drops quickly allowing the growth of the well-ordered pores. The first step will take around 7 hours. In the second step of the anodization process, the foil was anodized for an hour in phosphoric acid to get the required pore depth [31].

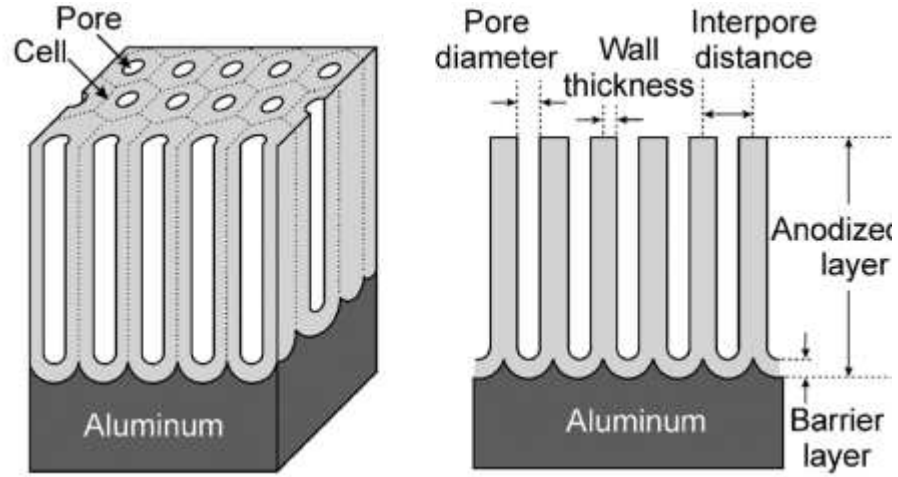


Figure 2-8: Schematic drawing of AAO structure prepared by electrochemical anodization of Al [29].

### 2.1.6 Bulk Metallic Glass Inserts

One of the main challenges faced by the micro/nano injection molding industry is the ability to create durable mold cavities that can be machined to have sufficiently small cavity features for the desired part. There are several methods for creating silicone-based inserts, but their strength, durability, and heat transfer characteristics are often inadequate for high volume, high-speed molding. One technology that is addressing this deficiency is creating inserts using Bulk Metallic Glass (BMG) [15,32] for more generally referred to as amorphous metals. Traditional metals form crystalline micro-structures when they freeze. The grain boundaries in metals serve as crack propagation paths, so when machining operations remove metal, it is challenging to consistently machine features smaller than the average grain size. In machinable steels, the typical grain size is on the order of 100 $\mu$ m, several orders of magnitude larger than the nano-scale features often required in micro/nano injection molding. A new class of metal materials (BMG's) is used for inserts

in micro/nano injection mold tools. These metals are amorphous, meaning they are free from crystal micro-structures and free from grain boundaries. This amorphous microstructure is obtained by quenching these special alloys so that the atoms do not have time to arrange themselves into crystals before being frozen. These alloys are typically composed of more than four metals, and each substituent comprises a significant percentage of the alloy. For example, the commercially available BMG named Vitreloy is an alloy of Zirconium (41.2%), Beryllium (22.5%), Titanium (13.8%), Copper (12.5%), and Nickel (10%). In contrast, P2 Tool Steel, which is commonly used as a mold cavity material, is made of Iron (98%), Carbon (.15%), Manganese (.5%), Chromium (.7%), Molybdenum (.5%), and Silicon (.2%). Since steel is 98% iron, the iron atoms have no problem finding other iron atoms nearby, and crystals are easily formed. Each atom type in Vitreloy 1-b, on the other hand, has a very high probability of not being close to another like atom while in the molten state. Therefore, if the metal is frozen at a rate quicker than the atoms ability to congregate, no crystal structure is formed. The micro or nano-features can then be established onto the surface of the alloy with high precision because instead of removing grains of metal from the bulk material, individual atoms are removed. Another feature of the alloy that helps lock the atoms in place during cooling is the large size of the atoms. Their size restricts their mobility within the matrix, and therefore their ability to organize. Coincidentally, the cooling or quenching rates of these alloys do not need to be fast at all.

A few fabrication methods have been used to imprint the desired features onto the surface of the BMG insert. One method is to mold or imprint the geometry onto the surface

using a silicon master. The silicone master can have the relief features added to it either by lithography or electroplating Nickel. These methods consume the silicone master so that it cannot be reused, and can be very time to consume. Another method to machine the nano-features directly onto the BMG insert is a method called Focused Ion Beam (FIB) machining. FIB machines closely resemble Scanning Electron Microscopes (SEMs), but instead of deploying focused electrons, they deploy focused ions. These ions are generated from a highly energized liquid metallic source, usually Gallium, which is wetted onto the tip of a tungsten needle. When heated and electrically charged, the Gallium forms a cusp on the tip of the needle with a radius of approximately 2nm. When the needle is placed near the mold insert, the large electric field causes a focused emission of Gallium ions, which is only a few nanometers wide. This beam is capable of creating features on the order of 10nm. The high-energy emission of the ion beam essentially evaporates the BMG material, and therefore directly etches the micro-features onto the BMG insert. Machining rates using FIB are slow (about 30 minutes to remove 500 $\mu\text{m}^3$  of material from pure copper), but it is still much faster than creating a silicone master to imprint the features onto the insert. Once the FIB machining is complete, the BMG insert is ready to install into the mold base, and since it is metallic, it will have the heat transfer properties necessary to transfer the heat into and out mold cavity quickly. It will also have very high compressive strength, and therefore, be able to withstand tens of thousands of injection cycles, something that silicone-based inserts cannot withstand.

### 2.1.7 Laser Micro-Drilling

Precise laser micro drilling is used to cut through many substrates. Laser drilling is capable of fabricating holes down to 15  $\mu\text{m}$  in diameter, but the process needs a minimum feature spacing of 35  $\mu\text{m}$  to prevent refilling of drilled holes with expelled molten material as seen in Figure 2-9. Figure 2-10 shows 15  $\mu\text{m}$  cylindrical holes with 35  $\mu\text{m}$  spacing that was drilled on a steel substrate photo provided from Oxford Laser [33].

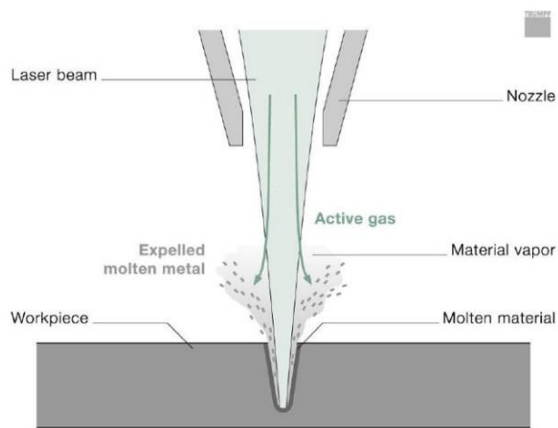


Figure 2-9: Schematic of a laser cutting machine.

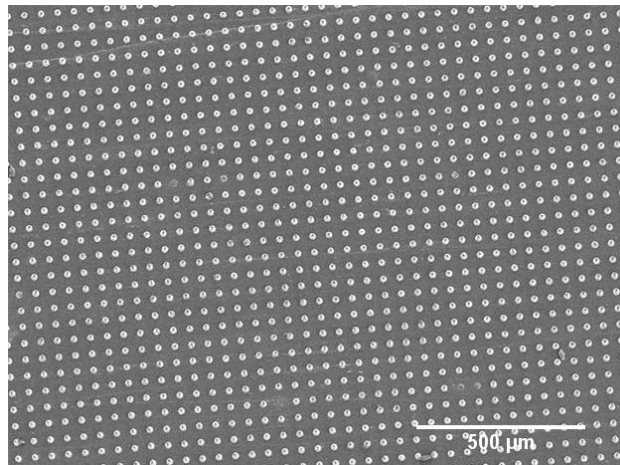


Figure 2-10: 15  $\mu\text{m}$  holes laser drilled with a pitch of 30 $\mu\text{m}$  on metal mold[33].

### 2.1.8 Nickel-phosphorus Plating (NIP)

Ultra-precision machining with diamond tool has ability to fabricate mirror like molds. Hardened steel is the most metal used as mold material in the manufacturing industry. In order to cut hardened steel with diamond tools, preparation of the steel surface is required to eliminate extreme tool wear and surface failure[34]. Wear in the diamond tool can be minimized when it is used to machine NIP layer which leads to high tool life cycle. Amorphous deposited layer of NIP can facilitate higher accuracy of microscale features replication for injection molding insert.

Nickel phosphorous plating (NIP) can be done using many different methods including vapor deposition, melt spinning, chemical autocatalytic (Electroless), and Electrolytic deposition. Electrolytic and electroless methods have shown a vast improvement to plated substrates and taking it to a higher level of material characterization depending on the deposited thickness.

An electroless deposition allows for producing uniform thin layers of pure metals or alloys with properties that are distinct and often negates the shortcoming of the substrate material. It is commonly used in the plating industry due to its high capability in hard to reach areas, reasonable wear and corrosion resistance, high surface finish, high hardness. These properties can also be enhanced further by heat treatment of the coated sample.

Electrolytic NIP is deposited with a phosphorus content up to 28 %[35]. The process is carried in an electroplating cell containing nickel sulfate ( $\text{NiSO}_4$ ), nickel chloride ( $\text{NiCl}_2$ ), phosphoric acid ( $\text{H}_3\text{PO}_4$ ), phosphorus acid ( $\text{H}_3\text{PO}_3$ ), and wetting agents (sodium

lauryl sulfate). The pH is adjusted to be in the range of 3 to 4.5. The source of nickel ions is maintained by nickel sulfate at a range of 150-300(g/L).

Nickel chloride is necessary for anode corrosion and to enhance the conductivity of the plating bath. Concentrations of phosphoric, phosphorus acids and current density play an important role in the deposited layer thickness. The bath temperature is also a critical parameter that affects both phosphorus content and stress deformation on the plated layer, so it is required to maintain at 75 C°[36]. Phosphorous content (P) has a primary effect on the mechanical properties of the deposited layer. It has been observed that a heat treatment at 400° C for an hour can result in superior hardness level (12 Gpa)(Figure 2-11).

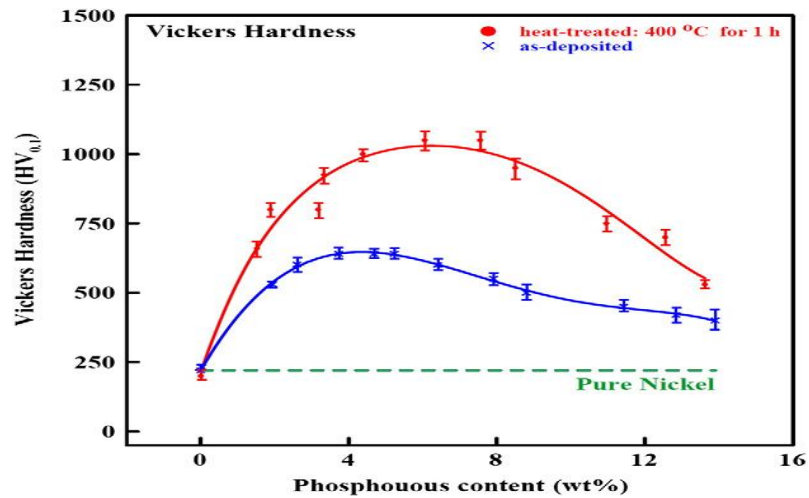


Figure 2-11: Effect of annealing on the hardness of Ni–P alloys10 [37].

Higher phosphorus content is associated with the amorphization of original crystalline structure. High machining accuracy was verified with higher phosphorus content (11% and higher) [36]which makes the deposited layer suitable for diamond turning applications for fabrication high precision parts. Figure 2-12 (a-d) shows that grain

size in the micrometer scale is reduced to nanometer scale when phosphorous content increased. The average grain size ranges from 17 nm to 45 nm after heat treatment.

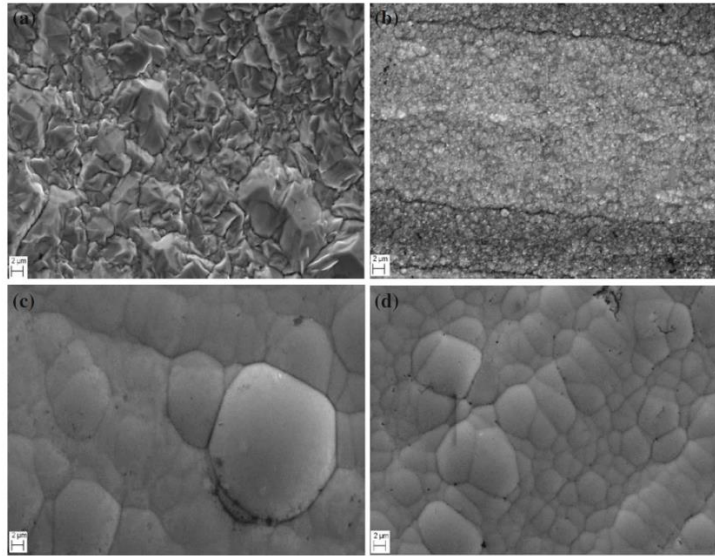


Figure 2-12: SEM micrographs of Ni-P electrodeposits with different P contents. (a) 0% P, (b) 4.64% P, (c) 9.14% P, (d) 15.22% P [38].

### 2.1.9 Sacrificial Tooling

Sacrificial tool fabrications start with patterning a sacrificial tool with a reverse pattern to form a polymer-based mold. This method is widely used in microfluidic systems due to its simplicity, but it is limited to the adhesion between the master tool and polymer. Barry et al. invented a hybrid metal-polymer mold formed by patterning a reverse pattern of silicon wafer over polymer film using the nanoimprinting technique. After metal coating with aluminum or titanium, the polymer mold is used for either injection molding or any other technique for micro molding[39,40].

### 2.1.10 Soft lithography

Soft lithography is a low-cost patterning method which utilizes a master mold to fabricate micro and nanoscale features by applying heat and pressure (some examples are provided in Figure 2-13). The master mold with intended pattern is made via photolithography (described in previous part). Polymers such as polydimethylsiloxane (PDMS) is poured and after it solidified, the PDMS-silicon assembly is submerged in potassium hydroxide (KOH) solution that dissolves the Si wafer. Now the master mask is ready, a layer of thermoplastic resist placed, and mold is heated above glass transition temperature  $T_g$  of the resist. As mold comes in contact, the resist will become hotter and soften to fill mold cavities under certain pressure and time [39,41].

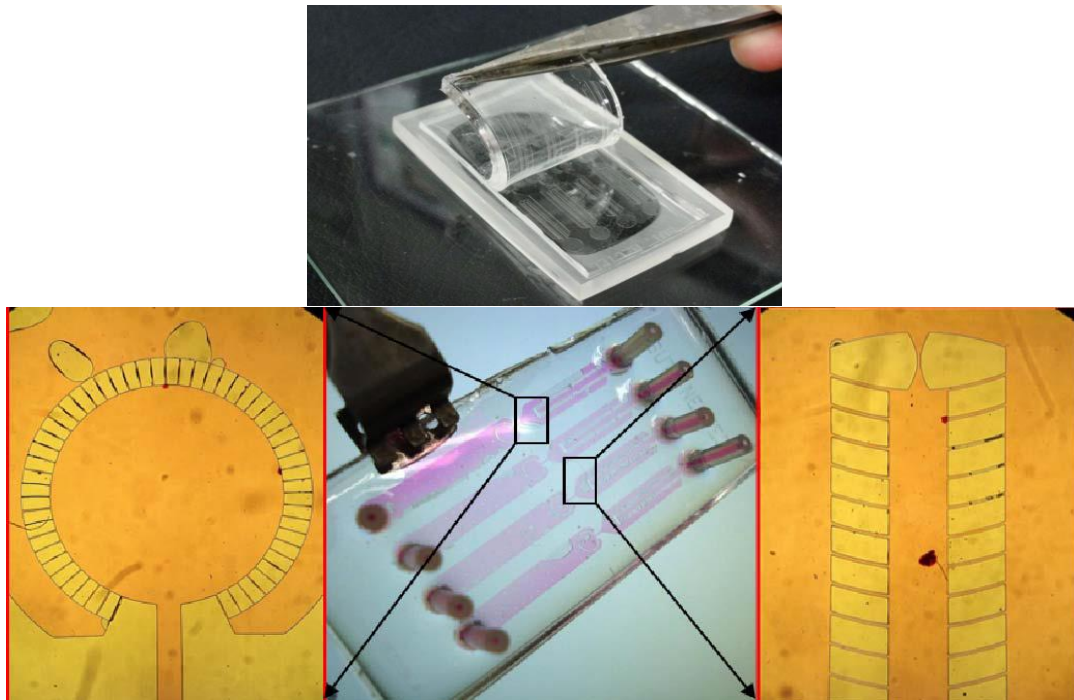


Figure 2-13: PDMS microfluidic chips [29].

### **2.1.11 Demolding Agents**

Mold coating is mostly done to improve cavity filling and reduce frictional forces between mold wall and the polymer during parts demolding. A variety of antistiction coatings has been investigated in the literature with low surface energy as diamond-like carbon, chromium nitride, nickel, aluminum, and fluorocarbon-based coatings. These type of coatings led to better tool-polymer interactions and enhanced tool life.

Yoon et al. did a study., an antistiction fluorosilane based coating deposited on silicon-based mold for injection molding thermoplastic polymers. The inference from this study was that the antistiction coating increases the injection velocity by 10 mm/s and an enhancement of 18% in the replication ratio[42].

## **2.2 Polymer Micro Fluidic Flow**

### **2.2.1 Macro/ Micro interface**

The characterization of rheological properties of polymers on a macro scale is a well-developed science and has been used for decades. In the micro/nano injection molding world, traditional assumptions concerning flow and heat transfer characteristics lose their validity. Since the cavity features are so thin, the surface area-to-volume ratio of features can become orders of magnitude higher than macro-scale injection molded parts. Heat transfer through the thickness of the feature becomes a significant factor in the control of the melt flow behavior. The polymer has to maintain a temperature high enough to keep its viscosity at a low enough level to allow the polymer to flow into the cavity. The interaction forces between the polymer and microcavities are also believed to influence

filling patterns. Classical rheometers have been designed based on the assumptions which are relevant to classical injection molding, but there isn't a commercially available instrument suitable for characterizing melt rheology at the nano-scale. Zhang et al. studied the rheological behavior of the polymer using pressure/temperature combined transducers built directly into the cavity of micro-scaled "dog bone" test specimen [15]. In this particular study, the pressure and temperature data generated during injection molding trials of dog bone specimens made at thicknesses varying from 200um to 600um were incorporated into a "slit flow" model in order to calculate the apparent viscosity of the polymer Pebax 7233 from Arkema group as a molding material. It was observed that the viscosity of polymer melts depends on the slit thickness. An increase in the slit thickness resulted in decreasing the polymer viscosity. They also suggest that at the micro-scale, wall-slip becomes an important factor, and maybe a significant contributor to lowering viscosity. They also found that the plasticization parameters also influence the in-cavity viscosity. In conventional injection molding, the effects of the plasticization process do not transfer with the polymer into the mold cavity. Plasticization is the process of melting the virgin resin by inducing shear stress and heat with the screw and barrel of the injection unit. It is evident that as molded features decrease in size down to the micro or nanoscale, the polymers' rheological behavior no longer follows conventional theory, and more work is needed in order to be able to predict it.

### 2.2.2 Viscosity

The cross WLF model is used to simulate the viscosity behavior of the melt during the filling stage. It describes the viscosity is a function of shear rate, temperature, and pressure[43]:

$$\eta = \frac{\eta_0}{1 + \left(\frac{\eta_0 \dot{\gamma}}{\tau^*}\right)^{1-n}} \quad (2.1)$$

Where  $\eta$  is the melt viscosity,  $\eta_0$  is the zero shear viscosity or the Newtonian limit in which the viscosity approaches a constant at very low shear rates.  $\dot{\gamma}$  is the shear rate (1/s),  $\tau^*$  is the critical stress level at the transition to shear thinning, determined by empirical curve fitting.  $n$  is the power law index in the high shear rate regime, also determined empirically. The zero shear viscosity is further defined as:

$$\eta_0 = D_1 \exp \left[ -\frac{A_1(T-T^*)}{A_2 + (T-T^*)} \right] \quad (2.2)$$

Where  $T$  is the temperature (K),  $T^*$  is the glass transition temperature, determined by curve fitting equation (6).

$$A_2 = A_3 + D_3 p \quad (2.3)$$

Where  $p$  is localized pressure (Pa).  $A_2, A_3, D_3$ , and  $D_1$  are empirically determined coefficients, and the glass transition temperature is given by the equation:

$$T^* = D_2 + D_3 p \quad (2.4)$$

Where  $D_2$  is again an empirical coefficient.

### 2.2.3 Wall Slip Velocity

Wall slip based velocity phenomena are mostly neglected in conventional injection molding simulation. When it comes to microscale molding, however, these effects can severely impact the final molded part. High shear stress is created between the wall and nearby molten polymer chains induced by high pressure and a corresponding increased velocity profile can be expected in the wall region. The power law model is introduced without any incorporation of pressure and temperature[44].

$$V_s = \frac{\alpha}{1+(\tau_c/\tau_w)^{10}} \tau_w^m \quad (2.5)$$

Where  $V_s$  is the slip velocity,  $\tau_w$  is wall shear stress,  $\tau_c$  is the critical shear stress,  $\alpha$  is the slip coefficient, and  $m$  is the slip exponent. Masato et al studied the effect of surface coating on wall slip velocity compared to uncoated tooling using polystyrene. The author concluded that the velocity increases for coated tool around 28% this led to a pressure drop in the cavity [45].

### 2.3 Previous Lehigh Research

An extensive knowledge base exists within the Micro/Nano Molding Research Group with significant contribution from various ex-students including Alan Tom, Aleksandar Angelov, Israd Jaafar, and John Rogers. Their research has resulted in a better understanding about mold fabrication and micro/nano injection molding processing. The previous work had been carried out using 12-ton BOY and 3-ton Nissei 2 stage micro injection molding machines. The enduring overall goal for this research is to expand the

understanding of both mold preparation and micro injection molding process further while simultaneously discovering a better mold material and design with high life expectancy.

Previous research included:

- Dr. Tom used Ultraviolet (UV) lithography to fabricate a micro gear with  $D=1200\mu\text{m}$ . High-density polyethylene (HDEP), Polyoxymethylene (POM), and cyclic olefin copolymer (COC) were molded against silicon wafer and used Taguchi array to analyze mechanical properties for the final product with a heated mold. It was observed that molded parts under heated mold exhibited high mechanical properties as material stiffness, indentation hardness, and reduced modulus [46].
- Dr. Angelov used E-beam followed by deep reactive ion beam DIRE to etch a silicon wafer. Nano-features were successfully molded on COC parts with 500 nm diameter and  $4\mu\text{m}$  height using 12-ton BOY micro injection machine and the silicon mold. An high aspect ratio of 8 was achieved. Additionally, 25nm features were produced on the pillar side as a result of the passivation process during the DIRE process[47].
- Dr. Jaafar used E-beam followed by deep reactive ion beam DIRE to fabricated nano-features with 400 nm diameter nanochannels spaced 800 nm apart (center-to-center spacing) and 200 nm deep. He molded two materials (PGS, PS) with different mechanical properties, for *in vitro* stem cell-substrate interaction investigation[48].

- Dr. Rodgers used UV lithography followed by DIRE to fabricate  $2\mu\text{m}$  features that were  $14\mu\text{m}$  deep and had different center-to-center spacing (3, 4, 8, and  $12\mu\text{m}$ ). An aspect ratio of nine was accomplished in the parts ( instead of 8) due to stress generated during part ejecting. The excess stress was generated because of anisotropic etching and the high frictional forces interacting along the walls[49].

## **2.4 Remaining Scientific Challenges**

Achieving microstructures consisting of micro/nano pillars of such high aspect ratio is difficult. The low strength and high surface adhesive forces between the silicon mold and polymers result in structures that either tear during fabrication or collapse to the ground or collapse laterally when the aspect ratio exceeds 6:1[50].

### **2.4.1 Process Parameters Optimization**

Process parameter optimization is still one of the challenges for fabricating product with high aspect ratio and high quality. Several studies have focused on optimizing micro injection molding processes in order to enhance the filling of microcavities. Rodgers et al. investigated the effect of mold temperature and injection velocity and concluded that injection velocity did not affect filling at mold temperatures below  $T_g$ . Increasing mold temperature (above  $T_g$ ) improves polymer micro flow inside microchannels by reducing melt viscosity[51]. Other investigations focused on processing parameters to enhance replication quality with respect of micro-feature size, spacing, and the position related to the injection gate [42,52,53]. Further investigations are needed to enhance the scientific

understanding of the process and the effect of other processing parameters such as packing pressure, injection velocity, and cooling time on replication.

#### **2.4.2 Better molds**

Mold fabrication is one of the most critical concerns once the required pattern in micro/nanoscale is determined. Molds can be made of a variety of materials such as steel, nickel shims, epoxy resin, silicon, and other materials. The limitations of each technique are related to the defined size of the patterns that can be transferred to the mold substrate [54]. It is still a challenge for the micro molding industry to create durable mold cavities that can be machined to have sufficiently small features for the desired part. Silicon based mold is widely used in microinjection molding but the brittleness and the strength of silicon is one of the weaknesses for this type of molds.

#### **2.4.3 Large Surface area**

Filling large areas of the high aspect microstructure consistently with quality is still a challenge. Cavities close to the gate fill easier compared to the cavities away from the injection gate due to the formation of a frozen layer that hinders the flow of the melt. Shot size of microinjection molding is small compared to the conventional molding machine. This limits the possibility of increasing the micro-replicated features surface area.

#### **2.4.4 Parts Demolding**

The demolding conditions influence the final replication rate and the distortions of the created micro features. A proper ejector system has to be designed to minimize the

distortion of replicated features and to prevent possible mold failure. Ejection force has to attain sufficient tensile force to overcome the tool and polymer adhesion and the frictional forces. Antistiction coating can reduce the effect of adhesion and friction between tool and polymer. However the antistiction coating tends to wear off after a certain number of cycles.

### **2.4.5 Inspection/Metrology**

The demand for micro/nanostructured surfaces is tremendously high. There are several methods to inspect the presence of micro/nanostructures such as scanning electron microscope (SEM), atomic force microscope (AFM), and other scanning spectrometry. The operation of these instruments are complicated and their availability are limited. There is a critical need for a simple nondestructive method for inspection of the patterned surfaces for quality control that could be performed rapidly without requiring any prior sample preparation.

#### **2.4.5.1 Scanning Electron Microscope**

A scanning electron microscope (SEM) is a powerful tool that uses an electron beam to characterize sample topography, morphology, and chemical composition. Electrons are generated and accelerated through electromagnetic lenses to interact with the sample of interest. These interactions generate electrons with a wide range of energies. The backscattered electrons (BSE) could be used to generate mass-contrast images composition of the sample while SE is used for surface topography[55,56]. When imaging polymer samples, low accelerating voltages are preferred to prevent any damage caused by

the absorption of the high energy of the electron beam. [57]. Sample charging is a concern for polymers as they are insulators and do not provide a path for the electrons to dissipate. This could be avoided by coating the polymer surface with a thin layer of electrically conducting material (metal, carbon etc.) and grounding the layer to the metal sample stubs.

### 2.4.5.2 Water Contact Angle

Water contact angle (WCA) is a surface measurement that can be used to measure wettability over a given surface. Wettability is a measure of the degree of spreading of a liquid droplet with a solid surface. On a flat surface the contact angle is described by Young's equation which demonstrates that the contact angle is dependent on surface tension between three interfaces as follow:

$$\cos\theta = \frac{\gamma_{SV} - \gamma_{SL}}{\gamma_{LV}} \quad (2.6)$$

Where  $\theta$  is contact angle,  $\gamma_{sv}$  is solid- vapor surface tension,  $\gamma_{sl}$  is solid-liquid surface tension, and  $\gamma_{lv}$  is liquid-vapor surface tension.

A surface is considered hydrophobic when WCA is greater than  $90^\circ$ . On the other hand, the surface is hydrophilic when WCA is lower than  $90^\circ$  as seen in Figure 2-14[58].

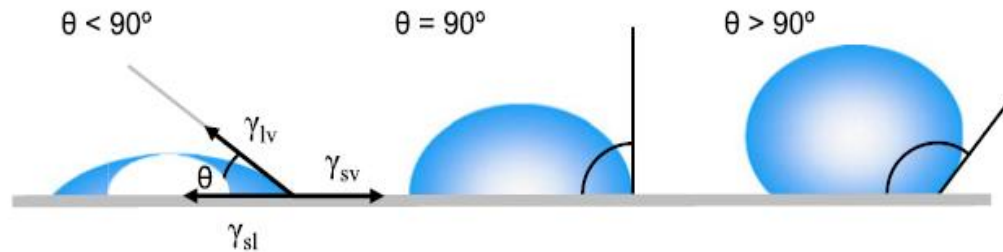


Figure 2-14: illustration of contact angle formed on hydrophobic and hydrophilic surfaces[58].

The above illustrations depicts an equilibrium case scenario for wetting behavior which is not always practically feasible to measure accurately. A more practical method to measure WCA is under dynamic conditions. Advancing contact angle  $\theta_a$  and receding contact angle  $\theta_r$  as illustrated in Figure 2-15 could be carried by adding and removing the droplet on the surface. Contact angle hysteresis (H) is the difference between the advancing and the receding angle. It can be used as a sign of surface roughness as hysteresis increases.

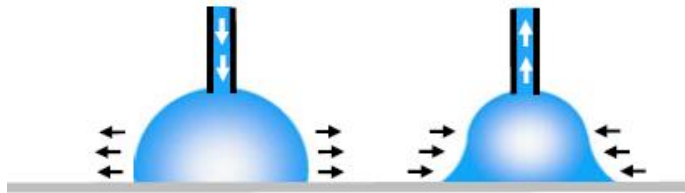


Figure 2-15: Advancing and Reseeding contact angle techniques [58].

In general, WCA measurement techniques can be classified into two categories: flat surfaces measurement and rough surfaces measurements. Young's equation is valid for an equilibrated liquid droplet on a flat surface. It needs to be modified to understand the wetting behavior of a liquid on rough or textured surfaces. Most micro/nano injection molded surfaces are considered non-ideal (rough) surfaces. Wenzel and Cassie-Baxter models were established to model the wettability on non-ideal surfaces.

According to Wenzel, the water droplet is placed on the surface with nanoscale features penetrates between micro-features. The increased surface area results in an altered water droplet surface tension that can change the contact angle to  $\theta^*$ , defined by the following equation:

$$\cos\theta^* = r \cdot \cos\theta_0 \quad (2.7)$$

Where  $\theta_0$  is the contact angle on a flat surface,  $r = a/b$  is the roughness coefficient which ratio between actual surface areas over projected surface area. This model assumes that the surface wettability is primarily affected by the overall surface roughness. Hence, Wenzel contact angle will be associated with the increase of  $\theta_0$ .

On the other hand, Cassie- Baxter model demonstrates that water droplet remains on the top of micro/nano pillars carried by air support between pockets (Figure 2-16). The Cassie angle  $\theta^*$  can be defined by the following equation:

$$\text{Cos}\theta^* = f_s \text{Cos}\theta_0 (1 - f_s ) \quad (2.8)$$

Where  $f_s$  is the liquid-solid contact area over the projected surface area.

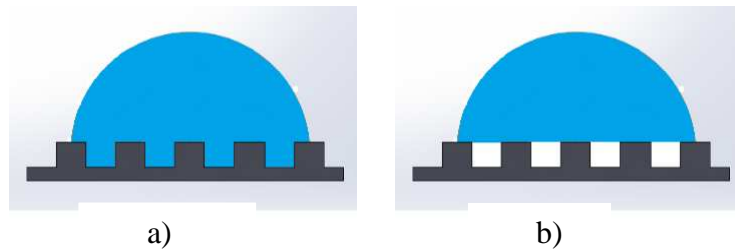


Figure 2-16: Schematic of water droplet interfaces for Wenzel model (a) and Cassie-Baxter model (b).

Surface topography of the surface can play an important key in the surface hydrophilicity [59]. A study by Z. Yoshimitsu found that water contact angle increases with the increase of pillars height. They found that the Wenzel model is applicable when the roughness factor ( $1.00 < r < 1.10$ ). If the roughness becomes high ( $r > 1.23$ ) the water contact angles follows the Cassie-Baxter model[59]. Roughness factor is calculated based on surface diameter, height and pitch of micro and nanofeatuers.

### **2.4.5.3 Atomic Force Microscope**

Atomic force microscope (AFM) is a physical contact imaging technique that uses a cantilever probe with silicon tip. A laser beam is reflected on the cantilever and monitored by the position detector. AFM measurement relies on the force between the tip and the sample. Force is calculated through Hook's law by measuring the deflection of the probe multiplied by the stiffness of the cantilever. The probe is physically tapping on the scanned area generate the image of the surface[60,61]. AFM tapping mode was used in this investigation to characterize the surface topography for molded samples with 5  $\mu\text{m}$  diameter with 2.45  $\mu\text{m}$  height while bigger features needed a high aspect ratio probe.

### **2.4.5.4 Focused Ion Beam (FIB)**

Focused Ion Beam (FIB) is a fabrication tool widely used in nanofabrication patterning and semiconductors analysis. FIB is capable of milling features down to 5 nm. It utilizes an accelerated beam of ions to precisely ablate materials. These ions are generated from a highly energized liquid metallic source, usually Gallium that is wetted onto the tip of a tungsten needle. When heated and electrically charged, the Gallium forms a cusp on the tip of the needle with a radius of approximately 2nm. Galium ions strike the sample and locally remove away material [62].

## **2.5 Objectives in More Details**

The overall objective of this dissertation is to develop a scientific understanding of the microinjection molding process by numerical and experimental methods. .

Moldflow is an injection molding simulation tool that could provide valuable insight about the injection molding process and processing parameters for successful molding of parts. It minimizes cost and time, and the probability of silicon mold breakage during molding experiments. In particular it provides a preliminary analysis for the filling stage and recommendations for V-P switchover setting. In this research, Moldflow simulations were performed to study the filling process of a mold cavity having a 12mm diameter, with patterned arrays of two different micro-structures: i. an oval profile with a diameter (D) of 15,10  $\mu\text{m}$  and height (H) of 15,10  $\mu\text{m}$ , and ii. A circular profile with D = 5  $\mu\text{m}$ , and an H = 2  $\mu\text{m}$ .

Processing parameters derived from Moldflow simulation was used for experimental investigations for different materials such as Polystyrene (666D Styron), Thermoplastic polyurethane (TPU) ( Texin 985), Low-Density Polyethylene (CP 851), High-Density Polyethylene (HD 6733), and Cyclic Oflen Copolymer (TOPAS 5013S-04). Molded samples were characterized using a scanning electron microscope to confirm the replication rate and validate the optimum processing conditions.

Silicon (Si) molds with microfeatures were fabricated using photolithography followed by deep reactive ion etching (DRIE). Scanning electron microscopy (SEM) was used to validate the fabricated mold cavities were met the targeted dimensional specifications.

In an effort to develop more robust molds, Zr-BMG molds were fabricated. Silicon molds with micropillars were fabricated by a similar DRIE process as described in the previous paragraph. Zr-BMG was pressed onto the silicon molds to replicate the structures and the silicon was subsequently dissolved using potassium hydroxide (KOH) solution.

Both molds (Si and Zr-BMG) were analyzed numerically using Ansys software to predict the tool life under optimal processing parameters.

A theoretical model was developed to bear the beam deflection as stiffness agent to simulate apparent elastic modulus that focal adhesion regions would signal during cell culturing development. The approximation provided a better understanding of cell mechanosensing of the contact surface for efficient design of textured substrates. Such model will provide a better method to design pillar arrays and significantly improve the ability to study cells developments.

## CHAPTER 3: Micro/Nanoscale Features for studying Cell Mechanosensing

### 3.1 Introduction

Polymeric culture platforms with micro/nano topographies have provided a powerful approach to modulate cell to substrate interactions. Substrate stiffness and topography has been widely explored in order to study physical cues that cell exert. Cells respond to chemical and mechanical signals from surrounding microenvironments. While chemical signals have been well studied in the last decade [63], mechanical cues are also very important to cell growth owing to a surface rigidity and compatibility. It has been recognized that substrate stiffness has a significant effect on traction forces as well as cell differentiation, growth, and mobility.

*The goal of this given study is to investigate beam deformation in order to simulate apparent elastic modulus that focal adhesion regions would signal during cell culturing. Furthermore, this approximation would be a superior tool that helps cell mechanosensing investigators design an efficient substrate for their studies that match the tissue's elastic moduli.*

In this chapter, an expression of cell elastic modulus will be derived from the amount of deflection on cantilever beams based on cellular transduction forces on focal adhesion areas. Euler –Bernoulli and Timoshenko approximations for slenderness beams ( $L/D < 10$ ) has been utilized in the literature widely to calculate the amount of deflection

and shear deformations on a single pillar. The different material selection was utilized to elucidate the effect of the elastic modulus of elasticity and poisson ratio on the apparent tissue elastic modulus. Moreover, a geometrical dimensions sensitivity analysis was performed to determine the most influential dimension.

### **3.1.1 Influence of substrate stiffness on Cells**

In recent years the cell to substrate interactions has attracted in both academic laboratories and industry. A tissues is a cellular organization in which cell are adherent to their surrounding extracellular matrix (ECM) performing a specific function. ECM comprises of three dimensional network of macromolecules that provide both physical support and mechanosensing distribution in both directions. Cells explore the substrate via traction forces in order to migrate across their micro environment, and also sense the characteristics of the substrate.

Substrate stiffness plays an important role in cells mechanosensing to determine a proper microenvironment during the cell culturing process. It has been recognized that substrate stiffness has a significant effect on traction forces as well as cell differentiation[9].

### **3.1.2 Influence of substrate Micro/Nano topography and geometries on Cells**

Fabrication of substrates with micro and nanopillars have made it possible to estimate cell traction forces through pillar deflection. Compared to flat surfaces, cells show a drastically different morphology and behavior. Cells respond to the substarte physical

parameters such as stiffness and the topography of the substrate. Topography on can be manipulated to achieve different substrate stiffness through the aspect ratio of the features on the surface as well as the spacing between the features. Aspect ratio of the pillar is mainly a high factor that could control substrate rigidity. However, fabricating micro or nano structures with high aspect ratio is a challenge. Spacing between the microstructures could have similar effect on the substrate stiffness.

Chen et al. [64] investigated the apparent young modulus as a function of cylindrical micropillars aspect ratio and pillars spacing. They found either aspect ratio or pillar spacing can tune the substrate young modulus. Higher aspect ratio can result in lowering the apparent young modulus that appears on the substrate while increasing the spacing can also lead to lower modulus as well (Figure 3-1).

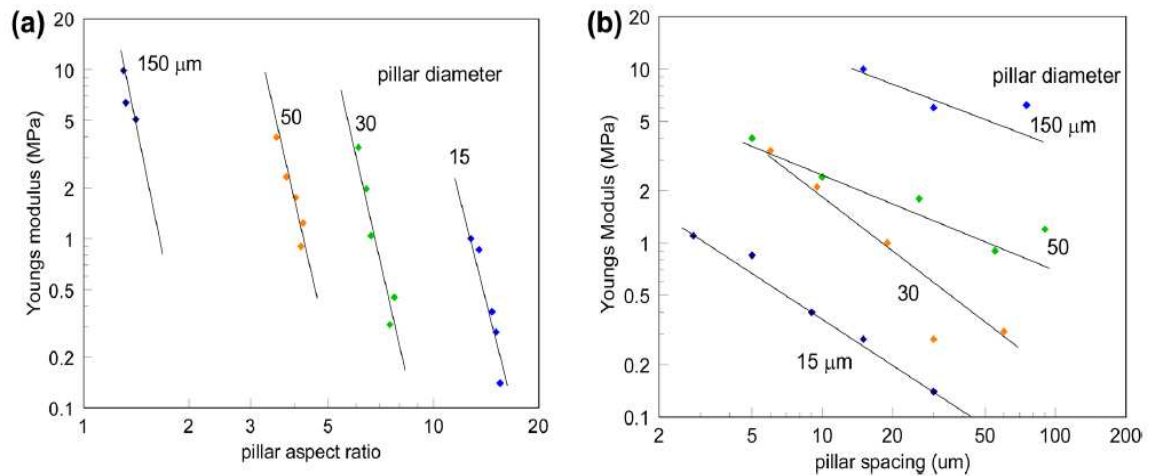


Figure 3-1: Apparent modulus of elasticity (a) pillar aspect ratio and (b) pillars spacing of various diameters.

### **3.1.3 Remaining Challenges**

Researchers have shown that human mesenchymal stem cells (hMSCs) respond differently to the apparent elastic modulus of the substrates with micro/nanoscale surface features. The future challenge is to engineer substrates/constructs that could be manufactured into products such as petri-dishes with contact surfaces having specific elastic modulus and topography that would steer hMSCs into specifically targeted lineages. Ideally, these products would also facilitate the cells towards differentiating into fully functional mature cells of required phenotypes.

## **3.2 Micro/Nano-Pillars Bending Mechanism**

Pillars deflection is calculated using Euler –Bernoulli and Timoshenko approximations for slenderness beams. The amount of deflection and shear deformations on a single pillar is assumed to match the amount of the stress that appears on cell. Different material selection will show the effect of elastic modulus of elasticity and Poisson’s ratio on the apparent tissue elastic modulus.

### **3.1.4 Euler – Bernoulli Approximation**

The amount of deflection of a beam when a load is applied can be determined utilizing Euler-Bernoulli (E-B) beam bending theory. The deflection behavior is a function of the geometry and material of the constructed of the pillars. Consider a slender beam in with length,  $L$ , and diameter,  $D$ , with a concentrated load,  $F$ , acting at the free end, such

that it deflects by  $\delta$  in the y-direction as shown in Figure 3-2. The pillar bending due to the force can be approximated using the Euler-Bernoulli model which assumes:

- a. An elastic beam where the deflections are small.
- b. Rigid cross sections that do not deform under to the transverse (or axial) load.
- c. Cross sections that remain planar and normal to the neutral axis of the beam
- d. Beam aspect ratio ( $L/D$ ) should be less than or equal to 10.

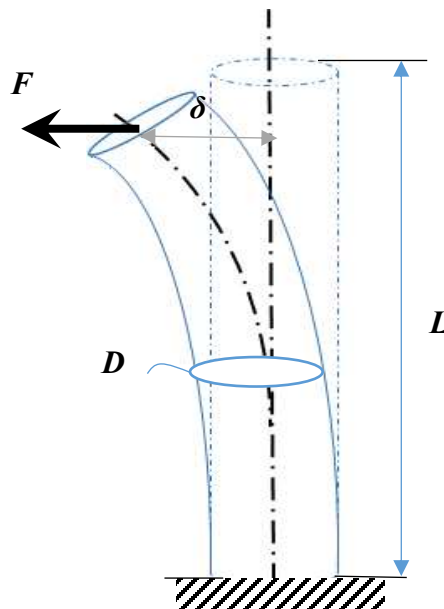


Figure 3-2: Schematic of Cantilver Beam deflection

The cantilever deflection  $\delta$  can be derived from the Euler Bernoulli equation based on the applied load at the tip and cross-section of the beam as follows:

$$\delta = \frac{F L^3}{3EI} \quad (3.1)$$

Where  $F$  is applied a load,  $L$  is the height of the pillars,  $E$  is the elastic modulus of pillars,  $I$  is the area moment of inertia attributed to pillars cross-section.

### 3.1.5 Accounting for Shear Deformation by including the Timoshenko Beam Approximation Deflection Term

In cases when the beam does not satisfy the slenderness criterion ( $L/D < 10$ ), which is the typical case for micro-fabricated pillars, shear deformation may be significant. This can be accounted for by employing the Timoshenko beam approximation term[65,66] :

$$\delta = F \frac{L^3}{3EI} + F \frac{\alpha L}{GA} = F k_{bending}^{-1} + F k_{deformation}^{-1} \quad (3.2)$$

Where the new terms,  $\alpha$  is the shear coefficient specific to a cross section,  $G$  is the shear modulus, and  $A$  is the cross sectional area.

#### 3.2.1.1 Circular cross-section

For a cylindrical pillar (beam) the area moment of inertia is

$$I = \frac{\pi D^4}{64} \quad (3.3)$$

The force required to bend a micro/ nanoscale pillar with a fixed base is given by the Euler-Bernoulli formula:

$$\frac{F}{\delta} = \frac{3\pi E D^4}{64 L^3} = k_{bending} \quad (3.4)$$

Where L is pillar height, D is pillar diameter, E is Young's modulus, and  $\delta$  is a deflection on a pillar

Shear coefficient ( $\alpha$ ) for pillars with a circular cross-section, as a function of the Poisson's ratio ( $\nu$ ) of the material, is given by [67]:

$$\alpha = \frac{6(1+\nu)^2}{7+12\nu+4\nu^2} \quad (3.5)$$

The relationship between G and E is given by:

$$G = \frac{E}{2(1+\nu)} \quad (3.6)$$

Combining equations 2-5 the deflection for a single cylindrical pillar can be derived as

$$\delta = F \frac{64L^3}{3\pi ED^4} + F \frac{4\alpha L}{G\pi D^2}$$

$$\delta = \frac{8F}{\pi E} \left[ \frac{8L^3}{3D^4} + \frac{(1+\nu)\alpha L}{D^2} \right] \quad (3.7)$$

The force required to bend a pillar by a distance  $\delta$  is highly dependent on the relationship between the diameter D, and the height L. High aspect ratio pillars seem to have high deflection distance. Thus, indicates that low force is needed to bend pillars with higher length compared to diameter.

### 3.2.1.1.1 Cell Sensing Model [49].

The objective is to create suitable polymeric substrate that match the tissue's elastic moduli of a particular cell with controlling the micro and nanoscale substrate surface. The approach involves equating the deflection ( $\Delta x$ ) caused by the cellular force ( $F_{\text{CELL}}$ ) of a cell covering a focal adhesion (FA) area ( $A_{\text{FA}}$ ) of a hypothetical flat substrate to the previously derived deflection of an array of pillars ( $\delta$ ) that would lie within  $A_{\text{FA}}$ . This concept is shown in Figure 3-3.

The main assumptions in the model are as follows.

1. Cellular transduction forces occur are no greater than that of focal adhesion (FA).
2. Cellular forces applied at FAs are purely shear in nature (i.e., they are applied parallel to the surface).
3. The equivalent cellular force at a FA is equally divided among the number of pillars that would lie within the area of the FA, and hence each pillar would deflect at the same magnitude.

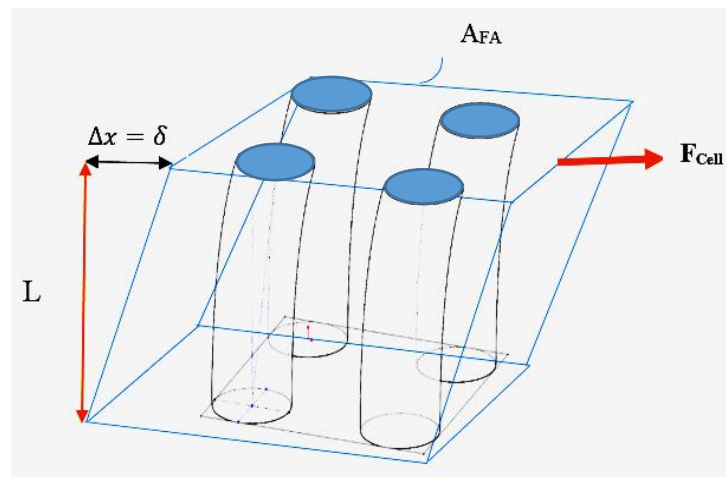


Figure 3-3: Injection Molded Array of Bending Micro/Nano-Structures due to Force Exerted by Cell.

If a human stem cell is in contact with an extracellular matrix (ECM) of a particular tissue, the stem cell will deform the tissue such that  $\Delta x$  is dependent on the properties of the tissue. The shear force ( $\tau$ ) to shear strain ( $\gamma$ ) relationship is given by:

$$\tau = G_{CELL TISSUE} \gamma \quad (3.8)$$

Where  $G_{CELL TISSUE}$  is the shear modulus of the targeted cell tissue, and for small angles of deflection  $\gamma = \frac{\Delta x}{L}$ .

Hence,

$$\frac{F_{CELL}}{A_{FA}} = G_{CELL TISSUE} \frac{\Delta x}{L}$$

$$\Delta x = \frac{F_{CELL} L}{G_{CELL TISSUE} A_{FA}} \quad (3.9)$$

Where,

$$G_{CELL TISSUE} = \frac{E_{CELL TISSUE}}{2(1+\nu_{CELL TISSUE})} \quad (3.10)$$

For human embryos, we assume that  $A_{FA} = 100 \mu m^2$ ,  $\nu = 0.5$  [68,69].

$$G_{CELL TISSUE} = \frac{E_{CELL TISSUE}}{3} \quad (3.11)$$

In an orthogonal array of pillars (Figure 3-4), for a given center to center spacing (C2C spacing) ( $\chi$ ), there will be an equivalent of 1 pillar per C2C spacing square area. This is illustrated in Figure 3-4.

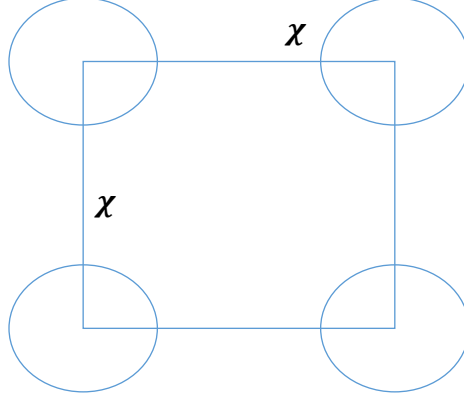


Figure 3-4: Orthogonal Array with C2C spacing( $\chi$ ).

Hence, the number of pillars per unit area ( $\rho_{pillars}$ ) can be written as a function of the C2C spacing,

$$\rho_{pillars} = \frac{A_{FA}}{\chi^2} \quad (3.11)$$

Hence, with the assumption that all pillars bear equal force, the force that is exerted at the tip of each pillar is given by,

$$F_{PILLAR} = \frac{F_{CELL}}{\rho_{pillars}} = \frac{F_{CELL} \chi^2}{A_{FA}} \quad (3.12)$$

Since  $\Delta x = \delta$ , equations 7-10 can be combined to correlate the elastic moduli of the cell tissue and the substrate as follows.

$$\begin{aligned} \frac{F_{CELL} L}{G_{CELL TISSUE} A_{FA}} &= \frac{8F_{CELL} \chi^2}{\pi E A_{FA}} \left[ \frac{8L^3}{3D^4} + \frac{(1+\nu)\alpha L}{D^2} \right] \\ \rightarrow \frac{3F_{CELL} L}{E_{CELL TISSUE}} &= \frac{8F_{CELL} \chi^2}{\pi E} \left[ \frac{8L^3}{3D^4} + \frac{(1+\nu)\alpha L}{D^2} \right] \end{aligned}$$

$$E_{CELL TISSUE} = \frac{3 \pi E}{8\chi^2} \left[ \frac{8L^2}{3D^4} + \frac{(1+\nu)\alpha}{D^2} \right]^{-1} \quad (3.13)$$

Where  $E$  is the elastic modulus and  $\nu$  is Poisson ratio of the substrate material. This final equation relates the manufactured substrate's intended elastic modulus to be mimicked as a function of the polymer surface's geometric ( $L$ ,  $D$ , and  $\chi^2$ ) and material properties ( $\alpha$  and  $\nu$ ).

### 3.2.1.1.2 Apparent tissue Modulus for micro/nanopillar arrays:

Many variables govern the apparent elastic modulus including shapes, aspect ratio, center to center spacing, and young modulus of the substrate. In this study, an estimation of the elastic modulus that cell will sense to provide an equivalent modulus as target biological tissues. As noticed from the previous expression that the presence of shear deformation offers additional pillar deflection resulting in a lower apparent modulus as seen in Figure 3-5.

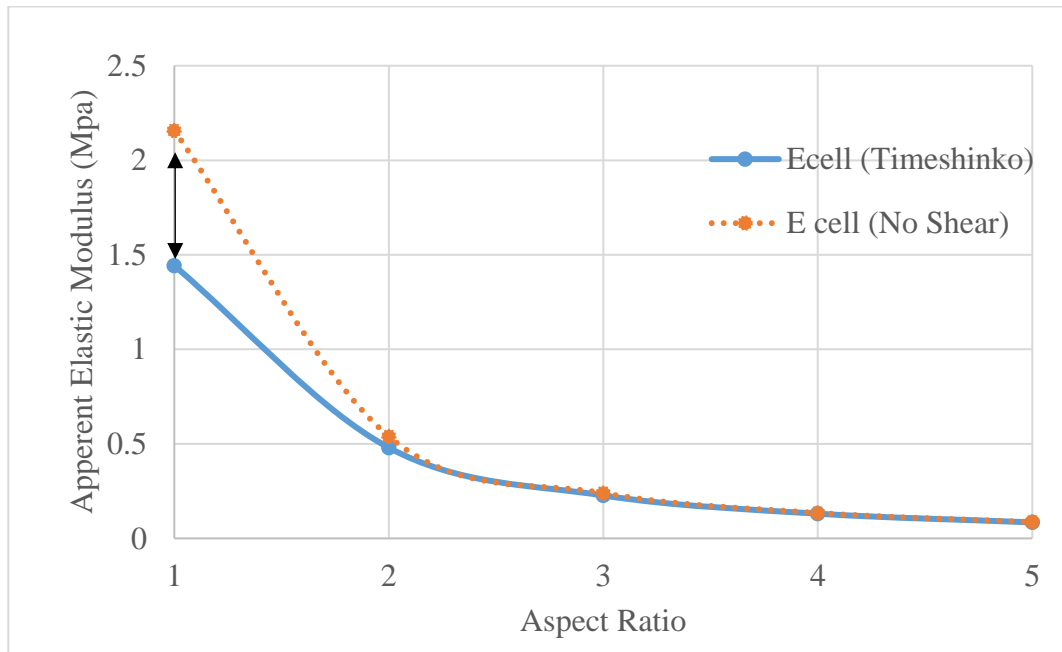


Figure 3-5: Effect of shear on the apparent elastic modulus of 5um diameter, 8 um center to center spacing made of TPU with  $E=12.5$  MP.

When creating the model a few different assumptions were made to match the human uterus elastic modulus of 1.4 MPa. Circular geometries were chosen with the diameter of 5 $\mu$ m with different aspect ratio and C2C spacing to reach a desired apparent elastic modulus that is equal to the elastic modulus of the cell tissue ( $E_{CELL\ TISSUE}$ ). Figure 3-5 shows that the presence of shear provides additional pillar deflection resulting in a lower apparent elastic modulus. This difference becomes fairly small when aspect ratio becomes greater than 2.

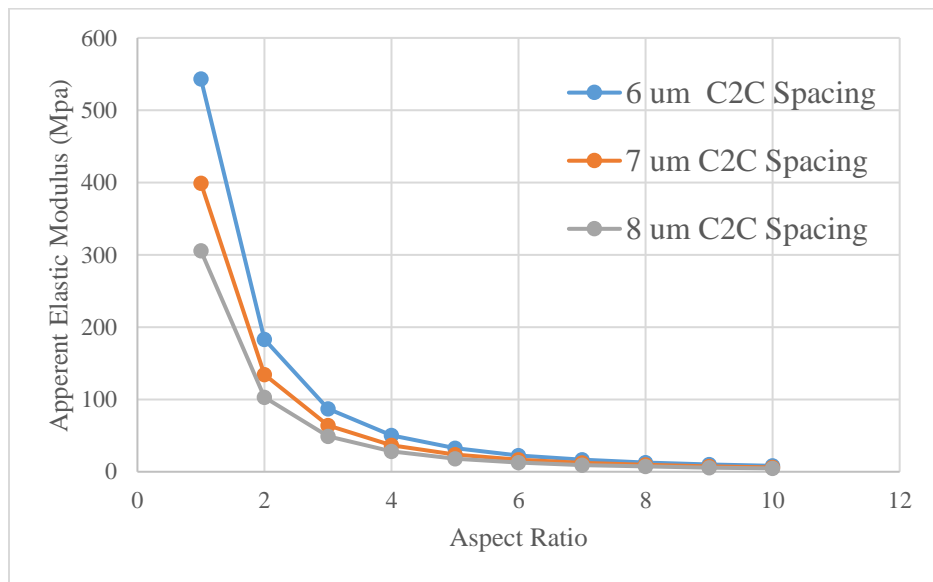


Figure 3-6: 5 um diameter Cylindrical Polystyrene pillars with 6, 7, 8 um C2C spacing.

Polystyrene substrates (which widely used in the petri- dishes industry), even with microtopography have shown that the apparent modulus is too high for the cells lying on the top of it to mimic a majority of biological tissues. As shown in Figure 3-6 the apparent elastic modulus calculated were excessively high to match the human uterus of 1.4 MPa. The demand for mimicking substrates with a lower modulus of elasticity directed us to

softer materials such thermoplastic polyurethane (TPU), Low-Density Polyethylene (LDPE), High-Density Polyethylene (HDPE), and other thermoplastic polymers with low elastic modulus as shown in Figure 3-7. The effect of spacing on the apparent modulus on different substrate material is shown in (Figure 3-8Figure 3-9Figure 3-10).

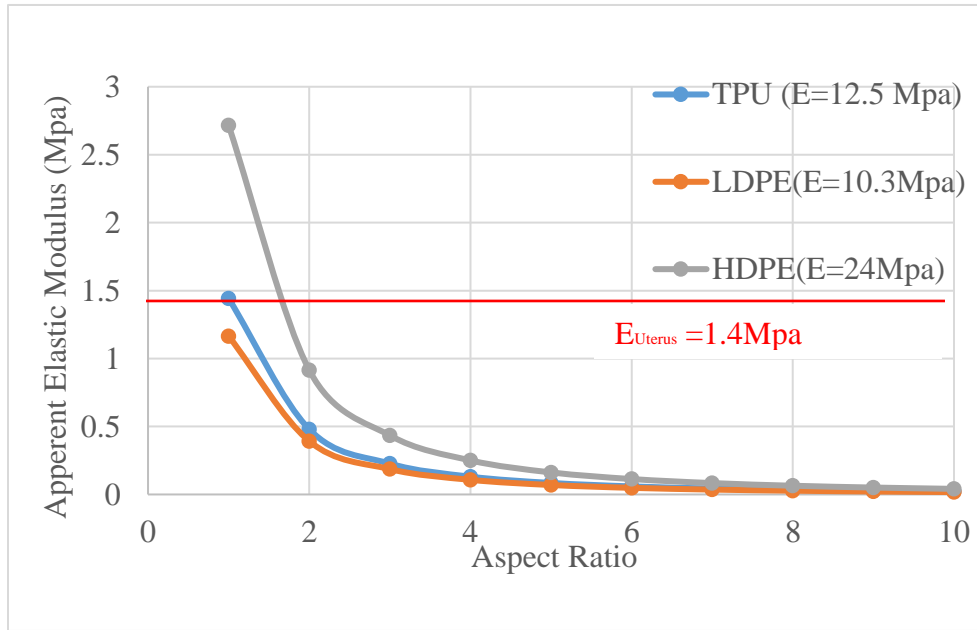


Figure 3-7: 5um diameter cylindrical pillars with 8 um C2C spacing with different material.

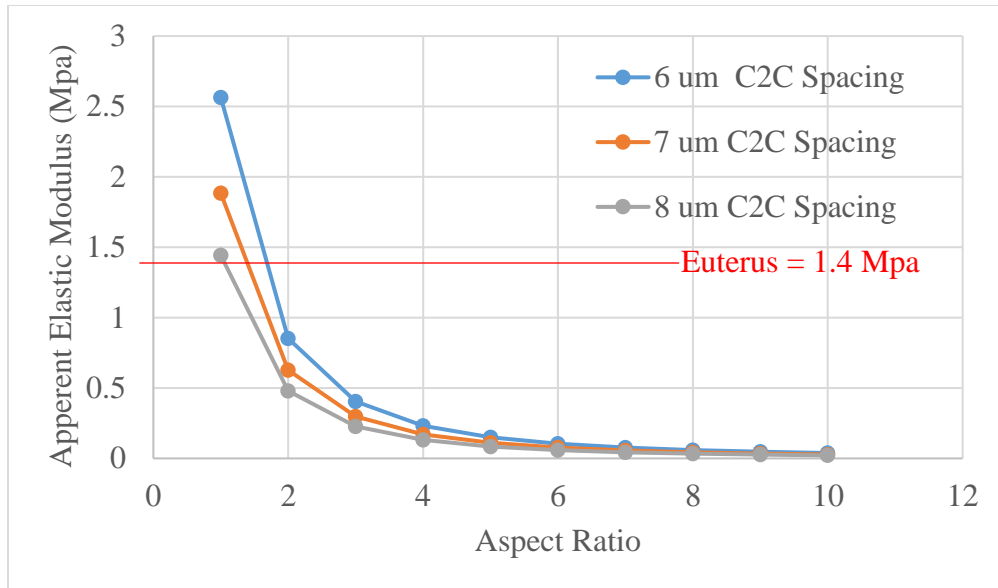


Figure 3-8: TPU 5um diameter cylindrical pillars with a different C2C spacing.

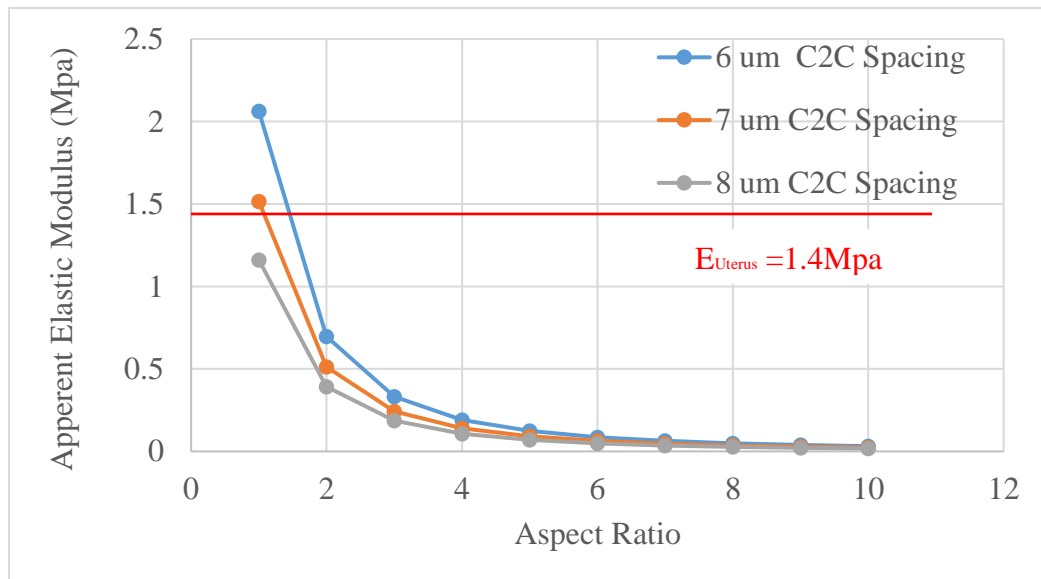


Figure 3-9: LDPE 5um diameter cylindrical pillars with different C2C spacing.

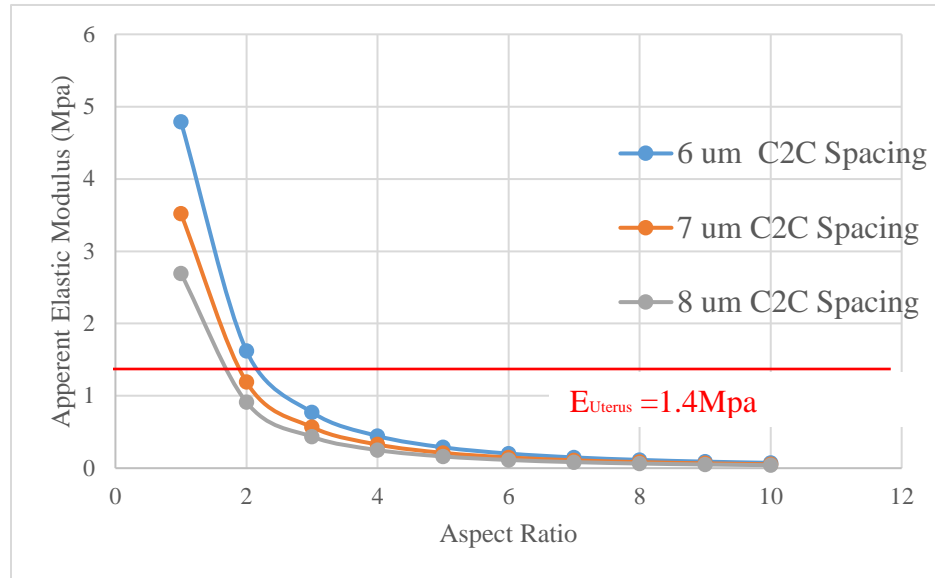


Figure 3-10: HPDE 5um diameter cylindrical pillars with different C2C spacing.

### 3.2.1.1.3 Pillar dimensions relationships to Apparent elastic modulus on cell [5 um Circular Pillars with Different C2C spacing( $\chi$ )].

Patterns dimensions are mainly affecting the apparent moduli on cells. As noted from Figure 3-11 and Figure 3-12, the pillars diameter and height have a smaller effect compared to the spacing between pillars which could be the easiest way to manipulate the targeted apparent moduli. As the spacing between pillars increased a considerable drop in  $E_{Apparent}$  is presented due to inversely proportional relationship shown in Equation (3.13). When fabricating such substrates with micro/nanopillars achieving high aspect ratio is a huge challenge. So, controlling the spacing between pillars would be a more practically viable approach for fabricating these types of substrates.

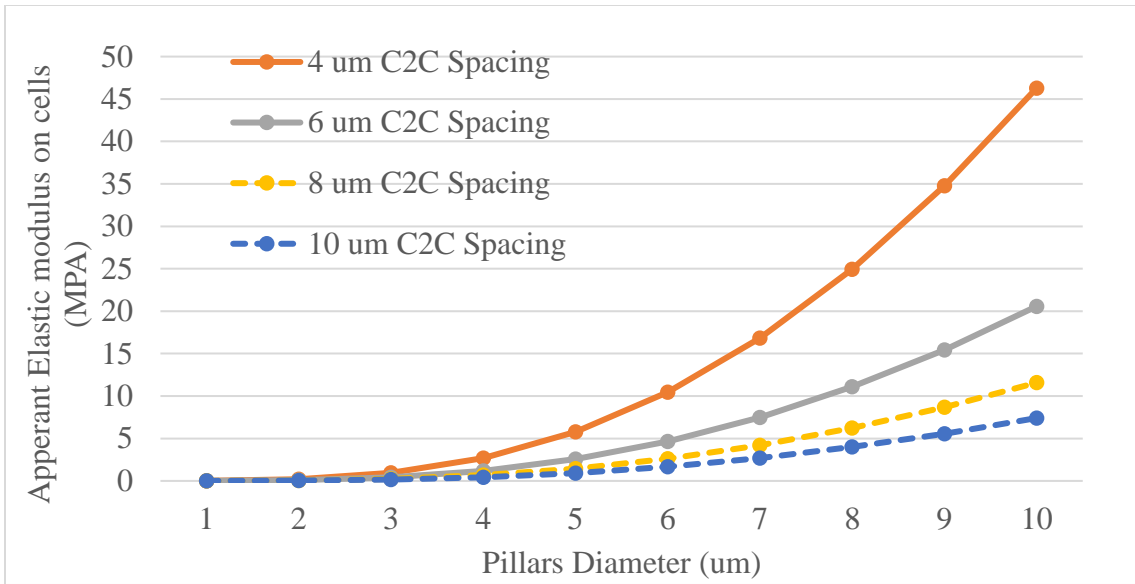


Figure 3-11: TPU micro pillars with diameter (D) sensitivity analysis to Apparent Elastic modulus on cells.

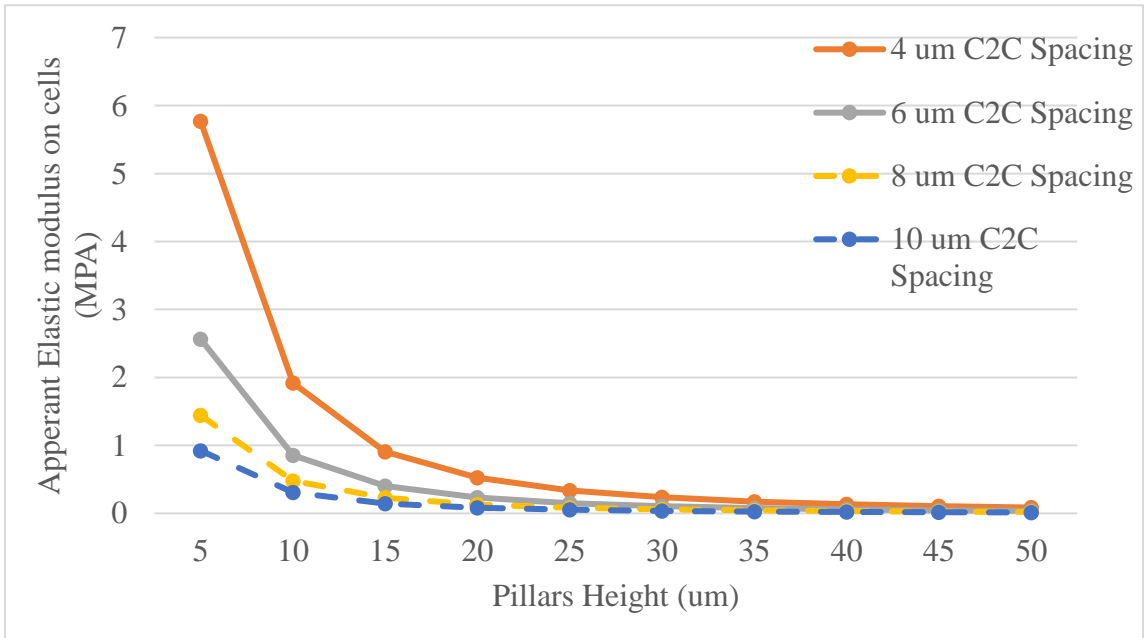


Figure 3-12 TPU 5um micro pillars with height (L) sensitivity analysis to Apparent Elastic modulus on cells.

### 3.2.1.2 Elliptical cross section

When dealing with an elliptical cross-section a combination of semi-major diameter (a) and semi-minor diameter (b) will replace the diameter (D) in circular pillars. This will carry out an extra resistance to bending which could result in a higher apparent elastic modulus to cells due to an anisotropic cross-section of the cantilever beam.

For simplifying the calculations we consider the moment of inertia  $I_y$  acting on the semi-major diameter of an elliptical pillar for our study:

$$I_y = \frac{\pi}{4} a^3 b \quad (3.14)$$

The shear coefficient ( $\alpha$ ) is specified to an elliptical cross-section as a function of Poisson ratio  $\nu$ , semi-major diameter (a), and semi-minor (b) [67]:

$$\alpha = \frac{12(1+\nu)(3a^4+a^2b^2)}{(40+37\nu)a^4+(16+10\nu)a^2b^2+\nu b^4} \quad (3.15)$$

The relationship between G and E is given by:

$$G = \frac{E}{2(1+\nu)} \quad (3.16)$$

By substituting  $I_y$ ,  $\alpha$ ,  $A$  and  $G$  into Equation (3.7) pillar deflection  $\delta$  for an elliptical cross section turns into:

$$\delta = F \frac{L^3}{3EI} + F \frac{\alpha L}{GA}$$

$$\delta = \frac{2F}{\pi abE} \left[ \frac{2L^3}{3(a^2)} + \alpha L(1 + \nu) \right] \quad (3.17)$$

### 3.2.1.2.1 Cell Sensing Model for Elliptical Pillars:

In an orthogonal array of oval pillars, for a given C2C spacing ( $\chi$ ) is illustrated in Figure 3-13.

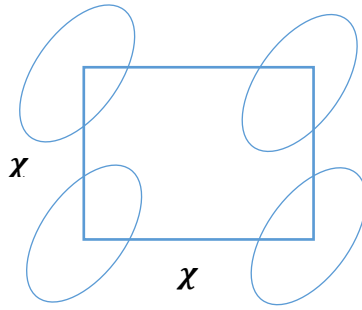


Figure 3-13: Oval Cross section with a rotating angle

The number of pillars per unit area ( $\rho_{pillars}$ ) can be written as a function of the C2C spacing,

$$\rho_{pillars} = \frac{A_{FA}}{\chi^2} = \frac{1}{\chi^2} \quad (3.18)$$

Hence, with the assumption that all pillars bear equal force, the force that is exerted at the tip of each pillar is given by,

$$F_{PILLAR} = \frac{F_{CELL}}{\rho_{pillars}} = \frac{F_{CELL} \chi^2}{A_{FA}}$$

$$\Delta x = \frac{F_{CELL} L}{G_{CELL TISSUE} A_{FA}}$$

Since  $\Delta x = \delta$

$$\frac{F_{CELL} L}{G_{CELL TISSUE} A_{FA}} = \frac{2 F_{PILLAR}}{\pi a b E} \left[ \frac{2 L^3}{3(a^2)} + \alpha L(1 + \nu) \right]$$

$$\frac{3 F_{CELL} L}{E_{CELL TISSUE}} = \frac{3 F_{CELL} \chi^2}{\pi a b E} \left[ \frac{2 L^3}{3(a^2)} + \alpha L(1 + \nu) \right]$$

Apparent Elastic moduli on cell tissue is calculated as:

$$E_{CELL TISSUE} = \frac{3 \pi a b E}{2 \chi^2} \left[ \frac{2 L^3}{3(a^2)} + \alpha L(1 + \nu) \right]^{-1} \quad (3.18)$$

Where E is the elastic modulus of the substrate material, and  $\nu$  refers to its Poisson's ratio.

This final equation relates the manufactured substrate's intended elastic modulus to be mimicked as a function of the polymer surface's geometric (L, a, b,  $\chi^2$  and material properties ( $\alpha$  and  $\nu$ )).

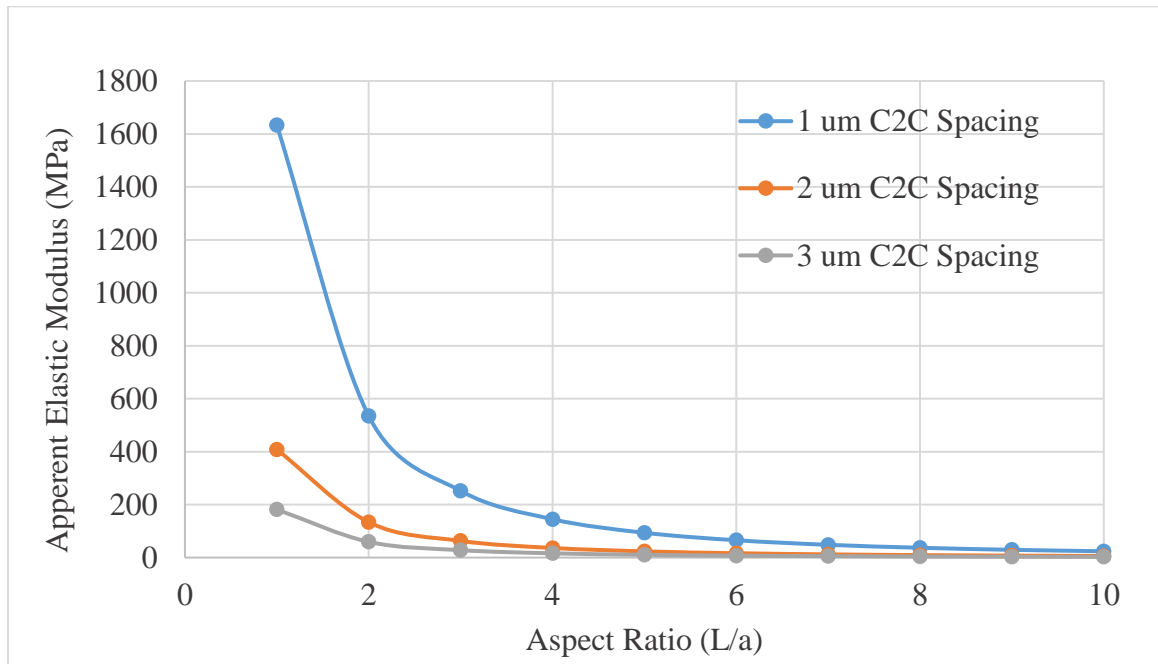


Figure 3-14: PS Elliptical pillars with semi-major diameter a=1 um and different pitch (C2C spacing).

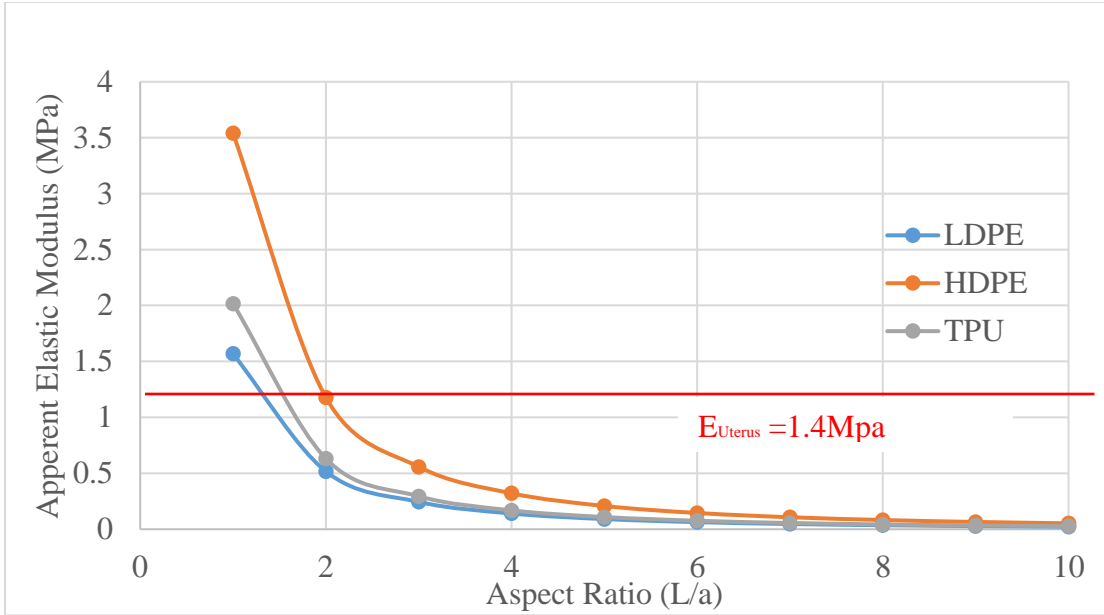


Figure 3-15: Elliptical pillars with semi-major diameter  $a=1 \text{ }\mu\text{m}$ ,  $b=0.5 \text{ }\mu\text{m}$  and  $2 \text{ }\mu\text{m}$  C2C spacing.

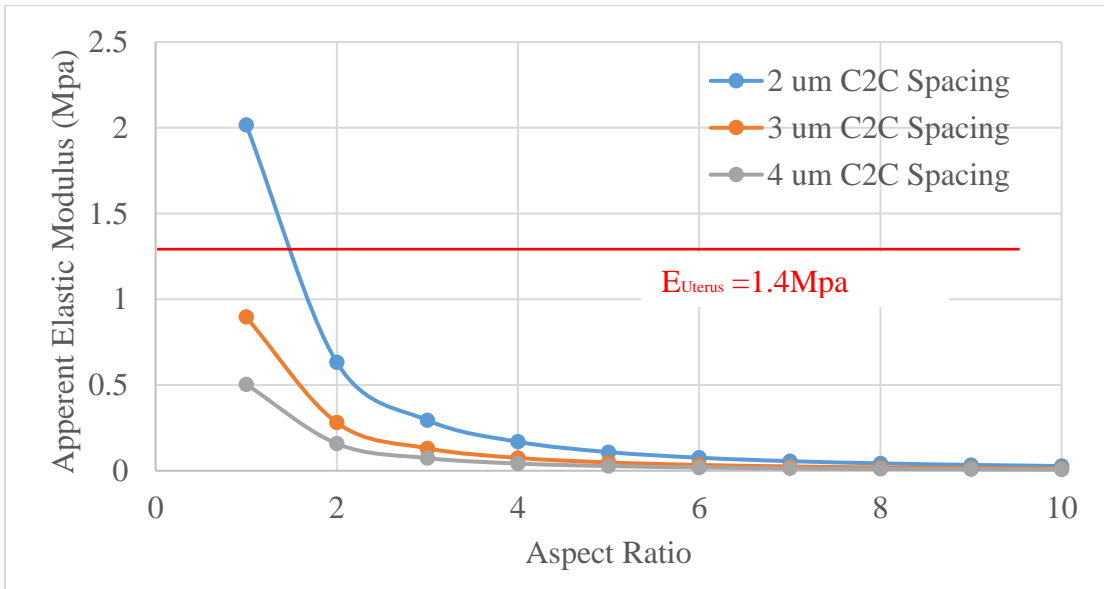


Figure 3-16: TPU Elliptical pillars with semi-major diameter  $a=1 \text{ }\mu\text{m}$ ,  $b=0.5 \text{ }\mu\text{m}$  and different C2C spacing.

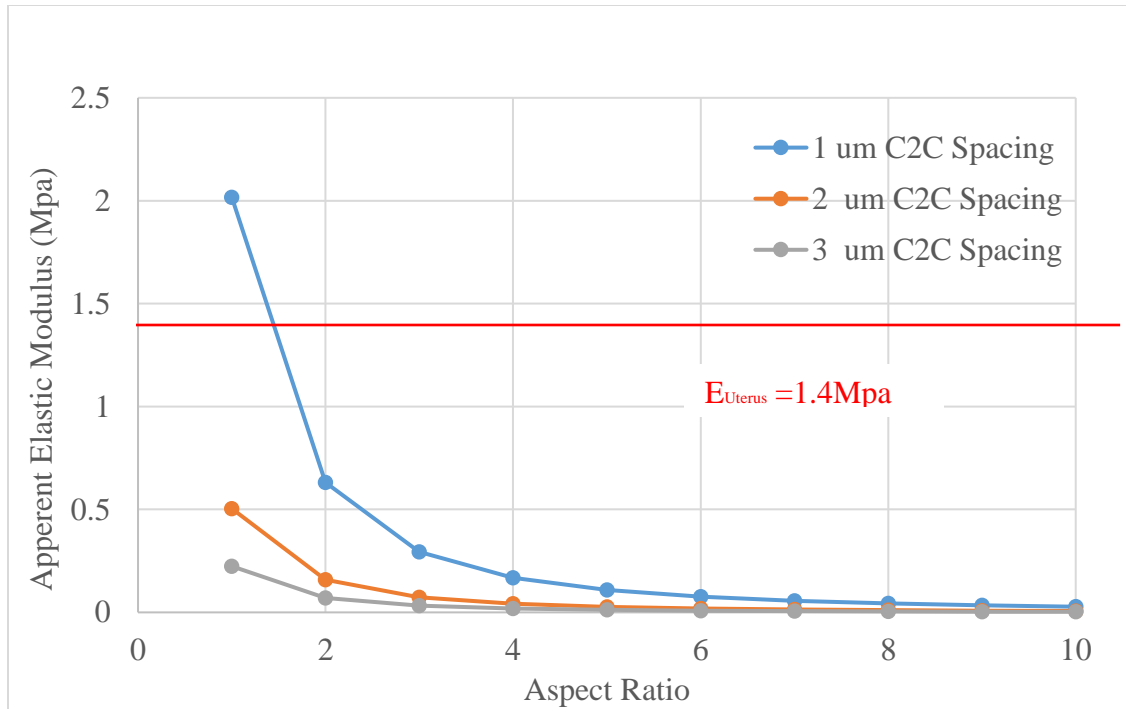


Figure 3-17: LDPE Elliptical pillars with semi-major diameter  $a=1 \mu m$  and different C2C spacing.

Elliptical PS micropillars (Figure 3-14) exhibit higher elastic modulus approximately three times higher than cylindrical pillars (Figure 3-6) even though the diameter of circular pillars is 2.5 times bigger than the major diameter (2 $\mu m$ ).

Additionally, the type of material is used can manipulate the elastic modulus as shown in Figure 3-15. Using TPU as molding material can drop the elastic modulus to match the human uterus ( $E=1.4 \text{ MPa}$ ) at lower aspect ratio as presented in Figure 3-16. Similarly, if using LDPE material (Figure 3-17) aspect ratio of 1.5 is needed with 1  $\mu m$  C2C spacing to match the required modulus.

### 3.2.1.2.2 Pillar dimensions relationships to $E_{\text{Apparent}}$ [2 $\mu\text{m}$ elliptical pillars with different C2C spacing( $\chi$ )].

Patterns dimensions are the main keys drive the apparent moduli on cells.

2  $\mu\text{m}$  diameter elliptical pillars was used in this analysis to find the main driving dimensions on elastic modulus. Figure 3-18Figure 3-19 shows that pillars diameter and height have a minor effect on the elastic modulus. Spacing between pillars is the most effective dimension that can control the apparent elastic modulus.

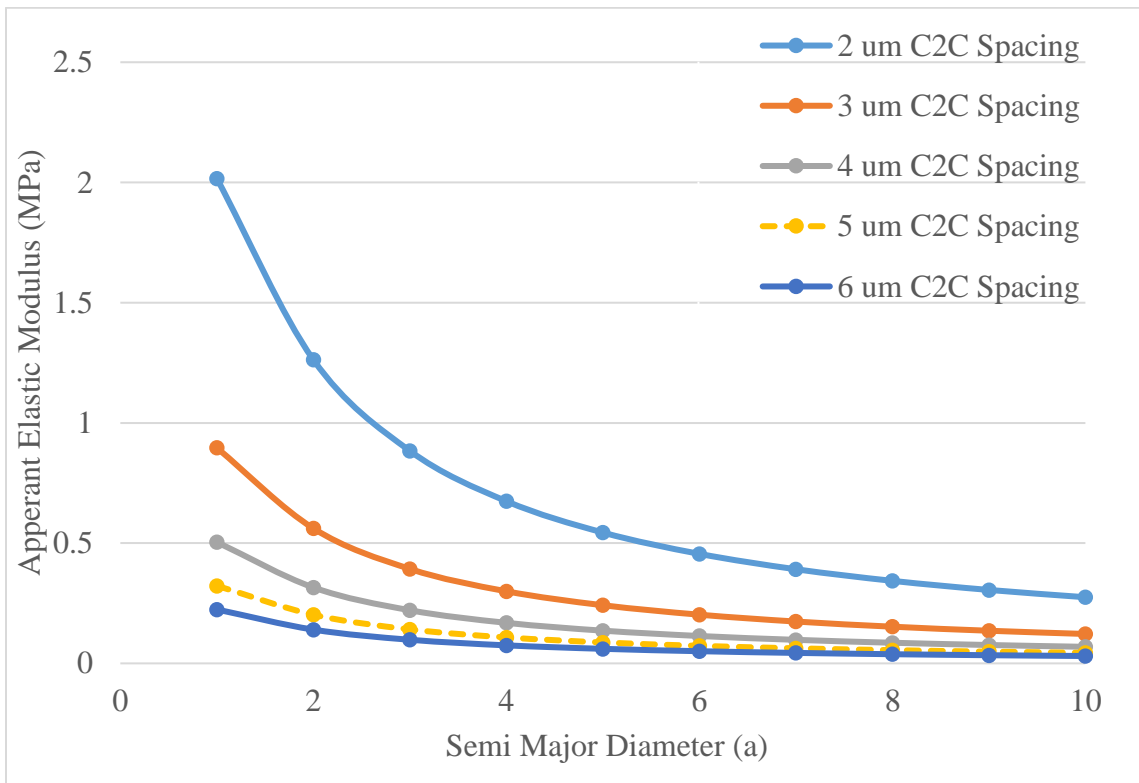


Figure 3-18: TPU micro pillars with semi-major diameter (a) sensitivity analysis to Apperant Elastic modulus on cells.

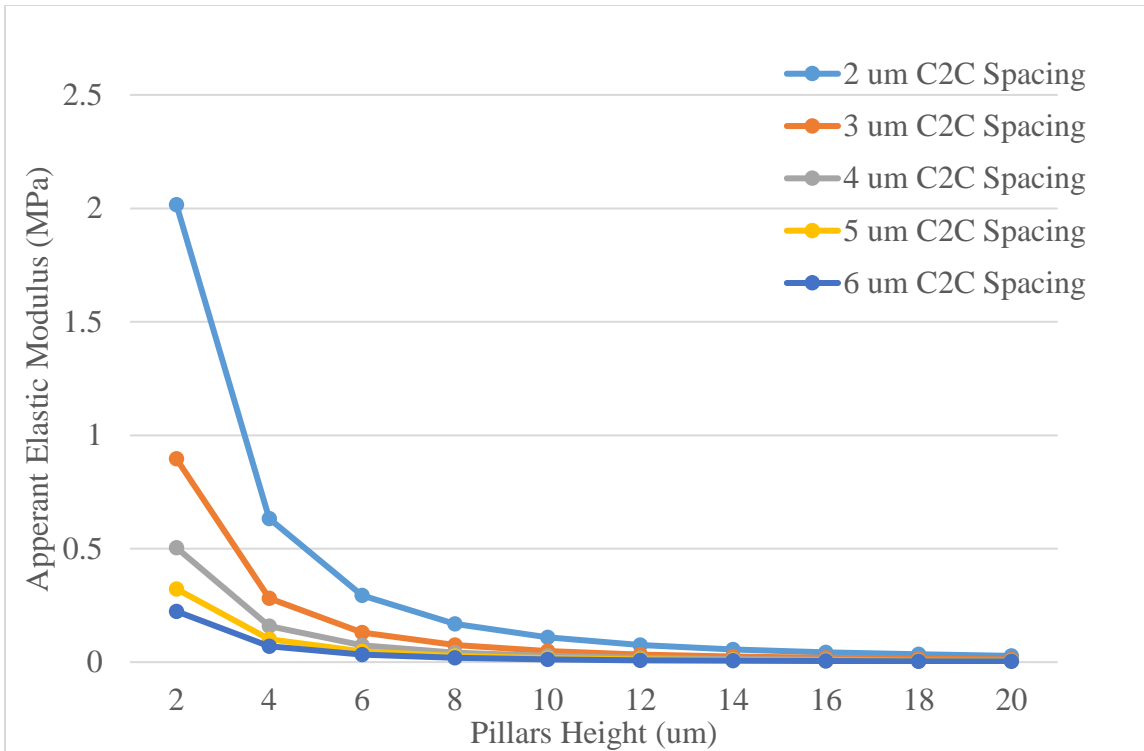


Figure 3-19: TPU 2 um micro elliptical pillars with height (L) sensitivity analysis to Apperant Elastic modulus on cells.

### 3.2 Ansys Simulations

Ansys simulations were done to confirm the deflection of 5  $\mu\text{m}$  diameter and 10  $\mu\text{m}$  long micropillar. Simulations were done to justify the amount of deflection described earlier in equation 6 with a similar study done by K. Kim et al. [66]. Polydimethylsiloxane (PDMS) polymer was used with Poisson's ratio of 0.49, and elastic modulus of 750 KPa. Force applied in the simulations were adopted from K. Kim et al. [66] where a platform was demonstrated to measure cell traction forces for rat cardiomyocytes. Force was in the range of 20-100 nN on a PDMS micropost array. It was observed that the theoretical model derived previously gives similar results as the finite element method as seen in Figure 3-21

with 5% difference. This model demonstrated here could be an alternative method to predict the amount of deflection that micro pillars deform under given range of forces.

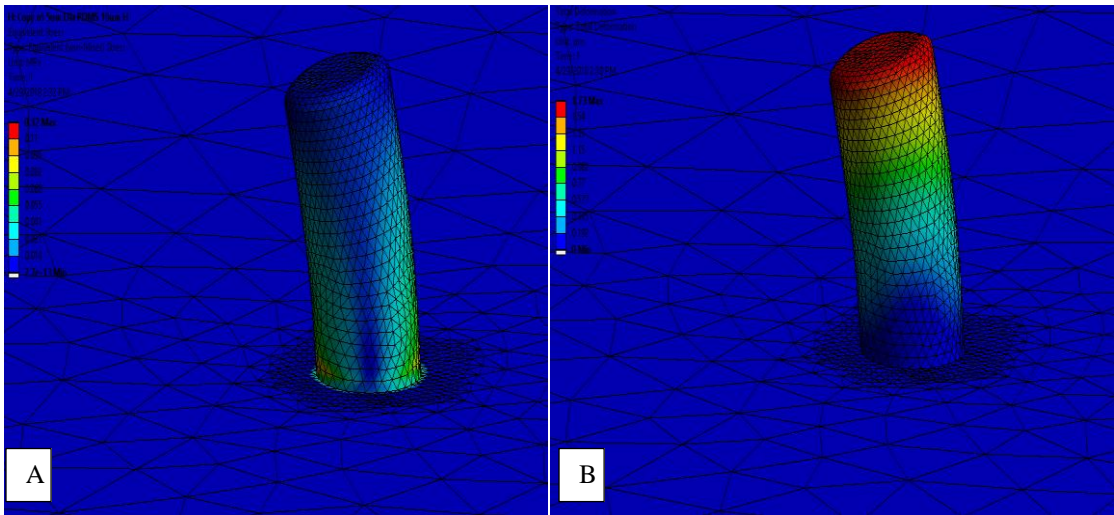


Figure 3-20: A) Equivalent stress result (MPa). B) Displacement result (um).

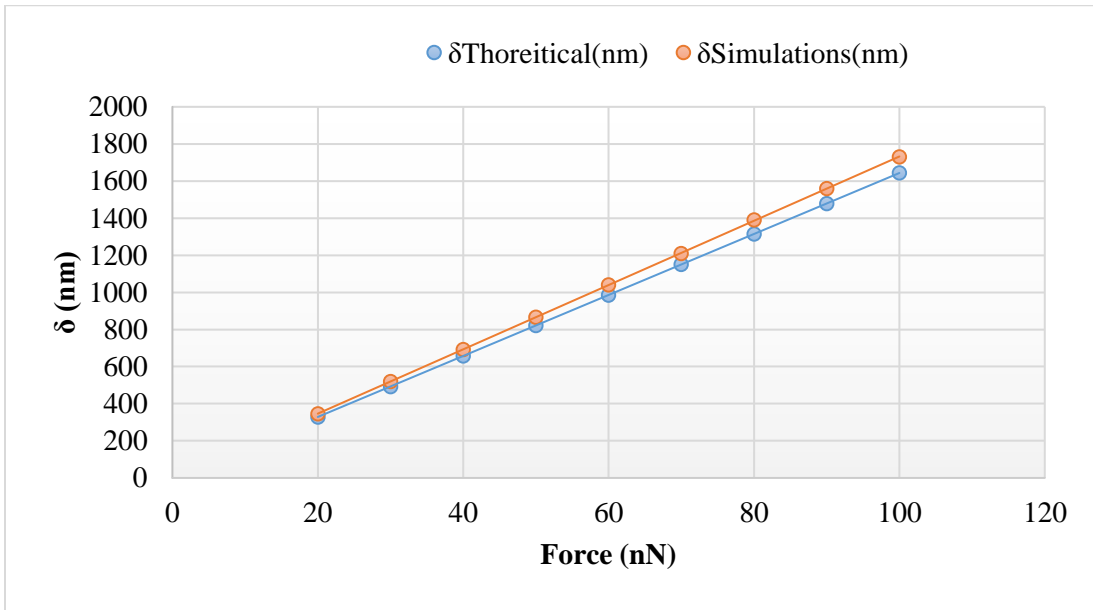


Figure 3-21: Force-displacement plot for 5um diameter post with 10 um height.

### 3.3 CONCLUSION

Analytical cell sensing model showed here will tolerate a proper understanding of pillar deflection and shear occur during cells culturing process based on Euler-Bernoulli and Timoshenko approximations. This model will provide a better method to design pillar arrays prior to cell culturing procedure and significantly improve the ability to study cells developments. There are many variables that govern the apparent surface stiffness including shapes, aspect ratio, center to center spacing, and young modulus of the substrate. In this study, a novel approach to determine an appropriate elastic moduli that cell will sense was provided. As noticed from the derived expression, the presence of shear deformation offered additional pillar deflection resulting in a lower apparent modulus. Material selection also influence the apparent modulus. It was determined in this investigation that polystyrene would not be the proper choice when targeting lower apparent modulus. Additionally, it was noticed that elliptical pillars contribute higher modulus of elasticity compared to other cross section.

## CHAPTER 4: TOOLING DEVELOPMENT AND TESTING

### 4.1 Silicon-based Tooling

#### 4.1.1 Photolithography

Mask design through available software packages AutoCAD and L-edit and were sent to mask provider for fabrication. The mask design is presented in Figure 4-1 . 4 quadrants each with an area of 25x25 mm were patterned with 15, 10  $\mu\text{m}$  oval shapes and 5  $\mu\text{m}$  circular shapes with 3  $\mu\text{m}$  edge to edge spacing. The process of photolithography has a sequences of steps (*Figure 4-2*). The process in more details is explained in the next section.

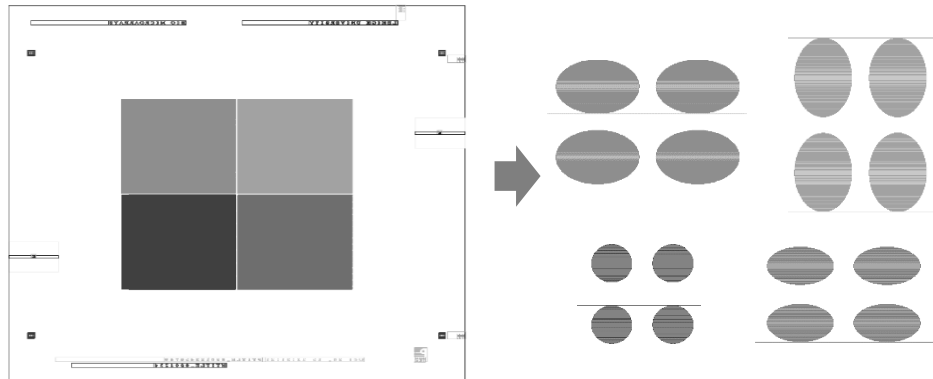


Figure 4-1: a) Photolithography Mask, b) 4 micro-features regions.

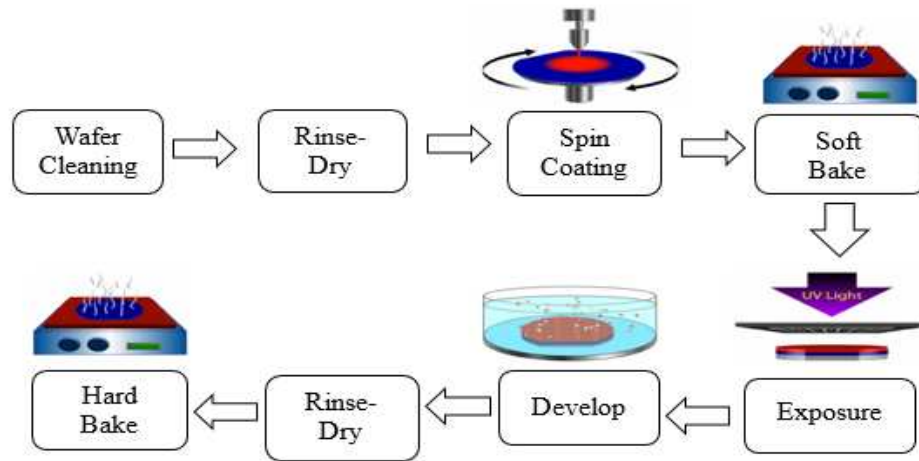


Figure 4-2: Schematic of photolithography process.

#### 4.1.1.1 RCA Cleaning

The Si wafer was first cleaned using distilled water (dH<sub>2</sub>O), ammonium hydroxide (NH<sub>4</sub>OH), and hydrogen peroxide (H<sub>2</sub>O<sub>2</sub>), at a ratio of 5:1:1 for 5 minutes at 75 °C. This was followed by rinsing five times in a 1000 mL beaker. This cleaning step removed insoluble organic contaminants from the wafer surface. The wafer surface, was hydrophobic at this stage. A hydrophilic was required to ensure better bonding with the photoresist [70]. The wafer surface was first vapor primed in a closed container for 10 minutes using a 1:1 ratio of hexamethyldisilazane (HMDS) and xylene (C<sub>6</sub>H<sub>10</sub>). This procedure causes the formation of ammonia (NH<sub>3</sub>) due to HMDS decomposition into trimethylsilyl groups. The methyl groups form a hydrophobic surface, thereby improving photoresist adhesion as described Figure 4-3 [23,24,70].

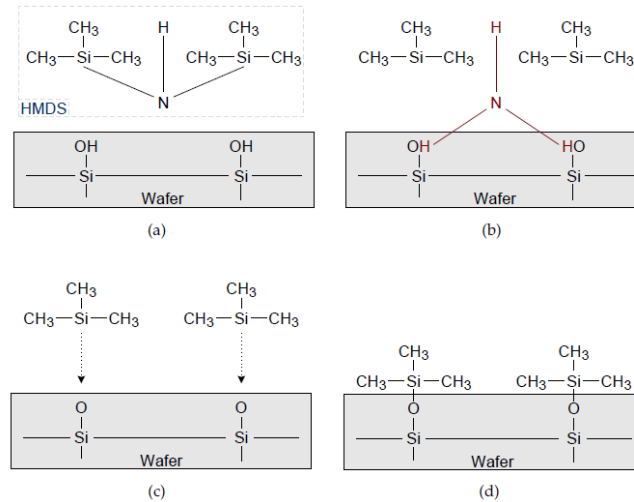


Figure 4-3: Wafer Surface Modification with HMDS

#### 4.1.1.2 Positive Photoresist Spin Coating

The wafer was then spin-coated with positive photoresist (OCG 825) at 5000 rpm for 40 seconds, followed by baking at 100 °C for 40 min. The coated wafer was then loaded onto a mask aligner and exposed to UV light for 1.5 seconds, set at a power of 25 W. Prolonged exposure time has a higher effect on features dimensions as seen in Figure 4-4. It was found that overexposed wafers have an overall dimensional change by 5%.

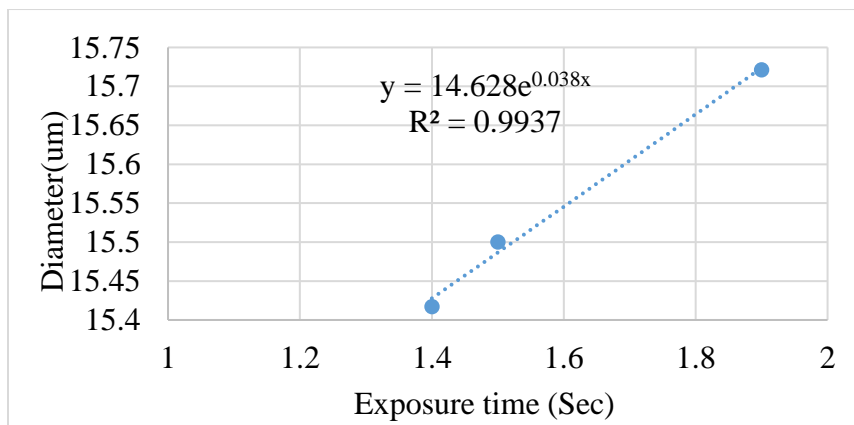


Figure 4-4: Exposure time effects on features dimensions.

A developer (OCG 809) was then used to remove exposed areas which represent the targeted geometries. A spin dry step was followed by a hard-bake at 130 °C for 30 minutes to remove moisture residues. For wafers with a SiO<sub>2</sub> layer, wet etching step has a wet etching process removed the oxide layer and act as a second mask for deep etching. Depending on the SiO<sub>2</sub> thickness, wafers were immersed in buffered hydrofluoric acid (BHF) for 6-7 minutes and rinsed in distilled water and spin-dried followed by a 20 minutes baking to remove moisture remains.

## **4.2 Deep Reactive Ion Etching (DRIE) Trails**

The targeted geometries were prepared by a deep reactive ion etching process. The process utilizes repetitive alternating steps of exposure to plasma gases of sulfur hexafluoride (SF<sub>6</sub>) for etching, and octafluorocyclobutane (C<sub>4</sub>F<sub>8</sub>) for passivation of the side walls removing a small amount of material in etch cycle. A thin layer of C<sub>4</sub>F<sub>8</sub> deposition was deposited at the final step after the intended cavity depth was achieved. This layer serve as the antistiction coating, and facilitated mold release during the injection molding process. The recipe for the procedure is shown in .. Using these parameters, the etch rate varied depending on the substrate type. The etch rate for silicon wafer was found to be approximately  $1.54 \pm 0.05$   $\mu\text{m}/\text{min}$  while for SiO<sub>2</sub> wafers is  $1.39 \pm 0.05$   $\mu\text{m}/\text{min}$  as shown in Figure 4-5. The etch rate was measured from SEM images using ImageJ package. Some of Si mold inserts are shown in Figure 4-6.

Table 4-1: Bosch Processing Parameters.

Plasma	Plasma Flow [sccm]	Duration [seconds]	Source Power [W]	Total Processing Time [seconds]
SF <sub>6</sub>	125	3	1200	930 (21.52 μm deep) 630 (15.03 μm) 398 (10.02 μm) 330 (8.35 μm) 135 (2.49 μm) 83 (2.04 μm)
C <sub>4</sub> F <sub>8</sub>	100	2	1200	
C <sub>4</sub> F <sub>8</sub>	150	20	1200	

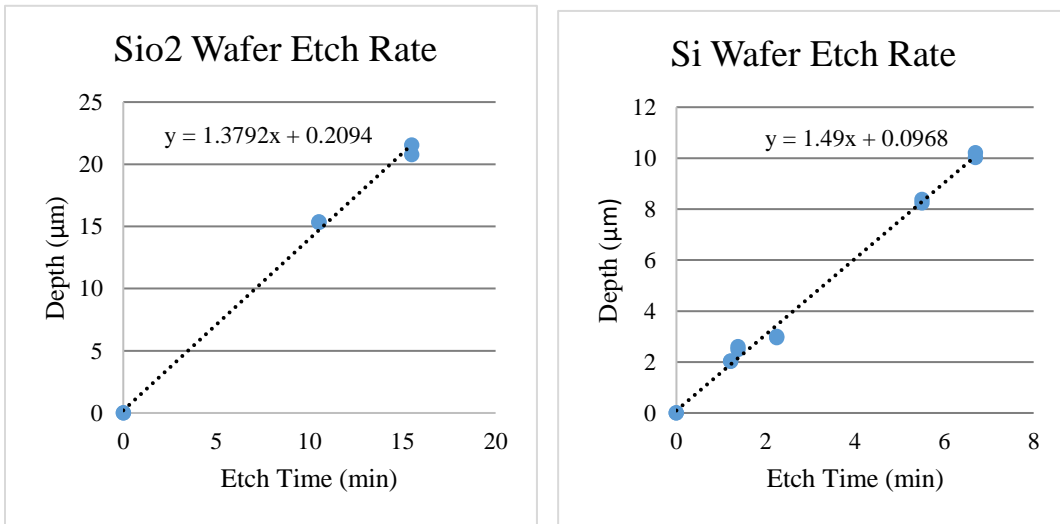


Figure 4-5: Etch rate curves for Si and SiO<sub>2</sub> wafers.

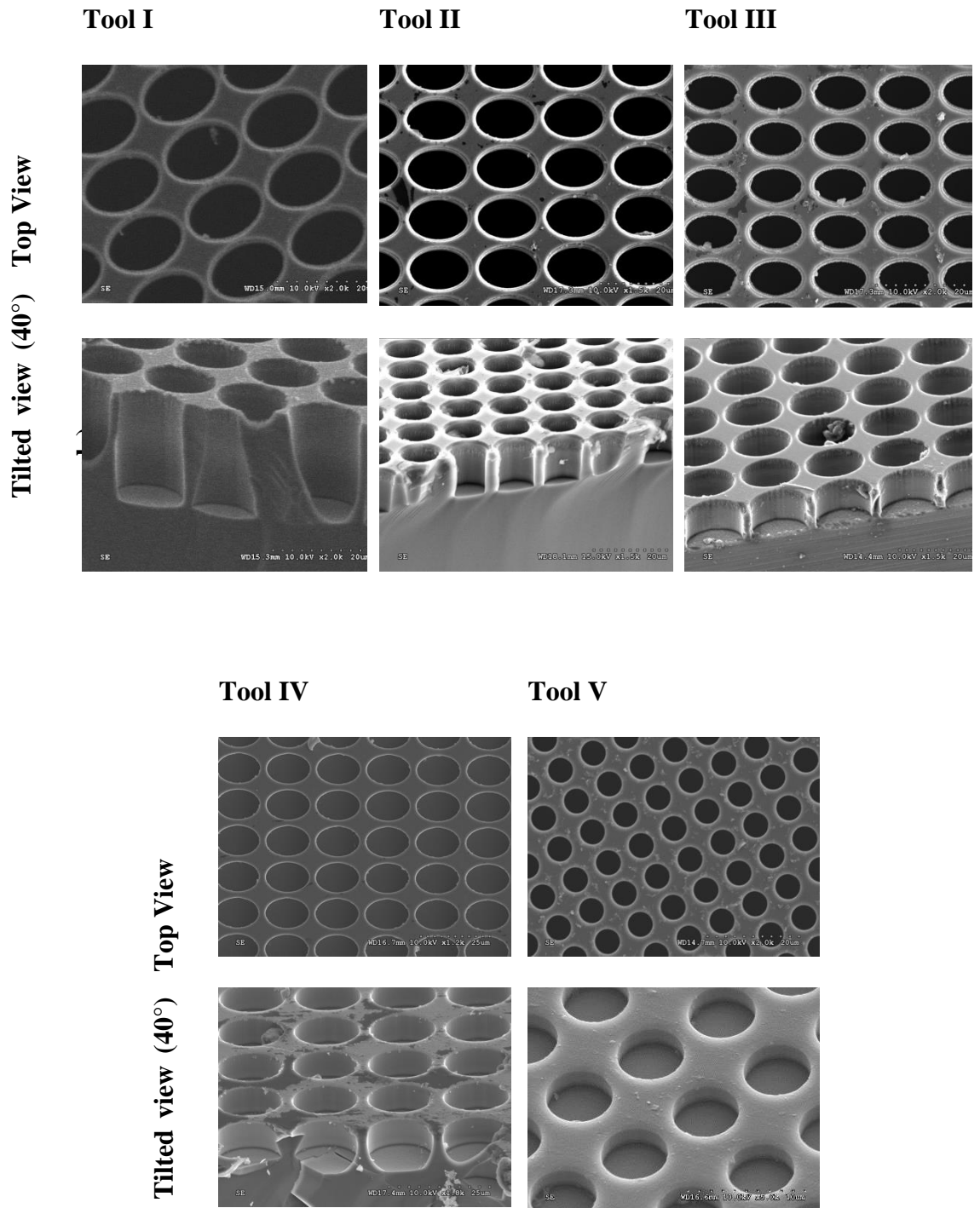


Figure 4-6: Silicon molds with different depth.

### 4.3 Silicon Mold Assembly

Silicon (Si) based inserts were fabricated using a photo-lithography process in Sherman Fairchild center here at Lehigh University. After the features were fabricated onto the wafers they were diced into  $6 \times 6$  mm squares in a mechanical scribing machine. The individual squares were bonded to the mold insert using a high-performance epoxy that can withstand temperature up to  $320\text{ }^{\circ}\text{C}$ . A rubber pad was placed (Figure 4-7) to uniform the surface underneath the wafer to balance the stress applied on the wafer during the molding process. After curing, the insert is plugged to the mold base in the  $\mu\text{IM}$  machine.

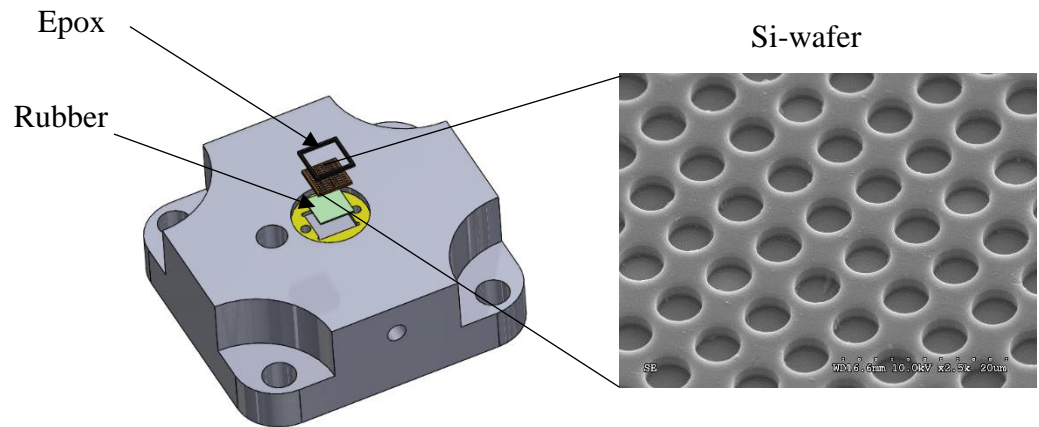


Figure 4-7: Si Wafer Bonded to Aluminum Mold base with Adhesive.

#### 4.3.1.1 Aluminum & Steel Inserts Assembly

Initially, aluminum 6061 alloy was used for fabricating the mold base due to the ease of machining. After many cycles, the aluminum mold base showed indication of severe wear and material started to leak outside the cavity. A steel mold based then CNC

machined to replace the aluminum mold base. It was perceived that the steel mold can withstand material impact and survive a higher number of cycles.

#### **4.3.1.2 Sprue Gate Insert**

A sprue gate single cavity was used in this investigation to maintain the pressure through the cavity. The disadvantage of the sprue gate is that molded parts need an extra step to cut the sprue out and polish the back surface. The injection pressure was kept below 30 MPa to avoid silicon mold breakage.

#### **4.3.1.3 Embedded Cartridge Heater Assembly**

Steel back mold base with embedded cartridge heaters was employed during the experiments to control mold temperature using a temperature controller.

### **4.4 BMG Based Mold**

Fabrication of robust high precision molds for injection molding has been investigated in recent years. For high volume manufacturing, long-lasting molds are necessary to maximize the economic potential.

As mentioned before, silicon based tooling may not be ideal for scaling up the manufacturing from laboratory testing to a production scale, due to the brittleness of the material and the adhesion properties to mold inserts. (BMG) are amorphous multicomponent metallic alloys that are isotropic, homogeneous, and free of crystalline defects. BMGs are preferred for their unique property combination of high strength, high elastic limit, formability, corrosion and wear resistance. In addition, BMGs exhibit a

viscous flow when they are heated above their  $T_g$  allowing these materials to be formed to desired shapes using hot-forming operations. These features make BMGs particularly attractive for fabricating mold inserts[71–75].

Micro/nanostructured BMG tooling inserts will be created by forming Si master templates manufactured via micro/nanoscale photolithography followed by deep reactive ion etching. BMG metal tooling will then be accomplished through relatively low pressure (approx. 20 MPa) superplastic forming (Figure 4-8b). Because it has been found to exhibit low viscosity Newtonian flow characteristics and excellent micro/nanoscale formability at 620K and low-stress levels, the specific BMG. Once the BMG mold insert is formed, the Si template will then be dissolved using a KOH treatment as shown in Figure 4-8c. This will yield a micro/Nanopatterned tooling insert of viable commercial size. This insert will then be subjected to an antistiction treatment and incorporated into a larger tooling assembly for injection molding of devices (Figure 4-8d-f). Mold life expectancy for microinjection molding is expected to exceed silicon mold fabrication allowing this plates to be widely spread to clinical laboratories[74,76].

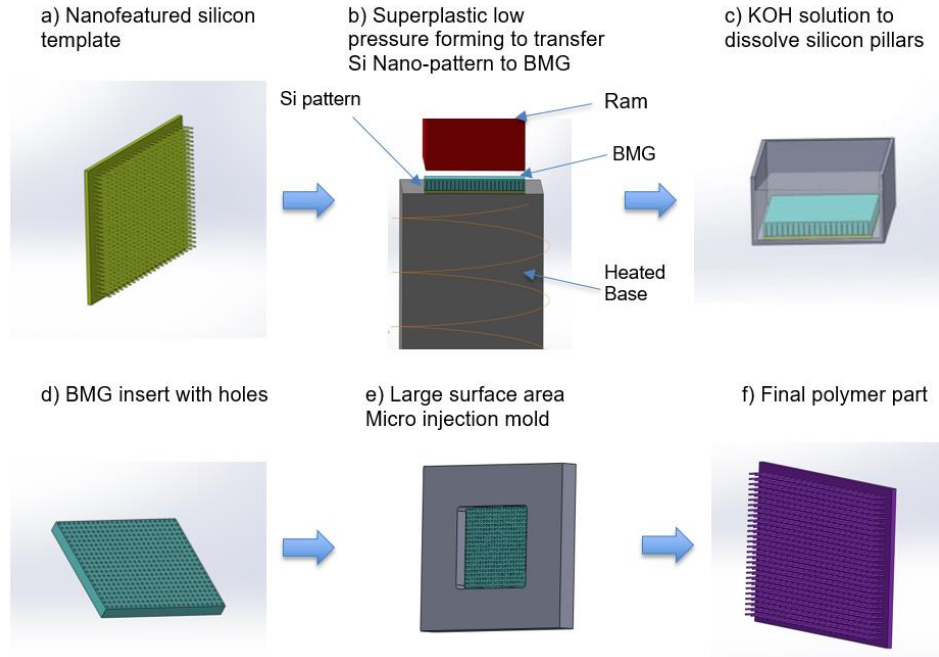


Figure 4-8: Bulk metallic insert fabrication using Micro/Nano structured silicon.

#### 4.4.1 Fabrication of Si Micro Pillars Molds

Efforts were made to fabricate silicon micropillars with the same mask used in fabricating silicon-based tooling described in section 4.1. A reverse image of the etched micro holes that were transferred using a negative photoresist (AZnLOF 2035) to fabricate micropillars patterns as explained below.

##### 4.4.1.1 Photolithography with Negative Photoresist

Wafers were first RCA cleaned as described in 4.1. Then wafers soft baked at 100 °C for 40 minutes. A thin layer of Hexamethyldisilazane (HMDS) was spin coated on the wafers at 3000 rpm for 10 seconds followed by a baking treatment on a hotplate for 2 minutes. A negative photoresist (AZnLOF 2035) was then spin coated at 4000 rpm for 30

seconds followed by a soft bake at 112 °C for 1 minute. After baking, the mask was held to a g-line exposure device on a vacuum stage. The wafer was placed on a vacuum chuck and aligned in contact with the mask with a lever. After the alignment is completed, the patterns in the mask was transferred to the photoresist by shining a ultra-violet light through the mask. The exposure time was varied from 30 to 45 seconds to ensure that targeted areas were fully exposed. A post exposure bake was performed at 112 °C for 2 minutes to improve the resist adhesion to the wafers and to reduce mechanical stress formed during the exposure process. Then the wafer is immersed in MF 300 developer for 30 sec and rinsed in distilled water. A spin dry step followed by a hard-bake at 100 °C for 2 min. was needed to remove any moisture residues. A schematic of the process is presented in Figure 4-9.

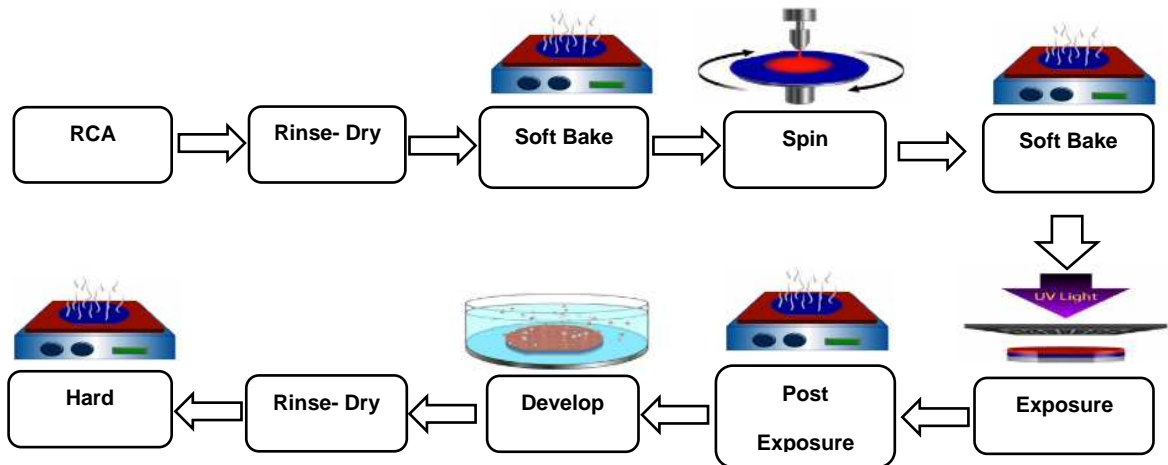


Figure 4-9: Photolithography Process.

#### 4.4.1.2 Deep Reactive Ion Etching (DRIE)

The etching process was performed using Adixen I Speeder 100 deep reactive ion etching (DRIE) instrument which utilized the BOSCH process to produce straight deep etched channels. A combination of processing parameters consists of SF<sub>6</sub>, C<sub>4</sub>F<sub>8</sub> flow rates, duration, power during etching and passivation, temperature and chamber pressure that affected the etching process.

After setting the etching conditions, a wafer was placed on a substrate holder then loaded to the reactor chamber. The wafer was maintained at a constant temperature during the etching process by flowing helium gas underneath the wafer. A SF<sub>6</sub> plasma etching step was alternated with a C<sub>4</sub>F<sub>8</sub> polymer coating step repeatedly until required depth was achieved.

##### 4.4.1.2.1 Exposure time Trail 1

Table 4-2: Etching processing parameters.

Etch Conditions	Plasma	Flow (SCCM)	Duration (Sec)	Chamber Temp.(C°)	Chamber Pressure(mbar)	Source Power(W)	Total Processing time
Etching	SF <sub>6</sub>	125	3	10	9.1*10 <sup>-3</sup>	1200	10 min 8 sec
Passivation	C <sub>4</sub> F <sub>8</sub>	100	2				6 min 38 sec
							7 min 09 sec
							1 min 13 sec

In the first run, tapered pillars were formed after DRIE etching. This was attributed to the underexposed photoresist. The exposure time was set at 35 seconds (Figure 4-10).

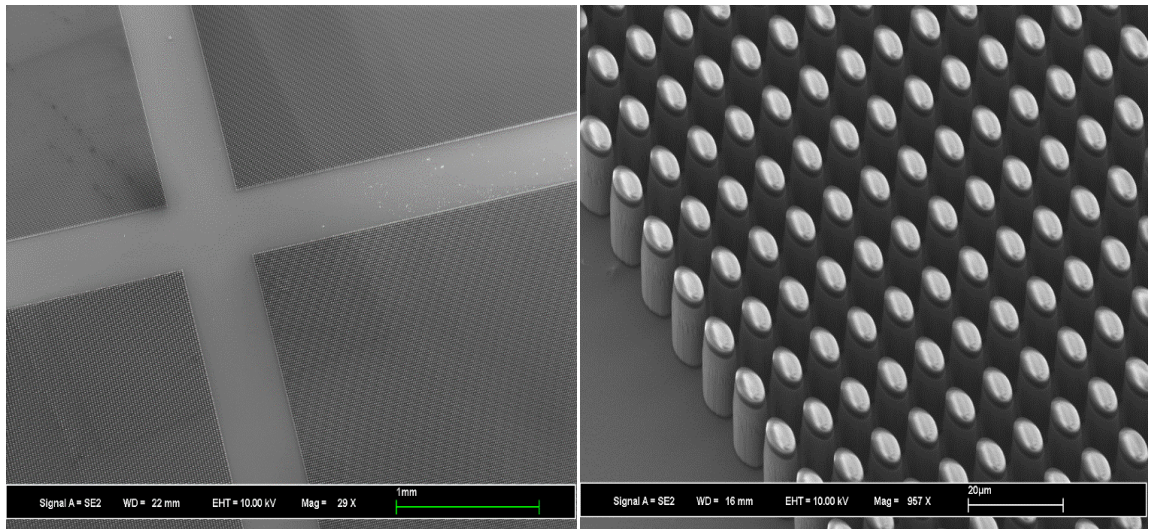


Figure 4-10: Trail 1 Tapered Si pillars.

#### 4.4.1.2.2 Exposure Time Trail 2

To avoid undercut that was happening due to underexposed photoresist, the exposure time was increased to 45 seconds in this trial. It was assumed that this exposure time would be sufficient to sustain the photoresist during etching as shown in Figure 4-11. The etching parameters were kept constant as in Trail 1.

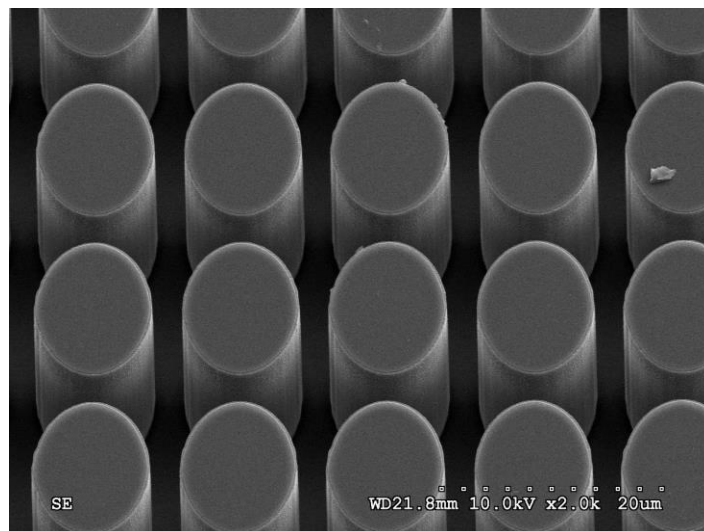


Figure 4-11: Si pillars with 15 µm diameter and 15 µm height.

### 3.1.1.1 O<sub>2</sub> Plasma Photoresist Ashing:

Oxygen plasma was performed in a plasma chamber to clean the wafers. First, the wafers were soaked in photoresist remover (PRS 3000) at 70 °C for 20 minutes. Then the wafers were rinsed with distilled water and spin dried for 3 min at 300rpm. Finally, the dried wafers were transferred to plasma chamber to remove residual photoresist. O<sub>2</sub> gas flowed at 50.9 sccm to clean the surface of the wafers for 10 minutes. The O<sub>2</sub> plasma cleaning time was highly dependent on exposure time. Samples that were exposed for 30 sec experienced high adhesion of the photoresist to the top of the created pillars. As exposure time was decreased to 25 sec, the wafers needed 5 minutes to remove all photoresist leftover from chemical cleaning in the first step. The plasma forming conditions were as follows

gas pressure of 347 mTorr,

power = 303 watts and

O<sub>2</sub> flow v = 50 sccm.



Figure 4-12: O<sub>2</sub> Plasma Ashing Machine.

#### 4.1.1 Thermoplastic forming of BMG

BMGs exhibit good formability when heated above their glass transition temperature ( $T_g$ ) in the supercooled liquid region (SLR) ( $\Delta T = T_x - T_g$ ) below the crystallization temperature,  $T_x$ . It was found that the cooling rates after the fabrication of BMG structures in the SLR are critical to maintain the amorphous state [77,78]. In the supercooled region, BMG viscosity can vary between  $10^{12}$  Pa.s at the glass transition temperature down to  $10^5$  Pa.s at the crystallization temperature [74,79]. In this project the intention was to soften the BMG by elevating the temperature of the BMG in the SLR and precisely replicate a reverse image of Si mold by the application of pressure.

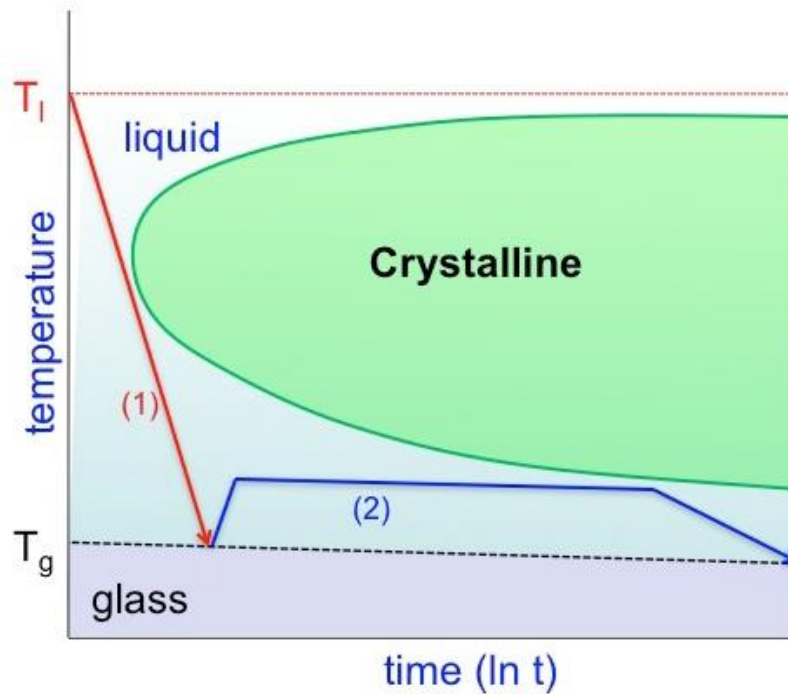


Figure 4-13: Schematic of a time-temperature-transformation (TTT) diagram showing that metallic glass can be formed via (1) direct casting. (2) Thermoplastic forming [77].

#### 4.4.1.3 Material Selection

A zirconium-based bulk metallic (Zr-BMG) alloy was used in this research with the composition of Zr67 Cu10.6 Ni9.8 Ti8.8 Be3.8 (wt%) which commercially available has a well-proven formability. This specific alloy has a high strength with an elastic modulus of 95 GPa and 2% elastic deformation. This Zr-BMG is highly resistant to severe environments and high wear resilient especially with added Beryllium which made it the best available choice for this investigation. Beryllium addition in the Zr-BMGs is known to provide unique characteristic of resistance to corrosion, wear, and fatigue; high electrical and thermal conductivity; strength; and hardness. The beryllium addition also increases the supercooled liquid region resulting in large molding window (~110 °C) for this specific alloy. With such a large molding window, it was cited that the crystallization could be avoided with controlling cooling rate at 10 K/s[80–82]. It is well known that beryllium is not an environment-friendly element, especially with a high content (>22.5%) [83]. The mechanical characteristics of the Zr-BMG alloy used in this research are given in Table 4-4.

Table 4-3: Mechanical properties of Zr-BMG (Provided by Materion Corporation).

Yield Strength (Mpa)	1800
Elastic Modulus (GPa)	95
Fracture Toughness $\text{MPa}\sqrt{m}$	55
Density (g/cc)	6.0
Glass Transition Temperature ( $T_g$ )(C°)	352
Crystallization Temperature ( $T_x$ )(C°)	466
Melt Temperature ( $T_m$ )(C°)	644

#### 4.4.1.4 Differential Scanning Calorimetry (DSC)

Differential scanning calorimetry (DSC) is a thermal characterization technique that measures that amount of heat absorbed or released by the sample. It is utilized to measure glass transition temperature, crystallization temperature, and melting temperature. In this study, DSC is used to find the super liquid region ( $T_g > T > T_x$ ) of Zr-BMG alloy. A DSC scan was performed to find  $T_g$  and  $T_x$  at a heating rate of 20 °C/min ( *Figure 4-14*). It was determined that the glass transition onset temperature ( $T_g^{\text{onset}}$ ) is 351.7 °C, and the crystallization onset temperature ( $T_x^{\text{onset}}$ ) is 461.4 °C. Thus, the SLR was determined to be ~110 °C in line with the published data. The DSC results are shown in Table 4-4.

Table 4-4: Characteristic temperatures of Zr-BMG found by DSC at a scan rate of 20 C°/min.

	$T_g^{\text{onset}}$ (C°)	$T_g^{\text{inflection}}$ (C°)	$T_x^{\text{onset}}$ (C°)	$T_x$ (C°)	$\Delta T$
Zr-BMG	351.7	363.25	461.4	494.5	110

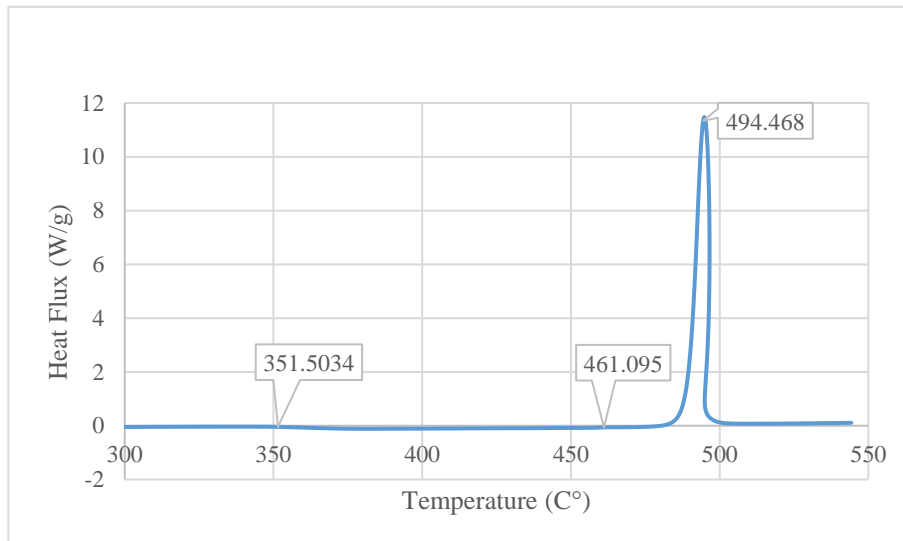
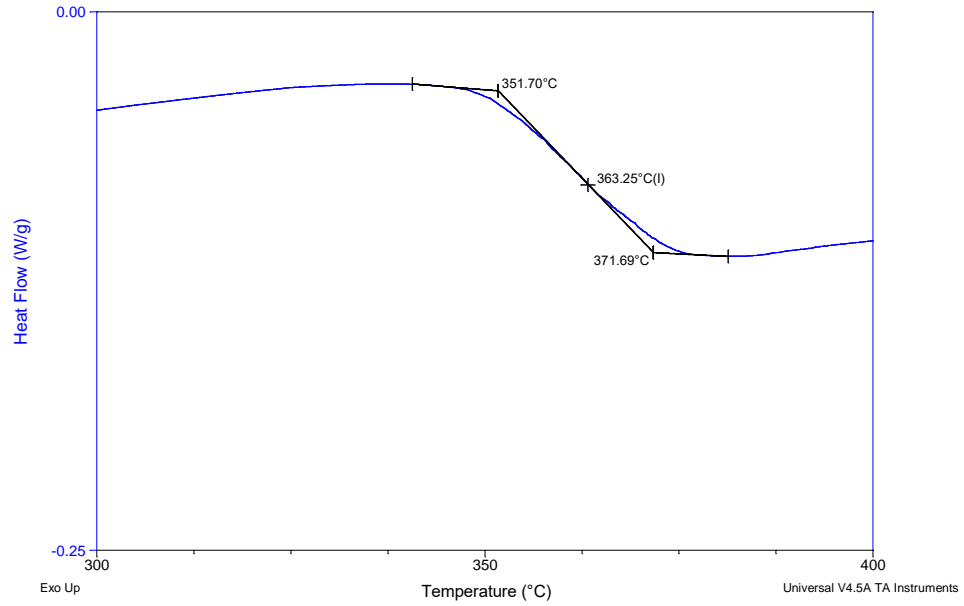


Figure 4-14: DSC curves of Zr-BMG sample with scanning rate of 20 C/min. (A) Zoom of glass transition peak between 300 C° and 400 C°. (B) Crystallization temperature peak.

#### 4.4.1.5 X-Ray Diffraction (XRD)

An as received Zr-BMG sample was characterized utilizing a x-ray diffraction (XRD) technique to confirm the amorphous nature of the alloy.. The x-ray diffraction data for the as received alloy is presented in Figure 4-15. There were two broad peaks with centers at  $\sim 38^\circ$  and  $\sim 65^\circ$  respectively. Such low intensity broad peaks are typical of amorphous materials.

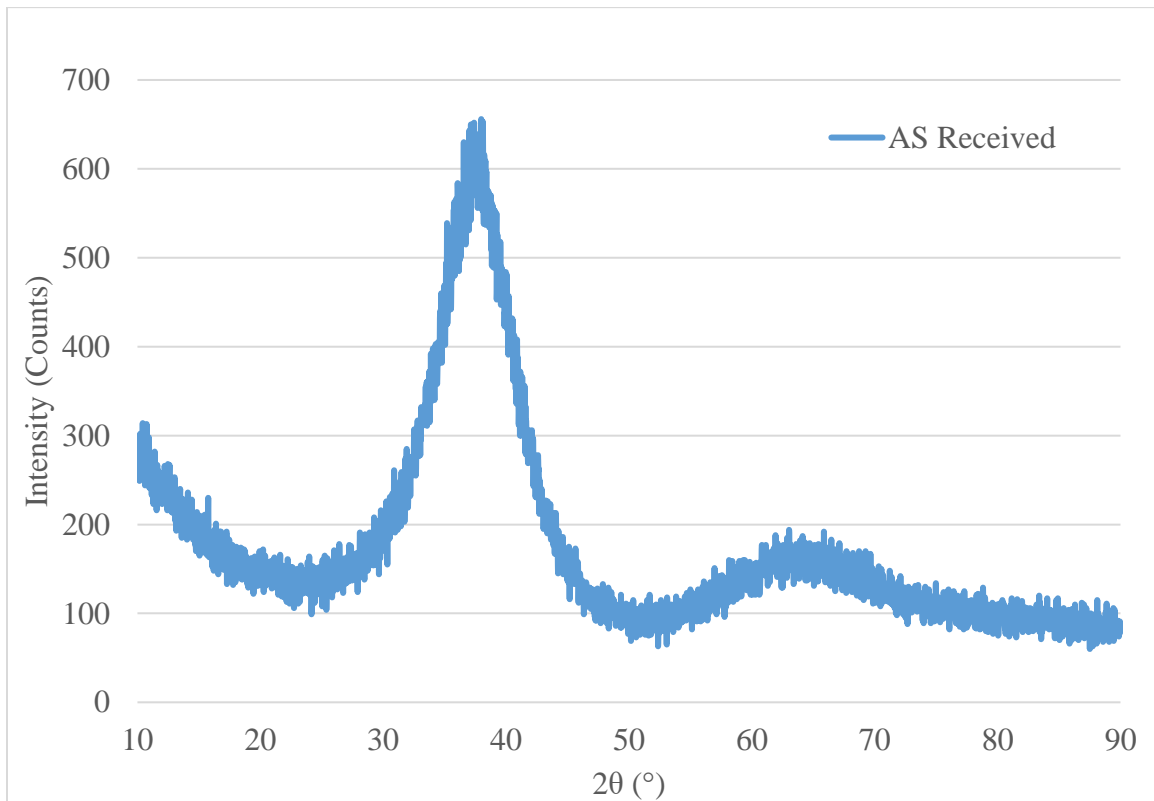


Figure 4-15: XRD scan of Zr-BMG after dicing to 12x12 mm.

#### 4.4.1.6 Vacuum Hot Press Machine

Vacuum hot press was used in these experiments to eliminate the oxidation presents on the BMG. This hot press had a graphite hot zone with a maximum operating temperature of 2000 °C. A water cooling system capable of cooling at 10 °C/min was available. A minimum initial load of 75kg had to be applied to hold the die and samples in place during heating, pressing, and cooling. A graphite tooling set consisting of a die, two punches and spacers was utilized for pressing the sample. A schematic of the die is illustrated in Figure 4-17. This instrument is capable of heating and cooling rate of 10 °C/min (Figure 4-16).

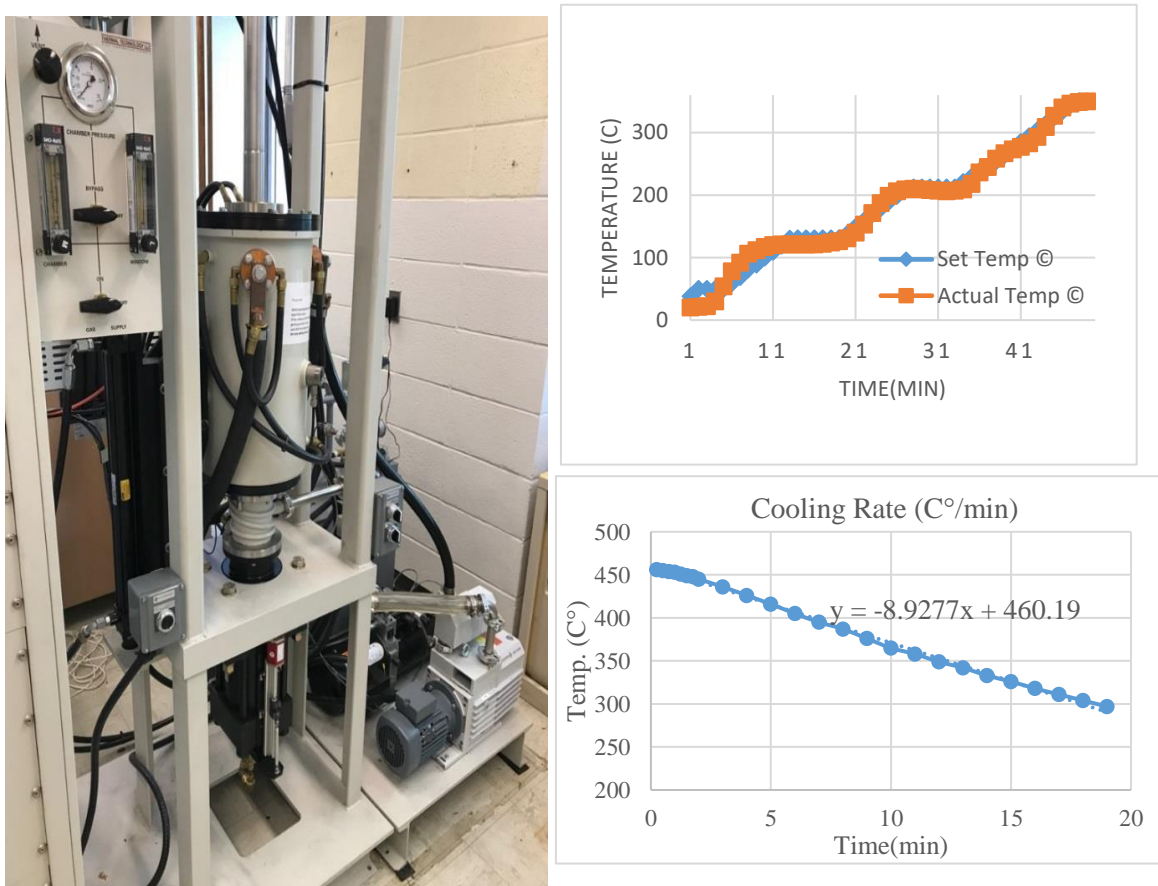


Figure 4-16: Vacuum Hot Press Machine with Cooling Rate and Heating Rate Calculated during Experiments.

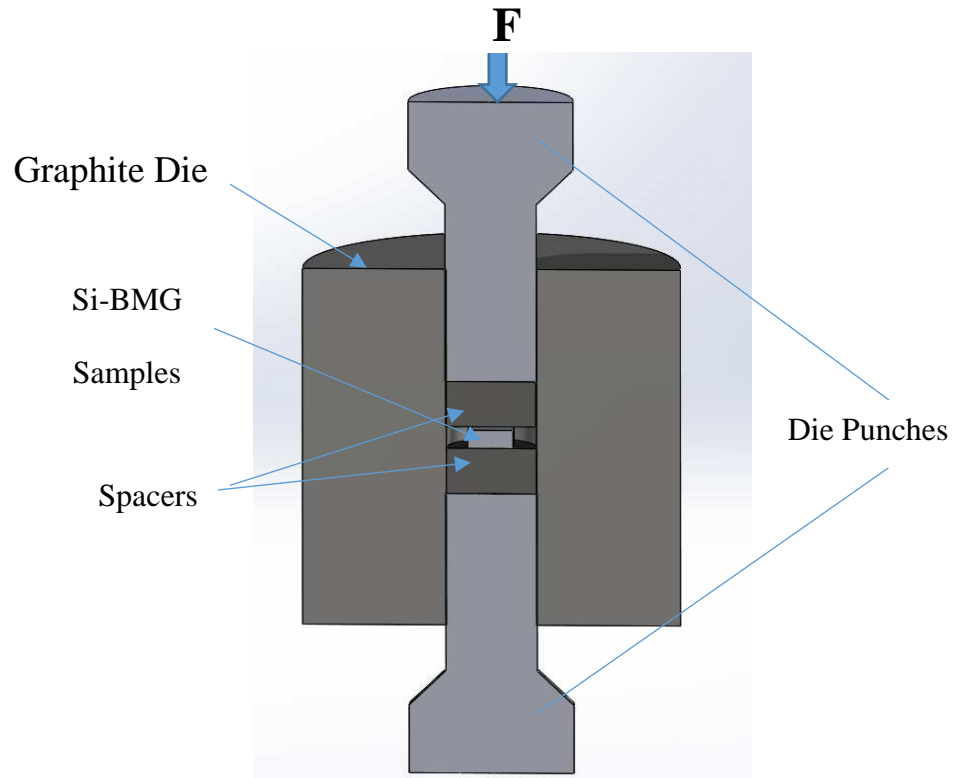


Figure 4-17: Schematic of the Graphite Die used in Hot Press Experiments.

#### 4.4.1.7 Thermoplastic Forming (TPF) under Vacuum

Certain factors such as pressure, and the application environment can affect the BMG during thermoplastic forming. It has been reported that increasing the applied pressure on amorphous alloys can raise the crystallization temperature[78]. Oxidation of the BMG could occur at certain temperatures if oxygen is present in the application environment. The Zr based BMG used in this research contained different elements as Zr, Ni, Ti, and Be. Experiments were performed in the hot press under vacuum to prevent such issue that can easily create replication defects.

#### 4.4.1.7.1 TPF under Vacuum Trail 1

A 12×12×4.85 mm Zr-BMG sample was ultrasonically cleaned successively in acetone, distilled water, and ethanol spending 5 minutes each step followed by air drying. The sample was put in a graphite die with a 1inch diameter cavity. The purpose of this experiment was to understand the deformation of the BMG in the super cooled liquid region. The hot-pressing temperature was set to 450 °C and a 458 Kg load was applied. The experiment was performed under vacuum (<60 mtorr). The temperature was chosen to be just below the bulk crystallization temperature (466°C) of this specific Zr-BMG to avoid any crystallization. It was observed during the trial that the travel of the pressing ram accelerated suddenly in the temperature range 267°C - 273°C. This was attributed to the softening of the BMG resulting in severe deformation in the material. This temperature was assumed to be a measure of the glass transition temperature of the Zr-BMG under the furnace conditions. The reported glass transition temperature of this material is 352°C.

The pressed BMG sample was found to be crystalline as can be observed from the x-ray diffraction plot presented in Figure 4-18. It was concluded that several phases coexist in the crystallized BMG. Two such phases,  $Zr_2Cu$  and  $ZrBe_2$  were clearly identified (Table 4-5). There were several peaks that could not be properly indexed. It was not clear why the glass transition temperature as well as the crystallization temperature appeared to be suppressed in this trial run. The temperature was reduced in the successive trial runs to gain insight on the working temperature range (the so called super cooled liquid region or SLR) for the BMG in this specific experimental setup.

Table 4-5: Zr2-Cu and Zr-Be2 XRD patterns.

Zr2-Cu		Zr-Be2	
Angle	Intensity	Angle	Intensity
31.686	20.317	26.933	100
35.736	36.697	27.551	26.813
37.984	34.623	38.91	96.226
41.5	23.525	47.577	29.745
64.205	34.623	55.861	22.07
77.095	18.494	63.681	22.24
		64.029	16.46
		82.685	20.454

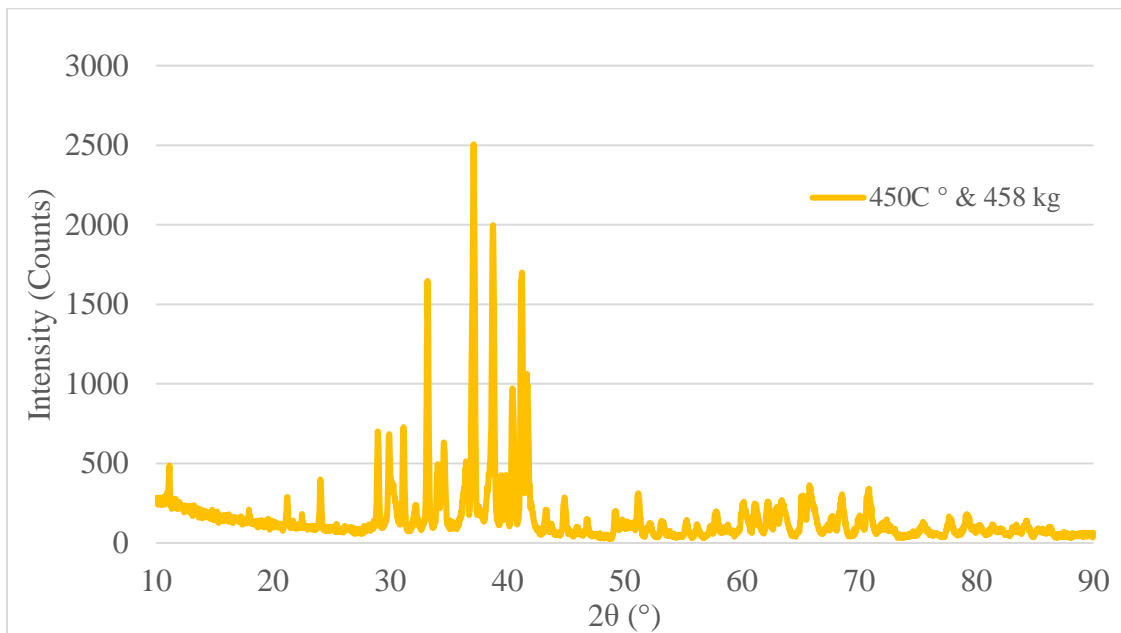


Figure 4-18: XRD Scan for Zr-BMG TPF at 450 C° at 458 kg.

#### 4.4.1.7.2 TPF under Vacuum Trail 2

Another trail run was performed at a hot pressing temperature of 350 C° with 75 Kg load. It was observed that BMG crystallized under these conditions, but the phase composition was different as compared to the BMG that was treated at 450°C under a 458 kg load (Figure 4-19).

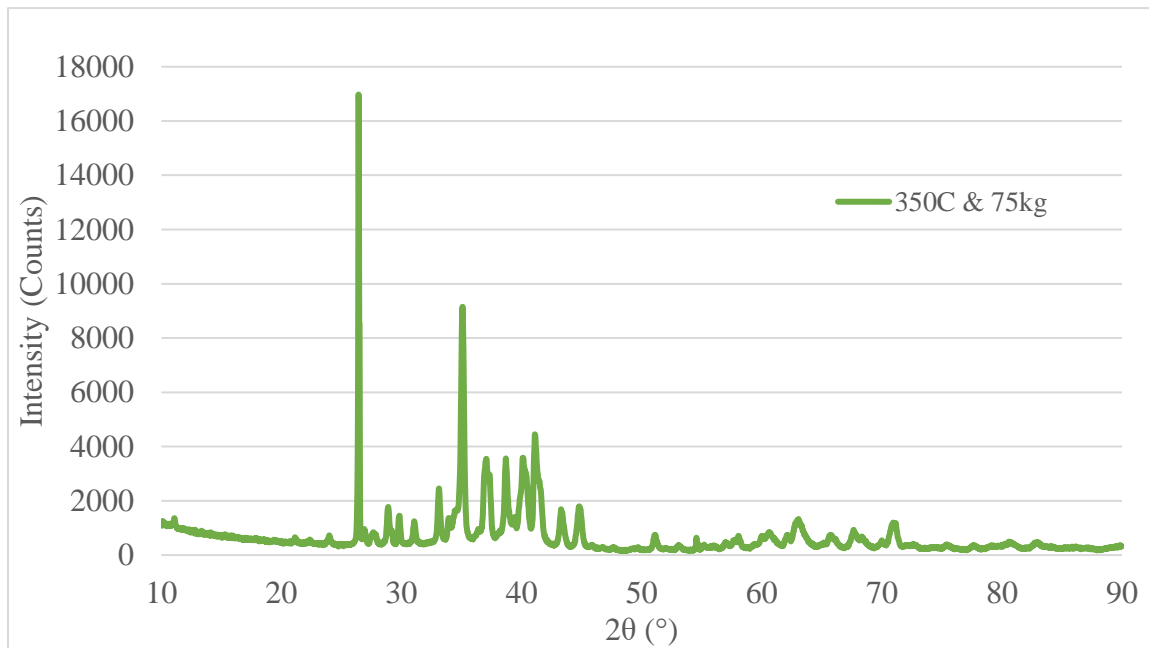


Figure 4-19: XRD Scan for Zr-BMG TPF at 350 C° at 75 kg Load.

#### 4.4.1.7.3 TPF under Vacuum Trail 3

In this trial run, the a Zr-BMG-Si mold assembly was hot-pressed at 275 °C under a 75 kg load for 1 minute before being cooled down to room temperature (Figure 4-20). The BMG was found to be crystallized under these conditions as well as shown in Figure 4-21. It was concluded that the applied pressure and the hot pressing atmosphere was affecting the crystallization process of the Zr-BMG. A nitrogen atmosphere was employed

instead of a vacuum environment to study the effects of the pressing atmosphere in a series of trial runs as described in the next section.

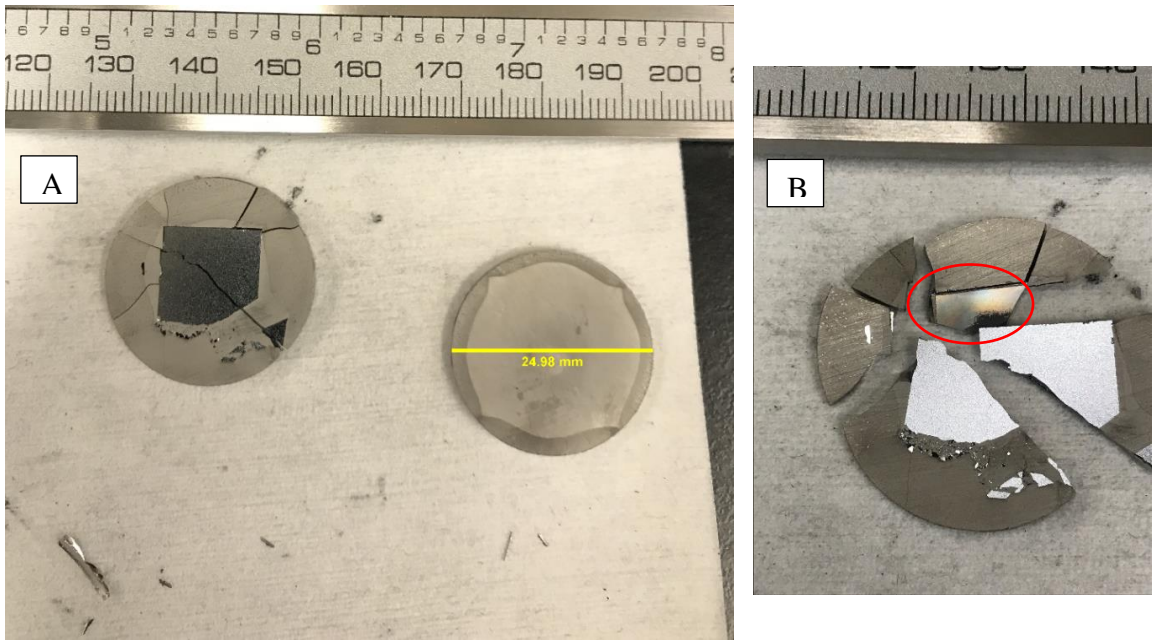


Figure 4-20: TPF Zr-BMG sample (A). Zr-BMG with Si mold breakage due to load during cooling (B) red area shows scatter light as a sign of microstructured region.

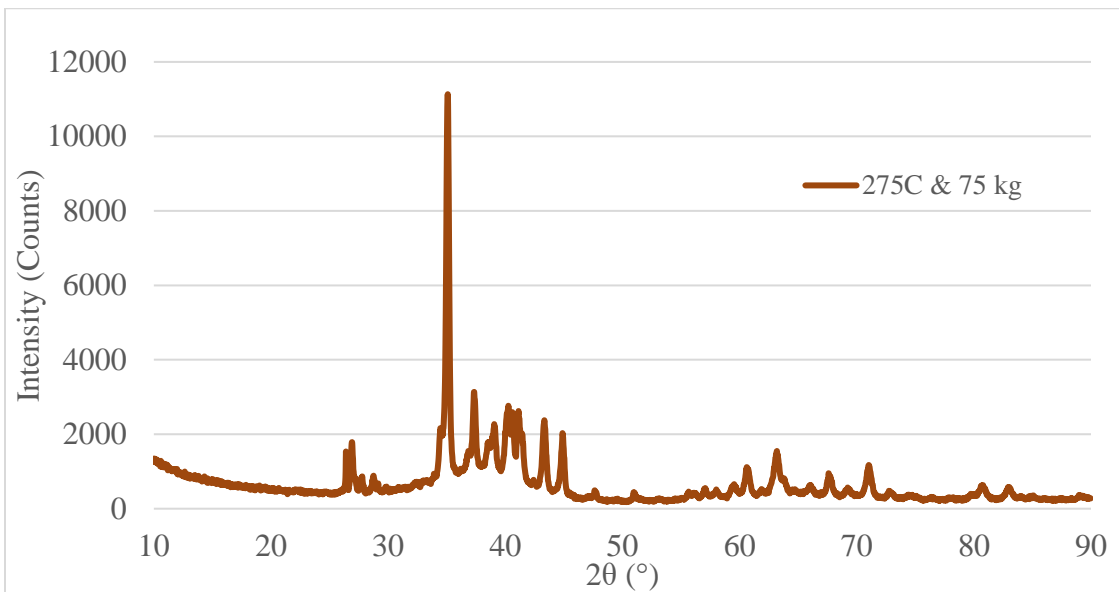


Figure 4-21: XRD Scan for Zr-BMG sample that was TPF at 275 C° at 75 Kg Load.

The depth of imprinting of the silicon micro-pillars on Zr-BMG sample was characterized using a SEM. At the center, the depth of filling was  $3.361\ \mu\text{m}$  as seen in Figure 4-22. The filling depth decreases away from the center to  $1.896\ \mu\text{m}$  at the edges (Figure 4-23).

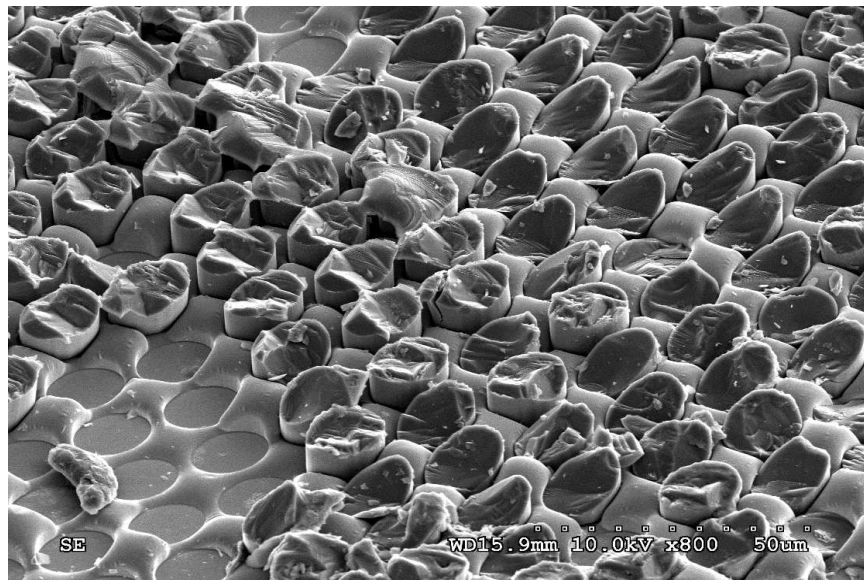


Figure 4-22: SEM Image of TPF Zr-BMG at the Center of the Sample.

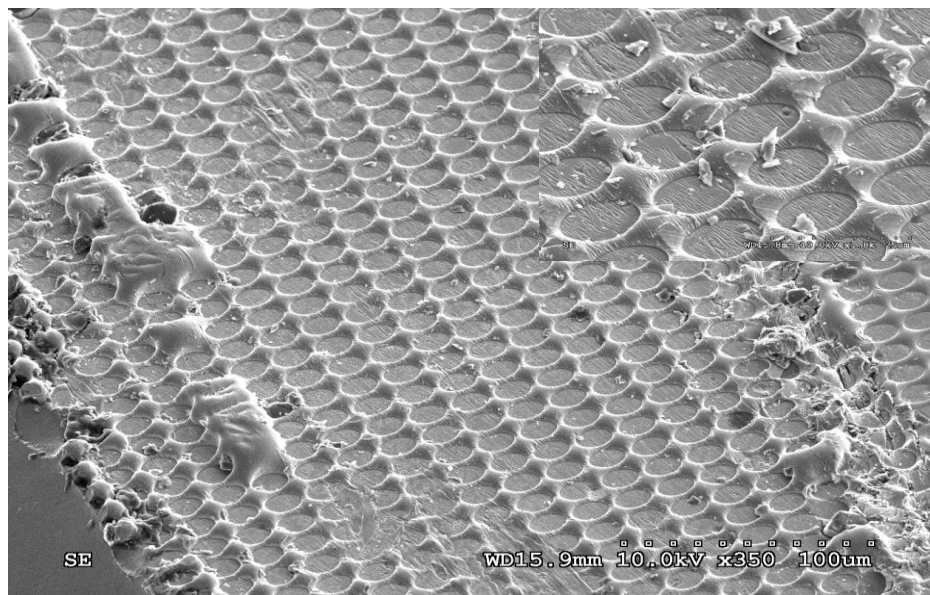


Figure 4-23: SEM Image of Zr-BMG sample at the Edge.

#### 4.4.1.8 Thermoplastic Forming at Atmospheric pressure with N<sub>2</sub> Flow

In these trials, a vacuum is first applied to remove any air in the furnace then the furnace back filled with nitrogen gas to atmospheric pressure. The thermal conductivity of nitrogen is 43.32 (mW/mK) will work like a convection heat transfer medium to stabilize the sample temperature.

##### 4.4.1.8.1 TPF with N<sub>2</sub> Trail 1

In this trial a BMG-silicon assembly was hot pressed at 375°C under 75kg load. It was observed that the displacement of the pressing ram accelerated at ~340°C during the heating process when held at a constant load of 75kg. This was an indication of severe deformation of the sample. It was estimated that the softening temperature of the BMG is ~340°C under a 75kg load in a nitrogen atmosphere. The softening temperature was observed to be ~270°C in vacuum. It was not clear, how the pressing atmosphere affected the softening temperature. Further research is required to understand this effect.

The sample obtained after the pressing had a diameter of 25.4 mm matching the diameter of the die cavity. The thickness of the sample was 1.5mm. The silicon mold fractured during the hot-pressing run. Figure 4-24 shows the topography of the BMG surface. It could be clearly seen that the silicon pillars were fractured at the base and embedded into the Zr-BMG sample. This was presumed to be an effect of the thermal expansion difference between the silicon mold and the Zr-BMG. The highest depth of filling was found at the middle of the sample (5.168 μm). The depth of filling was found to be 2.04 μm at the edges as seen in Figure 4-25. It was concluded that the force applied on the BMG-silicon assembly is primarily flattening of the BMG rather than imprinting the micro-pillars in the

BMG. Additionally, the BMG crystallized into a multiphase material during the hot pressing run. Each of these phases could have a different mechanical characteristics leading to improper imprinting of the pillars.

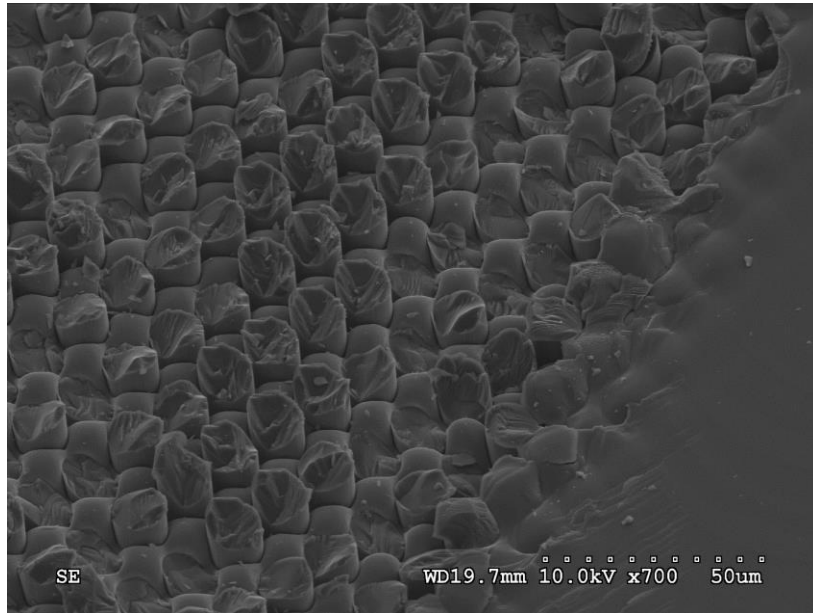


Figure 4-24: SEM Image of Zr-BMG TPF at 375 C° with 75 Kg Load.

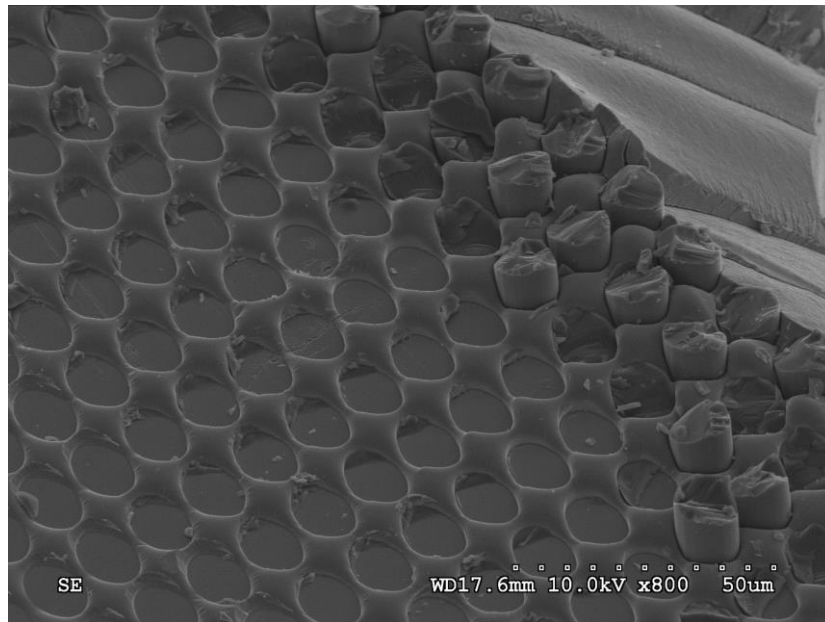


Figure 4-25: SEM Image of Zr-BMG TPF at 375 C° with 75 Kg Load.

#### 4.4.1.8.2 TPF with N<sub>2</sub> Trail 2

The second trail was performed at 275 °C with 75 Kg load to minimize the crystallization during the TPF process. The deformation of the sample was minimal under these conditions. It was observed that the sample was partially amorphous. A few sharp crystalline peaks overlapped a background consisting of two broad peaks (indicative of amorphous nature) in the x-ray diffraction data (Figure 4-26). The crystallization was limited to the surface. When the surficial layers (~100 μm) were removed by grinding, the BMG was observed to be amorphous as shown in Figure 4-26. It was not clear what caused the crystallization of the surface at temperatures far below the crystallization temperature of the BMG. Further research is required in this aspect.

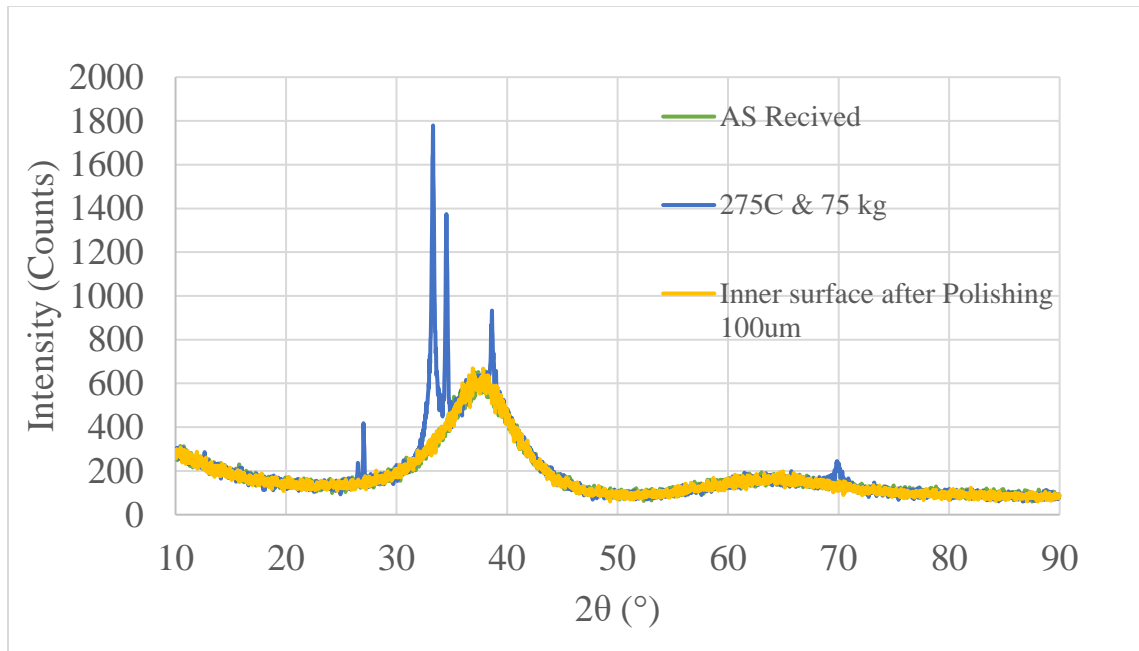


Figure 4-26: XRD Scans of TPF Zr-BMG at 275 C° with 75 Kg Load before and after polishing 100 μm of the surface.

#### 4.4.1.8.3 TPF with N<sub>2</sub> Trail 3

In this trial the hot pressing temperature was increased to 340 C° keeping the load constant at 75kg in an effort to accelerate the deformation of the BMG as the softening temperature was estimated to be 340°C. A BMG-silicon mold assembly was used in this trial run. The deformation of the Zr-BMG sample was minimal as shown in Figure 4-27. A thorough examination of the surface of the BMG indicated that the pillars were imprinted along the edges only (Figure 4-29). It was hypothesized that the temperature was not homogeneous throughout the sample during the short hold at the hot-pressing temperature, the outer edges were at temperatures slightly above the softening temperature but the bulk of the sample was still below the softening temperature. The hypothesis also explained why the sample did not undergo bulk deformation and flattened to the edge of the die. An x-ray diffraction scan of the silicon contact surface indicated the sample surface is partially amorphous as in to the sample hot-pressed at 275°C (Figure 4-28). It was determined that the crystalline phases were primarily Zr<sub>2</sub>Cu and ZrBe<sub>2</sub>.

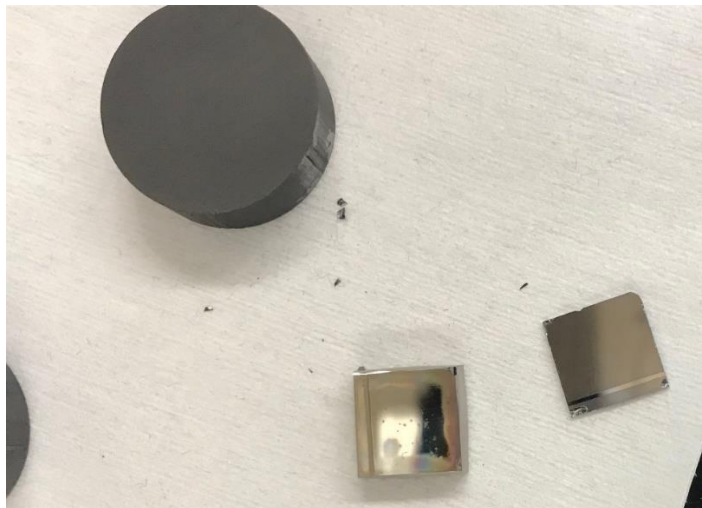


Figure 4-27: Zr-BMG sample was TPF at 340C with 75 kg load for 1 min.

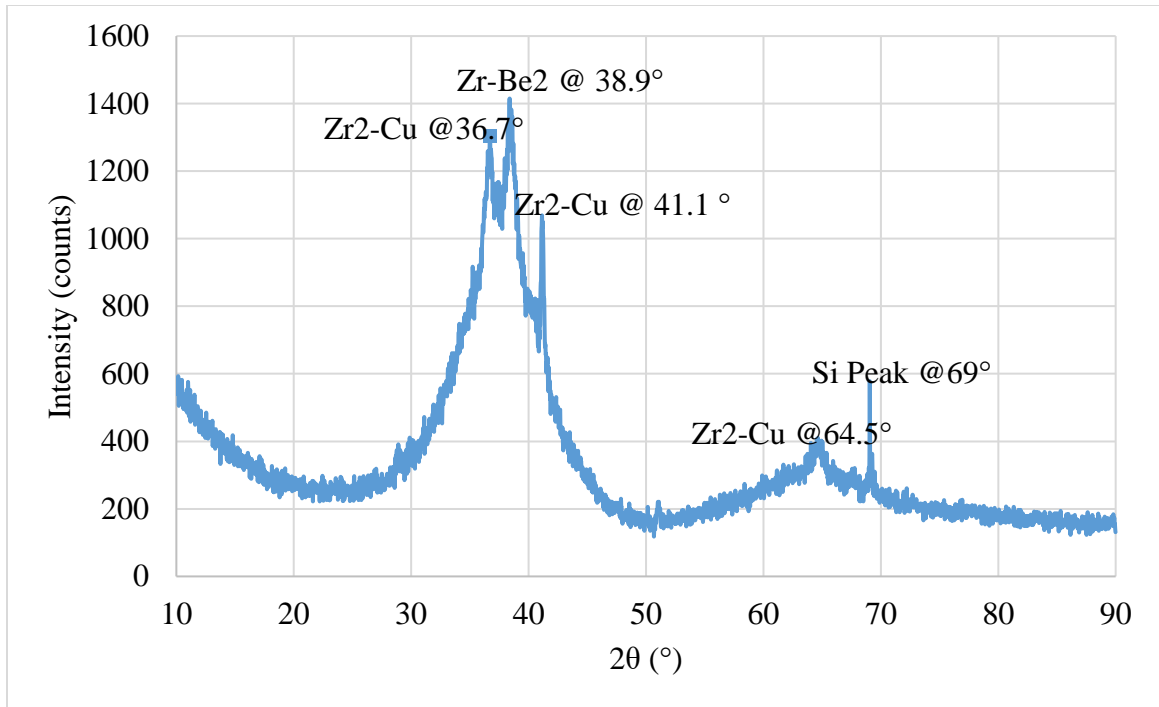


Figure 4-28: XRD Scan of TPF Zr-BMG sample at 340 C with 75 Kg load (Si contact area).

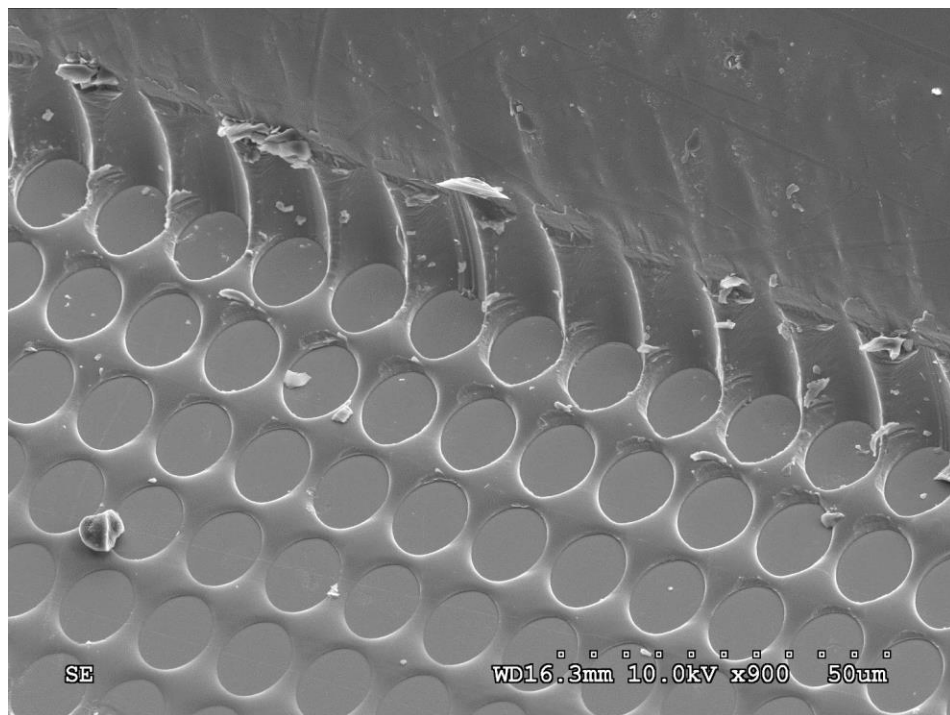


Figure 4-29: SEM Image of Zr-BMG TPF at 340C and 75 Kg Load.

#### 4.4.1.8.4 TPF with N<sub>2</sub> Trail 4

To overcome the sample temperature homogenization issue, the sample was held at 300°C for 20 minutes before increasing the temperature to 340°C as the previous trial run. Additionally, the load was increased to 250 kg. The BMG underwent severe deformation and presumably filled the die cavity after 15 minutes at 300°C. This observation highlighted the need for understanding the kinetics of heat transfer in this material and the subsequent mechanical deformation under load at an elevated temperature. An additional experiment was performed in which a BMG sample was held at 275°C for 1 hour. It was observed that the sample flattened to thickness of 1.5 mm (

Figure 4-30) and crystallization only occur at the surface of the sample. The increased load (250 kg) had a detrimental effect in this trail run, it led to the breakage of the entire BMG-silicon mold assembly as shown in

Figure 4-30. A closer inspection of the imprint quality indicated that there was no added advantage of increasing the load (Figure 4-31).



Figure 4-30: Zr-BMG TPF at 340C with 250 Kg.

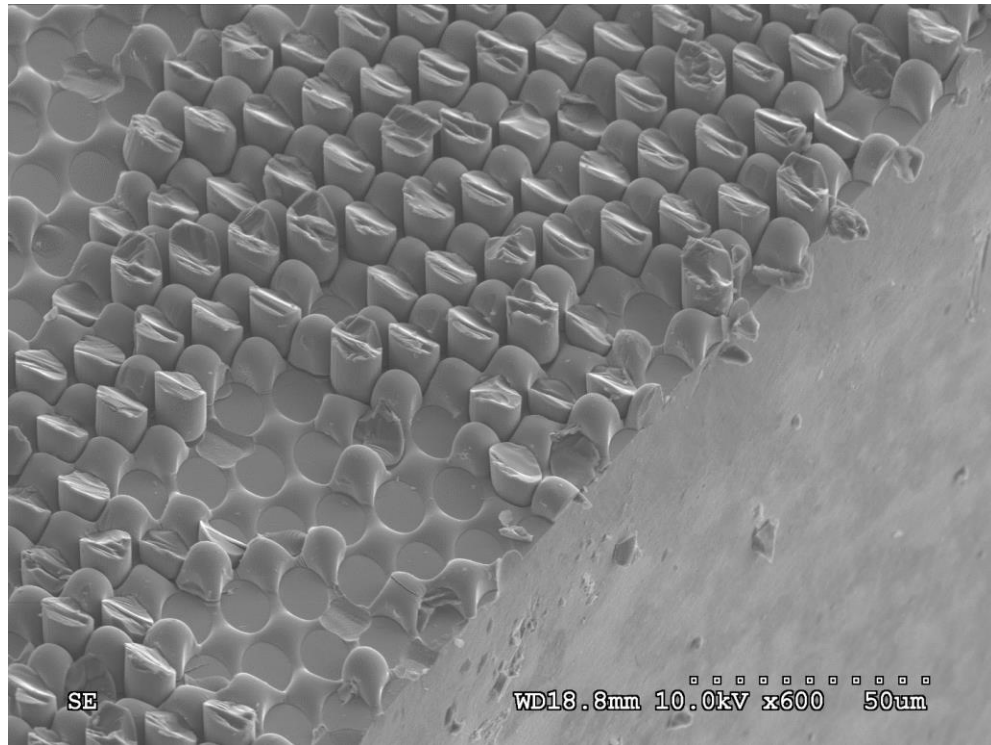


Figure 4-31: SEM Image of Zr-BMG TPF at 340C and 250 Kg Load.

#### 4.4.1.8.5 TPF with N<sub>2</sub> Trail 5

In this trial the BMG assembly was hot-pressed at 340°C for 3 minutes with a 150kg load. The sample was not completely flattened which improved the printing of the pillars to the BMG as shown in Figure 4-32. The increase in the load from 75kg to 150 kg resulted in increased crystallinity of the BMG as evident from the sharper peaks and lower relative intensity of the broad peak ~38°C in the x-ray diffraction plot (Figure 4-33). The depth of filling was improved to 7.542 μm in this sample toward the middle as seen in Figure 4-34.



Figure 4-32: Zr-BMG TPF at 340 C with 3 minutes hold and 150 Kg load.

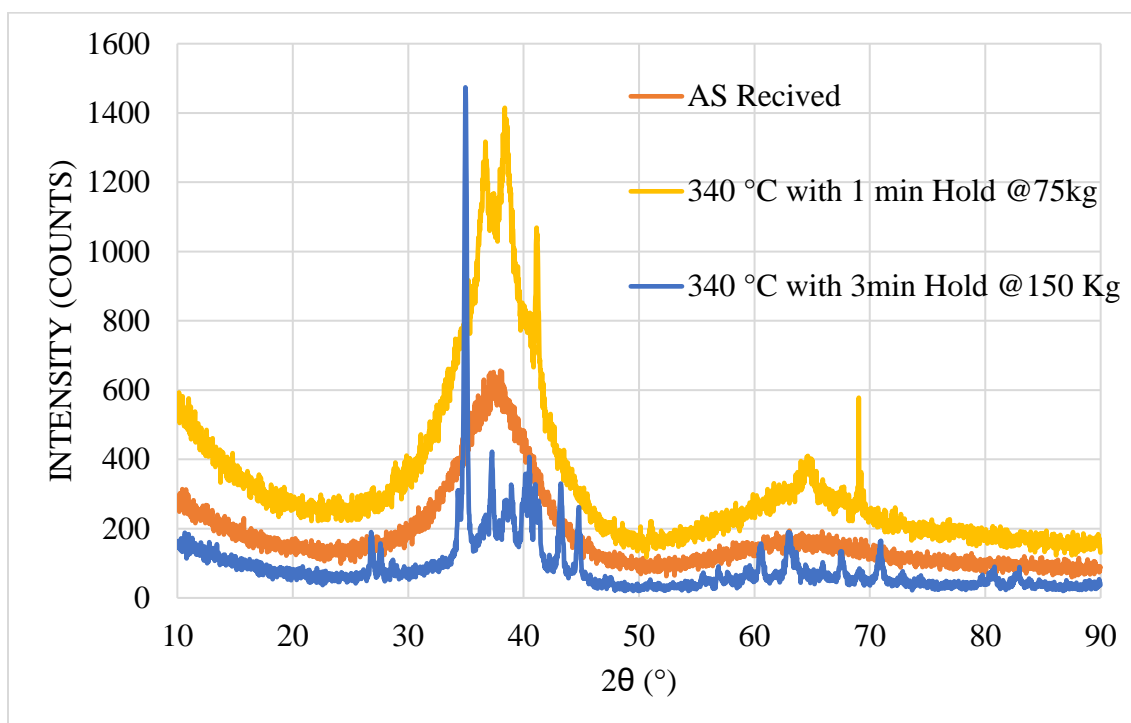


Figure 4-33: XRD results for micro molded BMG at 340C at 75, and 150 Kg load compared to as received scan.

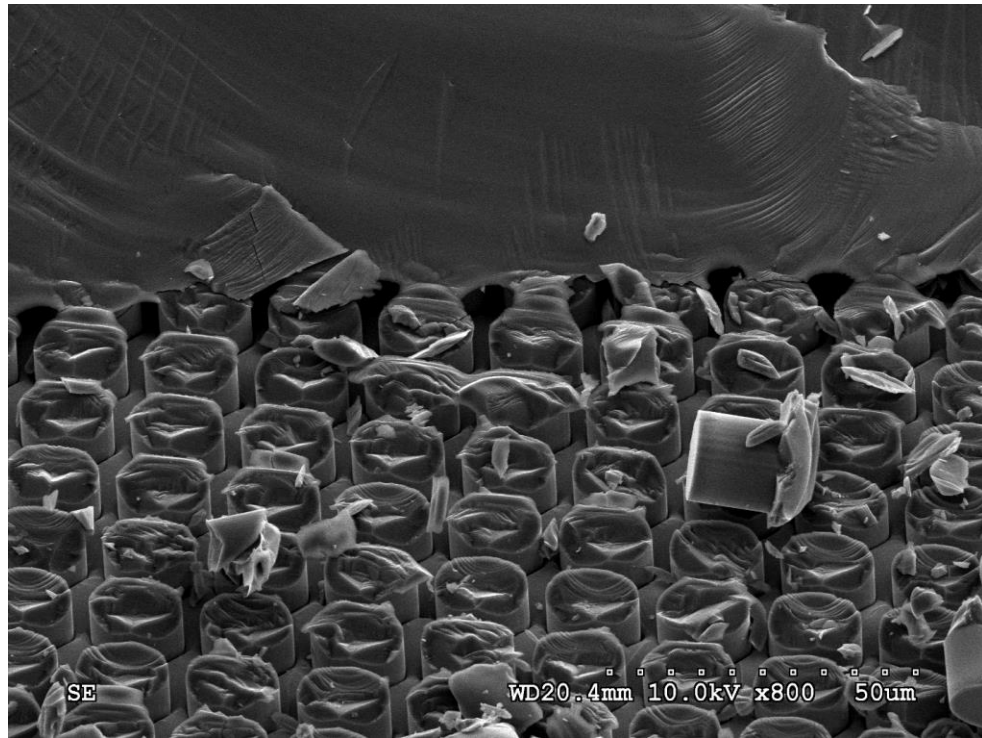


Figure 4-34: SEM Image of Zr-BMG TPF at 340 C with 3 Minutes Hold and 150 Kg Load.

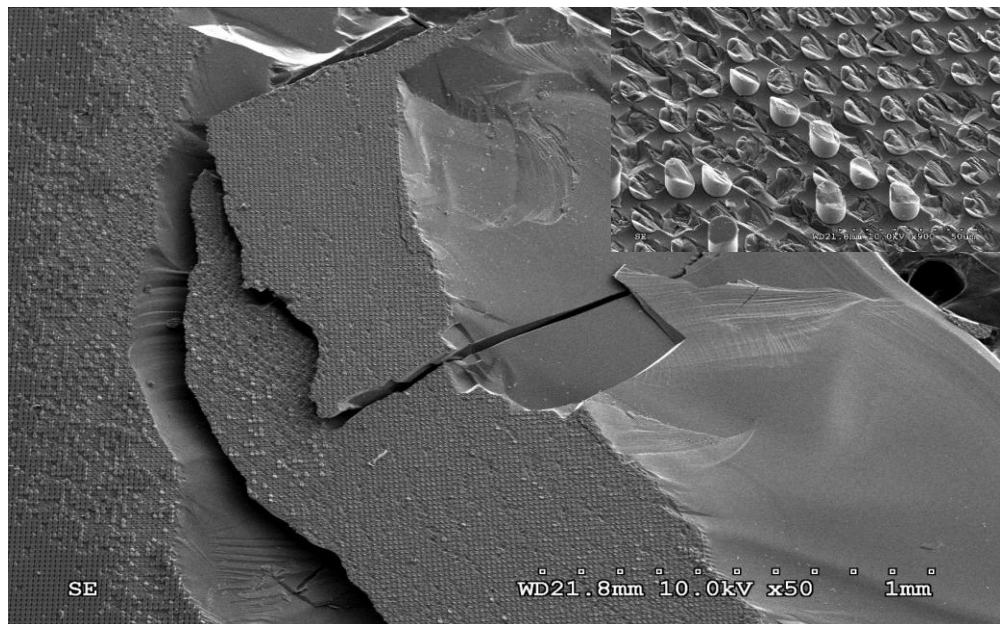


Figure 4-35: Si wafer used in 340 C with 3 minutes hold and 150 Kg Load trail.

The silicon wafer attached to the BMG was dissolved using potassium hydroxide (KOH) solution at 80 °C. After 15 minutes, certain areas of the BMG were exposed directly to KOH solution and the BMG was preferentially etched creating unique patterns as can be seen in Figure 4-36. . The imprinted patterns were intact in the areas of the BMG that were not directly exposed to KOH solution (Figure 4-36). It was concluded that the time for which the BMG-silicon assembly is immersed in KOH solution is critical. The assembly should be removed as soon as the color of the BMG started to change, which was considered as an indication of preferential etching of the BMG mold.

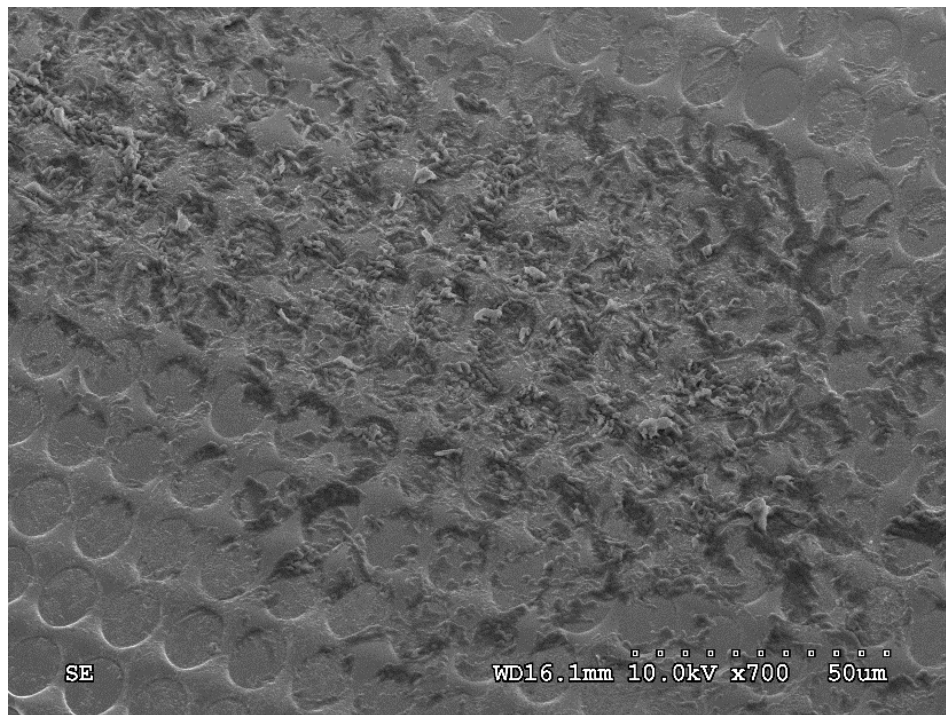


Figure 4-36: Zr-BMG mold after KOH dissolving (exposed area).

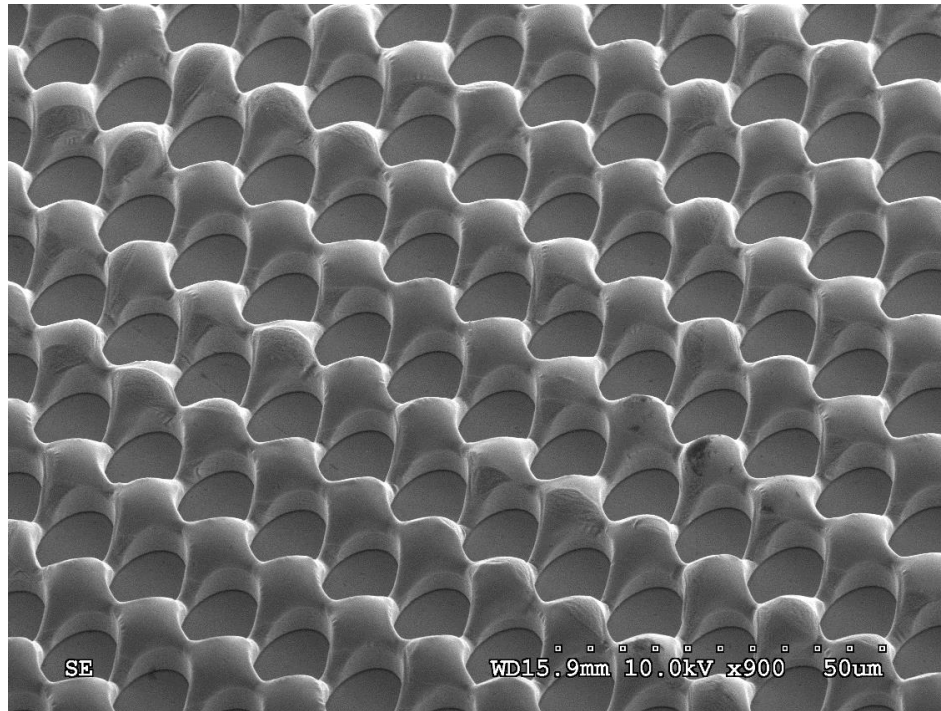


Figure 4-37: Zr-BMG mold after KOH dissolving (Si covered area).

#### 4.4.1.8.6 TPF with N<sub>2</sub> Trail 6

This trail was made to print 5  $\mu\text{m}$  circular pillars (Figure 4-38) with a height of 2.1  $\mu\text{m}$  (Figure 4-38) into Zr-BMG. A 125 kg load was applied for 3 minutes at 340°C to imprint the micor-features. The depth of filling was found to be higher in the middle of the sample (1.91  $\mu\text{m}$ ) as compared to the edges of the sample as shown in Figure 4-40.

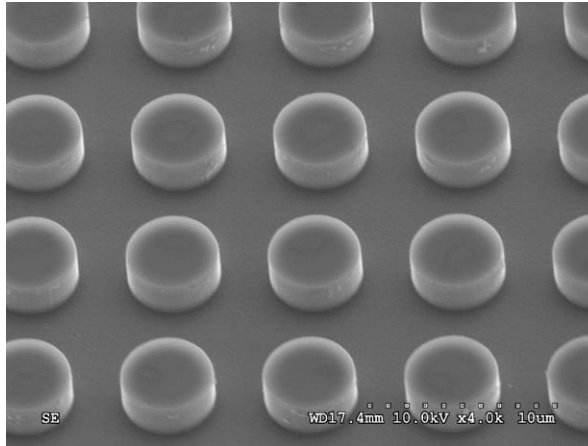


Figure 4-38: Si pillars with 5um diameter and 2.1 um height.

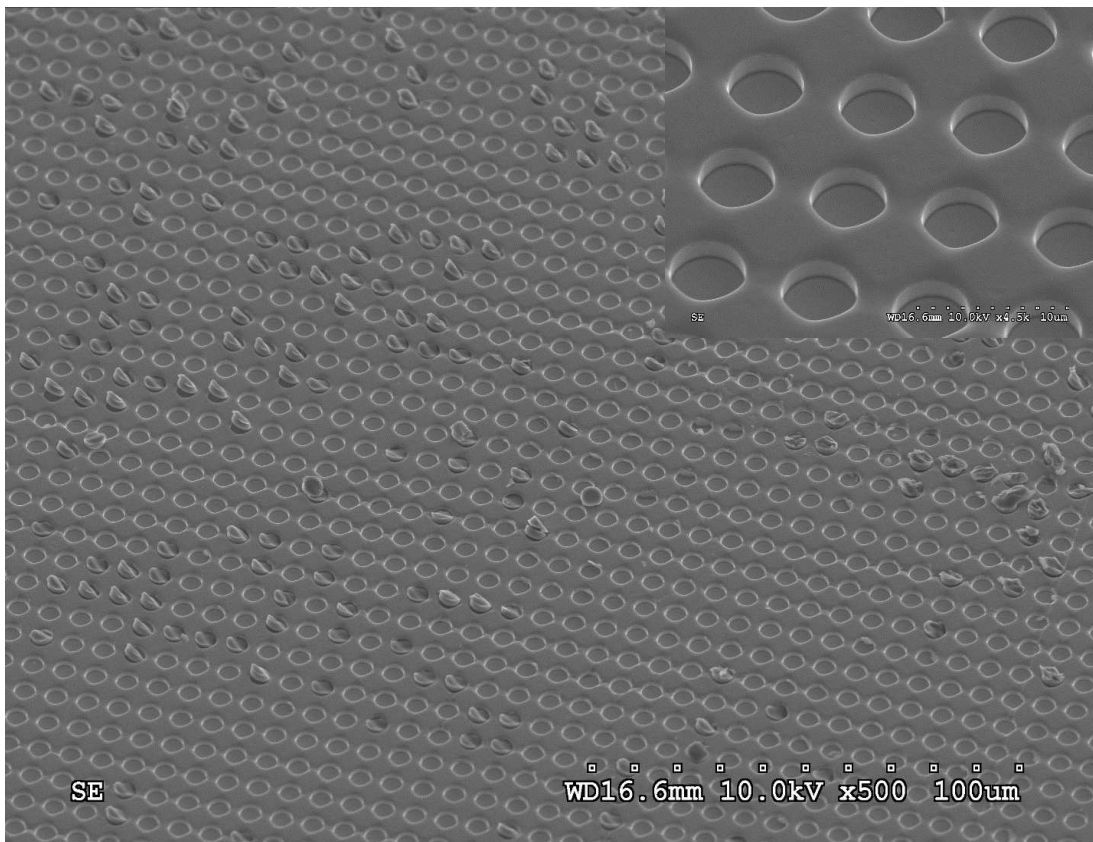


Figure 4-39: Middle region of Zr-BMG after TPF.

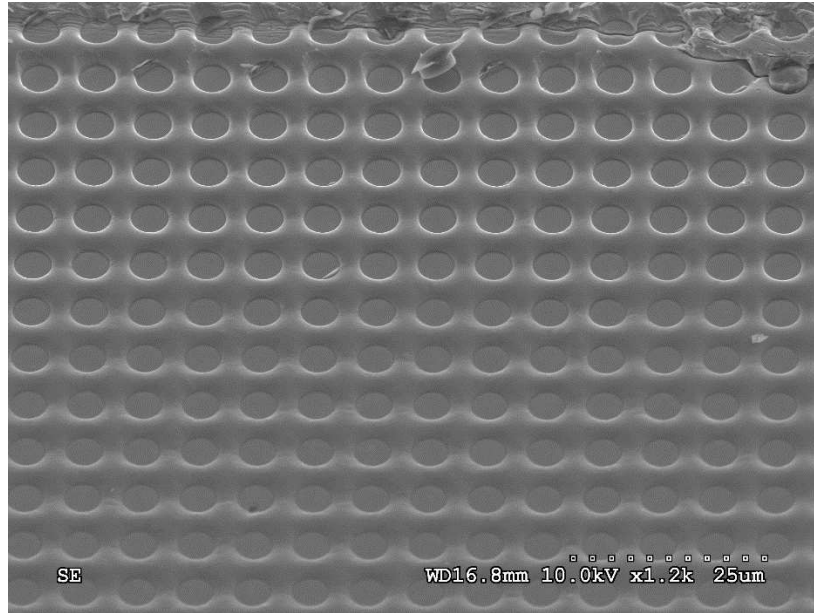


Figure 4-40: Zr-BMG after TPF towards the edges.

## 4.5 Mold Durability Simulations and Testing

### 4.5.1 Demolding Process of Micro molded Structures

Part demolding is one of the critical stages in microinjection molding where the created geometries can be easily distorted. The interactions between the polymer and the mold insert effect on the failure of created micropatterned features during demolding. The demolding force has to overcome both the adhesion force and frictional forces created during the demolding process (Figure 4-41).

### 4.5.1.1 Ejection Force Calculations

The total demolding force needed to demold a single microstructure from the microcavity can be described as follows[84].

$$F_D = F_R + F_V = \mu P_c A_c + P_v S \quad (4.1)$$

Where  $F_R$  is release force,  $\mu$  is the coefficient of friction,  $P_c$  contact pressure,  $A_c$  area of contact,  $F_V$  is the additional released force due the contact between the microstructure and the micro cavity exists.  $P_v$  Atmospheric pressure ( $P_v=1 \times 10^5$  Pa),  $S$  cross-sectional area of the micro-cavity.

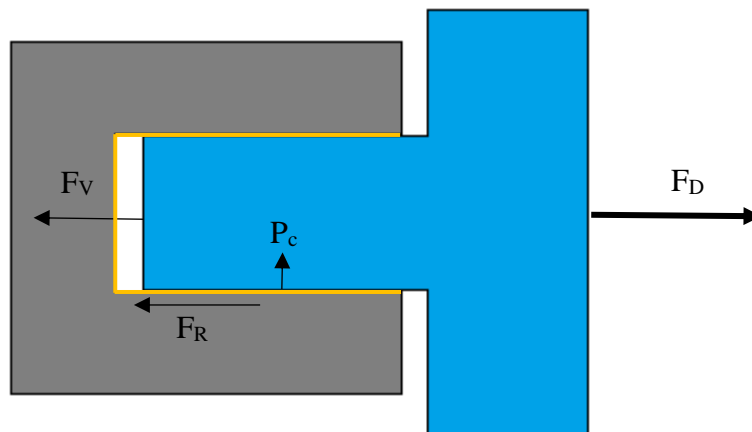


Figure 4-41: Schematic of demolding a single microstructure.

The contact pressure is the pressure needed to compact the microstructure with a diameter ( $d_d$ ) into a microcavity with a diameter ( $d$ ) as shown in Figure 4-42.

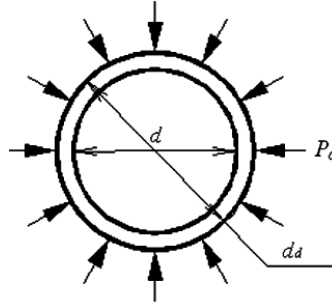


Figure 4-42: Contact pressure between the microstructure and microcavity [84].

The contact pressure during demolding stage can be calculated by:

$$P_c = E \frac{\Delta d}{d} = E \frac{d_d - d}{d} \quad (4.2)$$

Where E is the Young modulus of the polymer.

In order to determine the microstructure diameter at demolding  $d_d$ , the contact volume is calculated based on the pressure-volume-temperature (PVT) properties for the molding material. The PVT is used to determine the density of the material as a function of the temperature and pressure based on the two-domain Tait PVT model. The specific volume-temperature curves expressed in isobaric condition at different pressures are shown in *Figure 4-43* [85].

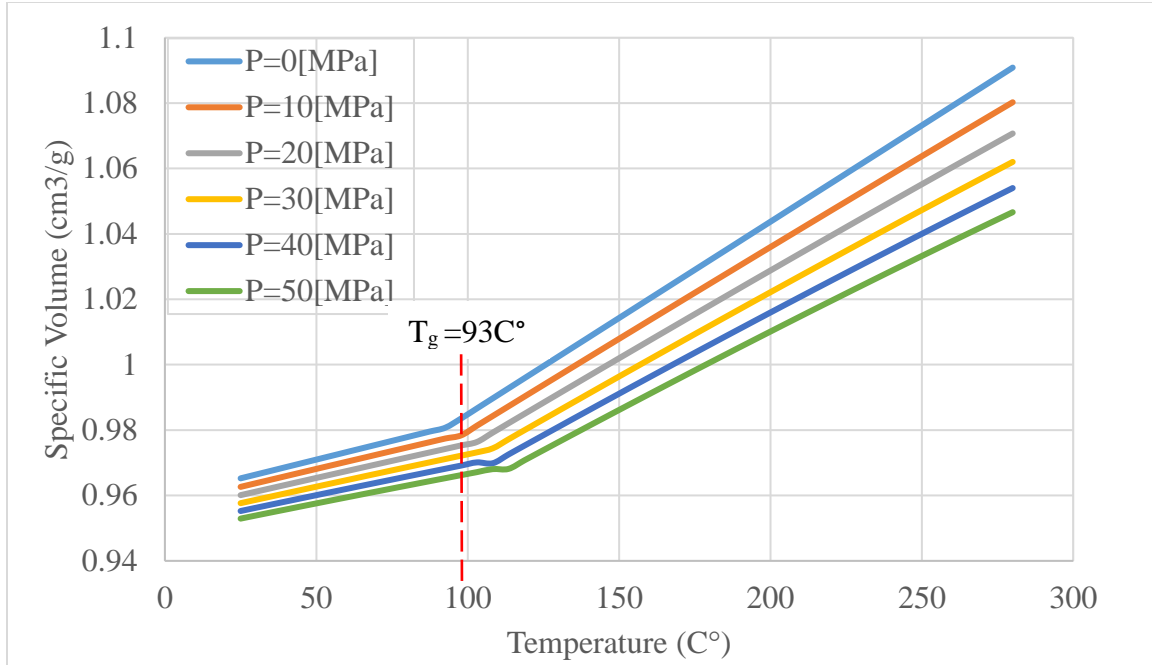


Figure 4-43: PVT curves of 666D STYRON.

The two-domain Tahi PVT equation is given below:

$$v(T, p) = v_0(T) \left[ 1 - C \ln \left( 1 + \frac{p}{B(T)} \right) \right] + v_t(T, P) \quad (4.3)$$

Where  $v$  is the specific volume,  $T$  is the mold temperature,  $P$  is the packing pressure,  $C=0.0894$  (universal constant),  $B(T)$  accounts to the pressure sensitivity of the material,  $v_t$  is specific volume at glass transition temperature and  $v_0$  is the specific volume at zero gauge pressure.

If  $T > T_g$ :

$$v_0 = [b_{1m} + b_{2m}(T_h - b_5)]$$

$$B(T) = b_{3m} e^{-b_{4m}(T_h - b_5)}$$

$$v_t(T, p) = 0$$

$b_{1m}, b_{2m}, b_{3m}, b_{4m}$ , are data-fitted coefficients.  $b_5$  represents the volumetric transition temperature,  $T_g$  at zero gauge pressure)

At the packing pressure phase, the temperature of microcavity is assumed to be at the glass transition temperature ( $T_h = T_g = 93C^\circ$ ), thus reduces  $(T_h - b_5)$  to zero.

The specific volume of the microstructure after demolding can be expressed as:

$$v(T, p) = b_{1m} \left( 1 - C \ln \left( 1 + \frac{p}{b_{3m}} \right) \right)$$

If  $T < T_g$ :

$$v_0 = [b_{1s} + b_{2s}(T_d - b_5)]$$

$$B(T) = b_{3s} e^{-b_{4s}(T_d - b_5)}$$

$$v_t(T, p) = b_7 e^{b_8(T_d - b_5)}$$

$b_{1s}, b_{2s}, b_{3s}, b_{4s}, b_5, b_7, b_8, b_9$  are data fitted coefficient

During demolding, the pressure is assumed to be zero (atmospheric pressure is small compared to the packing pressure). The specific volume of the microstructure after demolding can be expressed as:

$$v(T_d, 0) = [b_{1s} + b_{2s}(T_d - b_5)] + b_7 e^{b_8(T_d - b_5)} \quad (4.4)$$

The feedstock mass packed into the microcavity during the packing stage is given.

$$M = \frac{V_c}{v(T_g, p)} = \frac{\frac{\pi}{4} d^2 h}{v(T_g, p)} \quad (4.5)$$

Where  $V_c$  is the contact volume between the microstructure and microcavity.

The volume of the microstructure after demolding is equal to the feedstock mass multiplied by the specific volume of the material:

$$V_d = Mv(T_d, 0) = \frac{v(T_d, 0)V_c}{v(T_d, p)} = \frac{\pi}{4} d_d^2 h_d \quad (4.6)$$

The aspect ratio of the microstructures is maintained  $\chi = \frac{h}{d} = \frac{h_d}{d_d}$  due to the isotropic shrinkage of the material,  $h_d, h$  are the height of the microstructure.

$$d_d = \left[ \frac{4 V_d}{\chi \pi} \right]^{1/3}$$

$$d_d = \left[ \frac{4 V_c}{\chi \pi} \times \frac{v(T_d, 0)}{v(T_d, p)} \right]^{1/3}$$

$$d_d = \left[ \frac{4 \frac{\pi}{4} d^3 h}{\chi \pi} \times \frac{v(T_d, 0)}{v(T_d, p)} \right]^{1/3}$$

$$d_d = d \left[ \frac{v(T_d, 0)}{v(T_d, p)} \right]^{1/3}$$

$$d_d = d \left[ \frac{[b_{1s} + b_{2s}(T_d - b_s)] + b_7 e^{b_8(T_d - b_5)}}{b_{1m}(1 - C \ln[1 + \frac{p}{b_{3m}}])} \right]^{1/3} \quad (4.7)$$

$$P_c = E \frac{\Delta d}{d} = E \frac{d_d - d}{d} = E \left[ \left[ \frac{[b_{1s} + b_{2s}(T_d - b_s)] + b_7 e^{b_8(T_d - b_5)}}{b_{1m}(1 - C \ln[1 + \frac{p}{b_{3m}}])} \right]^{1/3} - 1 \right]$$

$$F_D = F_R + F_V = \mu E \left[ \left[ \frac{[b_{1s} + b_{2s}(T_d - b_s)] + b_7 e^{b_8(T_d - b_5)}}{b_{1m}(1 - C \ln[1 + \frac{p}{b_{3m}}])} \right]^{1/3} - 1 \right] A_c + 1 \times 10^5 \times S \quad (4.8)$$

The contact area and cross-sectional area for cylindrical and oval microcavities are expressed as follows:

Microcavity shape	Contact area	Cross-sectional area (S)
Circular	$A_c = \pi d h$	$S = \frac{\pi}{4} d^2$
Oval	$A_c = \pi (a + b) h$ Where $a$ is the semi-major diameter, $b$ is the semi-minor diameter	$S = \pi a b$

Demolding force is needed to eject a single microstructure from a circular cross-section cavity is given as follows.

$$F_D = \mu E \left[ \left[ \frac{[b_{1s} + b_{2s}(T_d - b_s)] + b_7 e^{b_8(T_d - b_5)}}{b_{1m}(1 - C \ln[1 + \frac{p}{b_{3m}}])} \right]^{1/3} - 1 \right] \pi d h + 1 \times 10^5 \times \frac{\pi}{4} d^2 \quad (4.9)$$

For oval cross-section microcavity is:

$$F_D = \mu E \left[ \left[ \frac{[b_{1s} + b_{2s}(T_d - b_s)] + b_7 e^{b_8(T_d - b_5)}}{b_{1m}(1 - C \ln[1 + \frac{p}{b_{3m}}])} \right]^{1/3} - 1 \right] \pi (a + b)h + 1 \times 10^5 \times \pi ab \quad (4.10)$$

Curve fitting constants were conducted from Moldflow database for polystyrene 666D STYRON as presented in Figure 4-44[85].

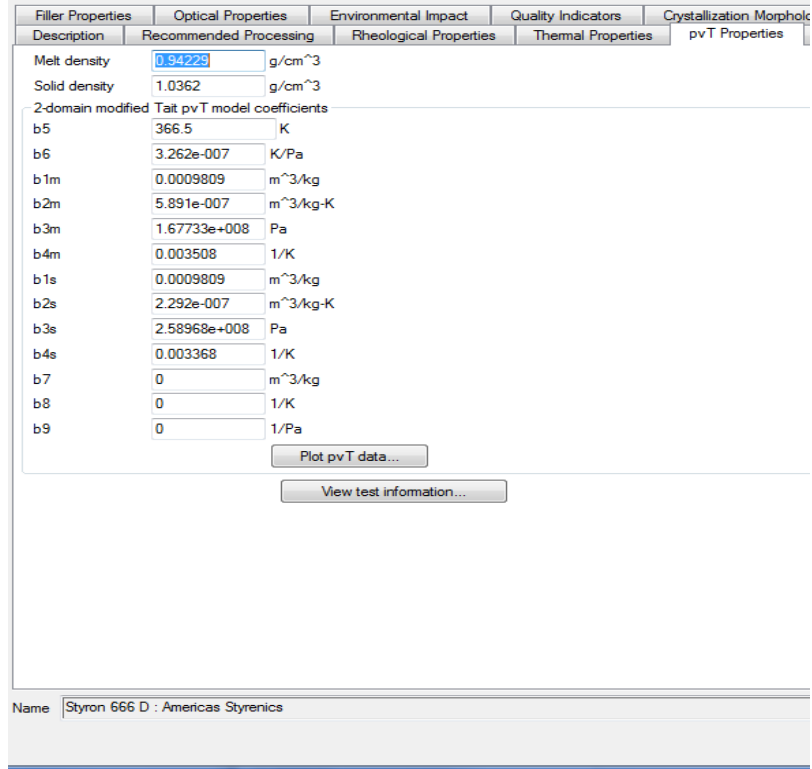


Figure 4-44: Curve fitting data for Polystyrene 666D STYRON [85].

Young Modulus for Polystyrene as a function of temperature is available in the literature and has been presented in *Table 4-6* [86].

Table 4-6: Polystyrene young modulus as a function of temperature.

Temperature	30	50	70	80	90
Young Modulus E(Pa)	1.74 X10 <sup>9</sup>	1.66 X10 <sup>9</sup>	1.18 X10 <sup>9</sup>	2.38 X10 <sup>8</sup>	13.51 X10 <sup>7</sup>

The coefficient of friction ( $\mu$ ) for polystyrene ranges from 0.3 to 0.5, in this calculations,  $\mu$  is set to be 0.5. Demolding forces were calculated at temperatures of 30, 50, 70, 80, and 90 C°. Figure 4-45 shows the demolding force needed to eject a single microstructure form a circular microcavity with a diameter of 5  $\mu\text{m}$  and height of 2  $\mu\text{m}$ . For Oval microcavity, the demolding force is high due to the increase in the contact area

that demolding force is needed to overcome to eject the microstructure successfully (Figure 4-46).

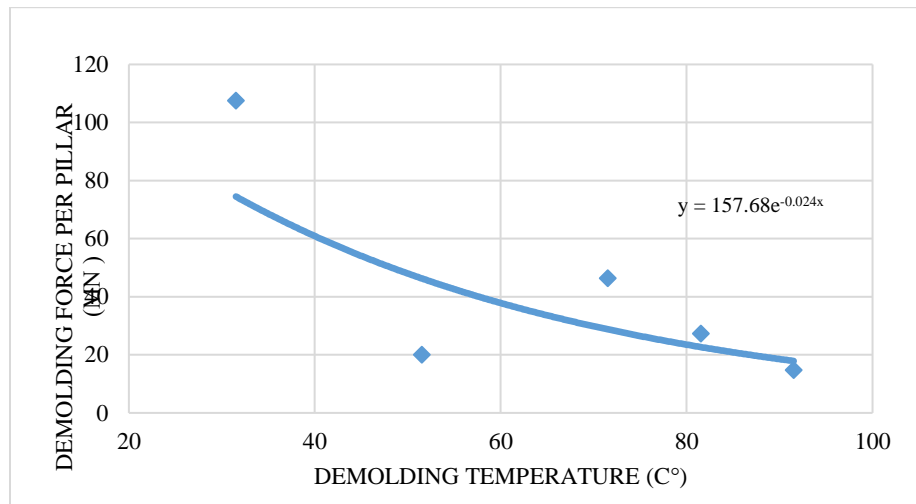


Figure 4-45: Demolding force is needed to demold a single microstructure from a circular microcavity with  $D=5\mu\text{m}$  and  $H=2\mu\text{m}$ .

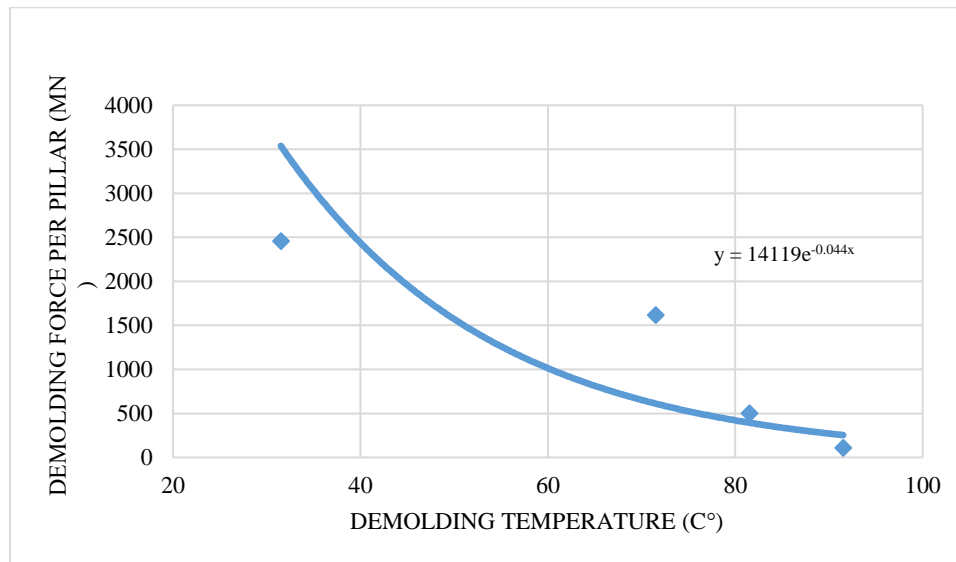


Figure 4-46: Demolding force is needed to demold a single microstructure from an oval microcavity with  $D=15\mu\text{m}$  and  $H=15\mu\text{m}$ .

## 4.5.2 Mold fatigue life analysis

### 4.5.2.1 Factors affecting silicon tool life

The heat load of the silicon-based mold is cyclic. The melt temperature during the filling stage is generally around 200°C or higher, while the cooling temperature is about 50°C. Frequently heating and cooling, stress concentration occurs in cavity surface which can lead to a thermal fatigue crack. During the demolding stage, the thermal fatigue crack may expand rapidly with the presence of tensile stress at each cycle. With this type of molds, cracks are initiated as a result of the Bosch process that is used to create the micro-cavities. This process consists of repeating steps of plasma etching and passivation step as a result of repeating steps sidewall scallops created and work as cracks propagation paths. Another factor that is also intensely affecting the Si-mold lifetime is the packing pressure due to the brittleness characteristics of the silicon [87].

### 4.5.2.2 ANSYS Simulations

During injection molding, the mold is continuously subjected to high temperature and pressure. The cyclic loading causes the mold to fail at some point depending on the mold material. The typical mold used in microinjection molding is silicon-based molds which have a high chance to break under repeating loads. Alternative BMG molds were also used in this investigation. Simulations were done using Ansys to find the number of cycles that both molds (Si and BMG) can survive before failure. Processing parameters were determined from Moldflow simulations in Chapter 5. Mold temperature was used in this simulation is 70 °C. The maximum pressure was found at 4 MPa when the

microcavities were filled by the end of the packing stage. Demolding forces were calculated previously and were used based on the mold type and demolding temperature (Figure 4-45Figure 4-46).

#### 4.5.2.3 Fatigue life prediction

Fatigue life prediction was made using Ansys simulations that utilize the Manson-Coffin relationship that relates the strain amplitude of the mold based on the elastic and plastic strain amplitudes. Manson-Coffin equation requires 6 parameters to define the strain life material properties[88,89].

$$\frac{\Delta\varepsilon}{2} = \frac{\sigma'_f}{E} (2N_f)^b + \varepsilon'_f (2N_f)^c \quad (4.11)$$

Where:

$$\frac{\Delta\varepsilon}{2} = \frac{\Delta\sigma}{E} + 2 \left( \frac{\Delta\sigma}{2K} \right)^{\frac{1}{n}} \quad (4.12)$$

$\Delta\varepsilon$ = total strain amplitude

$\Delta\sigma$ = the stress amplitude

$\sigma'_f$  = the stress at fracture in one stress cycle, Pa

$E$ = the elastic modulus of mold material, Pa

$\varepsilon'_f$ = fatigue ductility coefficient

$N_f$ = number of cycles before failure

$b$  = fatigue strength exponent

$c$ = fatigue ductility exponent

$K$ = cyclic strength coefficient

$n$ = cyclic strain hardening exponent

#### 4.5.2.4 Fatigue Life Simulations

The simulation approach was obtained by coupling microinjection molding parameters and demolding force over 6X6 mm mold with 10x10 number of cavities. Packing pressure was applied perpendicular to the mold while demolding forces act only on the microcavity sidewalls. It was observed from the simulation that the highest stress concentrations were on the microcavities edges (Figure 4-47). Mold fatigue life (Figure 4-48) was calculated using the Manson-Coffin equation described earlier with simulated stress amplitude in Figure 4-47. Fatigue life parameters for silicon were implemented from Varvani et al. study[90]. They used tensile and fatigue coefficients for silicon micro-sized components to predict fatigue life appeared with the formation of surface fracture. Fatigue life parameters are listed in Table 4-7. Microcavities edges were found to have the higher possibility to break after 387 cycles under the applied molding conditions (Figure 4-48).

Table 4-7: Silicon Fatigue life parameters.

E (MPa)	K (GPa)	n	$\sigma'_f$ (GPa)	$\epsilon'_f$ (%)	b	c
140	72	0.5	3.105	1.33	-0.02	-0.01

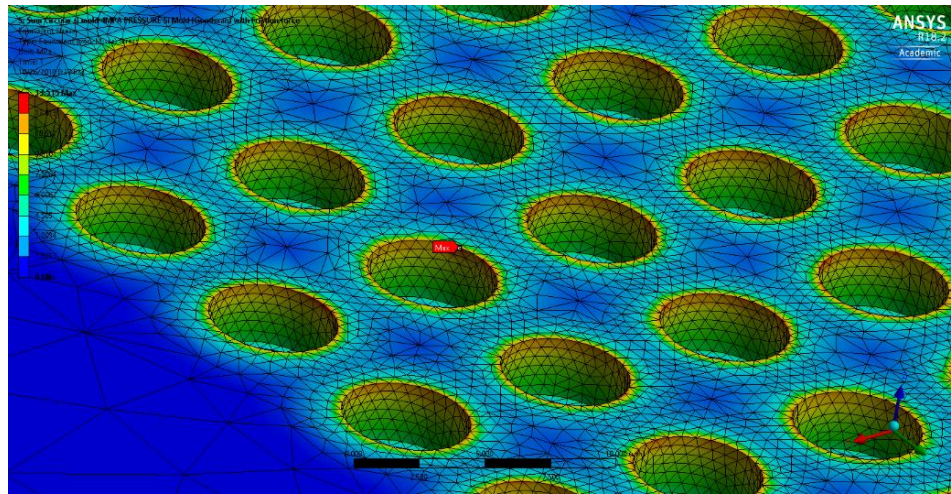


Figure 4-47: Equivalent stress (Von Mises stress) formed on Si mold 5µm circular microcavities with 8µm center-to-center (C2C) spacing under P= 4 MPa, T=80 C°.

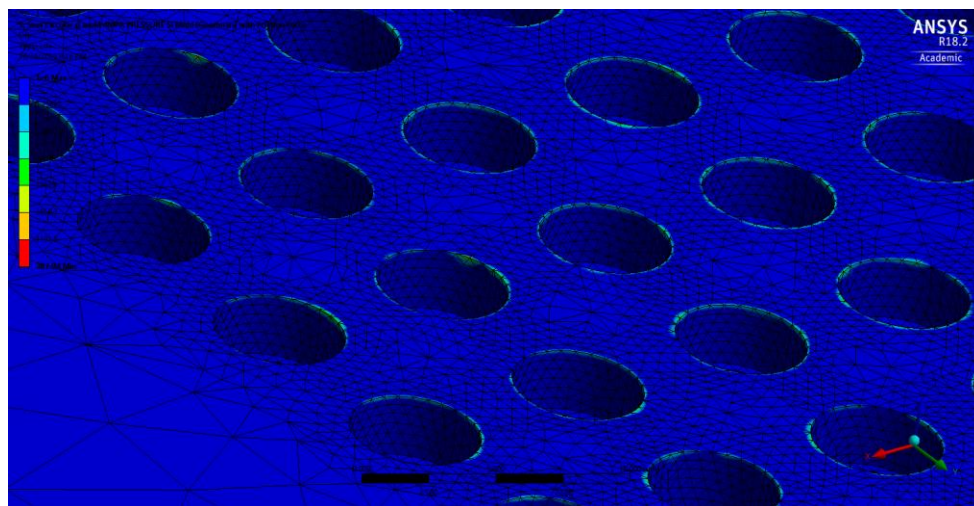


Figure 4-48: Si mold number of Cycles before failure for 5µm circular microcavities with 8µm C2C spacing under P=4MPa, T=80 C°.

It was also established that cavities spacing has an impact on the Si mold fatigue life. Table 4-8 shows the number of cycles before Si mold fails with respect to microcavities spacing. By increasing the spacing to 10 µm the number of cycles was jumped to 443 cycles.

Table 4-8: Fatigue life (cycle) for Si molds with 5um diameter, 2.5 depth, and different C2C spacing.

5um features with 2.5 um depth	Si mold fatigue life (cycle)
6 um C2C spacing	234
8 um C2C spacing	388
10 um C2C spacing	443

Another set of simulations were done for the same microcavities with BMG as the mold material. Fatigue parameters were used in these simulations are presented in Table 4-9. It was obtained that Zr-BMG mold exhibited a higher number of cycles than Si mold under the same molding conditions (Figure 4-49Figure 4-50). Changing the spacing between microcavities has an effect on the number of cycles before failure as seen in Table 4-10. Lowering the spacing induced higher equivalent stress generated on the microcavities edges. These edges tend to have the maximum influence by the cyclic loading and to cause to the mold to break.

Table 4-9: BMG Fatigue life parameters [91–93].

E (MPa)	Poisson ratio (ν)	K (GPa)	n	$\sigma'_f$ (GPa)	$\epsilon'_f$ (%)	b	c
1900	0.36	96	0.2	93	0.97	-0.35	-0.59

#### 4.5.2.5 5um features BMG Mold

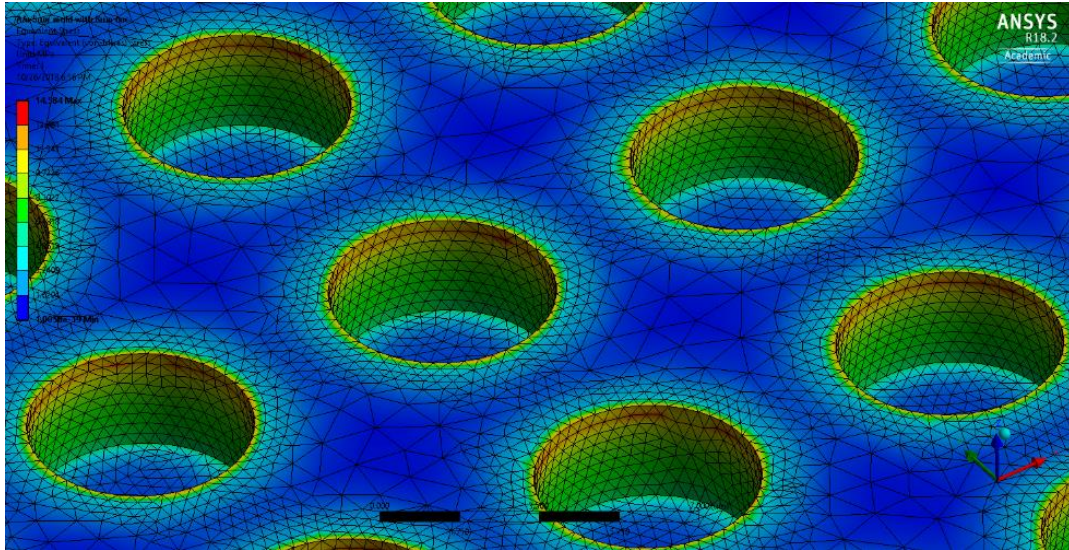


Figure 4-49: Equivalent stress (Von Mises stress) formed on Zr-BMG mold 5um circular microcavities with 8um C2C spacing under  $P=4\text{ MPa}$ ,  $T=80\text{ C}^\circ$ .

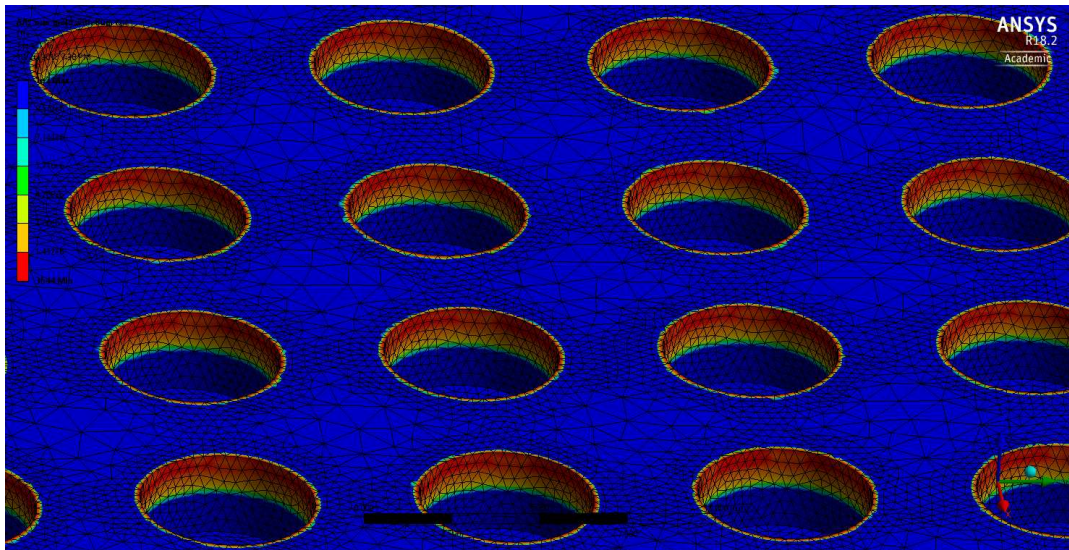


Figure 4-50: Zr-BMG mold number of Cycles before failure for 5um circular microcavities with 8um C2C spacing under  $P=4\text{ MPa}$ ,  $T=80\text{ C}^\circ$ .

Table 4-10: Fatigue life (cycle) for Zr-BMG molds with 5um diameter, 2.5 depth, and different spacing.

5um features with 2.5 um depth	Fatigue life (cycle) BMG
6 um C2C spacing	2506
8 um C2C spacing	3644
10 um C2C spacing	3846

The same simulations were carried to study the effects of molding parameters on oval microcavities with 15 um diameter and 15 um depth fabricated over Si and Zr-BMG molds. It was observed that edges in the major axis (longer diameter) exhibited the higher loading stress during the simulations (Figure 4-51). Si molds due its brittle properties tend to survive for only a few hundreds of cycles as shown in Figure 4-52. With higher C2C spacing the failure of the mold can be tuned to a high number of cycles as seen in Table 4-11. Zr-BMG molds were also examined under the same molding condition and demolding force calculated in Figure 4-46. It was found that Zr-BMG molds demonstrated a higher number of cycles before failure (Figure 4-54). Table 4-12 presents the number of cycles that Zr-BMG molds can last with increasing C2C spacing between microcavities.



Table 4-11: Fatigue life (cycle) for Si molds with 5um diameter, 2.5 depth, and different spacing.

15um features with 15 um depth	Fatigue life (cycle) Si
18 um C2C spacing	238
20 um C2C spacing	360
24 um C2C spacing	396

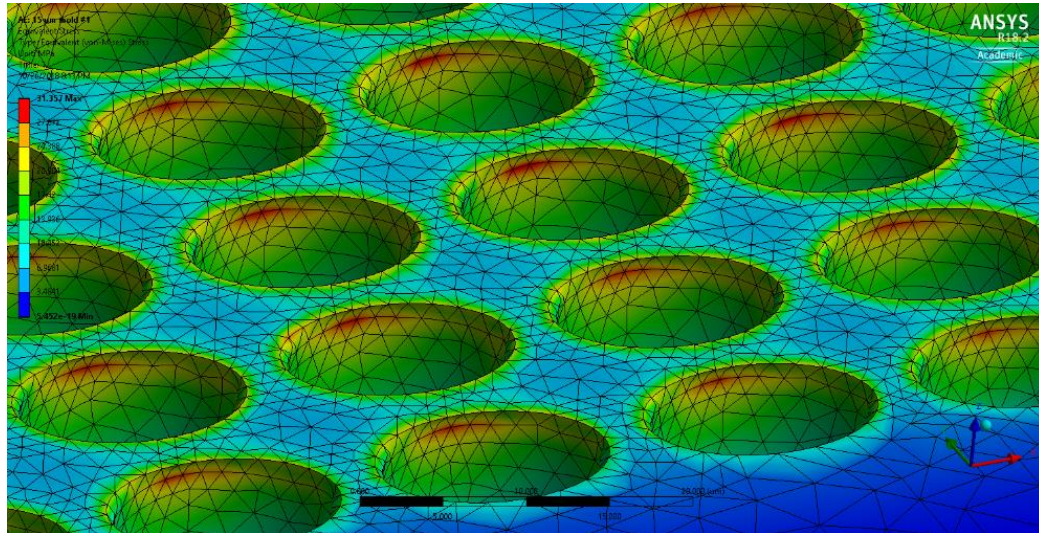


Figure 4-53: Equivalent stress (Von Mises stress) formed on Zr-BMG mold 15um circular microcavities with 18um C2C spacing under P= 4 MPa, T=80 C°.

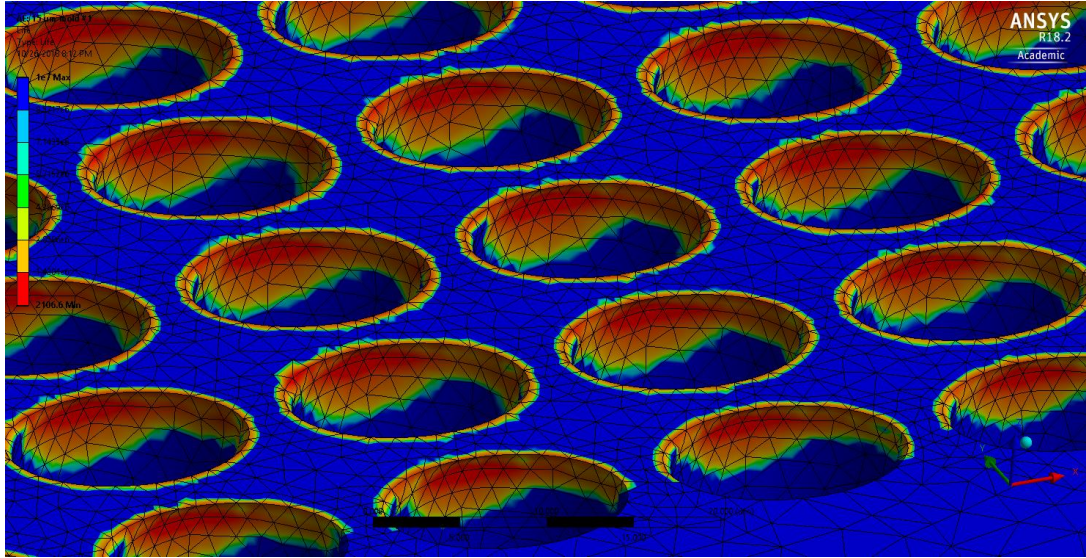


Figure 4-54: Zr-BMG mold number of Cycles before failure for 5um circular microcavities with 8um C2C spacing under P=4MPa, T=80 C°.

Table 4-12: Fatigue life (cycle) for Zr-BMG molds with 5um diameter, 2.5 depth, and different spacing.

15um features with 2 um depth	Fatigue life (cycle) BMG
18 um C2C spacing	2106
20 um C2C spacing	3321
24 um C2C spacing	3942

In conclusion, simulations were done to predict the number of cycles that Si and Zr-BMG molds (were fabricated previously) can last before failure. These simulations consider the sidewalls of the microcavities are flat, while in reality, these sidewalls have micro scallops in the case of Si molds turn into cracks initiators and cause the mold to break. The lifetime for silicon mold inserts could be overestimated due to the deficiency sidewall cracks in this simulation. BMG mold inserts lifetime might be more accurate as the scallops might not replicated during the thermoplastic forming of the BMG mold.

### 4.5.3 Experimental validations

#### 4.5.3.1 Si Mold

Although Si-based tooling may not be the proper method for microreplication via injection molding method due to its brittleness, a study conducted by Sun-Hwan et al. found that it can survive up to 1000 cycles while maintaining replication accuracy with 900 nm trenches [94]. In this work, 6x6 mm Si insert with 5  $\mu\text{m}$  circular cavities at a depth of 2.45  $\mu\text{m}$  with 8 $\mu\text{m}$  C2C spacing was examined for 105 cycles of replication. Molded samples with dense features were characterized for replication accuracy. Samples taken from 10, 30, 50, 70, 80, and 105 cycles of replication were imaged via SEM. The scanned pillar height was calculated based on the SEM stage tilt angle of 40°. The micro-pillars were replicated adequately within a  $\pm 0.03 \mu\text{m}$  tolerance (Figure 4-55), even up to 105 cycles of replication before Si mold failure. SEM micrographs for the samples indicate that a Si mold used with an antistiction layer can provide high-quality replication.

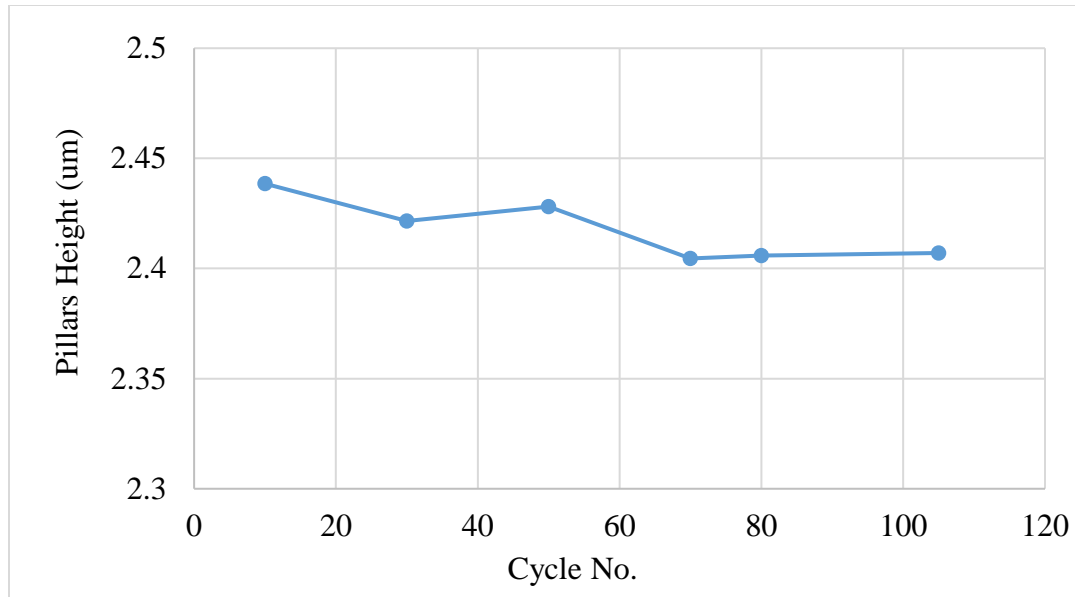


Figure 4-55: Molded samples height ( $\mu\text{m}$ ).

SEM micrographs were also collected at five different regions to analyze replication results across the molded parts (Figure 4-56). The most accurate replication appears to be near the injection gate (center) where the flow is parallel to the micro-cavities. Replication near the periphery of the insert, further away from the sprue gate, appears to be distorted. Slight distortion on top of the pillars appeared on sample#80 (right bottom enlarged image in Figure 4-56) may be due to previous replication residue that adhered to the Si mold. This may have caused incomplete replication and deflected the pillars during the demolding stage. Small rings were found on the base of molded pillars as were expected from mold life simulations in section 4.5.2.4. These rings will continue to expand until it extends a point where it reaches to the next pillars thus chips the Si mold and cause it to break. The 5um Si mold (with antistiction layer) failed after 105 cycles as seen in Figure 4-57.

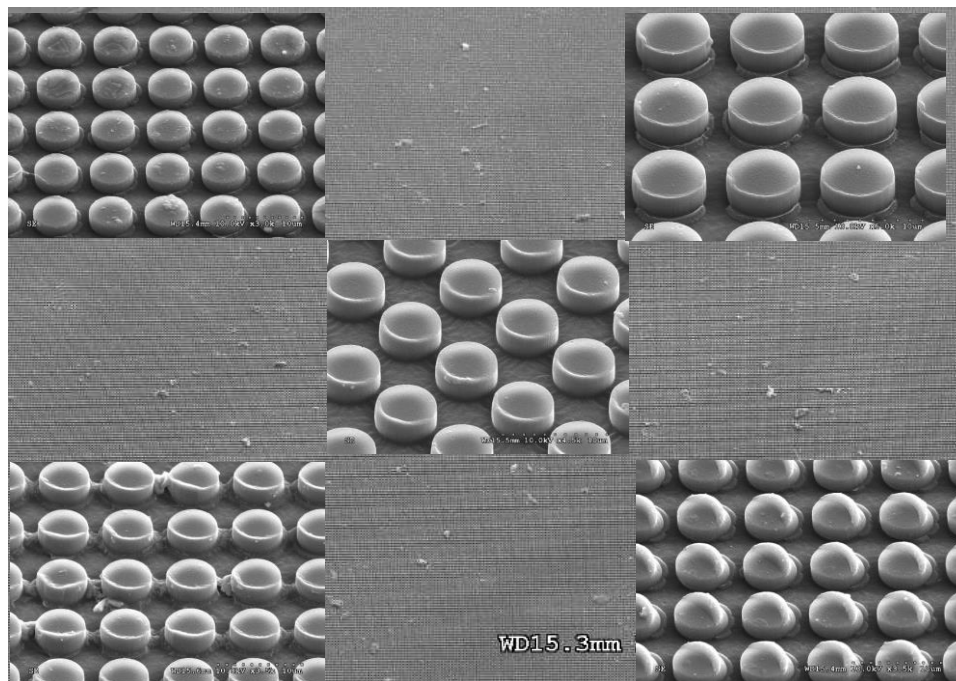


Figure 4-56: SEM photographs for molded part cycle no.80 at 5 different regions with  $T_{\text{mold}}=83\text{ C}^{\circ}$ . (Scale bar 10  $\mu\text{m}$ ).

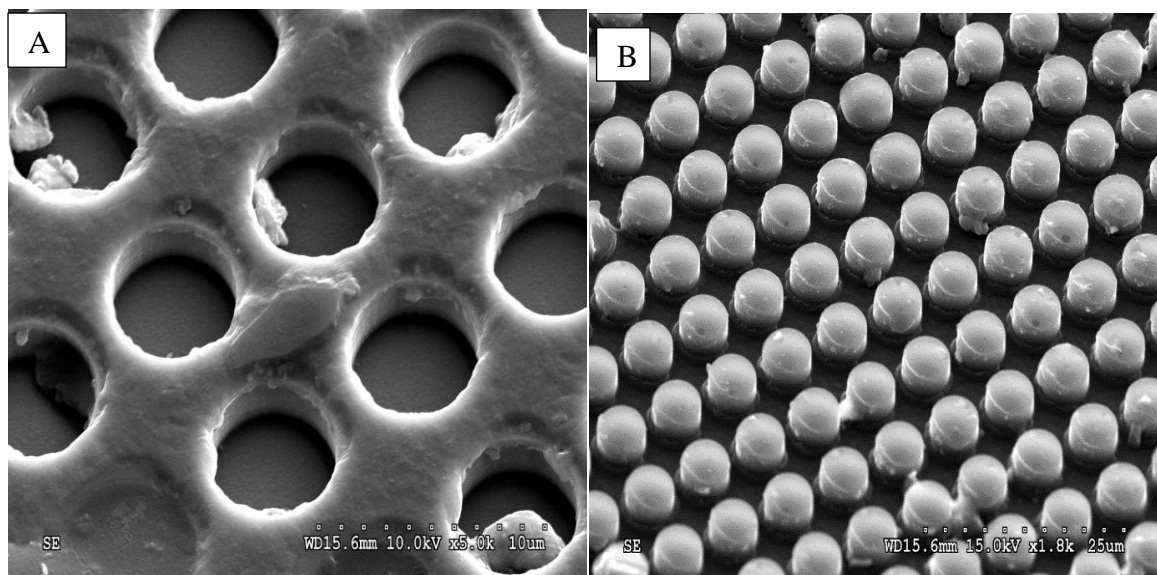


Figure 4-57: A) 5 $\mu\text{m}$  Si mold after 105 cycles. B) 5 $\mu\text{m}$  molded part after 105 cycles.

Replication residues were found as a sign of polymer adhesion to the Si mold. These sites work as extra forces that chip the Si mold at these areas. With 15 um oval microcavities molds, it was found that the micropillars start to overlap (Figure 4-58Figure 4-59) and increase the adhesion areas thus directly influence the amount of force needed to demold the part and cause the mold breakage.

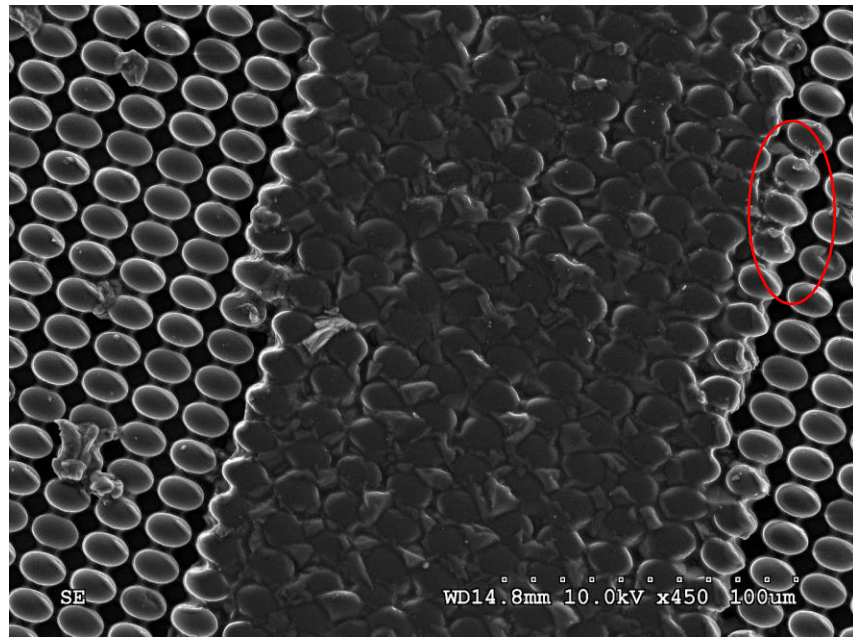


Figure 4-58: SEM image of molded part no.25 (15 um Oval).

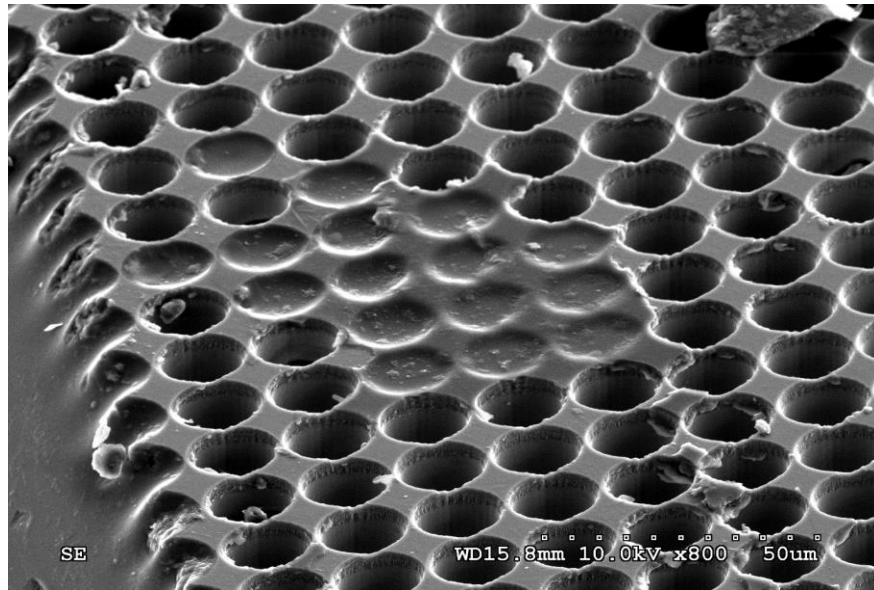


Figure 4-59: 15 um oval Si mold after 25 cycles.

## **CHAPTER 5: NUMERICAL ANALYSIS OF MICRO INJECTION MOLDING**

### **5.1 Introduction**

Effective numerical simulation of micro/nanoscale injection molding processes is important to advance nano-manufacturing. It can provide critical information of the entire product realization cycle that includes part design, mold design, and material/manufacturing process specification. If done correctly these simulations can reduce the number of experimental manufacturing trials performed and thereby directly influences the final product cost.

Moldflow<sup>®</sup> Insight is one the commonly used analytical software package that simulates the process of injection molding and provide extraordinary preliminary insight that enhances the process, mold, and part design [95–97]. It is a very convenient tool for determining optimal process settings for the injection molding machine before production actually begins.

### **5.2 Moldflow Theoretical Background**

#### **5.2.1 Mathematical Model**

Polymer flow is governed by a number of parameters during the injection molding process such as injection, packing pressure and velocity. These parameters critically impact microfeatures replication quality, and thus the micro injection molding process. In this investigation, a combination of macro (Sprue) and microscale geometries was studied to

enhance the filling of micro-cavities included as surface features on otherwise larger product geometries.

## 5.2.2 Governing Equations

Injection molding simulation software packages are commonly based on a Hele-Shaw Flow model (HS) to characterize the associated non-isothermal and non-Newtonian polymer flow behavior. [43,98]. Moldflow 2-D simulation is HS model based with fundamental governing equations expressed as follows:

$$\frac{\partial \bar{u}}{\partial x} + \frac{\partial \bar{v}}{\partial y} = 0 \quad (5.1)$$

$$\frac{\partial P}{\partial x} = \frac{\partial}{\partial z} \left( \eta \frac{\partial u}{\partial z} \right) , \quad \frac{\partial P}{\partial y} = \frac{\partial}{\partial z} \left( \eta \frac{\partial v}{\partial z} \right) \quad (5.2)$$

$$\rho c \frac{\partial T}{\partial t} + u \frac{\partial T}{\partial x} + v \frac{\partial T}{\partial y} = k \frac{\partial^2 T}{\partial z^2} + \eta \dot{\gamma}^2 \quad (5.3)$$

Where  $\rho$  is density,  $c$  is specific heat,  $k$  is thermal conductivity,  $\eta$  is viscosity and  $\dot{\gamma}$  is sheath rate.

### 5.2.3 Viscosity model:

The cross WLF model is used to simulate the viscosity behavior of the melt during the filling stage. It describes the viscosity is a function of shear rate, temperature, and pressure[43]:

$$\eta = \frac{\eta_0}{1 + \left(\frac{\eta_0 \dot{\gamma}}{\tau^*}\right)^{1-n}} \quad (5.4)$$

Where  $\eta$  is the melt viscosity,  $\eta_0$  is the zero shear viscosity or the Newtonian limit in which the viscosity approaches a constant at very low shear rates.  $\dot{\gamma}$  is the shear rate (1/s),  $\tau^*$  is the critical stress level at the transition to shear thinning, determined by empirical curve fitting.  $n$  is the power law index in the high shear rate regime, also determined empirically. The zero shear viscosity is further defined as:

$$\eta_0 = D_1 \exp \left[ -\frac{A_1(T-T^*)}{A_2+(T-T^*)} \right] \quad (5.5)$$

Where:

$T$  is the temperature (K)

$T^*$  is the glass transition temperature, determined by the curve fitting equation (5.6).

$$T^* = D_2 + D_3 p \quad (5.6)$$

$p$  is the localized pressure (Pa).

$A_2, A_3, D_3, D_2,$  and  $D_1$  are data-fitted coefficients.

#### 5.2.4 Wall Slip Velocity Model:

Wall slip based velocity phenomena are mostly neglected in conventional injection molding simulation. When it comes to microscale molding, however, these effects can seriously impact the final molded part. High shear stress created between the wall and nearby molten polymer chains induced by high pressure and a corresponding increased velocity profile in the wall region. The power law velocity slip model is introduced without any incorporation of pressure and temperature[44].

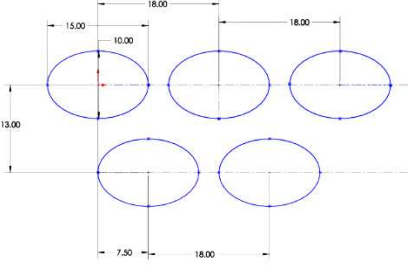
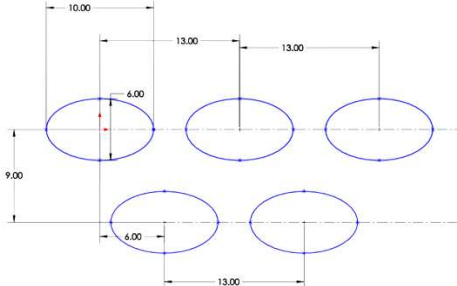
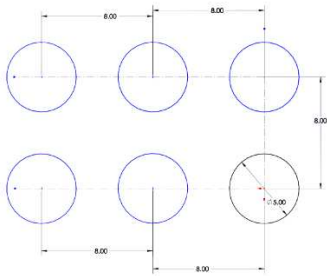
$$V_s = \frac{\alpha}{1+(\tau_c/\tau_w)^{10}} \tau_w^m \quad (5.7)$$

Where  $V_s$  is the slip velocity,  $\tau_w$  is wall shear stress,  $\tau_c$  is the critical shear stress,  $\alpha$  is the slip coefficient, and  $m$  is the slip exponent.

#### 5.3 Target Mechanotransduction Surfaces

The Simulations were performed to study the filling process of a mold cavity with a 12mm diameter, patterned with arrays of three different micro-structures: 1. an oval profile with a diameter (D) of 15  $\mu\text{m}$  and height (H) of 15  $\mu\text{m}$ , 2. an oval profile with a diameter (D) of 10  $\mu\text{m}$  and height (H) of 10  $\mu\text{m}$  and 3. a circular profile with  $D = 5 \mu\text{m}$ , and a  $H = 2 \mu\text{m}$  as shown in Table 5-1. Molded part consists of sprue runner as seen in *Figure 5-1* with diameter of 3.3 mm and length of 32 mm.

Table 5-1: targeted mechanotrasduction surface.

Pattern No.	Shape of Feature	Micro-holes Dimensions	Molded Pillars
1	Oval Micro-pillars with $D=15\ \mu\text{m}$	 <p>Technical drawing showing the layout of five oval micro-pillars. The top row contains three pillars with a center-to-center distance of 18.00. The bottom row contains two pillars with a center-to-center distance of 18.00. The vertical distance between the top and bottom rows is 13.00. The width of the top row is 15.00, and the width of the bottom row is 7.50. A dimension of 10.00 is shown for the top row.</p>	 <p>3D rendering of five green oval micro-pillars arranged in two rows: three in the top row and two in the bottom row.</p>
2	Oval Micro-pillars with $D=10\ \mu\text{m}$	 <p>Technical drawing showing the layout of five oval micro-pillars. The top row contains three pillars with a center-to-center distance of 13.00. The bottom row contains two pillars with a center-to-center distance of 13.00. The vertical distance between the top and bottom rows is 9.00. The width of the top row is 10.00, and the width of the bottom row is 6.00.</p>	 <p>3D rendering of five green oval micro-pillars arranged in two rows: three in the top row and two in the bottom row.</p>
3	Circular Micro-pillars with $D=5\ \mu\text{m}$	 <p>Technical drawing showing the layout of six circular micro-pillars in a 2x3 grid. The center-to-center distance between adjacent pillars is 8.00 in both horizontal and vertical directions. A dimension of 15.00 is shown for the diameter of one pillar.</p>	 <p>3D rendering of six green circular micro-pillars arranged in two rows of three.</p>

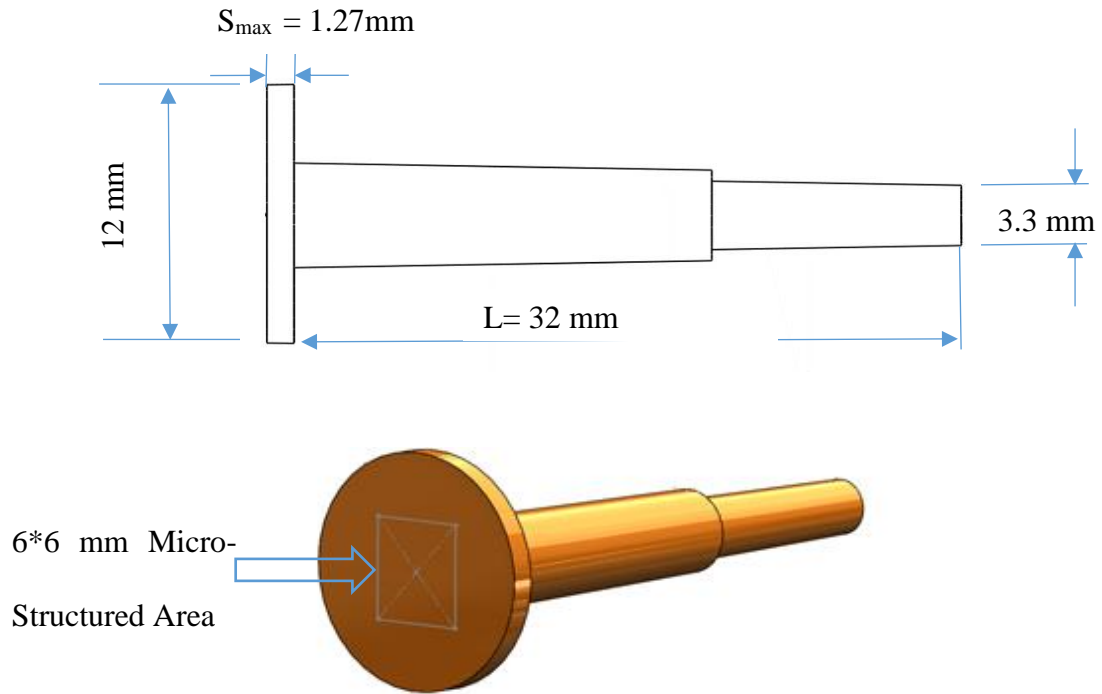


Figure 5-1: CAD model for molded part.

## 5.4 Materials

A wide variety of polymer are used in the manufacturing industry. Thermosets and thermoplastic are used in injection molding, the material is melted and plastically deform then injected into a mold cavity under high pressure then cooled and eject. Thermoplastic polymers mostly used in the injection molding segments. These types of polymers have distinguish characteristics such as strength, biocompatibility, and the easiness to process that make is it favorable in for many applications.

### 5.4.1 General purpose Polystyrene (GPPS)

Polystyrene is an amorphous thermoplastic that commonly used in packaging, CDs, medical applications, and food industry. Polystyrene consists of a styrene (Figure 5-2) which is obtained by reacting ethylene with a benzene group in the presence of aluminum chloride. It has an distinguish properties such as stiffness, low cost, non-toxic, and good dimensional stability which makes it as FDA approved for many medical applications[99,100]. STYRON 666D grade were used in the experiments with physical and mechanical properties presented in Table 5-2. Temperature dependency of viscosity-shear rate behavior of STYRON 666D is plotted in Figure 5-3 [85].

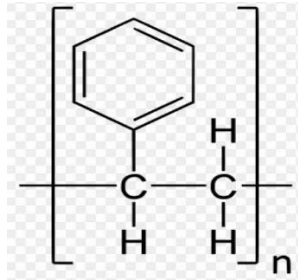


Figure 5-2: Polystyrene repeating unit [99].

Table 5-2: Physical and mechanical properties for 666D STYRON [85,101].

<i>Physical and Mechanical Properties</i>	<i>Value</i>	<i>Unit</i>	<i>ASTM Method</i>
<i>Melt Flow Index ( at 200 °C/5 Kg)</i>	8.0	(g/10min)	D-1238
<i>Specific gravity</i>	1.04		D-792
<i>Poisson's ratio</i>	0.35		E-132
<i>Tensile Modulus</i>	3172	(MPa)	D-638
<i>Coefficient of Linear Thermal Expansion</i>	9	(Cm/Cm°C)	D-696
<i>Mold Shrinkage</i>	4-7	(Cm/Cm)	D-955

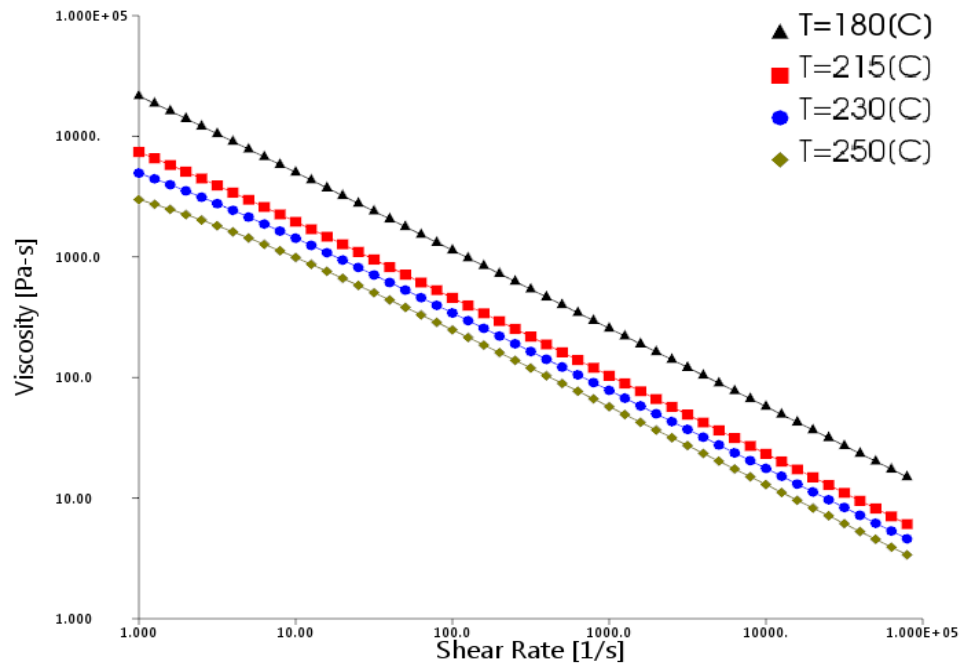


Figure 5-3: Cross WLF plot viscosity verses shear rate [85].

#### 5.4.2 Thermoplastic Polyurethane (TPU)

Thermoplastic polyurethane (TPU) is a multi-phases copolymer involves rigid and flexible segments. It consist of polyols (long chain diols), diisocyanates, and short chain diols. The polyols are generally polyester, or polyether diols react with the diisocyanates through polyaddition to form linear polyurethane. The rigid segments are made of a combination of short chain diols and dissocyanate (Figure 5-4)[102].

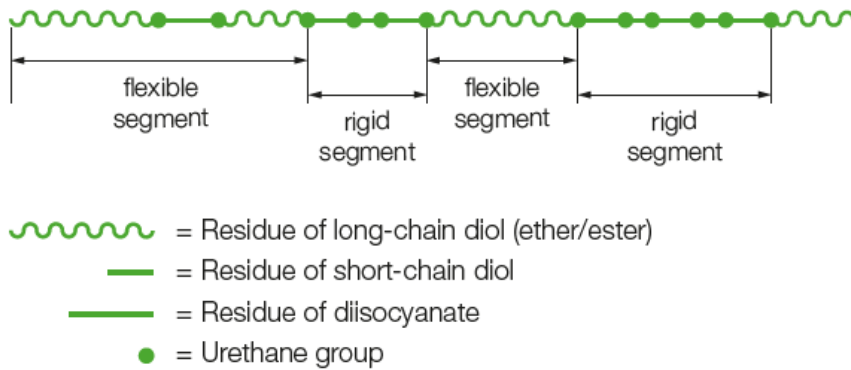


Figure 5-4: Thermoplastic Polyurethane Structure [102].

TPU is a biocompatible polymer that meet FDA requirements. It has a variety of characteristics that makes it remarkable for many applications. TPU melt has low viscosity that makes it detail the mold cavity well as seen in Figure 5-5. TPU is flexible over wide range of temperatures (Figure 5-6) with excellent resistance to many solvents. However, TPU tends to adhere to the mold, especially the softer grades. A mold release is often used to minimize the detrimental adherence properties when fabricating micro molds.

Table 5-3: Physical and mechanical properties for TPU Texin 985 [85,103].

Physical and Mechanical Properties	Value	Unit	ASTM Method
Density	1.12	g/cc	D-792
Poisson's ratio	0.395		E-132
Tensile Modulus	12.5	(MPa)	D-638
Vicat Softening Temperature	80	(°C)	D-1525
Coefficient of Linear Thermal Expansion	9.65e-5	(1/ °C)	D-696
Mold Shrinkage	0.008	(Cm/Cm)	D-955

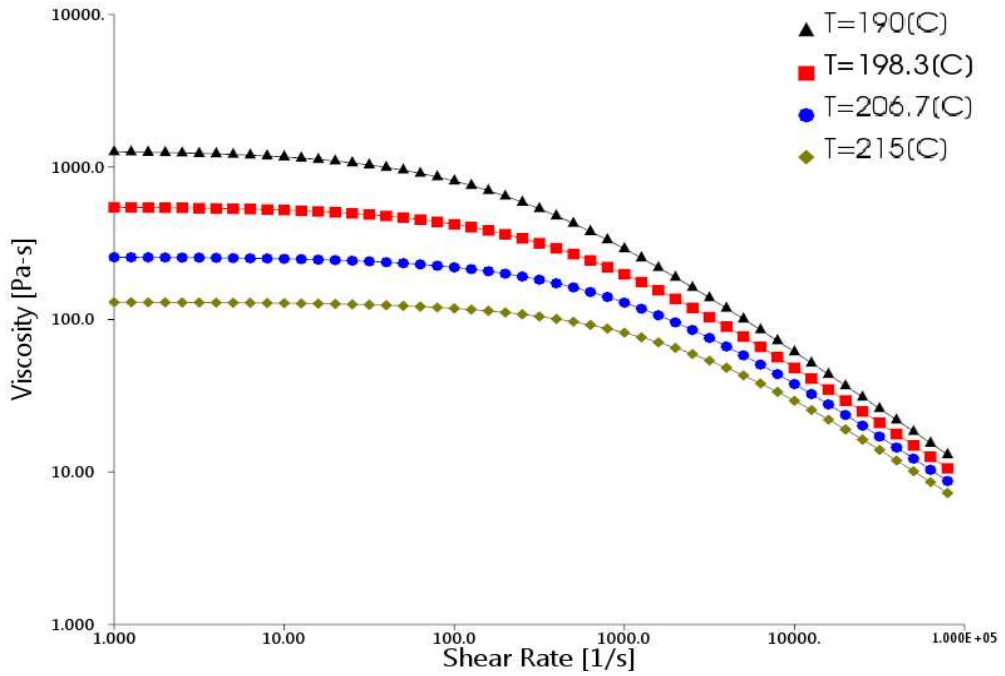


Figure 5-5: Cross WLF plot viscosity verses shear rate [85].

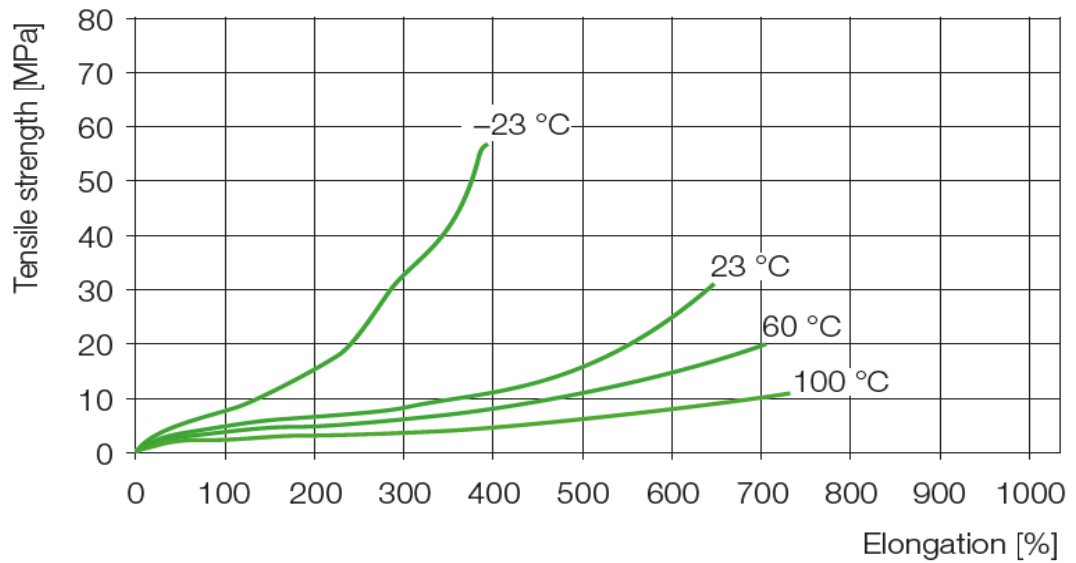


Figure 5-6: TPU Elongation % versus Tensile strength as function of temperature [102].

### 5.4.3 Low-Density Polyethylene (LDPE)

Low-density Polyethylene (LDPE) is a thermoplastic polymer produced from polymerization of ethylene with low density and long chain with short branches. LDPE has an excellent strength and toughness which is attractive for a wide range of applications including food containers, toys, medical parts, and plastic films[104,105]. Mechanical and physical properties are presented in Table 5-4.

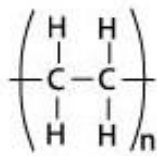


Figure 5-7: Polyethylene Polymer [105].

Table 5-4: Physical and mechanical properties for LDPE ASI CP 851 [85,106].

Physical and Mechanical Properties	Value	Unit	ASTM Method
Melt Flow Index ( at 190 °C/2.15 Kg)	20	(g/10 min)	D-1238
Specific Gravity	0.925	g/cm <sup>3</sup>	D-792
Poisson's ratio	0.41		E-132
Tensile Modulus	10.3	(MPa)	D-638
Vicat Softening Temperature	92	(°C)	D-1525
Mold Shrinkage	0.03	(Cm/Cm)	D-955

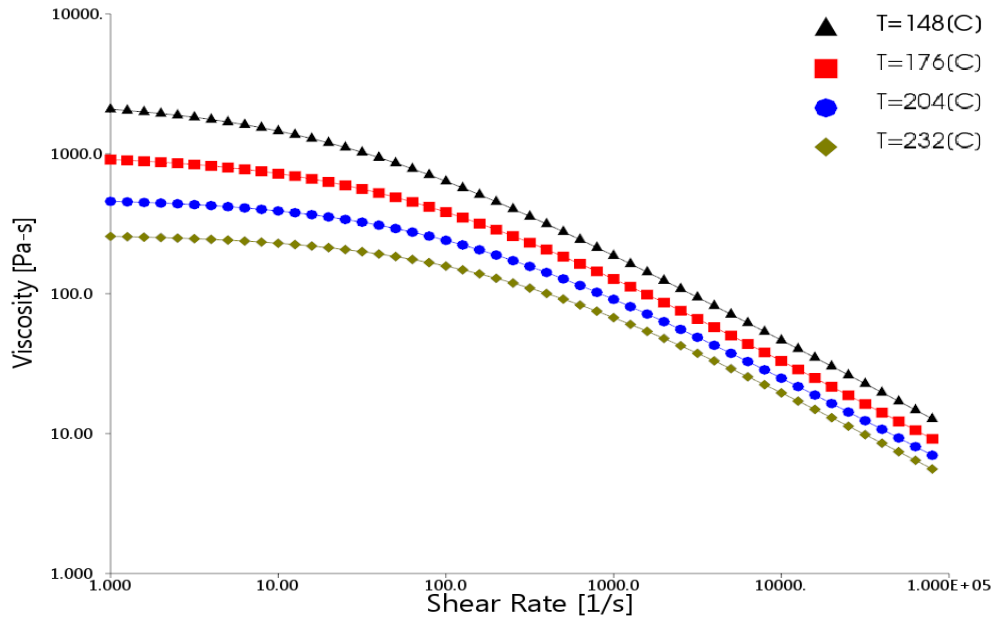


Figure 5-8: Cross WLF plot viscosity versus shear rate for LDPE ASI CP 851 [7].

#### 5.4.4 High-Density Polyethylene (HDPE)

HDPE is another type of polyethylene with higher density of greater or equal to  $0.941 \text{ g/cm}^3$ . It has lower degree of branching and high strength compared to low-density polyethylene. HDPE has numerous mechanical properties (Table 5-5) which makes it a good choice for a lot of applications such as food storage, furniture, automotive, and piping.

Table 5-5: Physical and mechanical properties for HDPE Exxon HD-6733 [85,107].

Physical and Mechanical Properties	Value	Unit	ASTM Method
Melt Flow Index ( at 190 °C/2.16 Kg)	33	(g/10 min)	D-1238
Specific Gravity	0.95	$\text{g/cm}^3$	D-792
Poisson's ratio	0.426		E-132
Tensile Modulus	24	(MPa)	D-638
Vicat Softening Temperature	116	(°C)	D-1525
Mold Shrinkage	0.0015	(Cm/Cm)	D-955

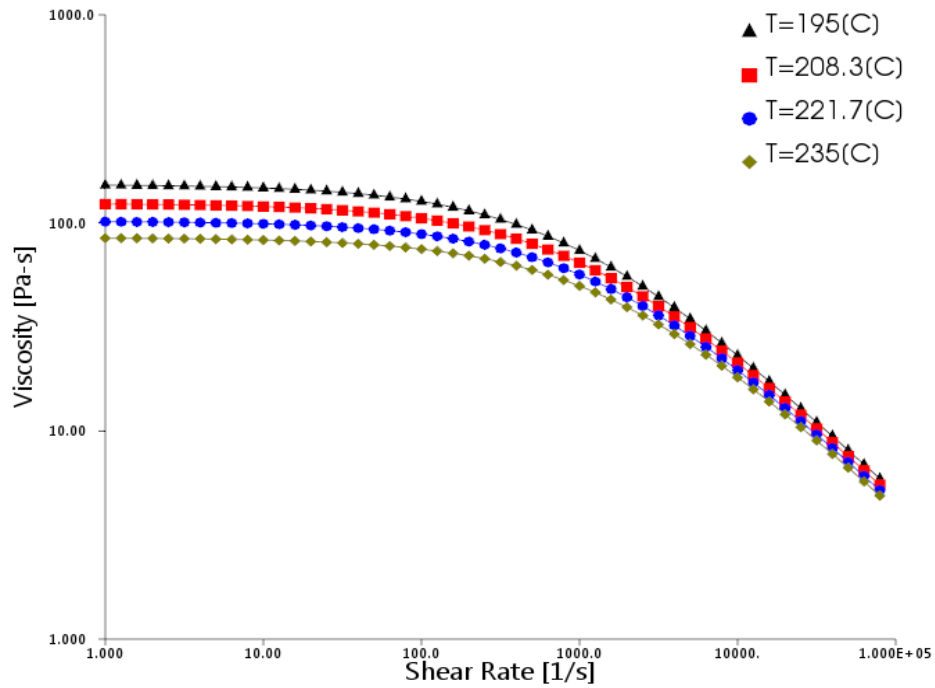


Figure 5-9: Cross WLF plot viscosity versus shear rate for HD-6733 [7].

### 5.4.5 Cyclic Olefin Copolymer (COC)

Cyclic Olefin Copolymer (COC) is a group of amorphous polymer that exhibits a combination of properties including high transparency, good blood compatibility, and excellent biocompatibility. COC is commonly used in packaging of pharmaceuticals devices, medical devices, and diagnostic disposal devices. COC provides a unique rheological flow behavior at high molding temperatures as presented in Figure 5-11.

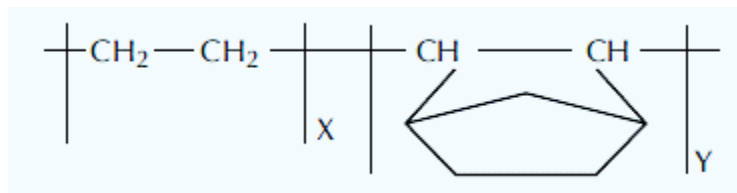


Figure 5-10: COC Chemical Structure [108].

Table 5-6: Physical and mechanical properties for COC TOPAS 5013S-04 [85,108]

Physical and Mechanical Properties	Value	Unit	ASTM Method
Melt Flow Index ( at 260 °C/2.16 Kg)	48	(g/10 min)	ISO 1133
Specific Gravity	1.02	g/cm <sup>3</sup>	ISO 1183
Poisson's ratio	0.402		E-132
Tensile Modulus	3200	(MPa)	ISO 527
Heat deflection Temperature	130	(°C)	ISO 75
Mold Shrinkage	0.4-0.7	(Cm/Cm)	D-955

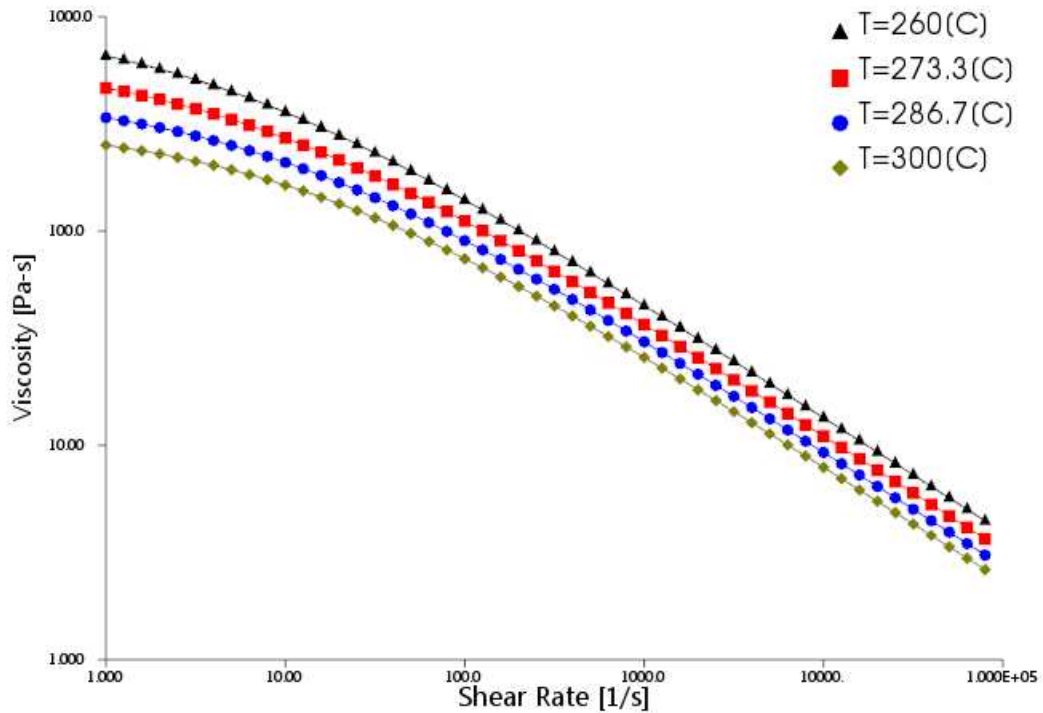


Figure 5-11: Cross WLF plot viscosity verses shear rate for COC TOPAS 5013S-04 [7].

## 5.5 2D Micro Filling Simulations (Molding Window Analysis)

Numerical simulation *Moldflow*<sup>®</sup> was used to gain a better understanding of the melt rheology inside a closed mold under high clamping pressure and optimize the processing with this newly acquired insight [109,110]. Simulations were performed to study the filling process of a mold cavity having an overall 12mm product diameter. The surface of this product was then assumed to have a micro-patterned surface with oval pillar-like projections (Pattern 1&2 as described in Table 5-1) and cylindrical pillars of diameter of 5 $\mu$ m with Height of 2  $\mu$ m.

CAD files with the microstructures were generated and then imported into *Moldflow*<sup>®</sup> for the analysis. *Molding Window Analysis (Dual Domain Analysis)*, a specific software feature, was initially utilized to determine at preliminary processing parameters for molding. Molding window analysis runs and verifies the process settings based on part geometry, material selection, and injection location then recommends the injection time and the temperature zones to mold the final part[111]. The recommended parameters were then used as the input for subsequent more detailed 3D-analysis (*Figure 5-12*).

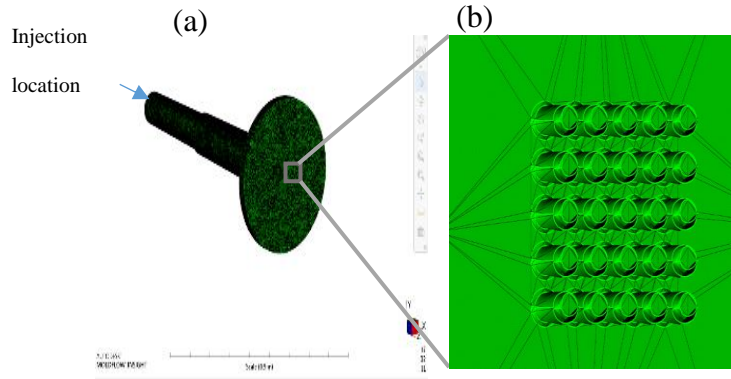


Figure 5-12: a) CAD model with tetrahedral mesh (3-D) in Moldflow. b) Array of ellipses (5x5) at D=15um and H=15um.

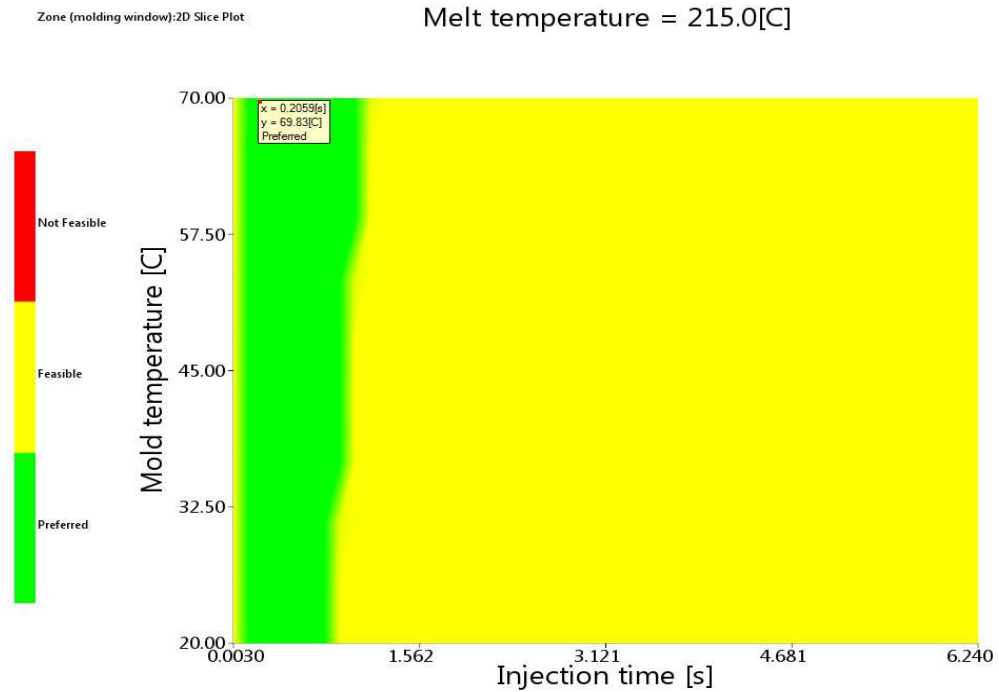


Figure 5-13: Zone (Molding window) result.

Figure 5-13 shows the zone plot for PS STYRON 666D by Americas Styrenics. The zone plot has two areas, which varies with melt, mold temperatures, and injection time. It is clear that the zone plot selected (at  $t_{inj}=0.2059$  sec according to Quality analysis results)

is within the green preferred area. This means part molding feasibility will be higher thus will directly increase final part quality.

Molding window analysis (Dual Domain Analysis) was done first to verify the best preliminary process setting for the design. The analysis provides quick recommendations for the Fill+Pack+Warp analysis that will be used later as input for the 3D analysis. It predicts an overall molded part quality as a function of mold temperature, melt temperature, and injection time. Molding window analysis runs and verifies the process settings each time based on part geometry, material selection, and injection location then recommend the injection time and the temperature zones to mold the final part[112,113]. It also gives a recommended cooling time which is mainly dependent on both mold and melt temperatures. The required cooling time for the given design was 88 sec which represents 80% of the total processing time. Replication quality as a function of mold temperature and at  $T_{melt}=215\text{ C}^\circ$  can be assessed as seen in Figure 5-14.

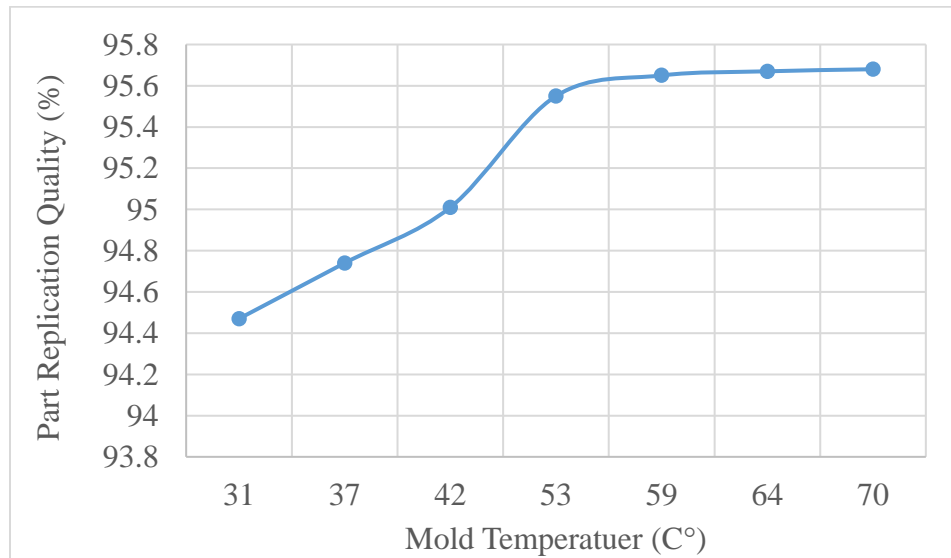


Figure 5-14: Molded Part Replication Quality (%) using STYRON 666D at Different Mold Temperature.

## 5.6 3D Micro Filling Simulations

3D modeling used Navier-Stokes equations solver at each node. The filling analysis was found to be significantly affected by the choice of velocity (V) during the filling stage prior to V-P switch-over. The simulation results indicate that the region with micro-featured is highly dependent on injection velocity control in the initial filling stage.

### 5.6.1 Analysis Sequences

3D Moldflow simulations have a Fill+Pack+Warp sequence for process analysis:

1. Fill: velocity control takes place in controlling the filling to replicate the mold cavity during this sequence.
2. Pack: Packing extra material to the cavity with excess pressure to ensure that the cavities are properly filled.
3. Warp: the warp analysis is done at each node to show the deflection of the molded part.

For this investigation, mold cooling sequence was done while the mold in active heating to the recommended mold temperature from 2D Simulations. So, the polymer melt is conducting heat into the mold walls based on cooling time in 2D simulations until the molded part is ejected.

## 5.6.2 Results and Discussions

Figure 5-15 shows the filling process through the cavity at 50, 85, 95, and 100% of part filled. The micro-featured region was filled in a total time of 0.1408 seconds (Figure 5-16). The suggested V-P switchover is 95% of cavity filling via velocity, followed by a switch-over to cavity filling via pressure.

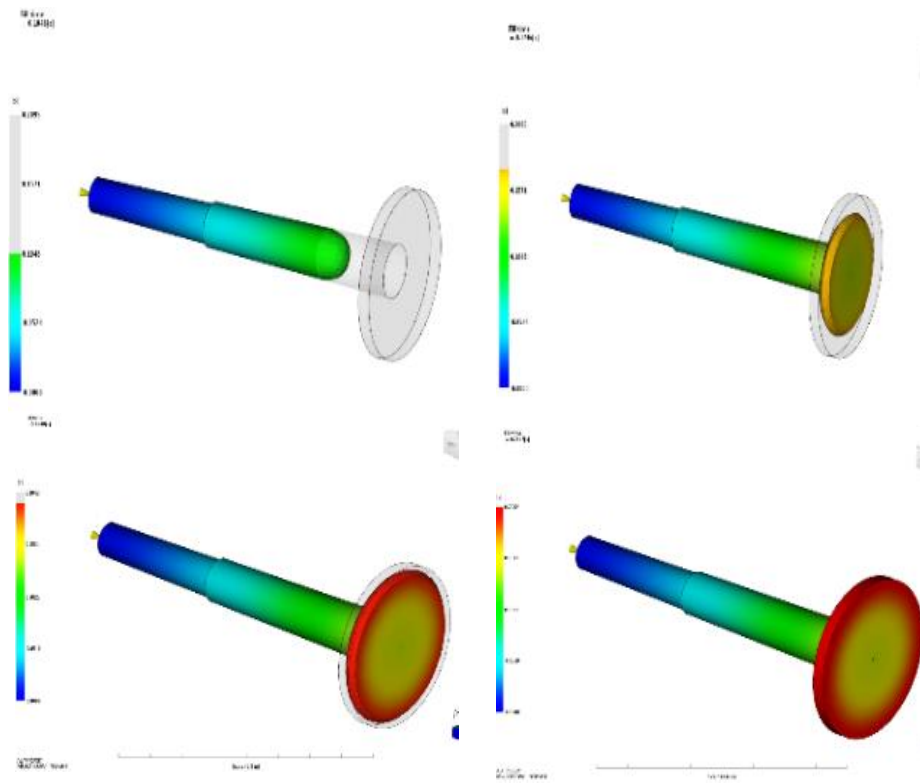


Figure 5-15: Filling simulation results at 50, 85, 95, and 100% of the part filled.

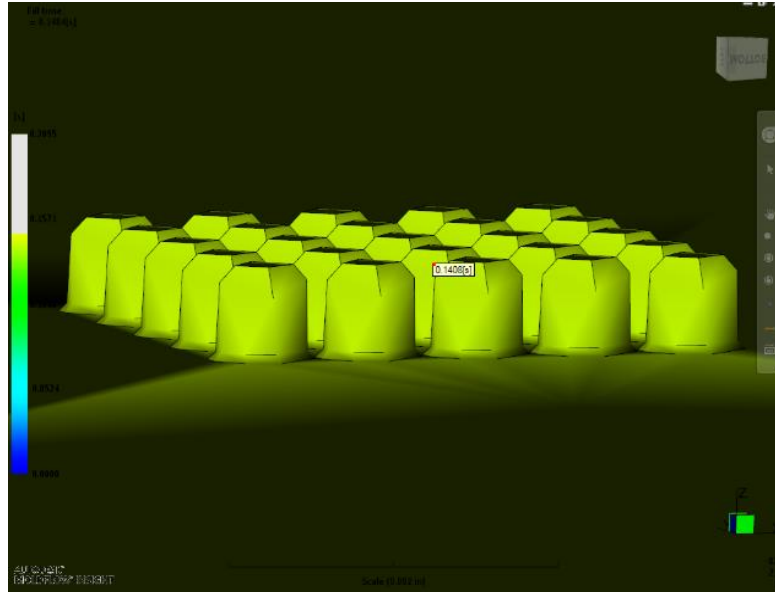


Figure 5-16: Micro-structured region filled at  $t=0.1408$  sec.

Velocity filling control is shown in Figure 8 at different fill time to identify micro-cavities filling behavior. The melt continued to flow through micro-cavities until the end of the first stage of filling (velocity control) at  $t=0.1923$  sec (Figure 5-18). The highest velocity inside the micro-cavity  $v=0.0001$  (cm/sec) was found to be at  $t=0.1923$  sec, the velocity near the injection location (gate) was 154.2 (cm/sec) and continued at the same level until filling was switched to pressure control. At the second stage, pressure control packed the melt inside these cavities until it solidifies. Pressure distribution varies inside the whole geometry as seen in Figure 5-19. The maximum pressure was found near the injection location. The pressure drops along the runner until it reaches the lowest value near the micro-cavity gates (location C in Figure 5-20). Figure 5-20

Figure 5-20 shows pressure at the end of the fill inside micro-cavity which will be applied in the ability to fill microcavities pressure has to extend until the part is totally filled and then solidified the ejected.

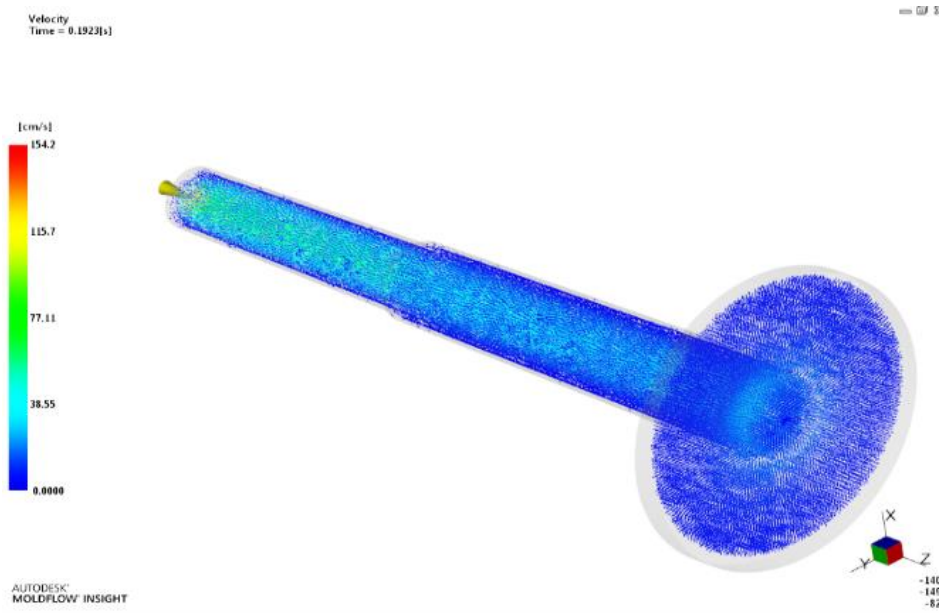


Figure 5-17: Velocity contours at the end of velocity filling stage ( $t_{inj}=0.1923$  sec).

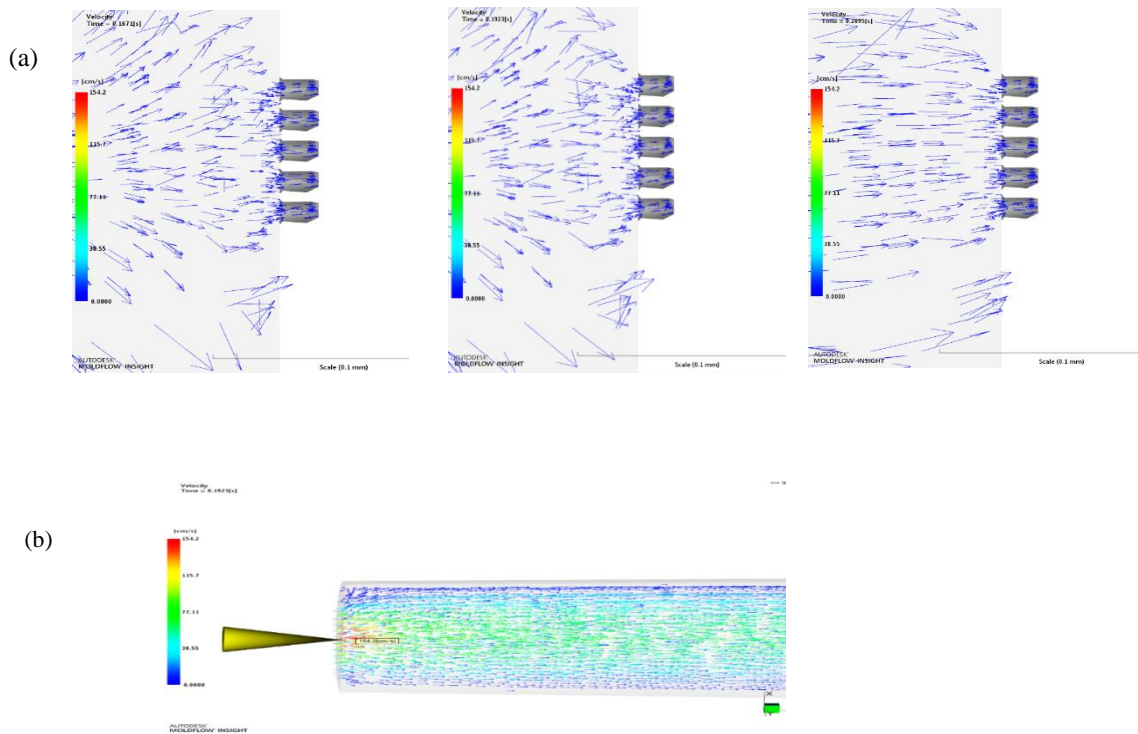


Figure 5-18: Velocity contours at different filling time (0.167, 0.1923, and 0.2095). b) velocity at the injection point.

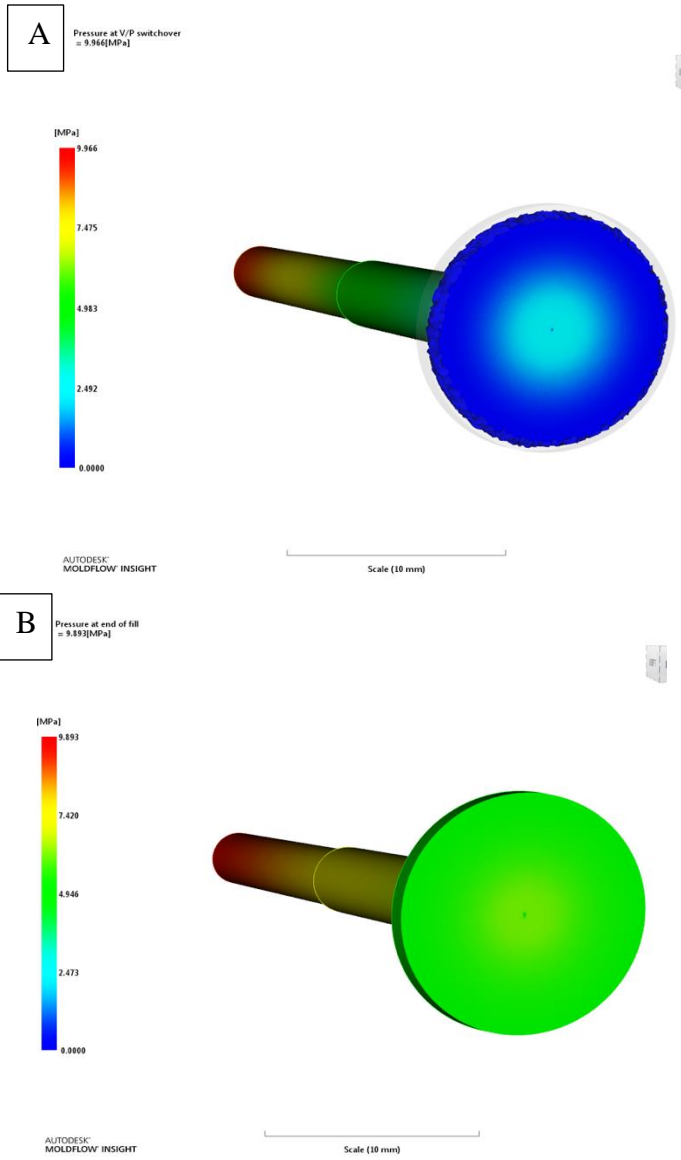


Figure 5-19: Pressure distribution at V/P switchover (A) and the end of fill (B).

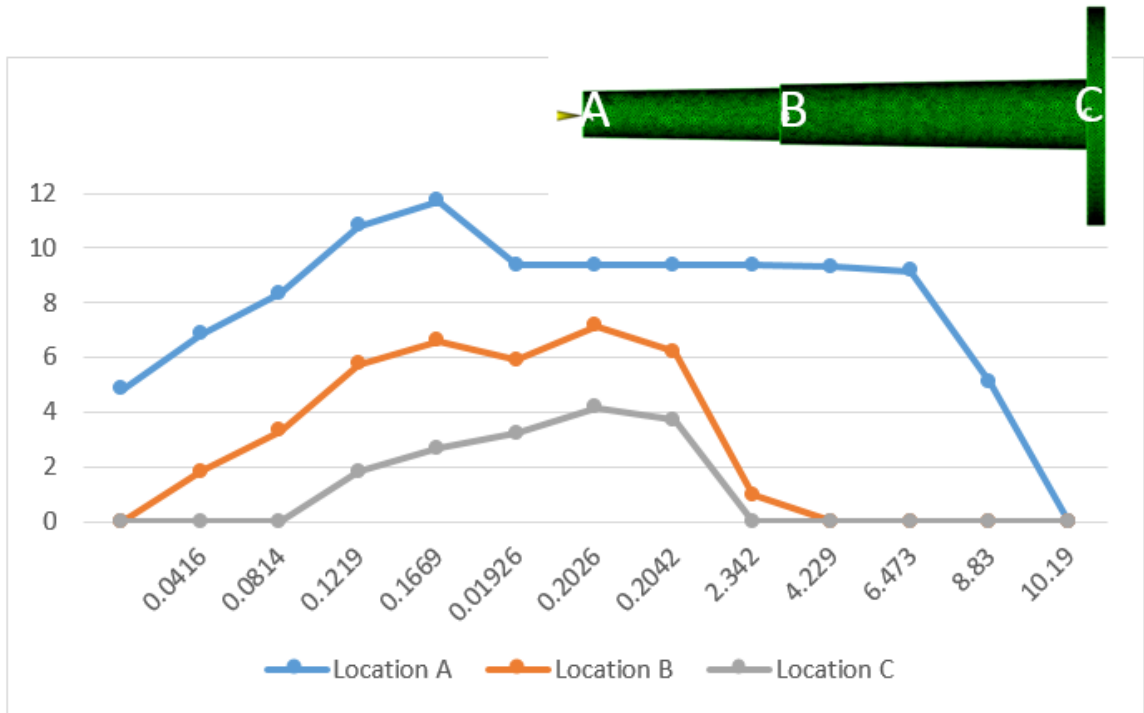


Figure 5-20: Pressure distribution during filling at different locations.

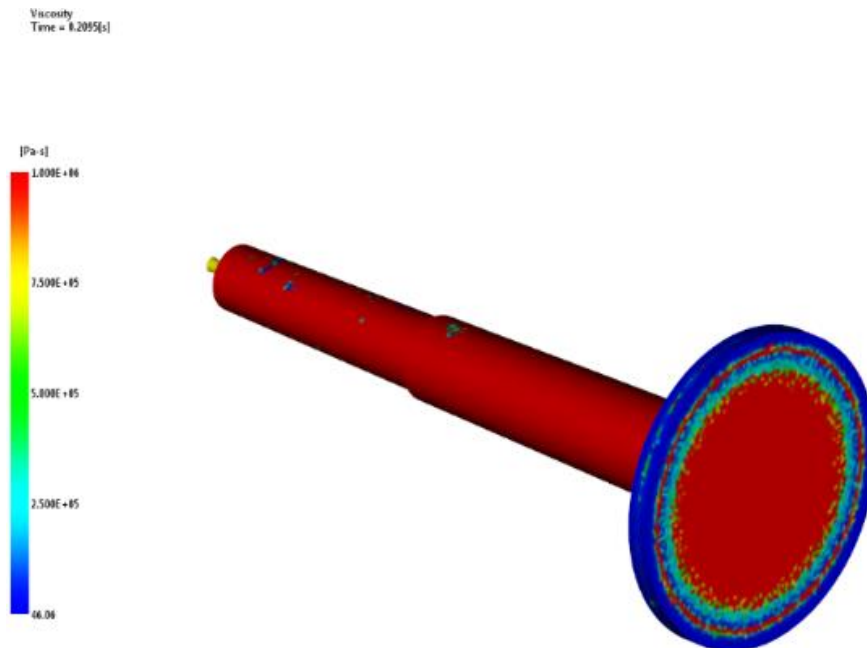


Figure 5-21: Viscosity distribution at the end of fill.

Temperature at flow front  
= 215.8[C]

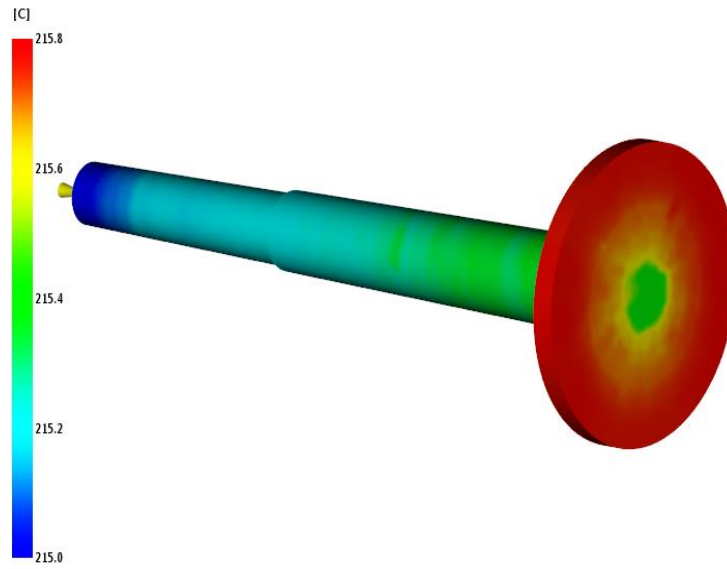


Figure 5-22: Temperature distribution at flow front.

Frozen layer fraction at end of fill  
= 0.0262

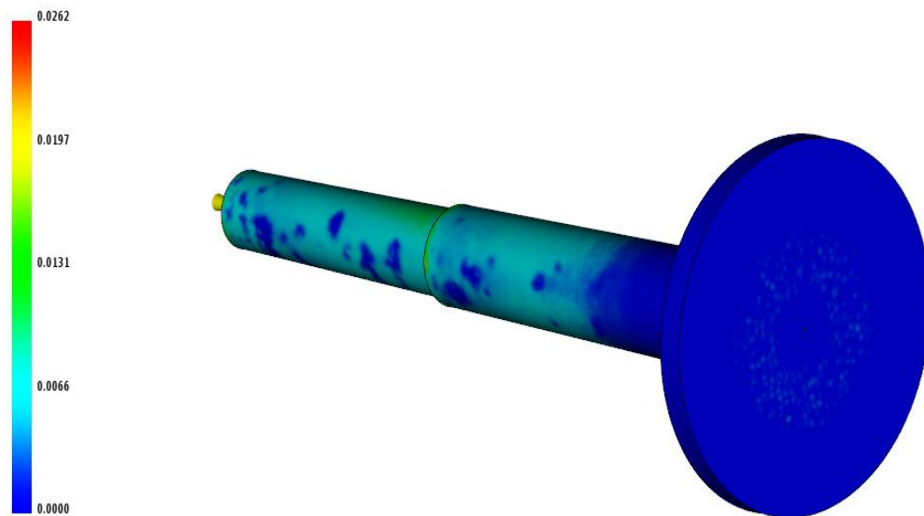


Figure 5-23: Frozen layer diffraction at end of fill.

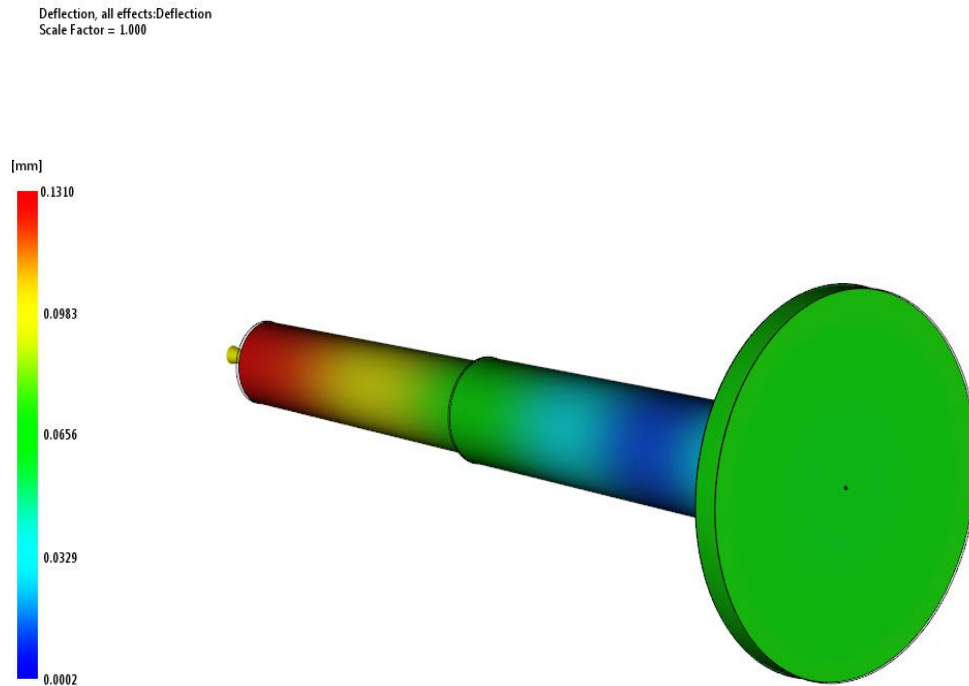


Figure 5-24: Warpage analysis.

Viscosity distribution across the flow indicates that a greater flow ability under applied pressure (Figure 5-21). Melt temperature at the flow front has to be maintained at  $\pm 10\text{ C}^\circ$  of set temperature as seen in Figure 5-22. The frozen layer represents the thickness of the frozen layer as a fraction of part thickness. A higher value signifies a thicker frozen layer and a higher resistance to flow (Figure 5-23) thus directly influencing the filling process in the micro-featured region. Figure 5-24 includes the results of a warpage analysis to show which regions of the molded part have highest deflection ratio. The sprue region near the injection point appears to have high deflection rate due to material shrinkage.

Velocity slip were studied in the simulations and found that at the entrance to micro cavities where slip might occur (Figure 5-25), shear stresses near the walls can exceed the

maximum shear stress recommended for the material (0.5 Mpa for STYRON 666D). In response the material does slip locally, and slip velocity levels can result such as those calculated and shown in Figure 2. As the melt passes the entrance to micro/nano cavities the wall shear stress drops through the cavity (Figure 5-26).

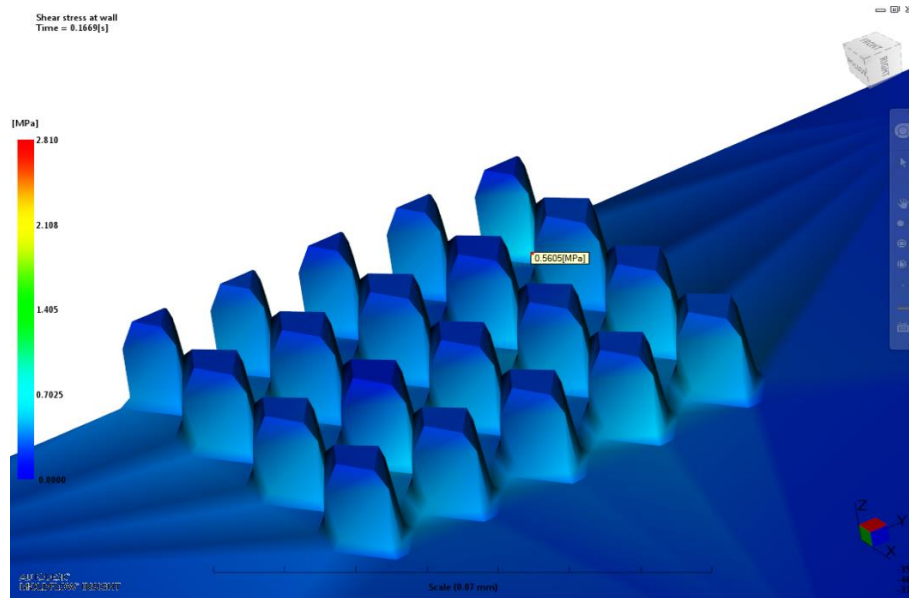


Figure 5-25: Shear stress at micro-cavities walls.

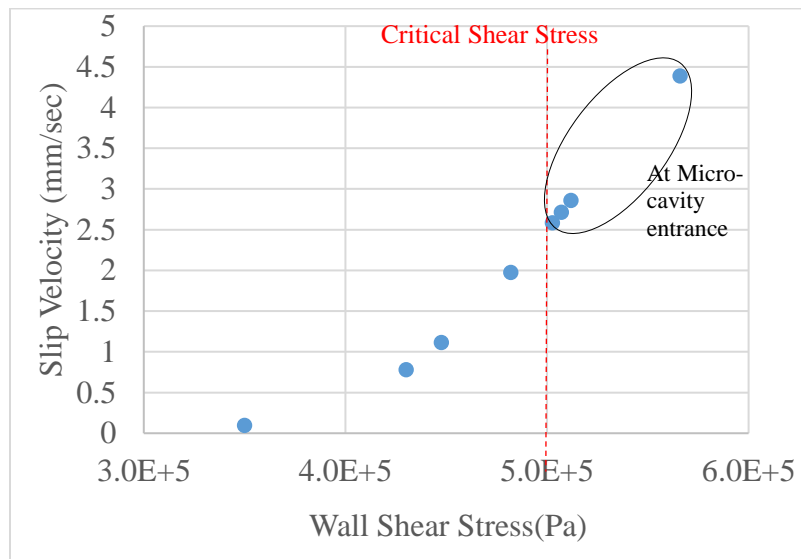


Figure 5-26: Velocity slip appearance inside the micro cavities.

### 5.6.3 Different Molding Material (PS, TPU, LDPE, HDPE)

Simulations were performed for Polystyrene (PS) STYRON™666D , Texin 985 Thermoplastic Polyurethane (TPU), Low-Density Polyethylene (LDPE ASI CP851), High-Density Polyethylene (HDPE Exxon HD-6733), and Cyclic Olefin Copolymer (COC) TOPAS 5013S-04. It was observed that cooling time was significantly dependent on material selection, mold, and melt temperatures. The effect of mold temperature on cooling time has been compared for STYRON™ 666D and Texin 985 as in Figure 5-27. At  $T_{melt}=215\text{ C}^\circ$ , Texin 985 exhibits higher temperature during process thus is reflected directly on cooling time and cycle time.

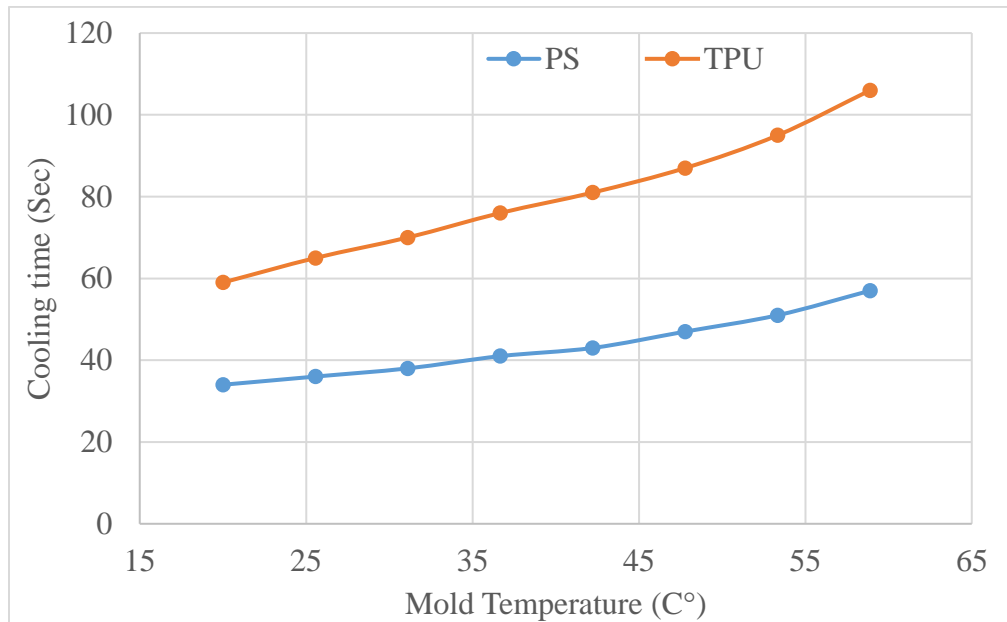


Figure 5-27: Cooling Time at different mold temperatures at  $T_{melt}=215\text{C}$ .

Different materials were used to simulate the filling of 5x5 array of oval micro pillars. It was observed from the simulations that cooling time is an important factor that is needed

to consider for each material during experimentations. Melt temperature, mold temperature, and material type determine the amount of time is necessary to ensure the molded pillars are solidified before demolding. Table 5-9 shows the recommended molding parameters using different materials. This molding parameters was used in experimentation validation in chapter 6.

Table 5-7: Moldflow recommended molding parameters for 15 um oval micro features using different molding materials.

Material	PS	TPU	LDPE	HDPE	COC
Fill time	0.209	0.2027	0.2809	0.2809	0.151
Velocity (mm/sec)	153.6	154.2	134.8	134.8	350.6
Injection Pessure (Mpa)	11.72	10.09	10.56	10.56	1.929
Packing pressure (MPa)	9.214	7.567	7.916	7.916	1.44
Tmelt (C°)	215	193	168.5	195	270
Tmold (C°)	70	50	36	37	125
Cooling time (sec)	88	88	42	33	114

### 5.1.1 Micro Features Simulation (15, 10, 5 um, and flat)

Simulations were performed to study the filling process of two mold cavities with 12 mm diameters with flat surface and 3 microstructures including oval shapes with diameter of (D=15, 10  $\mu$ m) and circular with D=5um. These particular features were chosen to mimic human tissues for clinical testing. It was identified that the depth of the microfeatures has an influence of the pressure needed for both injection and packing. Microfeatures with depth of 2 um required lower injection and packing pressures compared to deeper microfeatures under the same molding parameters as seen in Table 5-8.

Table 5-8: Recommended molding parameters for different micro features using PS STYRON 666D.

Micro features geometries	FLAT	5 um	10 um	15 um
Material	PS	PS	PS	PS
Fill time	0.2057	0.205	0.2545	0.209
Velocity	152.4	152.4	150.7	153.6
Injection Pressure (Mpa)	3.405	5.982	10.55	11.72
Packing pressure (MPa)	2.554	4.758	7.912	9.214
Tmelt	215	215	215	215
Tmold	70	70	70	70
Cooling time	88	88	88	88

### 5.1 Sprue Size Change Simulations

From simulations, it was identified that the sprue gate (Figure 5-28) was the last area to solidify which emphasize that most patterned region would be affected by sprue temperature. The cooling time need to be selected carefully to minimize any demolding damages. A new sprue size was designed based on the machine nozzle diameter to overcome long cooling time. The new sprue design is described in Chapter 6.2. Cooling time was reduced 35 % thus will directly cut the cycle time.

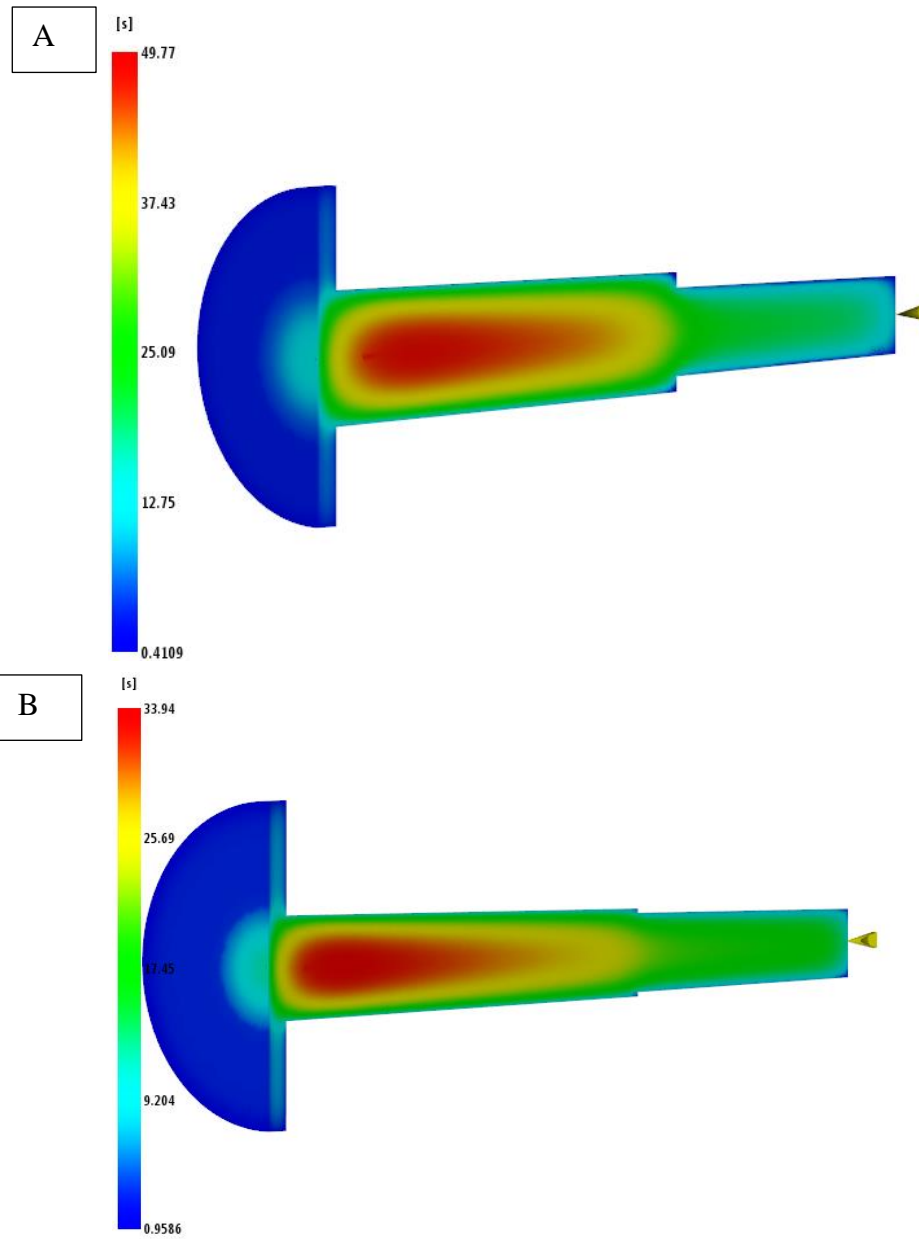


Figure 5-28: Time to reach ejection temperature A) old Sprue. B) Modified sprue.

Table 5-9: Processing parameters provided by Moldflow simulation.

Material	PS(Styron 666D)
Fill time (Sec)	0.2095
Velocity (mm/sec)	153.6
Melt Temperature (C°)	215
Mold Temperature (C°)	70
Injection Pressure (MPa)	13.23
Packing Pressure (Mpa)	9.854
Cooling time (SEC)	57

## 5.7 Discussion and Conclusion

Numerical simulations using Moldflow<sup>®</sup> Insight were done to optimize the filling of cylindrical micro-cavities with an oval shape and 15,10 $\mu$ m diameter and 15,10 height and circular micro-cavities with 5  $\mu$ m and 2  $\mu$ m height. The interface of macro to micro scale was considered in this simulation by reducing the mesh aspect ratio to 6. Moreover, inertia effects were included in the 3-D simulation to show the effect of the slip model at micro-cavity walls. Wall shear stress was higher than the critical shear stress at the micro-cavity entrances as previously discussed and reduces as the flow passes inside the micro-cavities.

Preliminary processing parameters conducted from molding window analysis led to better results in the 3-D simulation and assuring an optimum filling of the micro-cavities. Micro-cavities were completely filled at the end of the filling stage and the desired final microstructured surface pattern was attained by applying packing pressure when 95% of parts filled for 5 Sec. At the end of the filling, micro-cavity filling was influenced by

packing pressure that was applied at 75% of injection pressure for 5 sec to attain the complete fill of the micro-cavities. Arriving preliminary processing parameters as done during this study is a better alternative to trial and error type experiments. Reducing the sprue size is a sufficient method to reduce cooling time and reducing material waste since removal of the sprue is needed to use these molded plates. At this point, the study will be extended by experimental investigations in chapter 6 to validate the simulation results and to assess the effect of each parameter on the replication process.

## CHAPTER 6: EXPERIMENTAL RESULTS AND CHARACTERIZATIONS

### 6.1 Micro-Injection Molding Replication

Several studies have focused on optimizing micro injection molding processes to enhance the filling of micro cavities. Rodgers et al investigated the effect of mold temperature on injection velocity and concluded that injection velocity did not affect filling at mold temperatures below  $T_g$ . Above  $T_g$  as the temperature was increased, the melt viscosity decreased and the polymer flow inside the micro channels improved [51]. Other investigations focused on processing parameters to enhance replication quality with respect of micro-feature size, spacing, and the position related to the injection gate [42,52,53].

Using giving data from Chapter #5 and apply it on our Nissie AU3E micro injection molding machine to optimize filling cavity with small micro holes. The machine is suitable for this application as it has the capability to mold products with weights of at most 0.2g. The machine has an injection unit that utilized the filling process and provide better control of velocity and pressure. Processing parameters was examined to eliminate trail-and error experimentations using optimized simulations data in chapter 5 to achieve high replication ratios.

#### 6.1.1 Polystyrene (PS) Experimental Trails

Optimal molding parameters for Polystyrene (666D STYRON) were obtained from Moldflow simulations in Chapter#5. Micro-injection molding experiments were carried out using melt temperatures ( $T_{melt}$ ) set at 215 C°. The mold temperature ( $T_{mold}$ ) was set at 70

C°. Filling velocity was set at 150 mm/seconds, and cooling time varies between 45-95 seconds. Packing pressure was kept low at 5-30 Mpa to avoid fracture of the silicon wafer.

PS replications required high temperatures and pressures, the optimum cooling time was determined to be 88 seconds. The optimum cooling time was found by Moldflow simulation for  $T_{melt}=215\text{ C}^\circ$  and  $T_{mold}=70\text{C}^\circ$ . Cooling time is one of the critical processing parameters during the replication of microscale patterns. The cooling times had high influence on molded micro pillars at least 55 seconds were needed for this material to eliminate pillar distortions. Replication rate is defined as the ratio of the pillars height to the microcavity depth measured from SEM images using imageJ software.

Table 6-1: Moldflow recommended molding parameters for STYRON 666D.

Material	PS (Styron 666D)
Velocity	153.6
Injection Pessure (Mpa)	11.72
Packing pressure (MPa)	9.214
$T_{melt}$ (°C)	215
$T_{mold}$ (°C)	70
Cooling time (sec)	88

### 6.1.1.1 PS injection molding of 5 um circular pillars

- **Tooling**

Si mold (6X6 mm) with 5 um circular diameter cavities with 2.49 um depth was used in these experiments (Figure 6-1). Antistiction coating was applied at the end of DRIE etching to work as mold release and enhance demolding process of the micro pillars.

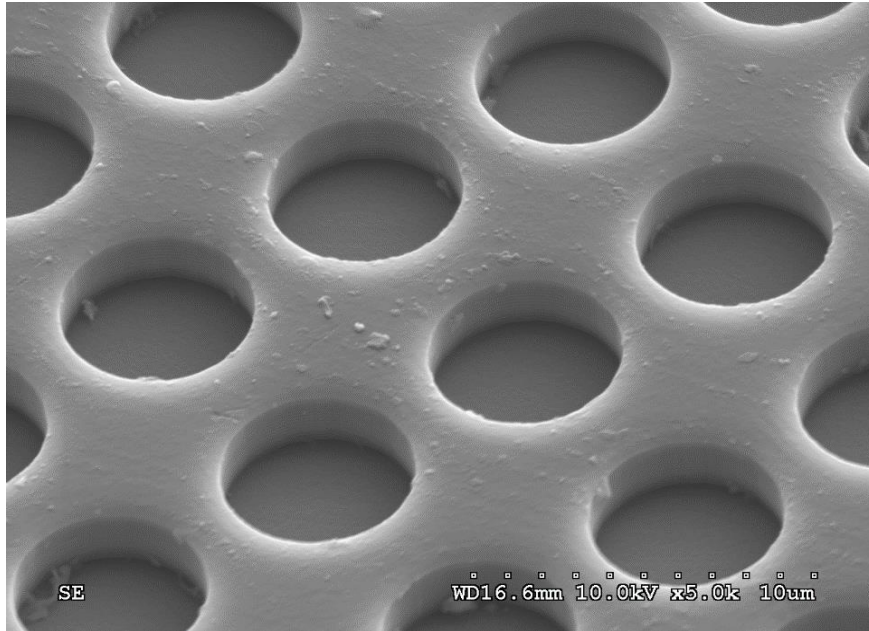


Figure 6-1: Si mold with 5  $\mu\text{m}$  diameter and 2.49  $\mu\text{m}$  depth.

- **Results**

SEM imaging were conducted using a *Hitachi 4300* to gain insight on the polymer replication accuracy. It was evident that that cooling time is a significant factor in replication accuracy. Molded parts with longer cooling time were found to acquire better precision in replication, with minimal distortion during demolding. Micro pillars needed at least 55 seconds for this material to eliminate pillar distortions (Figure 6-2Figure 6-3). As cooling time was increased to 65 seconds, the material started to preserve the micro cavities replica thus reduces the amount of distortion found on the pillars as shown in Figure 6-4. Minor distortions were observed on the pillars at cooling

time of 85 seconds. The best replications were found at the recommended cooling time at 88 seconds as shown in Figure 6-6. When cooling time was increased to 95 seconds, it was noticed that molded pillars started to bulge at the top due to heat gain from the mold base heaters (active variotherm heating with passive cooling). The replication rate was varied with the cooling temperatures. Highest replication rate of 1.458 was found at 55 sec cooling time in terms of pillars height but the amount of pillars distortion was found were not desirable. The optimum replication rate of 1.015 was found at the recommended cooling time of 88 sec.

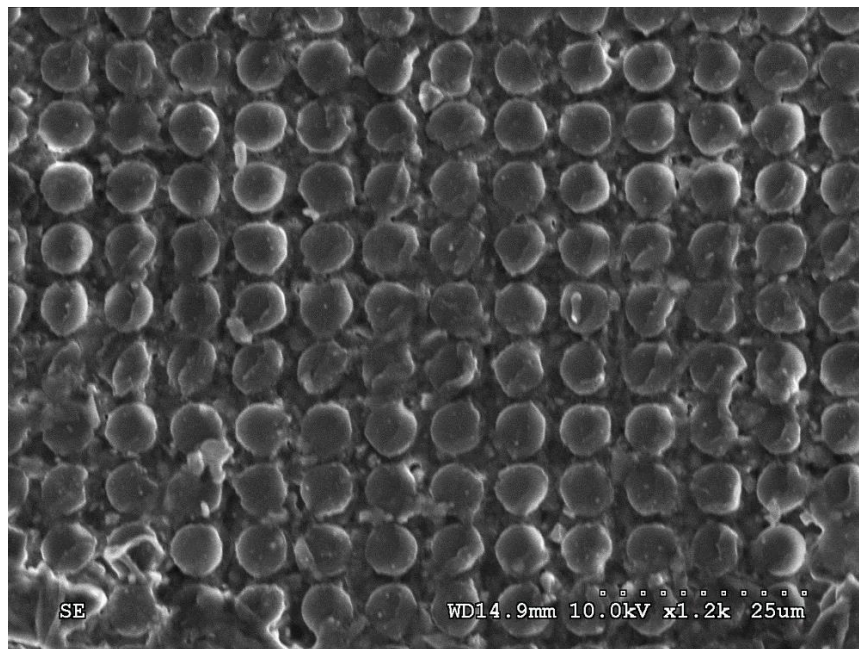


Figure 6-2: 5µm diameter molded pillars (666D STYRON) with 45 sec cooling time.

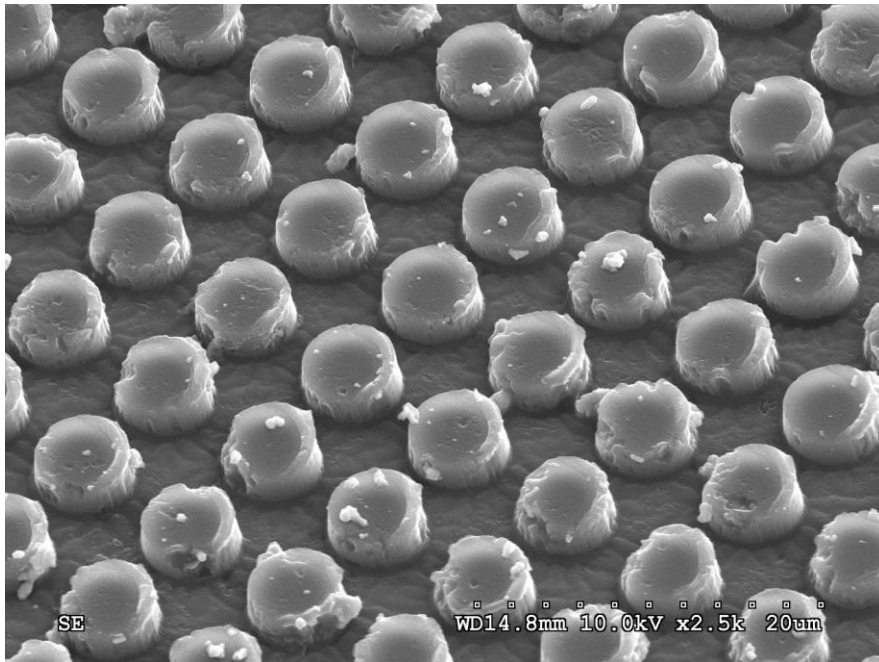


Figure 6-3: 5um diameter molded pillars (666D STYRON) with 55 sec cooling time.

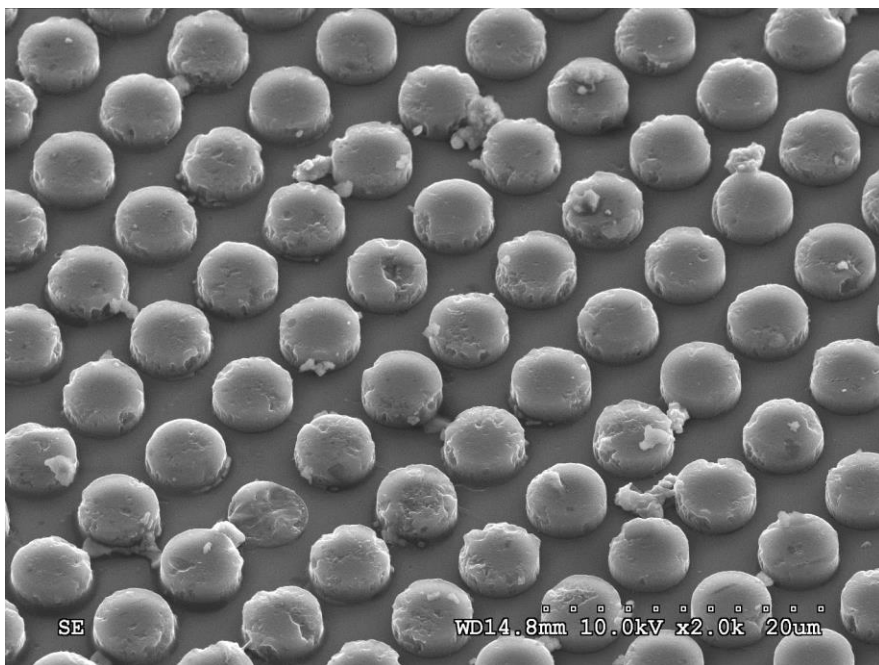


Figure 6-4: 5um diameter molded pillars (666D STYRON) with 65 sec cooling time.

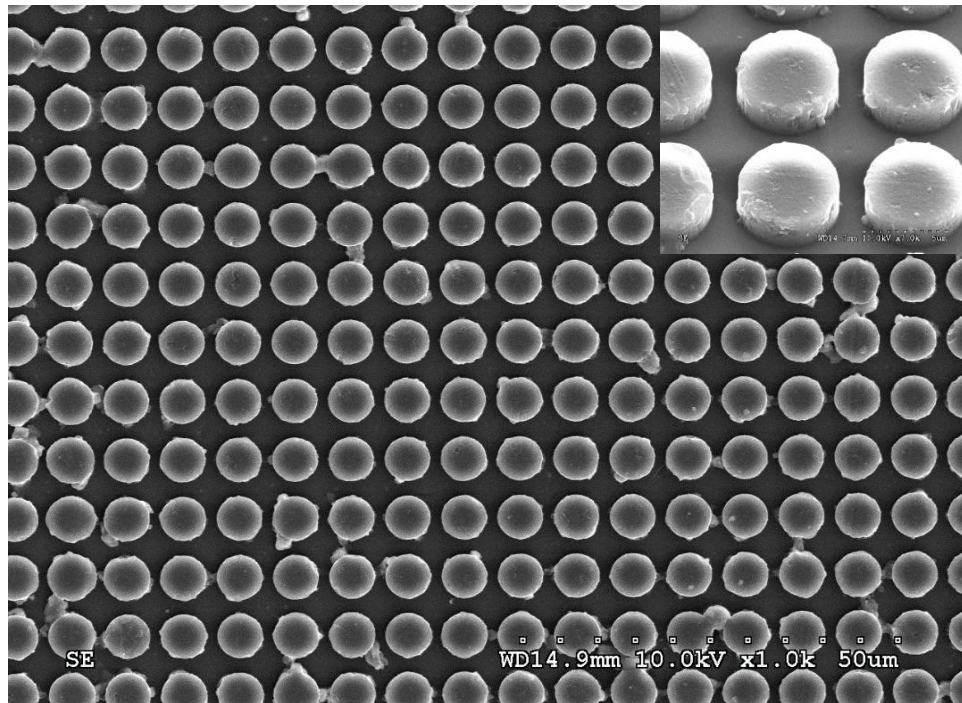


Figure 6-5: 5um diameter molded pillars (666D STYRON) with 85 sec cooling time.

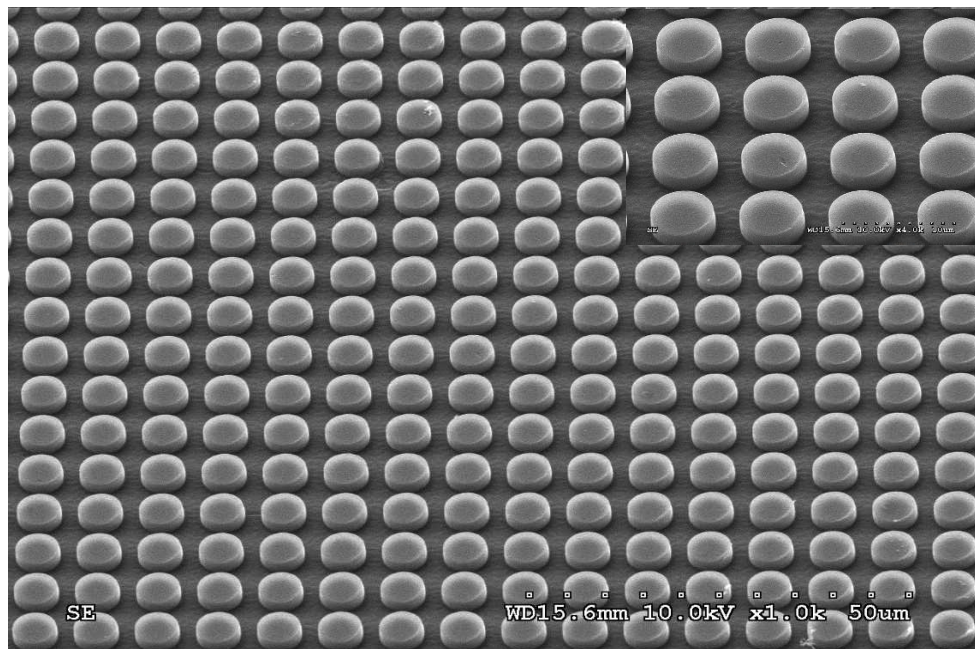


Figure 6-6: 5um diameter molded pillars (666D STYRON) with 88 sec cooling time.

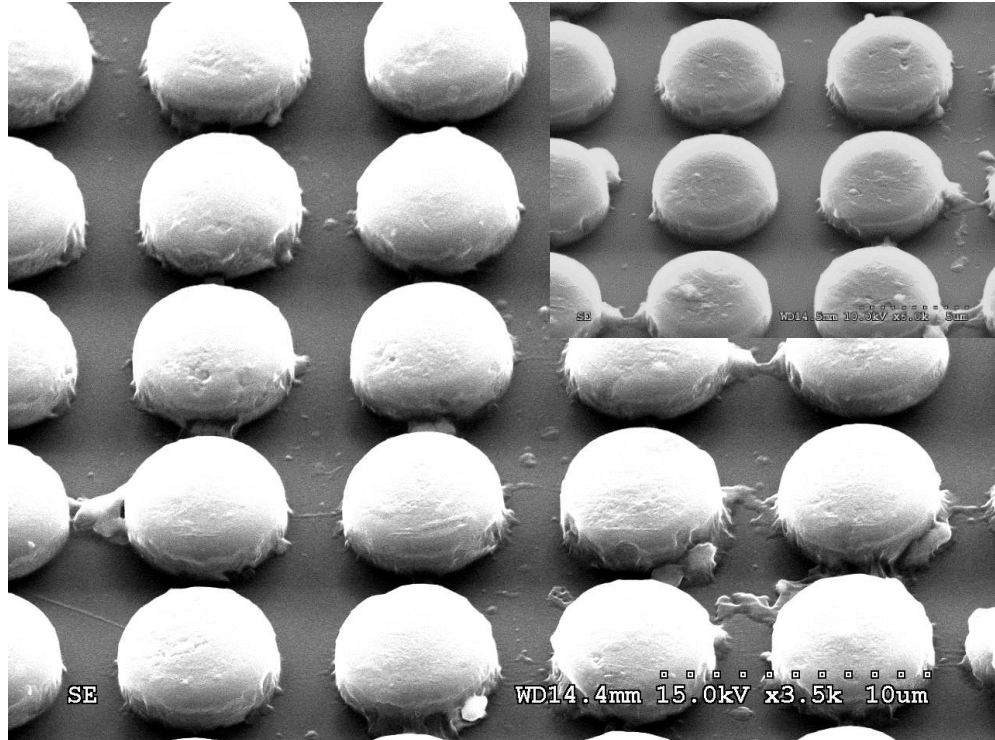


Figure 6-7: 5µm diameter with 2.136 µm height molded pillars (666D STYRON) with 95 sec cooling time.

#### 6.1.1.2 PS injection molding of 15, 10 µm Oval pillars.

Experiments were done to fill micro oval cross-sectional cavities with diameters of 15 µm major diameter with 15.03 µm height (Tool I), 10 µm major diameter with 10.02 µm height (Tool II) (Figure 6-8). The molding parameters utilized in this experiments are presented in Table 6-2. Guided by Moldflow simulations, the packing pressure was set at 9 MPa initially. It was found that suggested packing pressure was inadequate and the micro cavities were not filled to replicate the mold depth exactly. The packing pressure was achieved to 30 MPa to achieve satisfactory replication of the 10.02 µm deep micro cavities. The results are presented in Figure 6-9.

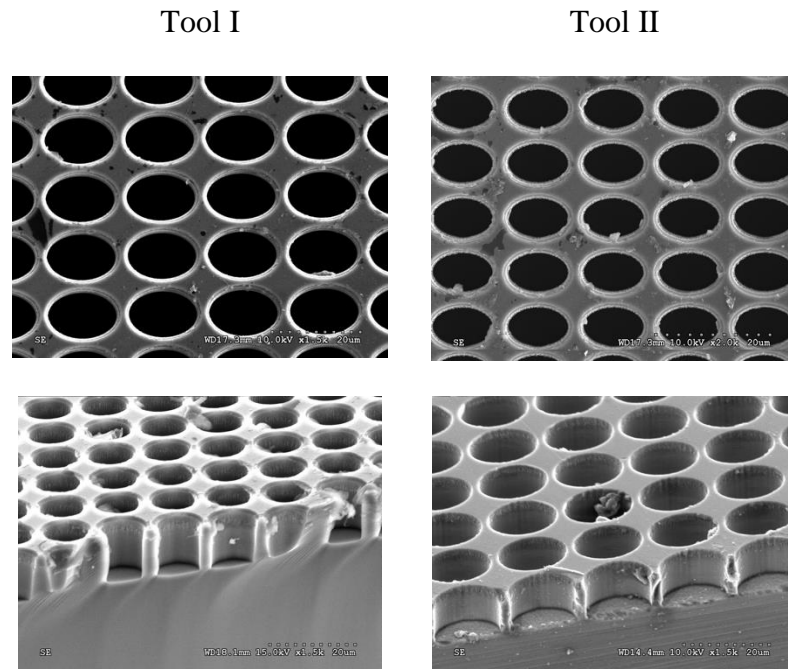


Figure 6-8: SEM image for Si molds tool I&II.

Table 6-2: Molding parameters for polystyrene (STTRON 666D).

<i>Parameter</i>	<i>Value</i>
<i>Injection pressure (MPa)</i>	20
<i>Packing pressure (MPa)</i>	30 - 9
<i>T<sub>mold</sub> (C°)</i>	71-83
<i>T<sub>melt</sub>(nozzle) (C°)</i>	215
<i>Velocity (mm/sec)</i>	153.6
<i>Cooling time (sec)</i>	88

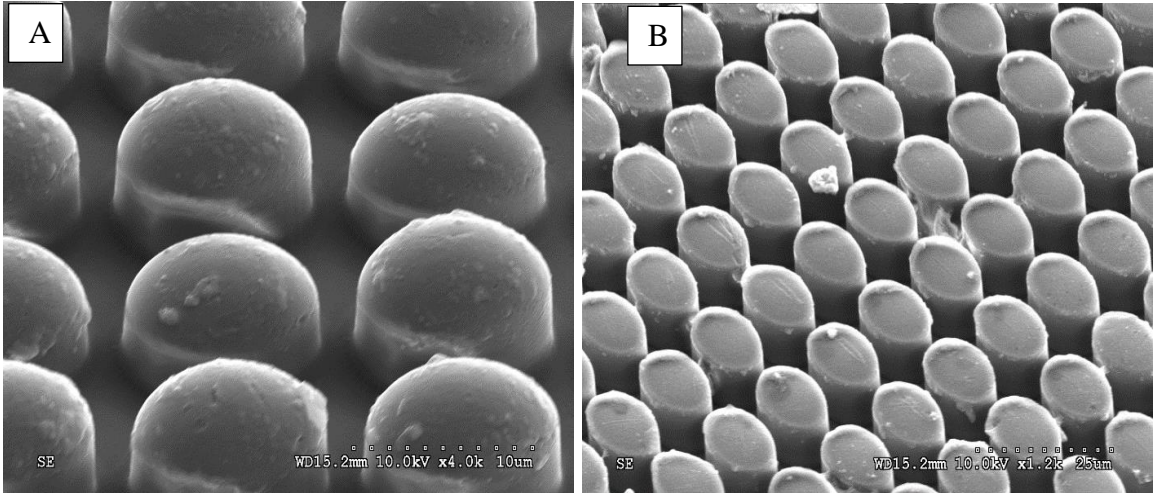


Figure 6-9: PS 10  $\mu\text{m}$  diameter with 6 (A), 30 (B) MPa packing pressure.

### 6.1.1.3 PS Velocity Study of 15 $\mu\text{m}$ pillars

Injection velocity is another factor that is affecting the replication rate at the first stage. For the lowest injection velocity (25 mm/sec), the replication rate was 0.206 (pillars height = 3.11  $\mu\text{m}$ ). The micro cavities filling improved significantly when the velocity was increased by factor of 4 as shown in Figure 6-10-C. When the injection velocity was increased to 150 mm/sec, the pillar height was found 14.932  $\mu\text{m}$  height as seen in Figure 6-10-D. The mold temperature was set at 83C° for this trails to prevent Si wafer damage due to high interaction with PS micro pillars during demolding.

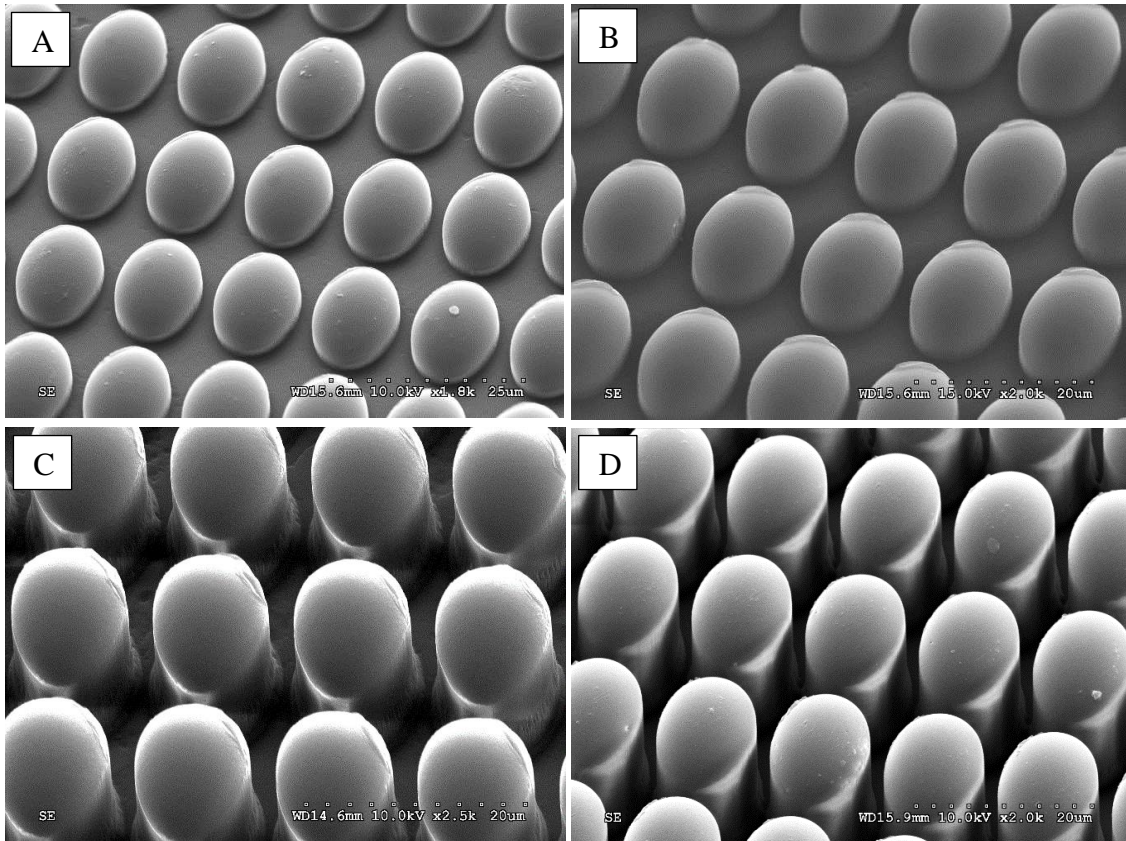


Figure 6-10: PS molded samples with injection velocity of A) 25, B) 50, C) 100, D) 150 mm/sec (scale bar 25,20,20,20 respectively).

### 6.1.2 Thermoplastic Polyurethane (TPU) Trails

In this study the effect of packing pressure, cooling times and antistiction coating on the micro injection molding of a thermoplastic polyurethane (Texin 985) was investigated. Furthermore, the ability to mold high performance micro pillars without using antistiction coating was examined.

The processing parameters for injection molding were optimized previously in a simulated environment utilizing 3D Moldflow<sup>®</sup> [16]. Thermoplastic Polyurethane (TPU)

(Texin 985) elastomer based material was used as the molding trails. Injection molding was performed with a Nissei AU3E injection molding machine. Micro-injection molding experiments were carried out using melt temperatures ( $T_{melt}$ ) set at 190°C. The mold temperature ( $T_{mold}$ ) was set at 54 °C. Filling velocity was in the range of 150 mm/s, and cooling time varies for this study between 15 to 88 seconds in this experiments. Injection pressure was set at 20 MPa while packing pressure kept between 15 MPa and 25 MPa for 5 sec to avoid fracture of the silicon wafer.

Table 6-3: Moldflow recommended molding parameters for Texin 985.

Materila	TPU
Velocity	154.2
Injection Pessure (Mpa)	10.09
Packing pressure (MPa)	7.567
Tmelt (°C)	193
Tmold (°C)	50
Cooling time	88

- **Tooling**

Silicon Mold inserts were used in this experiments with oval shapes with a major diameter of 15µm and two distinct depths 21.5, 8.38 µm (Tool I&II). An additional mold that had cavities with circular cross-section (5 µm diameter and 2.49 µm) was used (Tool III).

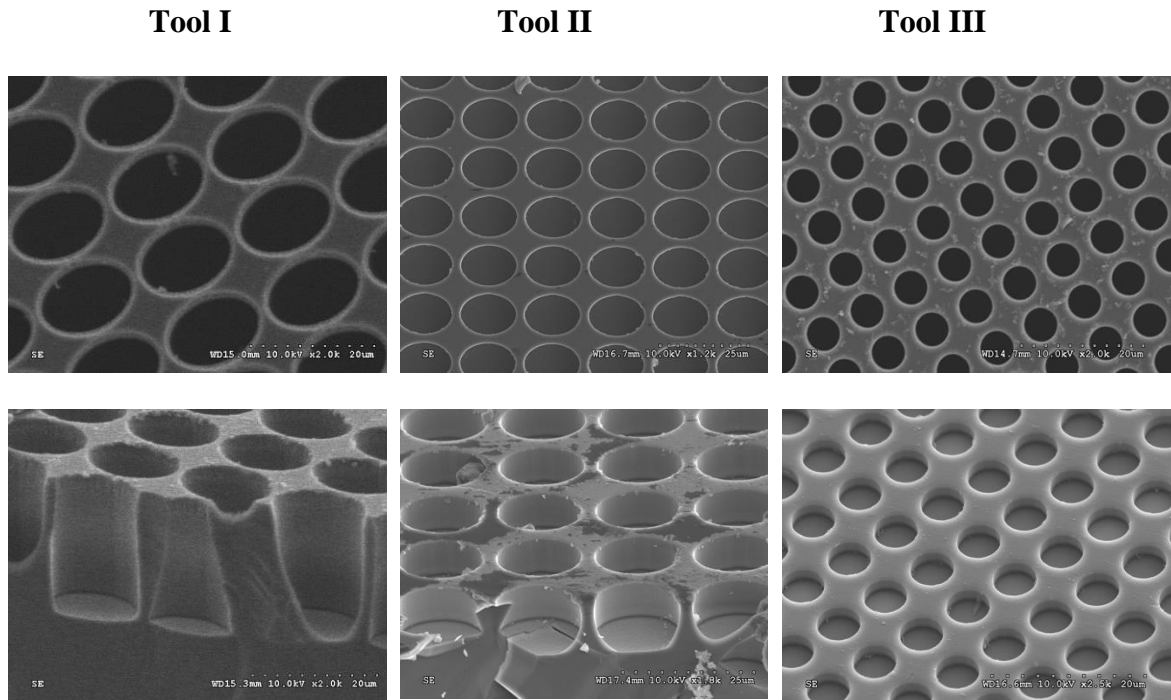


Figure 6-11: Silicon Mold inserts with Oval shapes with 15 $\mu$ m Diameter and 21.5, 8.38  $\mu$ m depth (Tool I & II (without antistiction coating)). And Cylindrical shapes with 5  $\mu$ m diameter and 2.49  $\mu$ m depth (Scale Bar for Tool I, II, and III is 20, 25, 20 $\mu$ m respectively).

### 6.1.2.1 Packing Pressure

The packing pressure is the major force that drives the melt to flow into the micro cavities and thus directly influence the replication rate. Thus, it should be optimized for the specific material being used, the material of the mold, as well as the shape and depth of the cavities. Micro injection molding trials were done using Tool I in Figure 6-11. The quality of the replication was investigated at different packing pressure, 15, 20, and 25 MPa and the representative results are shown Figure 6-12 A, B and C respectively. It could be clearly seen that the hemispherical top areas were formed at a packing pressure of 15Mpa. This is an indication of incomplete filling as the cavities had a flat surface at the bottom. By

increasing packing pressure to 20 MPa, the melt flow reaches the bottom walls and form flat areas in the middle of the molded pillars. The optimal packing pressure was found to be 25 MPa. At this pressure the polyurethane (Texin 985) filled the cavities completely and the micro features were replicated perfectly. Further increasing in packing pressure to 35MPa did not produce any noticeable improvement of the replication of the pillars.

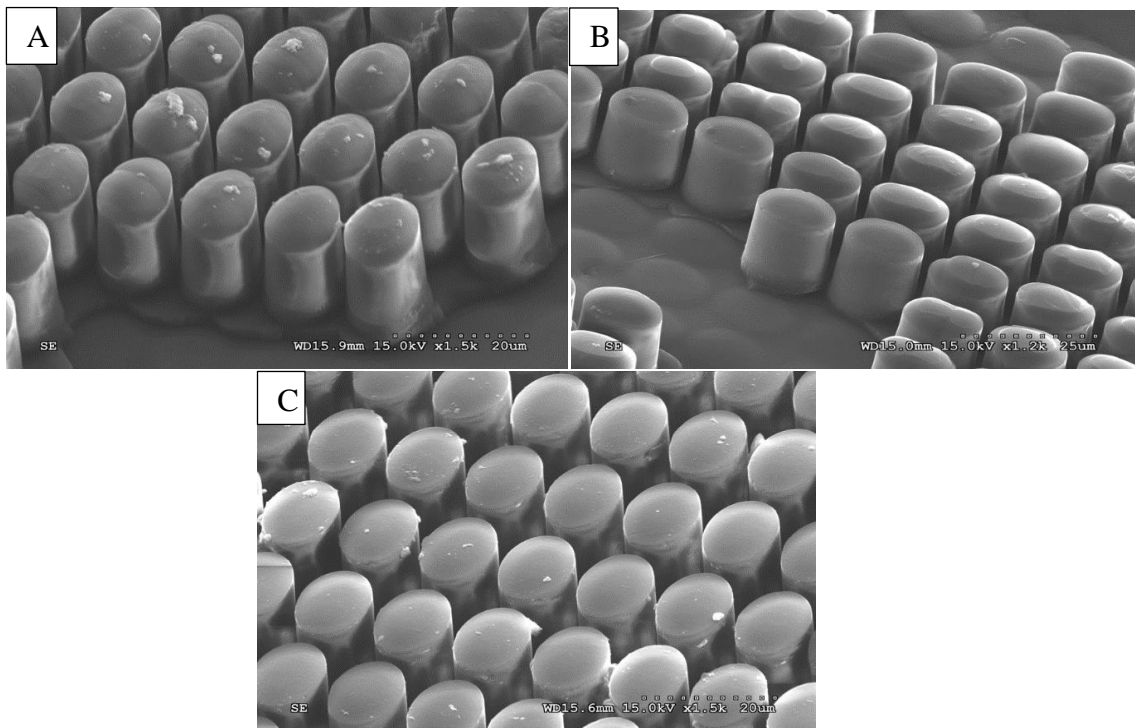


Figure 6-12: 15µm TPU Oval pillars molded at packing pressure of 15 MPa (A), 20 MPa (B), 25MPa (C).

### 6.1.2.2 Cooling Time

Cooling time is a significant factor when molding micro/nano scale features as it affects the solidification of the polymers in the micro cavities and the subsequent

demolding of the parts. During the injection process, the molecules get oriented due to the flow. Shorter cooling time will not allow the molecules to completely solidify in and cause elongation. On the other hand, longer cooling time will allow the molecules to relax and minimize elongation during demolding. If the demolding is performed before the mold reaches the recommended temperature, pillar stretching can be expected. The optimal cooling times were numerically simulated in a previous study [114,115]. The cooling time were varied between 15 sec and 88 sec in the experiments.

The effects of cooling time on molded pillars with different geometries were investigated utilizing two tools (Tool I&II). At the lowest cooling time, the micro pillars were stretched to a higher degree for tool I (oval cavities) due to both adhesion and friction forces as shown in Figure 6-14-A. The micro pillars had a mushroom like shape due to surface adhesion to the mold when the parts were molded in tool III (cylindrical cavities) as seen in *Figure 6-13 A*. At longer cooling times the features were replicated with minimal distortion for both tools. The stretching of the pillar was studied as a function of cooling time and the results presented in Figure 6-15. The height of the pillars fabricated using tool I were stretched by ~23% ( $4.95 \pm 0.005 \mu\text{m}$ ) when parts were demolded after 15 seconds cooling time. The extent of stretching decreased with increasing cooling time and it was ~1.25% when cooling time was increased to 88 seconds.

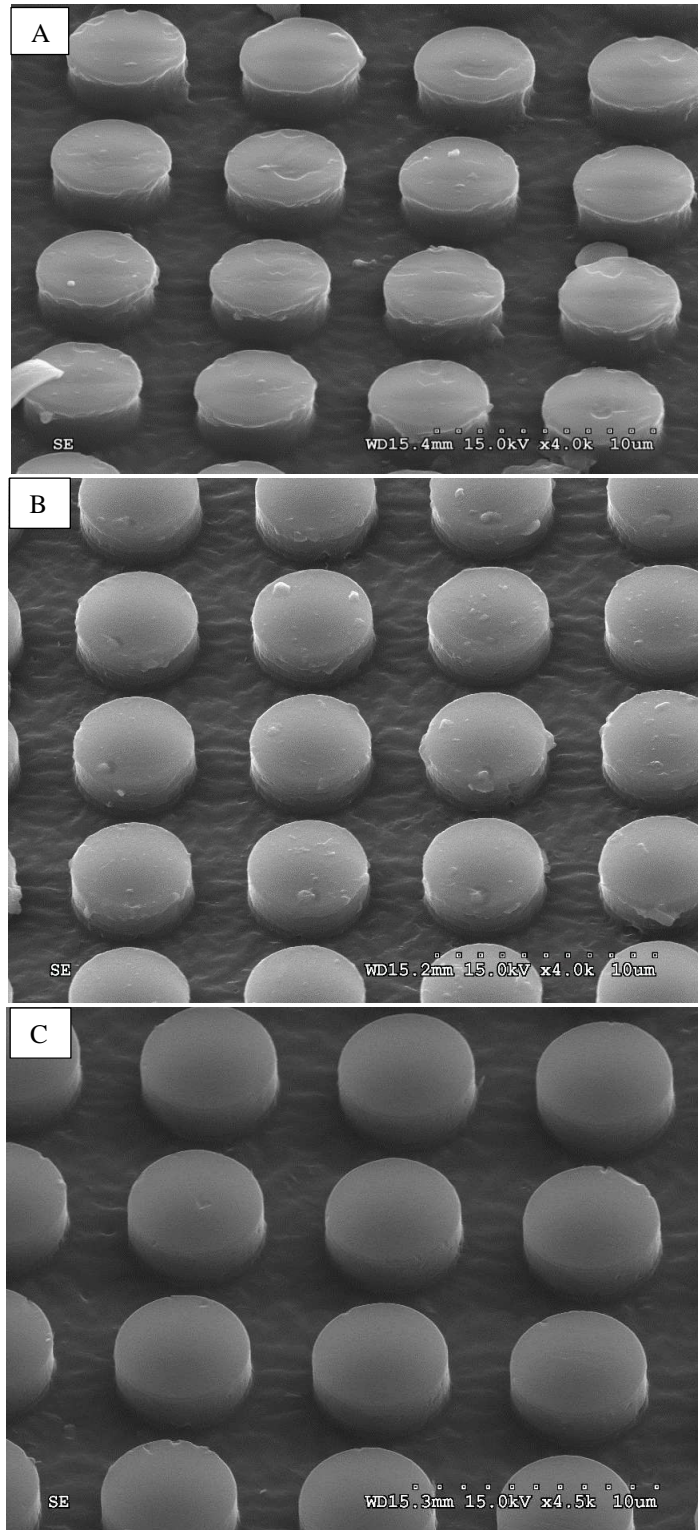


Figure 6-13:5µm TPU micro pillars A) 15 Sec, B) 60 Sec, C) 88 Sec cooling time.

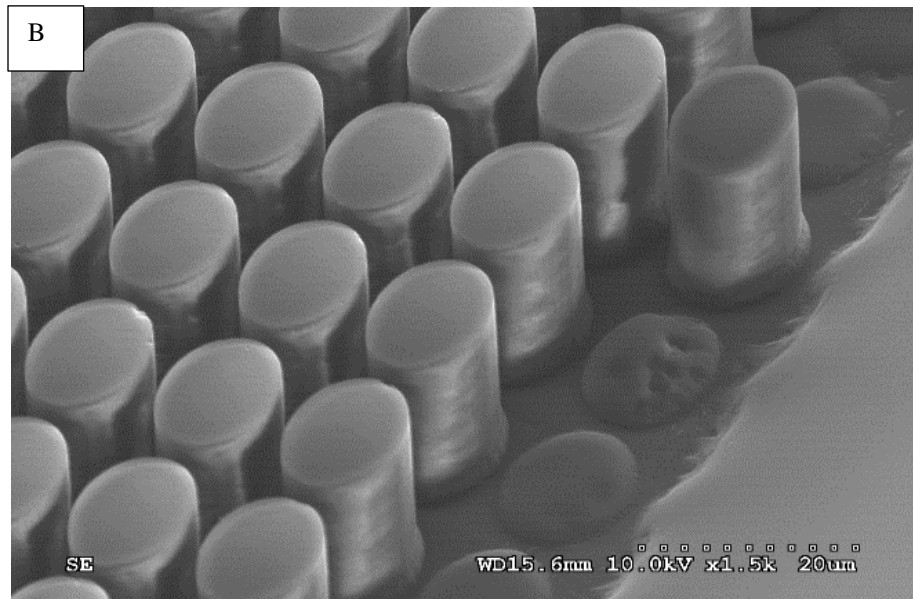
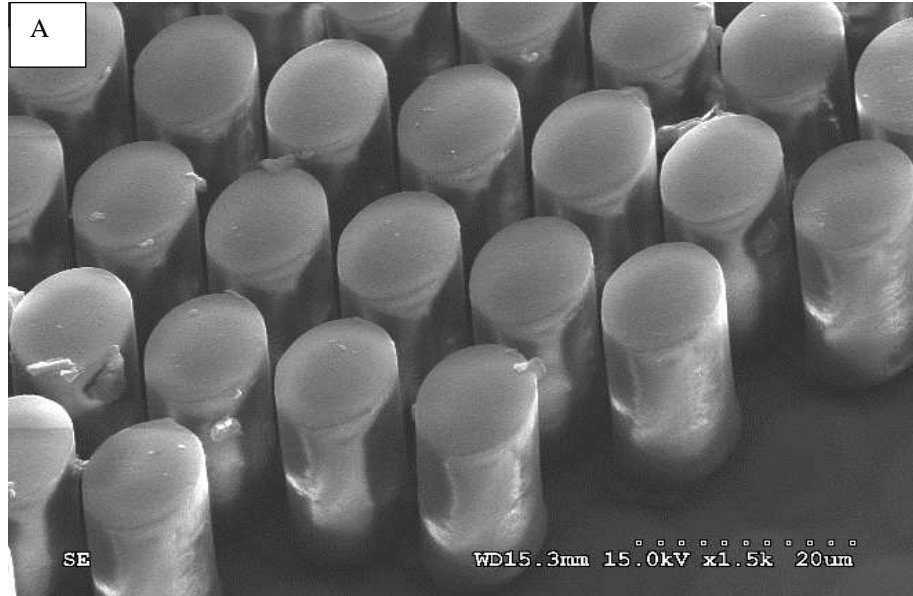


Figure 6-14: 15 μm TPU Pillars A) 15 Sec B) 88 Sec cooling time.

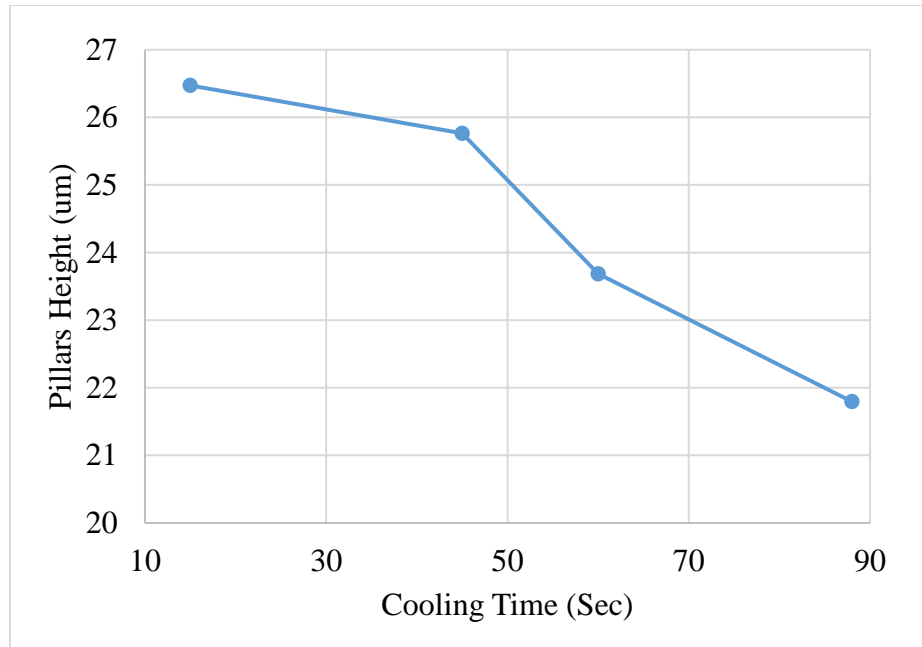


Figure 6-15: 15  $\mu\text{m}$  TPU oval pillars height demolded after 15, 45, 60, and 88 Sec cooling time.

### 6.1.2.3 Antistiction Coating

Part demolding is one of the essential stages in micro injection molding as the created geometries can be distorted if the demolding is not performed properly. It was established that the interactions between the polymer and the mold insert influence the failure of created micro patterned features during the demolding process in a significant way. To understand the role of antistiction coating for the specific materials (silicon mold and Texin 985) utilize in this study, several molds were fabricated without the antistiction coating. The cooling times were varied between 15 and 45 seconds to find the optimal conditions for demolding with minimal distortion of the features. At lower cooling time (15 seconds), the micro pillars were successfully demolded with minor distortion to the top surfaces of the pillars due to adhesion (Figure 6-16). Pillar adhesion was negligible when increasing cooling time to 45 seconds. However, the interactions between the sidewalls

and the pillars were high during demolding causing the polymer to chip and silicon mold breakage after a few cycles.

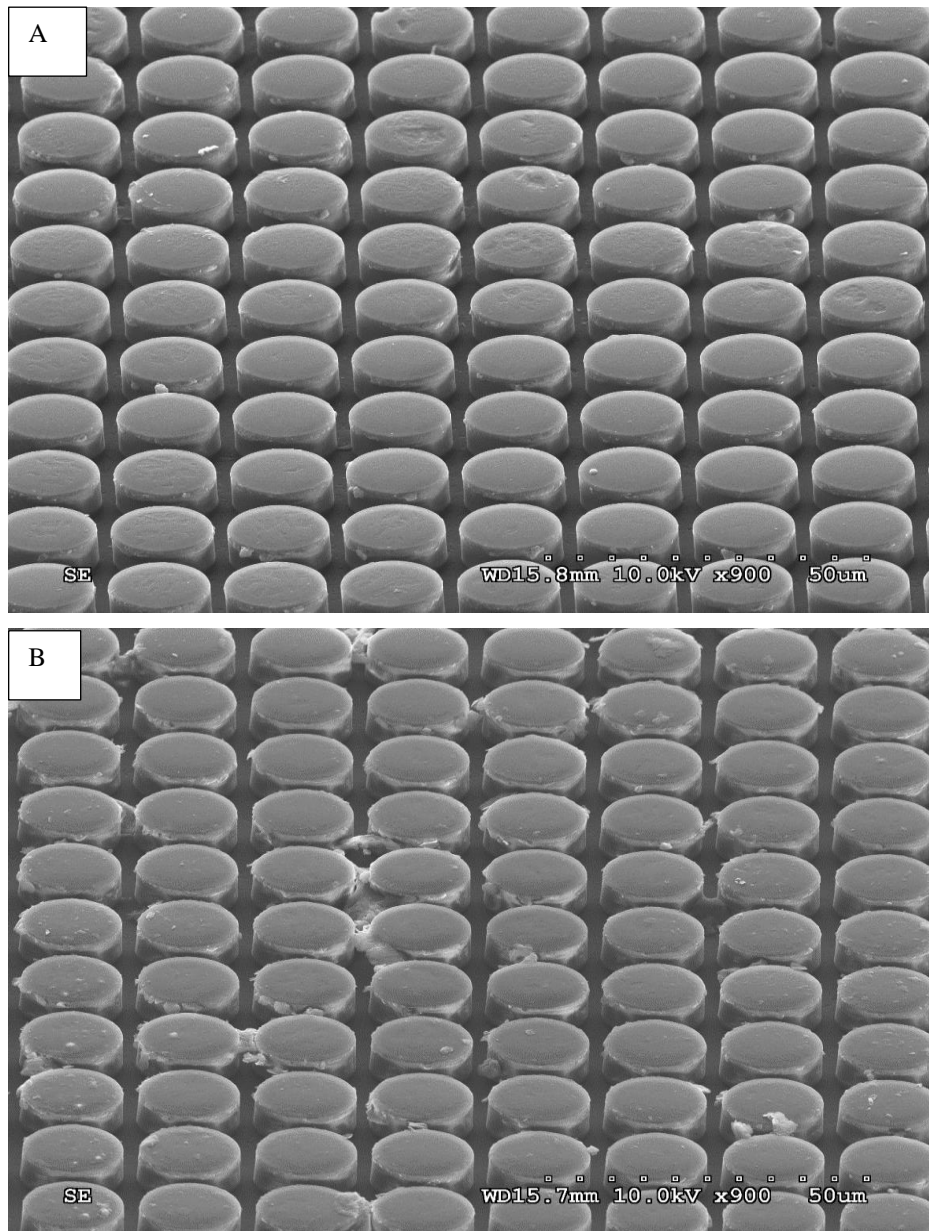


Figure 6-16: TPU 15µm micro pillars. A) 15 sec cooling time. B) 45 Sec Cooling time (Scale Bar is 50µm).

The role of packing pressure, cooling time, and antistiction coating on the quality of replication of the micro features as well as preserving the features during the demolding was studied. It was observed that a 25 MPa packing pressure was sufficient for this specific material (Texin 985) and setup for replication of the micro features. Cooling time had an essential effect on replication quality in terms of final dimension and the ability to remove the parts from the mold successfully. Molding micro pillars without antistiction coating resulted in pillars adhesion to the mold when the cooling times were lower, although it was possible to demold the part. When the cooling time was increased the silicon mold failed after a few cycles because of the high frictional forces during demolding.

#### **6.1.2.4 10 um features replications**

The replication of 10 um oval micro cavities were examined here using TPU TEXIN 985. Packing pressure was set at 25 MPa as described earlier to confirm the highest replication rate. Pillar height was measured using ImageJ and found to be 10.02 um. Higher replication was achieved as seen in Figure 6-17 with recommended processing parameters and cooling time.

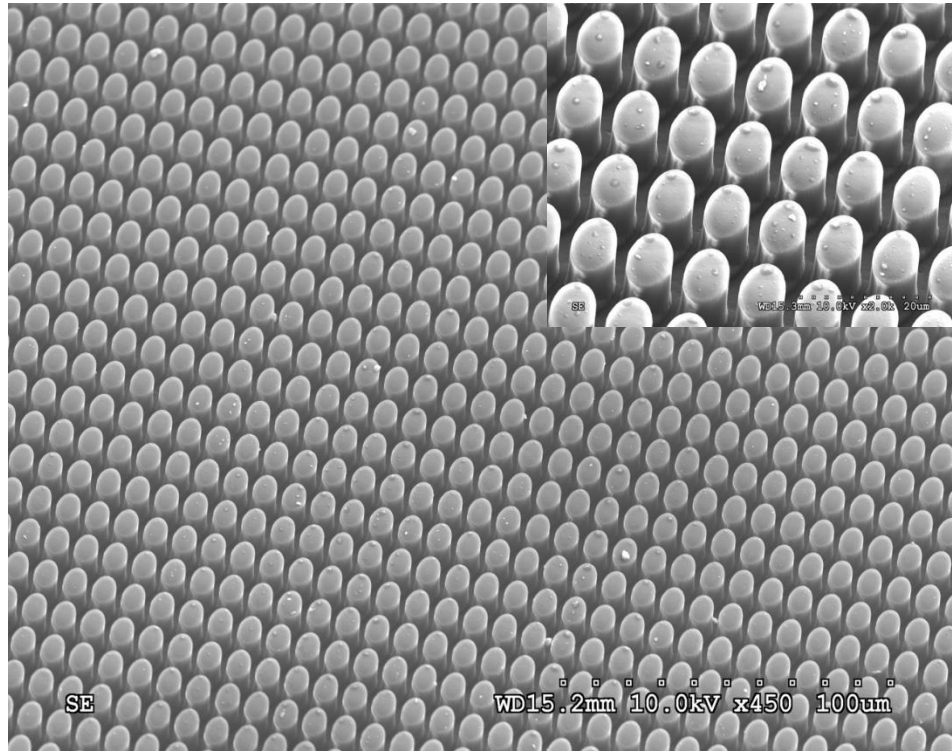


Figure 6-17: 10 um oval pillars with 10.02 um height.

#### 6.1.2.5 Replication uniformity over 6 X 6 mm Si wafer insert

Unsupported micro features were fabricated over 6 X 6 mm Si insert with 15 $\mu$ m diameter and 15.03 um depth. Replication quality over targeted area was affected by cooling time that was previously described, pillars were completely ejected from microcavities without distortion or damage as shown in

Figure 6-18. Pillars molded with lower cooling time stretched around 12% (16.823 um height). While higher cooling time results in 1.25% stretch (15.218 um height).

Figure 6-20 shows SEM images of 9 regions (

Figure 6-19) of TPU molded sample with high replication rate. Features at the center of the melt flow show that ejection force was minimal resulting in better micro pillars demolding.

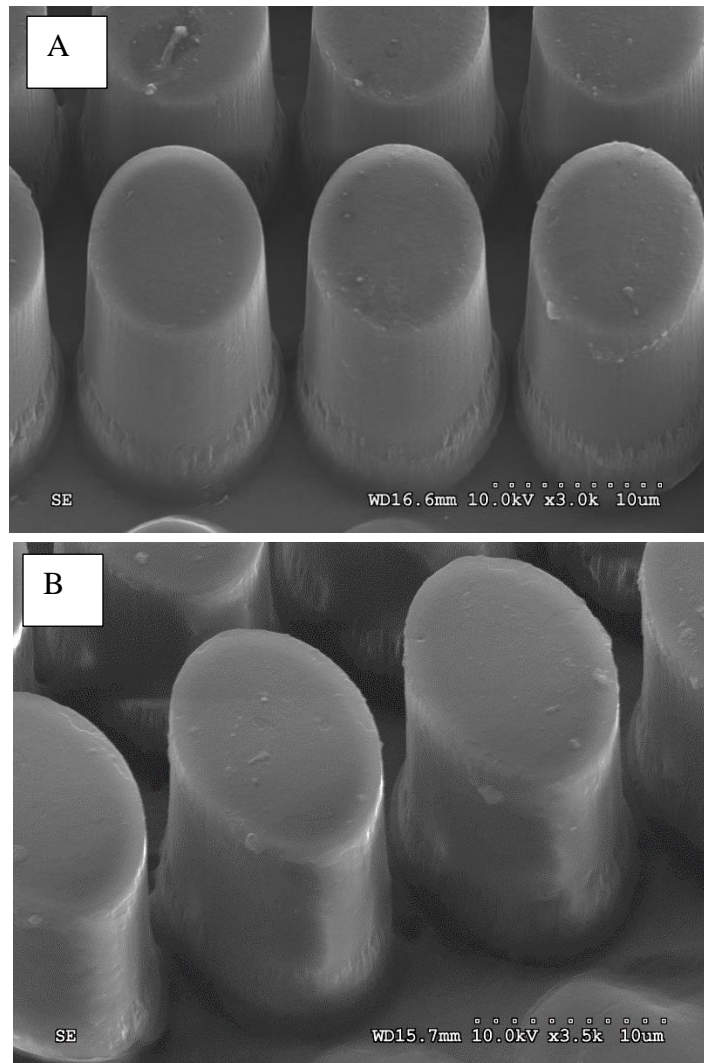


Figure 6-18: TPU molded sample with 15um at A) 15 sec, B) 88 sec cooling time.

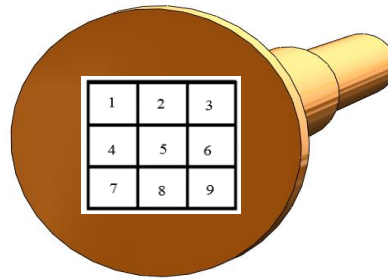


Figure 6-19: CAD model of molded part show the 9 regions that SEM were taken.

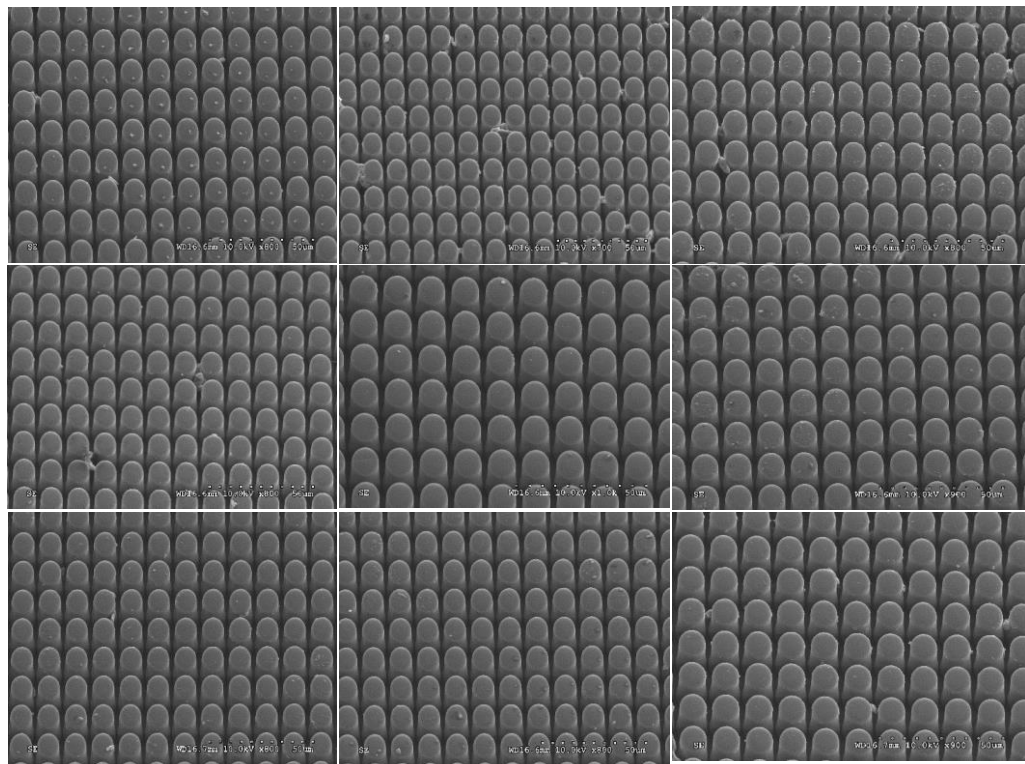


Figure 6-20: SEM Images of 9 regions of molded sample.

### 6.1.3 Low-Density Polyethylene (LDPE)

Experiments were done using LDPE CP 851 to fill micro cavities shown in Figure 6-21. The experiments were performed utilizing the molding parameters in Table 6-4, the

packing pressure was increased in successive trials starting with the recommended pressure to fill the targeted micro cavities completely.

Table 6-4: Moldflow recommended molding parameters for LDPE CP 851.

Material	LDPE
Velocity (mm/sec)	134.8
Injection Pressure (Mpa)	10.56
Packing pressure (MPa)	7.916
Tmelt (°C)	168.5
Tmold (°C)	36
Cooling time (Sec)	42

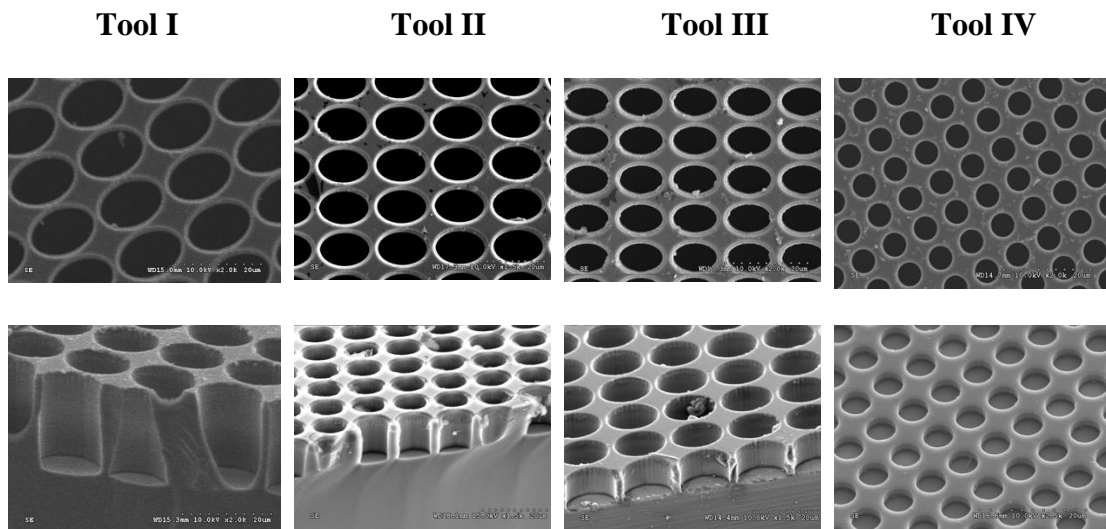


Figure 6-21: Silicon Mold inserts with Oval shapes with 15µm Diameter and 21.5, 15.03 µm depth (Tool I &II ), 10 µm diameter with 10.02 µm depth (Tool III) and Cylindrical shapes with 5 µm diameter and 2.49 µm depth (Tool IV) (Scale Bar is 20 µm).

Replication ratio was found optimal in the case of Tool I when increasing packing pressure to 30 MPa. Both injection and packing pressures were increased above recommended values to achieve better filling. Injection pressure was set at 20 MPa for all

trails using LDPE CP 851. SEM image shows that micro cavities were completely filled as shown in *Figure 6-22*. Replication rate of 0.99 was achieved using given molding parameters.

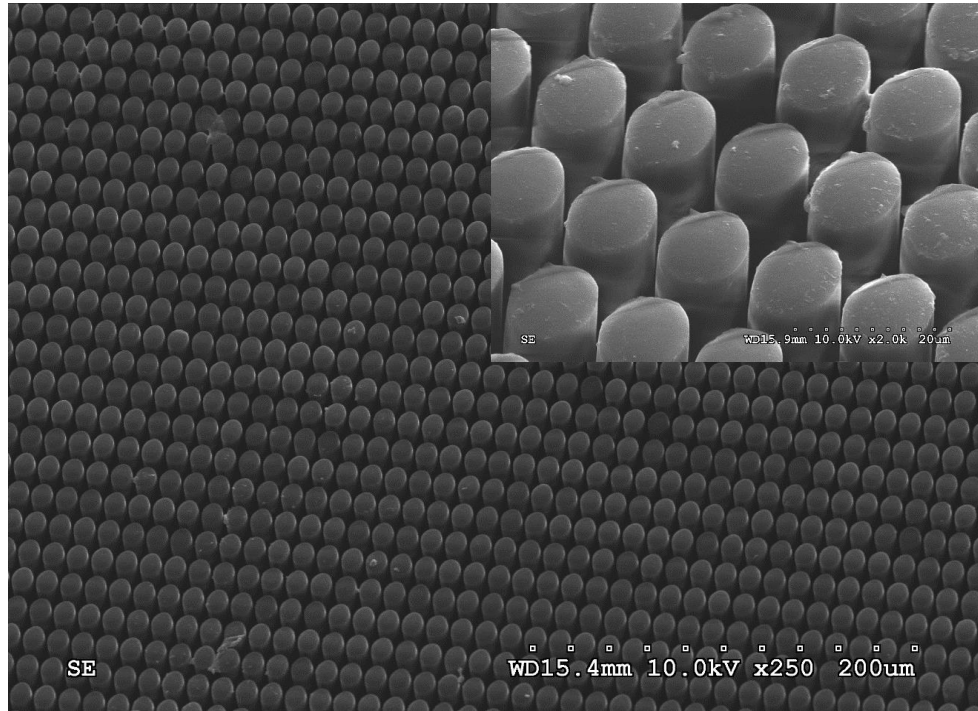


Figure 6-22: 15  $\mu\text{m}$  diameter with 21,391  $\mu\text{m}$  height LDPE.

Packing pressure was kept at 20 MPa when molding with Tool II, III, and IV and micro cavities were highly detailed as shown in Figure 6-23Figure 6-24Figure 6-25. Replication rate were found high for all LDPE molding trails with negligible pillar distortions.

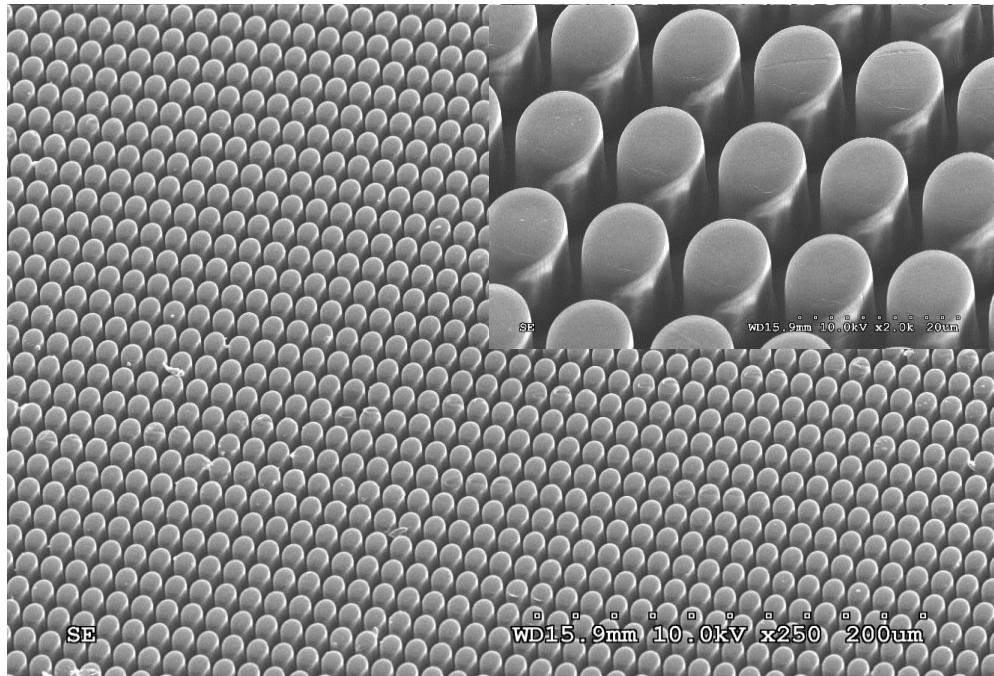


Figure 6-23: 15  $\mu\text{m}$  diameter with 15.09  $\mu\text{m}$  height

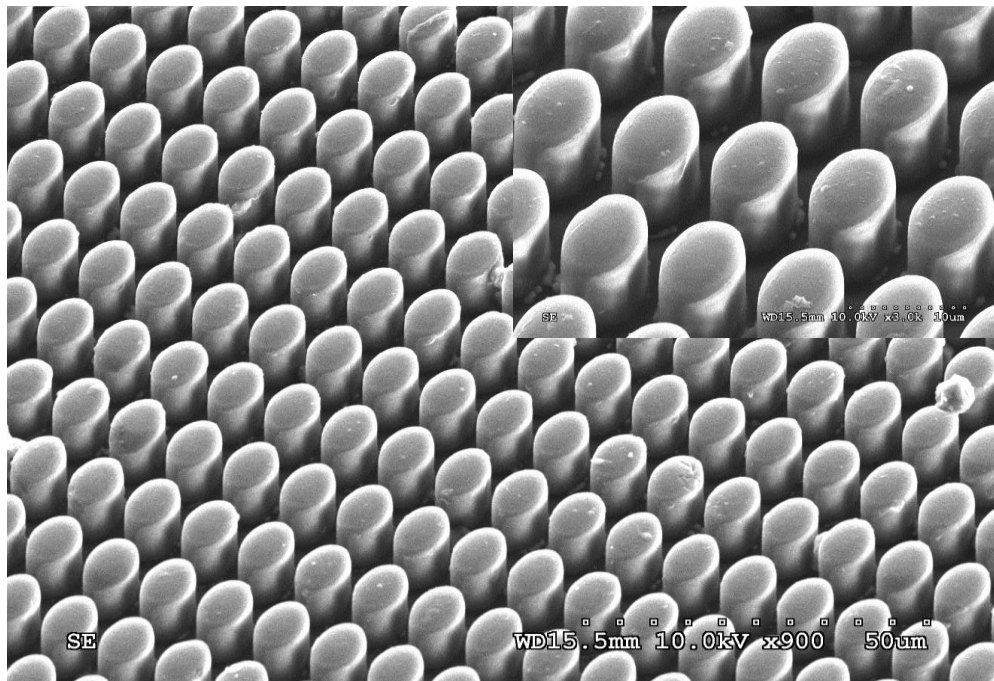


Figure 6-24: 10  $\mu\text{m}$  diameter with 10.031  $\mu\text{m}$  height.

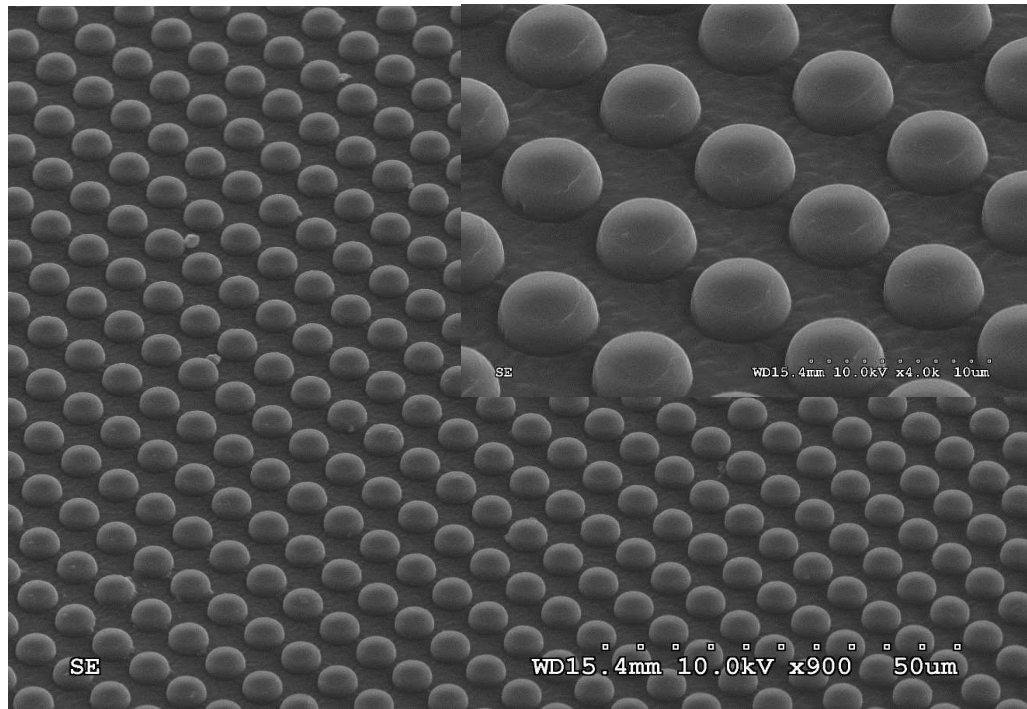


Figure 6-25: 5  $\mu\text{m}$  diameter with 2.434  $\mu\text{m}$  height.

#### 6.1.4 High-Density Polyethylene (HDPE)

Molding trials with HDPE were done to validate the replication of Si mold in *Figure 6-21*. Injection pressure was increased to 20 MPa with 15 MPa for packing pressure with recommended molding parameters in Table 6-5. Filling of tool I was not done completely as shown in *Figure 6-26* at the first. By increasing the packing pressure to 25 MPa, micro cavities were entirely replicated (*Figure 6-27*). When lowering cooling time to 15 second, pillars stretched as a result of frictional forces during demolding to 22.56  $\mu\text{m}$  (5.1% longer).

Table 6-5: Moldflow recommended molding parameters for HDPE HD 6733

Material	HDPE
Velocity (mm/sec)	134.8
Injection Pessure (Mpa)	10.56
Packing pressure (MPa)	7.916
Tmelt (°C)	195
Tmold (°C)	37
Cooling time (Sec)	33

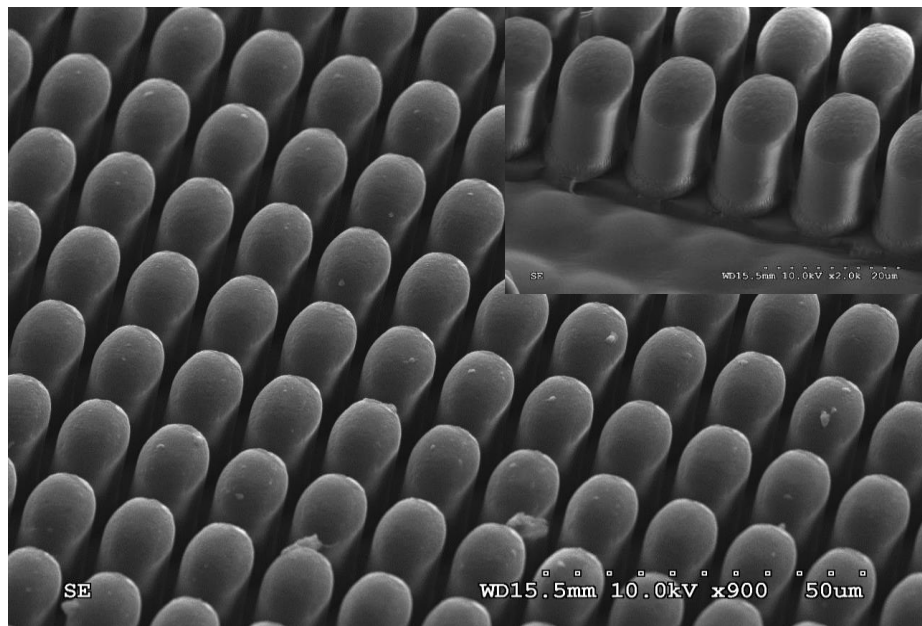


Figure 6-26: 15 um diameter with 19.833 height with lower packing

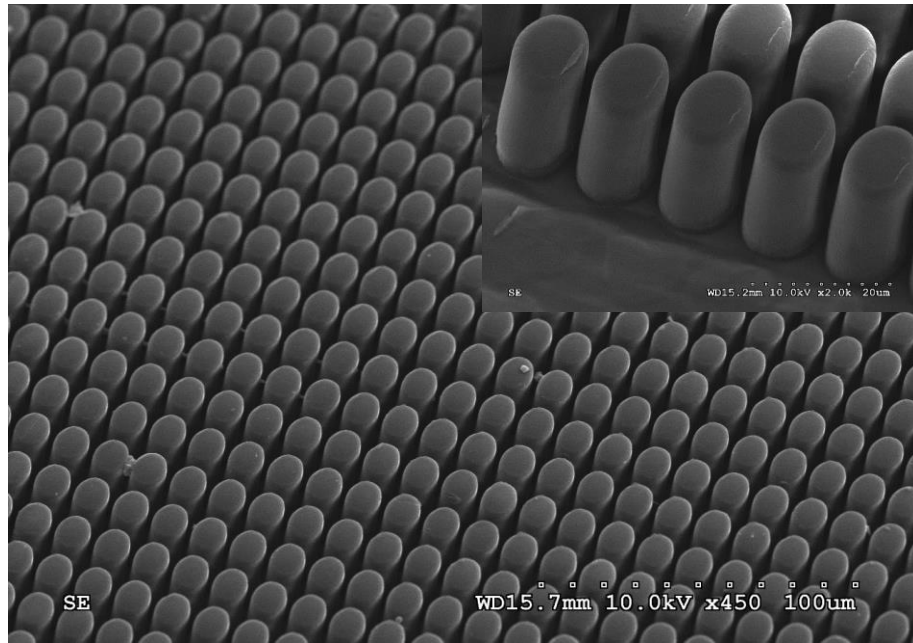


Figure 6-27: 15um diameter with 21.41 um height with 33 sec cooling time.

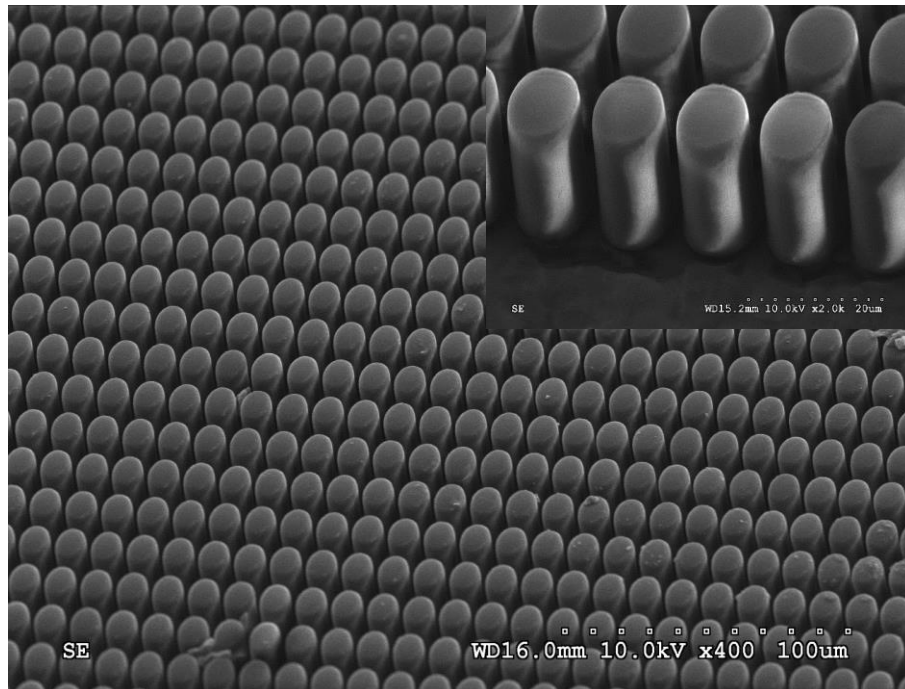


Figure 6-28: 15 um diameter with 22.56 at 15 sec cooling time

When replicating 15  $\mu\text{m}$  pillars molding parameters were kept that same as in Table 6-5 with increasing the injection pressure and packing pressure to 20, and 25 MPa respectively. It was observed that pillars were found to replicate the fine edges of the micro cavities as shown in Figure 6-29. Higher replication was also found in replicating 10  $\mu\text{m}$  features (Figure 6-30). In case of 5  $\mu\text{m}$  microcavities (Figure 6-31), micro pillars were demolded with minor damages to the sides compared to the 15, and 10  $\mu\text{m}$  pillars.

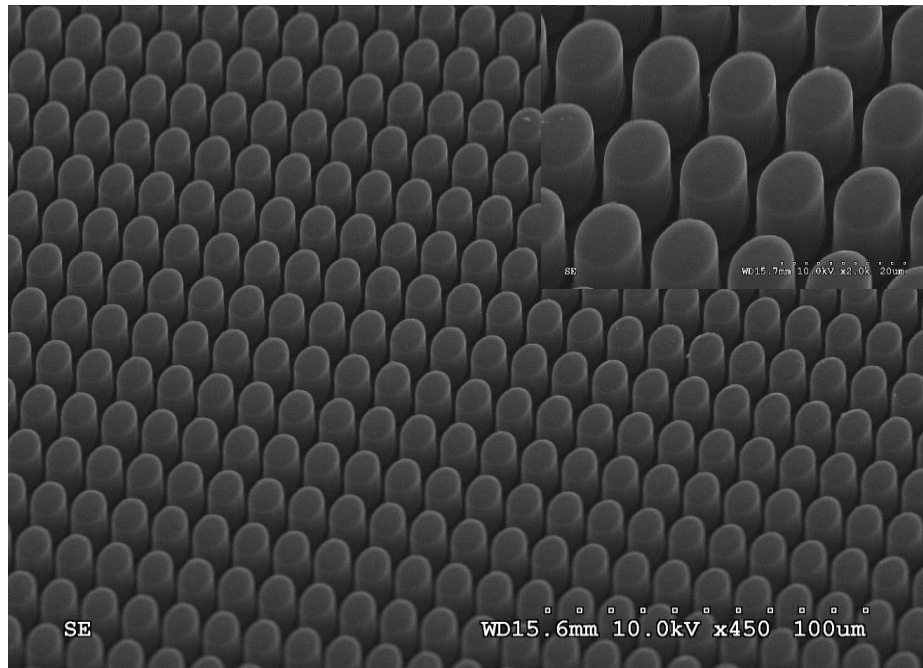


Figure 6-29: 15  $\mu\text{m}$  diameter with 15.263  $\mu\text{m}$  height.

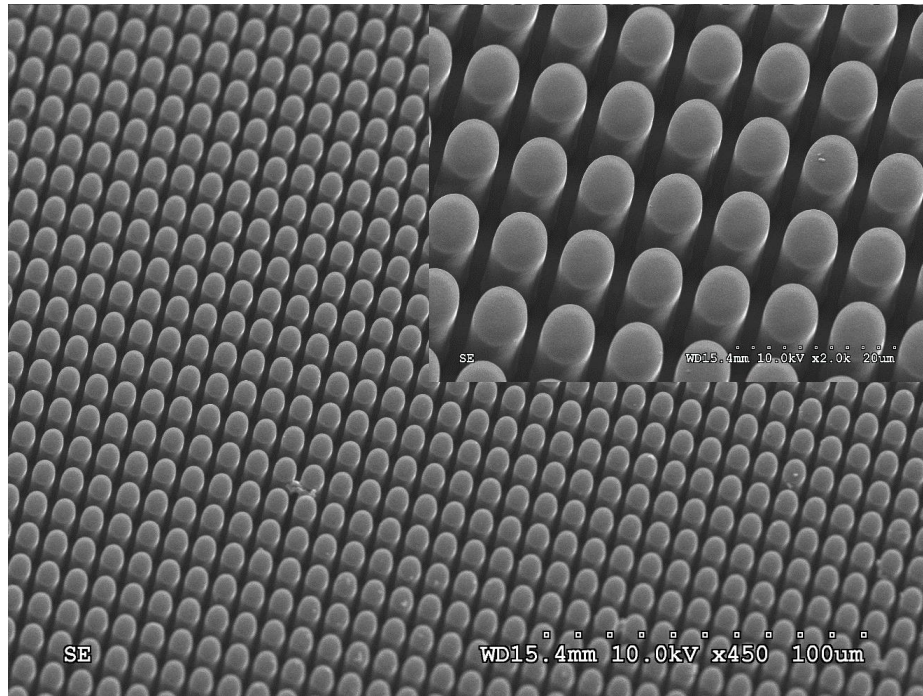


Figure 6-30: 10 um diameter with 10.049 um height.

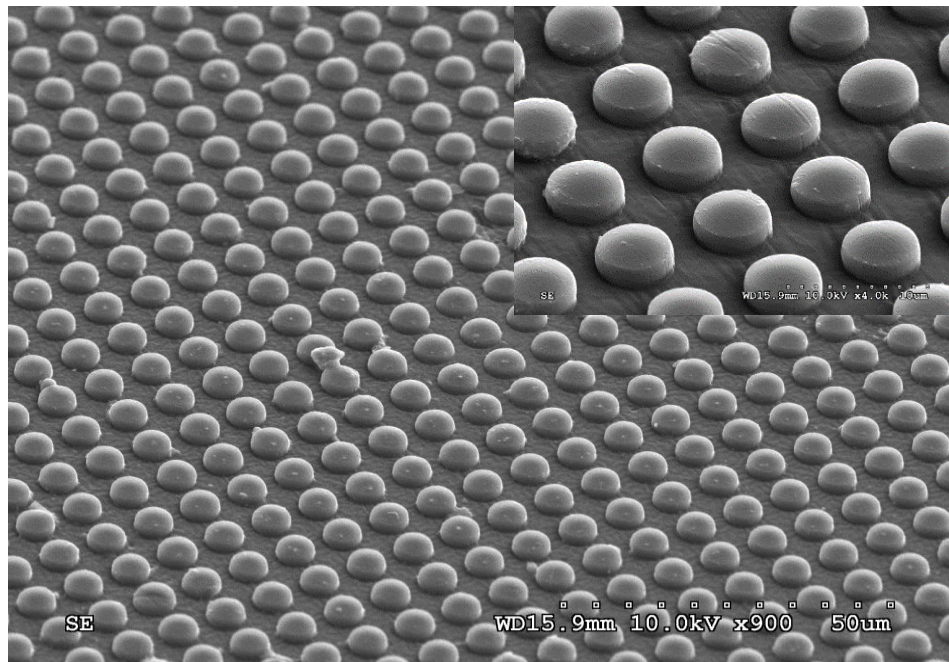


Figure 6-31: 5um diameter with 2.389 um height

### 6.1.5 Cyclic Olefin Copolymer (COC)

Molding parameters used in this trial were derived from Moldflow simulations described in Chapter #5 (Table 6-6). It was noticed that filling depth was not complete when the mold temperature,  $T_{\text{mold}}$  was 100 °C as shown in Figure 6-32-Figure 6-33. When increasing  $T_{\text{mold}}=125$  °C, COC melt start to replicate the micro cavities totally (Figure 6-34). Packing pressures were needed to increase to 15 MPa for 5 um features and 30 MPa for 15 um features to achieve high filling rate. Due to high frictional forces between micro cavity sidewalls and COC pillars (high  $E=3200$  MPa) Si mold with 15 um oval cavities failed after a few cycles. Injection velocity was kept at 150 mm/sec during these experiments for machine safety purposes.

Table 6-6: Moldflow recommended molding parameters for TOPAS 5013S-04.

<i>Material</i>	<i>COC</i>
<i>Velocity (mm/sec)</i>	350.6
<i>Injection Pessure (Mpa)</i>	1.929
<i>Packing pressure (MPa)</i>	1.44
<i>Tmelt (°C)</i>	270
<i>Tmold (°C)</i>	100-125
<i>Cooling time (Sec)</i>	114

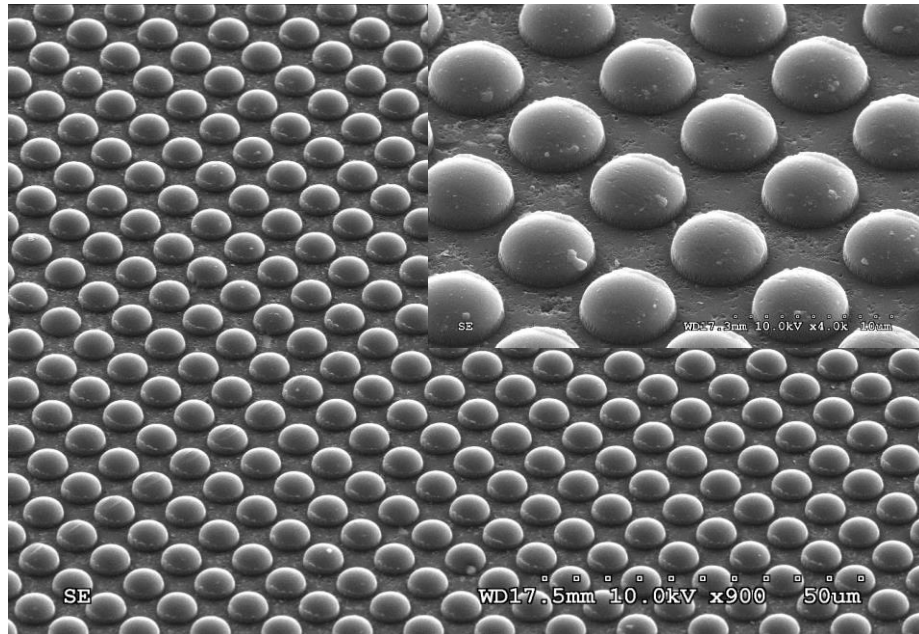


Figure 6-32: 5um diameter with 1.808 um height.

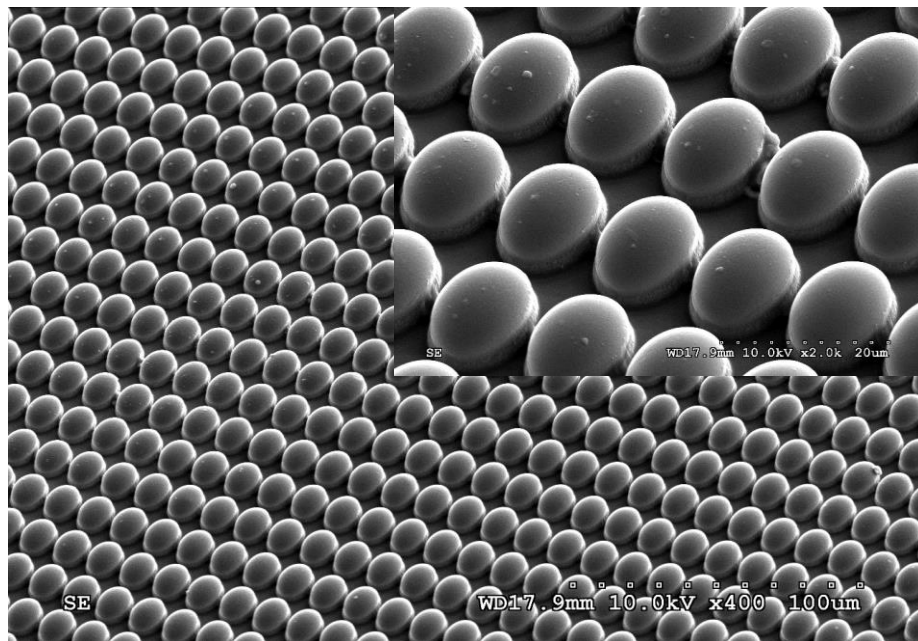


Figure 6-33: 15 um diameter with 5.172 um height.

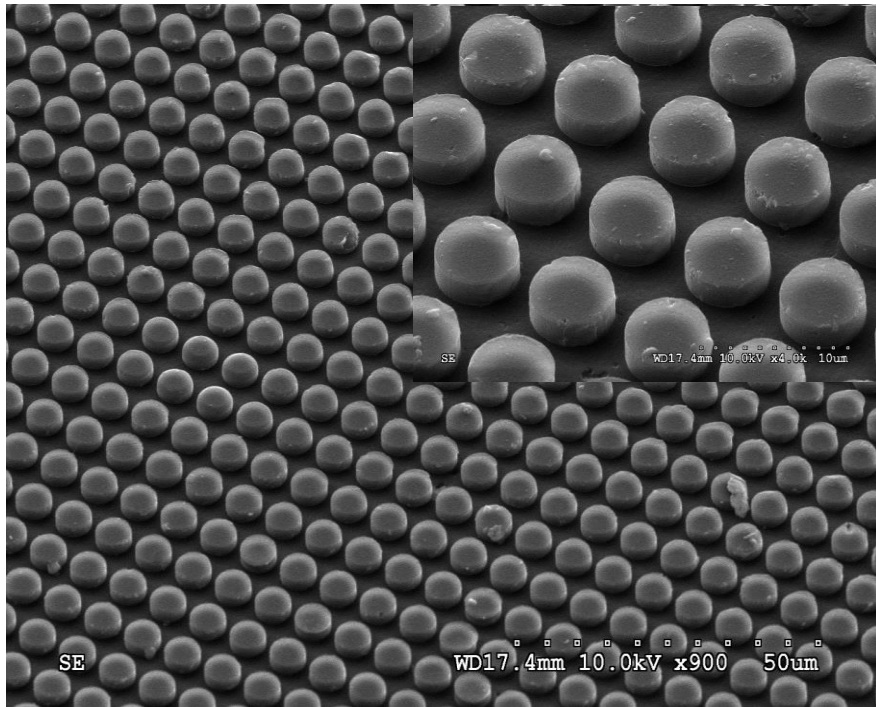


Figure 6-34: 5um diameter with 2.283 um height.

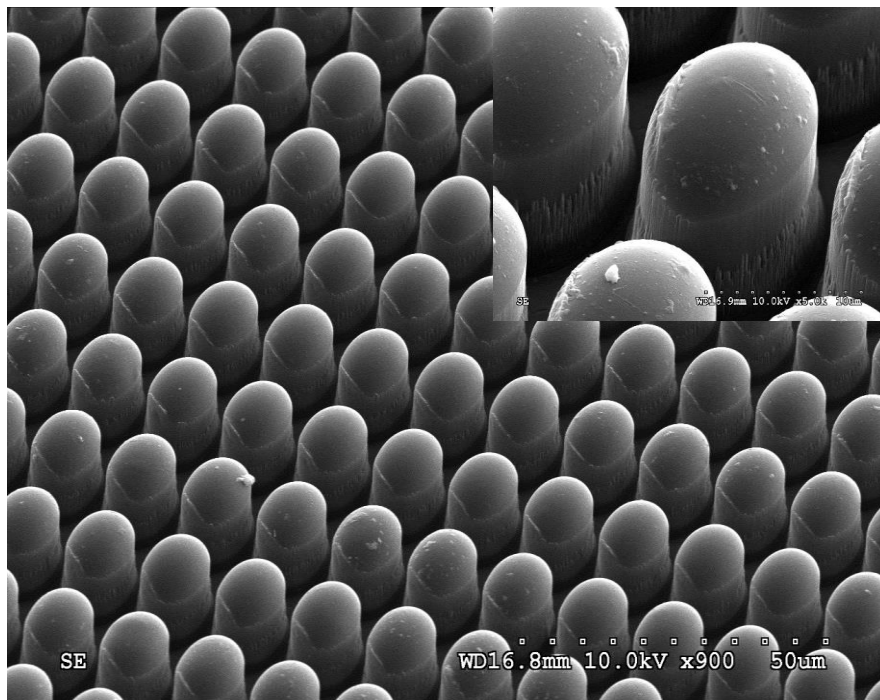


Figure 6-35: 15 um diameter with 11.325 um height.

## 6.2 Mold Modification

The mold design was modified to reduce the sprue size of injection molded parts in an attempt to reduce materials usage and cycle time. Both of these can lead to significant cost savings for large volume industrial production of parts with micron scale surficial features. Based on the simulations done in this research effort as described in chapter 4, sprue size was modified to reduce cycle time by 35%. Original sprue diameter as shown in Figure 6-36 is 5.6 mm (0.22in) near the gate then tapered with 1° angle towards the second part of the sprue that has 3.3 mm (0.13 in) diameter and also tapered with 1° angle towards the nozzle.

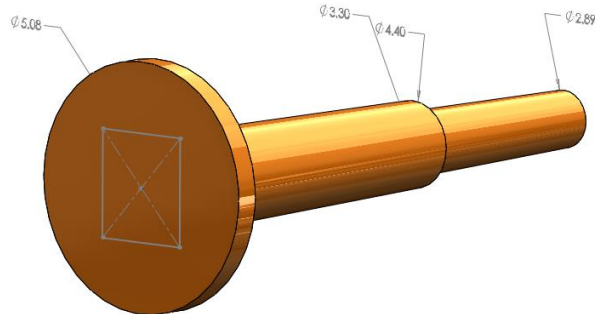


Figure 6-36: CAD Model for a molded part with sprue size.

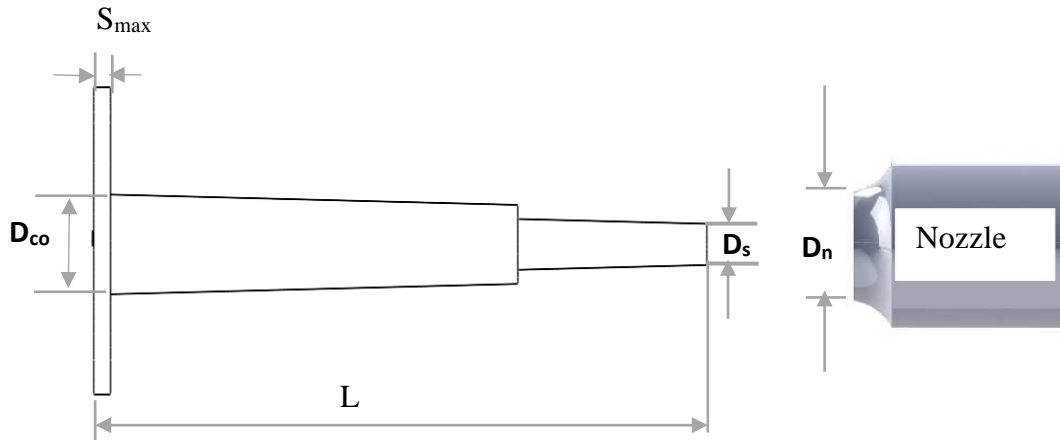


Figure 6-37: Sprue diameter configuration.

Mold modification was done based on equations below (*Figure 6-37*) [116]. Where mold cavity thickness  $S_{\max} = 1.27$  mm, Nozzle diameter  $D_n = 1.4$  mm was given from machine Nissei AU3E manual.

$$D_{co} \geq S_{\max} + 1.5 \text{ mm}$$

$$D_s \geq D_n + 1.0 \text{ mm}$$

$$\alpha \geq 1^\circ - 2^\circ$$

$$\tan \alpha \geq D_{co} - D_s / 2 L$$

Calculated sprue gate  $D_{co} = 4$  mm based on cavity depth  $S_{\max} = 1.27$  mm. then tapered towards the nozzle with an angle  $\alpha = 1^\circ$  with high finish to ease demolding of molded part. Sprue diameter in contact with the nozzle bushing is  $D_s = 2.03$  mm.  $D_s$  has to be smaller than nozzle diameter  $D_n$  to prevent flash and seal the contact area.

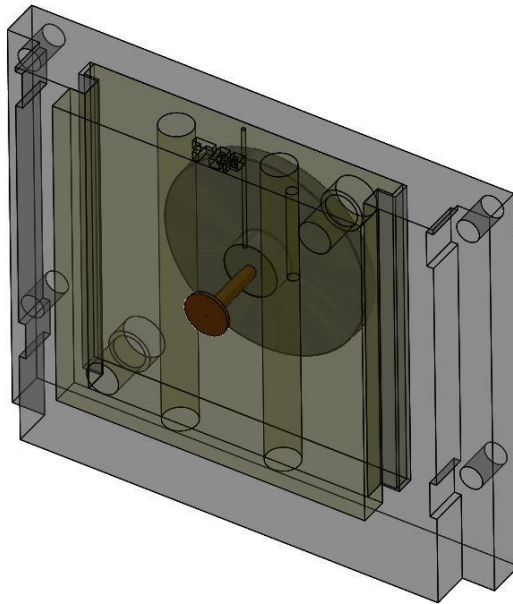


Figure 6-38: Nozzle bushing configuration with mold plate (yellow) and molded part (orange).

### 6.3 Experimental validation

Micro cavities mold with 5 $\mu$ m circular diameter were chosen for this study because it was observed from previous experiments that 5  $\mu$ m pillars showed a huge dependency to the cooling time. The cooling time for the original sprue was 88 second. When using the modified smaller sprue using the cooling time was then reduced to 57 seconds for polystyrene as recommended from Moldflow simulations. It was found a great agreement with the new cooling time. Pillars were precisely demolded at faster cooling time of 57 second as shown in Figure 6-39 with no damage compared to pillars where molded with original sprue.

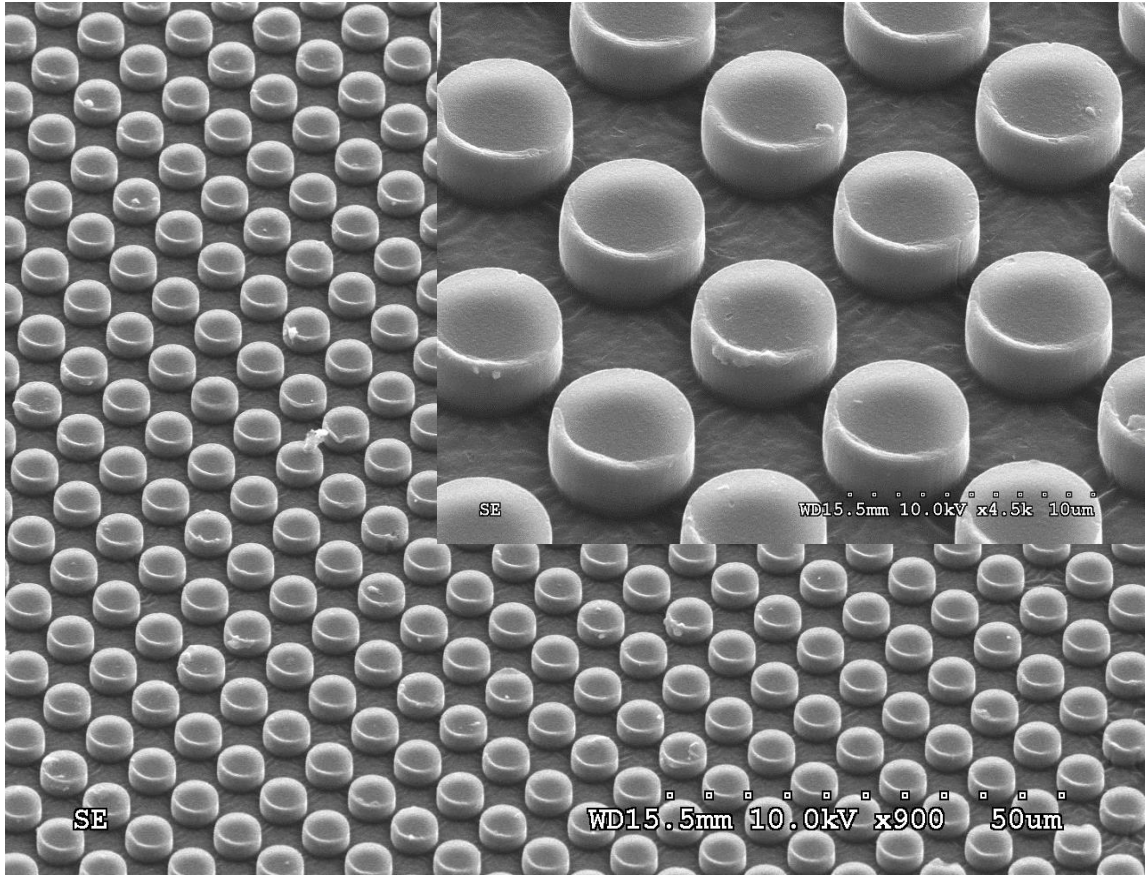


Figure 6-39: SEM image of Molded pillars with 5  $\mu\text{m}$  diameter

### 6.3.1 Atomic Force Microscope (AFM) Characterization

AFM Scan was done using Bruker instrument with Scan Asyst that adjusts image parameters (setpoint, gain, scan rate) to optimize image quality. Silicon nitride cantilever with silicon tip radius of 2 nm with stiffness ( $k$ ) of 0.4N/m. Scan rate was 0.977 Hz over an area of 35x35  $\mu\text{m}$  as shown in Figure 6-40. Pillars height was measured at 2.5  $\mu\text{m}$  with top pillar surface roughness of 12.8 nm (*Figure 6-41*).

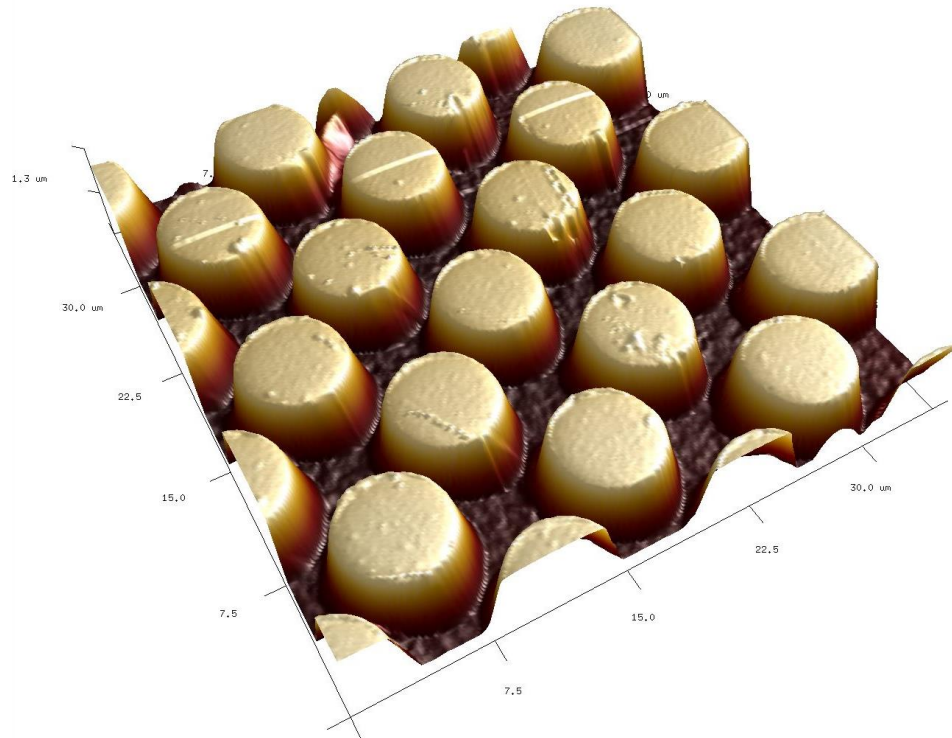


Figure 6-40: AFM image of molded pillars with 5µm diameter.

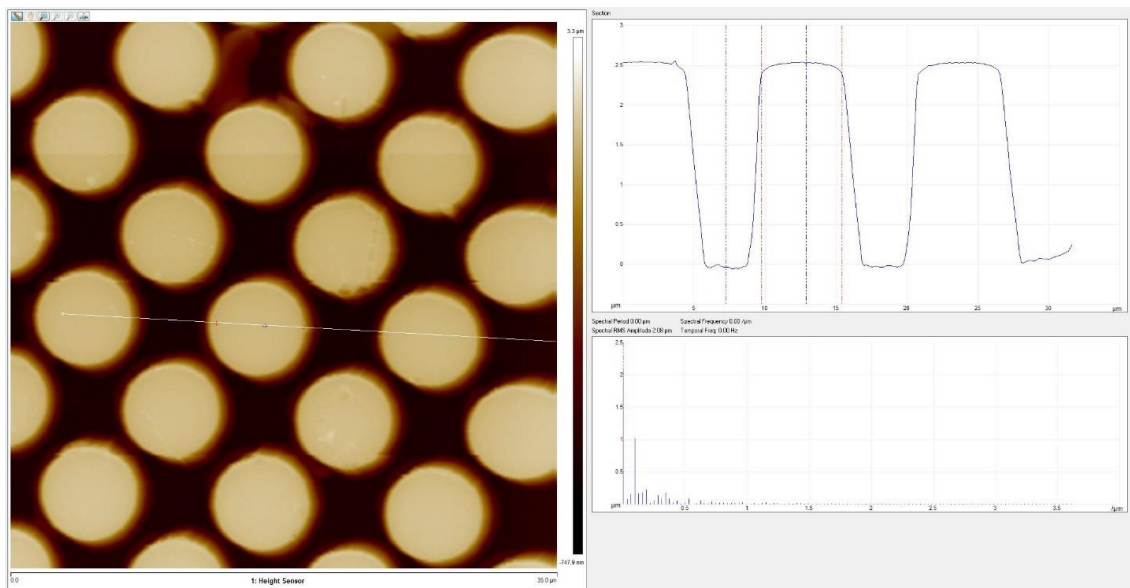


Figure 6-41: Cross sectional measurement of AFM scanned image.

## 6.4 Conclusion

Moldflow<sup>®</sup> has proven to be a valuable tool providing insight in the micro-molding process and an initial set of processing parameters for the experiments. It provides a preliminary analysis for the filling stage analysis, recommendations for V-P switchover setting. The initial processing parameters provided an efficient strategy to optimize the processing for precise replication of the micro features by reducing the number of trials that needed to be performed. If the parameters were to be optimized on an empirical basis the number of trials need would have been a few orders of magnitude higher than what was performed in this research.

Processing parameters, such as mold temperature, filling velocity, and cooling time were determined to impact the final product quality and replication capability at the micro-scale significantly. This work found that cooling time had a significant effect on replication quality in terms of final dimension and the ability to remove the parts from the mold with minimal distortion. The polymeric material had an important role as well. PS and COC showed signs of distortion due to a strong adhesion between the Si mold and material during demolding stage. The other polymers (TPU, LDPE, and HDPE) demonstrated pillar stretch at lower cooling times due to material relaxation time that is needed before demolding. At the lowest cooling time, the micro pillars were stretched to a higher degree of the micro cavities while higher cooling time maintain the micro cavities depth. Small micro pillars (5 $\mu$ m circular diameter) experienced huge distortions at lower cooling time instead of stretching when using polystyrene as the molding material.

It was observed that a 25-40 MPa packing pressure was sufficient for replication of the micro features at this scale depending on the molding material.

A major issue that may occur during demolding at the micro/nanoscale is stiction of the material to the cavities, and the friction occurs between the sidewalls and the material. Stiction occurrence may be reduced by increasing the amount of sputtering time of the C4F8 as a coating layer in the final step. The demolding procedure must ensure that the molded product is removed perpendicularly out of the mold. At the micro/nanoscale, any shear forces may damage the replicated geometries. Molding micro pillars without antistiction coating using Texin 985 was possible at lower cooling time with signs of pillars adhesion to the mold while increasing the cooling time led to silicon mold breakage during molding experiments due to high frictional forces during demolding.

## CHAPTER 7: MANUFACTURING COST ANALYSIS

### 7.1 Market Size

Micro injection molding is a process requires specialized molding machines capable of high injection speed with precise control pressure. The demand of micro features in several of applications including medical, electronics, telecom, and automotive is driving the micro injection molding market. According to Grand View Research, Inc. the global market of micro injection molding is projected to reach \$897 million by 2020[117]. Medical application for micro injection molding represented one-third of total market in 2012 (Figure 7-1)and expected to rise up 15.2% by 2020[118]. Thus, there is an extensive need for medical micro molded parts that are innovatively designed and made to satisfy the market needs.

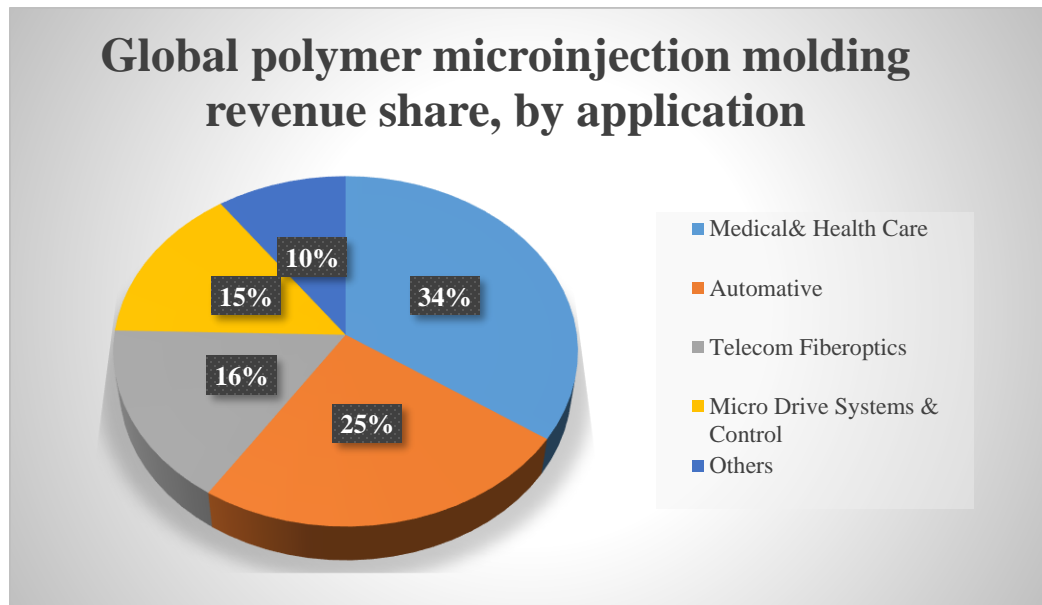


Figure 7-1: Global microinjection polymer molding revenue share by application [7].

## **7.2 Potential Opportunity**

Micro injection is a low-cost process that can fulfill the requirements of biological testing and microfluidic devices. Molded substrates with controlled stiffness play an important role in cells mechanosensing to determine a proper microenvironment during the cell culture process. It has been recognized that substrate stiffness has a significant effect on traction forces as well as cell differentiation. Existing cell culture devices have been modified through biological coating (collagen, laminin, and fibronectin), synthetic nanofiber surfaces, and plasma treatment to enhance hydrophobicity, cell performance, and functionality. These advancements require an additional cost to main culture devices, special handling, and storage. Due to previous requirements these products are not widely commercialized. Molded substrates with controlled stiffness that are fabricated in this research could be proper advancement for existing cell culture petri-dishes. This product will not need any modification, extra preparation, or storage which makes it a great substitution to existing products with low cost and sufficient functionality.

## **7.3 Substrates Commercialization Considerations**

The use of polymeric substrates for biological cell development has gained a tremendous attention in the research community. As a result, several competing technologies/devices have been developed in a laboratory scale and in the process of commercialization currently. The micro/nanostructured polymeric substrates could be beneficial to bio laboratories performing cell cultures in many ways.

- It would provide an affordable solution for existing petri-dish since no modification or preparation would be needed.
- Thermoplastic injection molding will be utilized for the fabrication of this parts. It is an ideal fabrication tool with high throughput and low cycle time within seconds which is ideal for mass-production replicas as required for commercial manufacturer.

#### 7.4 Dimensional analysis

A dimensional analysis is a beneficial tool that used to find the cost of injection molded unit. The cost includes the cost of mold design (including material, fabrication) and the cost of machine labor per hours (Figure 7-2).

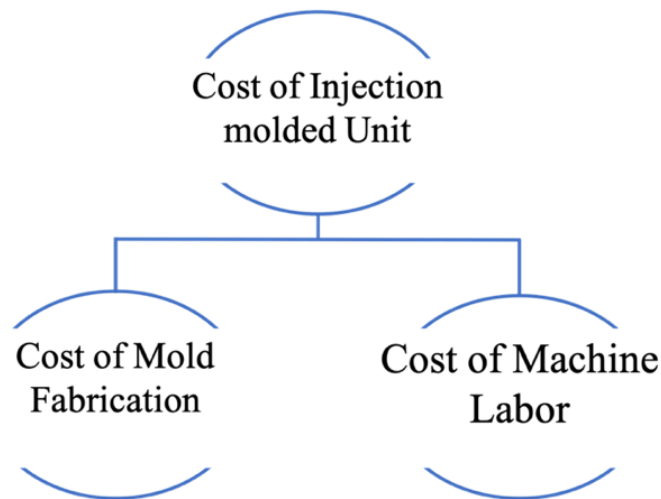


Figure 7-2: Cost of injection molded unit.

Determining the costs of a particular part depends on several factors including the complexity of the design of the part, the precision required, and the cosmetic effect of the

sprue gate. Cost of each unit: This includes the cost of material, machine, and set-up costs. The material cost is based on the amount of the material required to manufacture each part. The material is considered for this analysis is polystyrene which cost \$ 3.65 per pound.

There are two types of molds will be considered in this analysis including silicon (Si) mold and BMG mold. Cost of Si mold is calculated based on photolithography cost including the mask, wafers, DRIE etching, labor and wafer dicing as well. A 40 inserts can be fabricated on a 3 inches silicon wafer. The cost of each Si insert was determined to be \$ 33 as shown in Table 7-1. The cost of BMG molds is higher as the silicon mold is used during the fabrication process as sacrificial master mold. The final cost of BMG mold is \$76 for each insert as shown in Table 7-2.

Table 7-1: Silicon mold insert cost.

Si Wafer Etching Cost	Cost (\$)
Mask	820
Photolithography (35\$/ hour)	105
Wafer price each (\$)	16
DIRE Etching Per hour	35
Dicing	10
Epoxy adhesion per insert	1
No. of Insert per Wafer	40
Labor cost per Hour	40
No. of hours needed	8
Labor cost per Hour	320
Individual cost of Si Insert	33

Table 7-2: BMG mold insert cost.

BMG Insert Cost	Cost (\$)
BMG plate	1500
No. Of Inserts per Plate	80
BMG cost per Insert	19
Si mold for BMG	33
Si Wafer Dissolving in KOH	4
Labor Cost Per Insert (Thermoplastic forming)	20
Individual cost of BMG insert	76

### 7.5 Molded Part Cost Analysis

The unit cost is calculated based on the material weight per unit, machine cost, setup cost including the insert mold base machining. The machine time cost is widely based on hourly rates that could range anywhere from \$60/hour to \$100/hour, for automatic operation, depending on the size of machine used. The total molded part weight is 0.0144 oz (0.408 g) including the sprue, >1000 parts can thus be fabricated from a pound of the material. Based on the assumptions presented in Table 7-3 and Table 7-4 the cost of a molded part would be \$3.61 when a silicon mold is used. The cost per part dropped dramatically to \$1.86 when a BMG mold is used, even though the BMG molds cost more. The increased cost of the BMG molds is compensated by the drastic increase in mold life bringing the overall cost down as compared to the silicon mold case scenario as shown in Figure 7-3 and Figure 7-4.

Table 7-3: Molded part unit cost using Si mold.

Input	Value	unit
Si insert cost	33.00	dollars
Machine & Labor cost per hour	80.00	dollars
Al mold cost per insert	150.00	dollars
Cycle time	1.33	min
No. of parts per hour	45	Parts/hour
Mold life limit	100	cycle
Hours to mold failure	2.22	hours
Labor & machine cost for 22.22 hours	177.33	dollars
Molded part unit cost	3.61	dollars

Table 7-4: Molded part unit cost using BMG mold.

Input	Value	unit
BMG insert cost	76	dollars
Machine & Labor cost per hour	80	dollars
Al mold cost per insert	150	dollars
Cycle time (min)	1.33	min
No. of parts per hour	45	Parts/hour
Mold life limit	3000	cycle
Hours to mold failure	66.65	hours
Labor & machine cost for 66.65 hours	5,332.00	dollars
Molded part unit cost	1.86	dollars

## 7.6 Sensitivity Analysis

A sensitivity analysis is a financial way to determine the outcome of independent variables affect the unit cost under a given set of assumptions. Cost of molded parts is mostly sensitive to the operating cost which is ranging from \$60/hour to \$100/hour. Mold life is defined by the number of cycles in operation before failure could also have an important change on the final unit cost. Mold coating could increase the mold life and dramatically drop the unit cost. Si mold insert which are widely used to make these types of parts in research labs led to higher cost compared to BMG mold insert. Figure 7-3 shows the unit cost of molded part using Si mold insert as a function of operating cost and mold life.

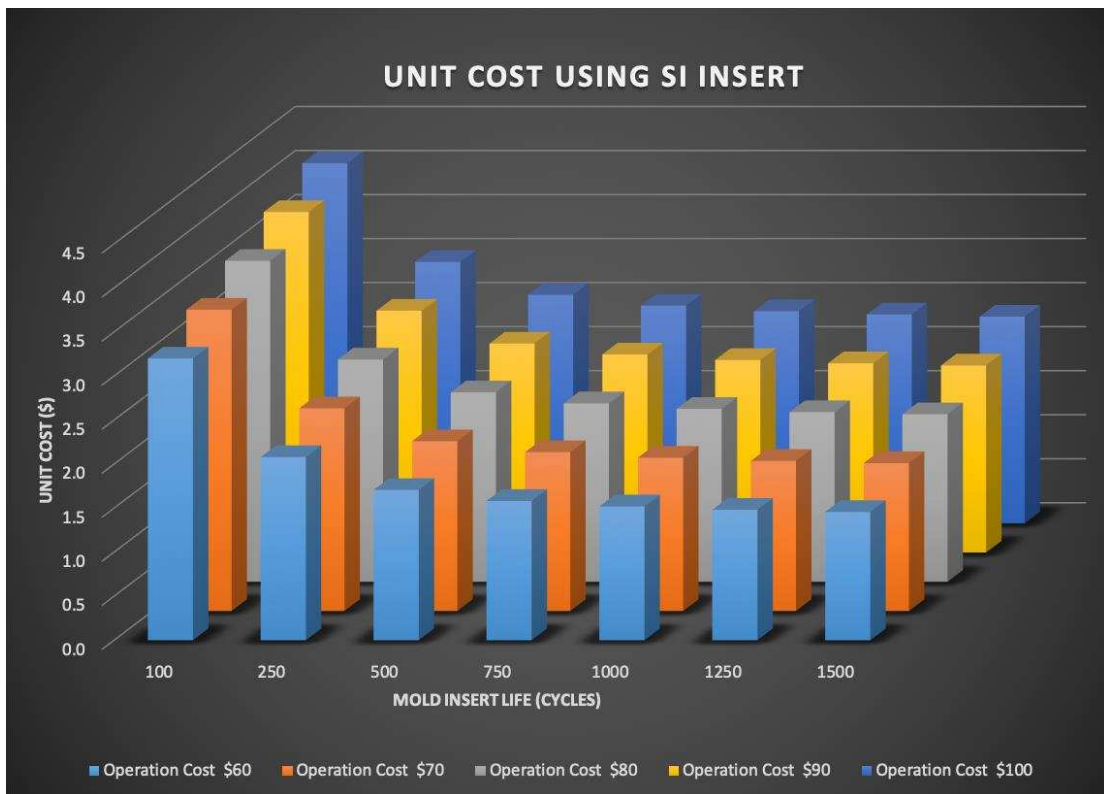


Figure 7-3: Molded part unit cost using Si mold versus mold insert life cycles.

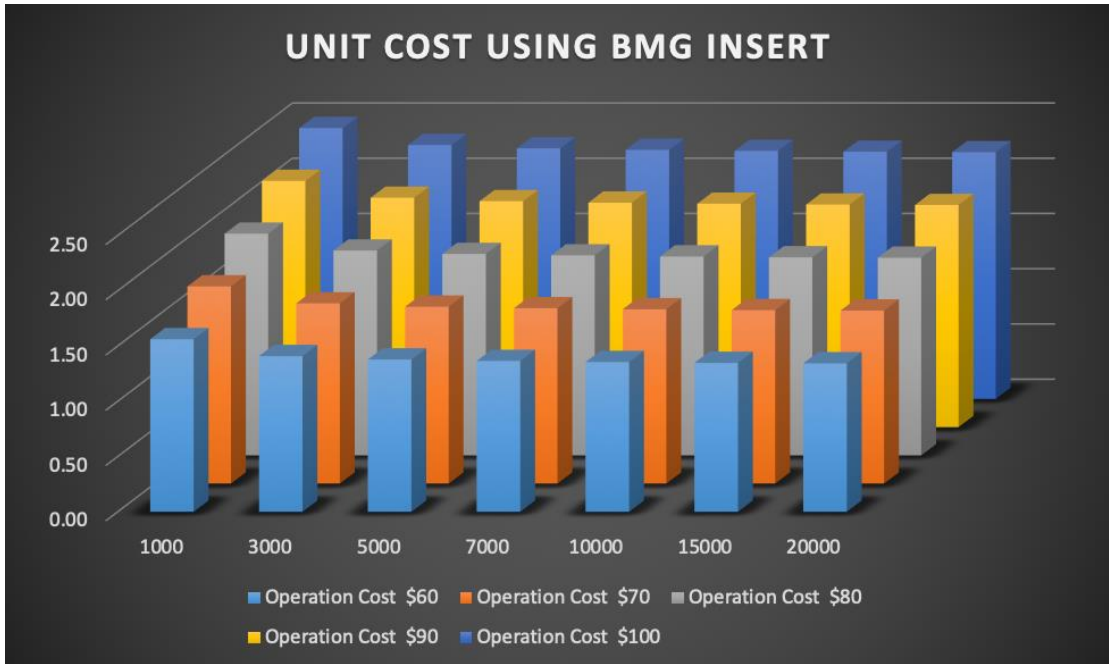


Figure 7-4: Molded part unit cost using BMG mold versus mold insert life cycles.

## CHAPTER 8: CONCLUSION AND FUTURE RECOMMENDATIONS

### 8.1 Research Summary

This research was demonstrated to fabricate biomedical parts with enhanced properties using micro injection molding process. Micro features were sufficiently molded over 6x6 mm dense area with high replication quality. This research found that Moldflow simulations is a key tool that advance the micro injection molding industry.

Theoretical modelling performed in this research indicated that the apparent elastic modulus of a texture surface can be tuned by manipulating the spacing between the pillars instead of aspect ratio which is hard to achieve. Micro pillars with elliptical cross-section exhibited higher apparent elastic modulus as compared to micro pillars with circular cross-section. There are many variables that govern the apparent surface stiffness including shapes, aspect ratio, center to center spacing, and young modulus of the substrate material. Pillars diameter and height have a minor effect on the elastic modulus. Spacing between pillars is the most effective dimension that can control the apparent elastic modulus.

The fatigue life simulations showed that silicon molds could survive hundreds of cycles before failure. In contrast, silicon mold survived a maximum of 105 cycles in an actual experiment. The discrepancy could be explained by the initiation of micro/nano cracks during the fabrication process that was not considered for the simulations. Antistiction coatings can reduce the effect of cracks, but the antistiction coatings would wear off after certain number of cycles.

Bulk metallic glass (BMG) showed potential for increased mold life for the scale of features investigated in this research. A silicon mold with the negative of the intended features was pressed on the BMG at an elevated temperature to fabricate the molds. A commercially available Zr-BMG was used for this purpose. The fabrication of the BMG molds proved to be a difficult proposition because of unintended crystallization of the BMG during the processing. Further research is required to understand how the working temperature range between glass transition temperature and crystallization temperature is effected by the simultaneous application of temperature and pressure during thermoplastic forming of this materials. The crystallization of BMG could potentially be avoided by applying the pressing load only during the forming for a few seconds.

Moldflow® simulations were performed to understand the effect of the molding parameters on micro-cavity filling and the replication of the features. These parameters were validated experimentally. There was great agreement between the predicted and the experimental data for several processing parameters such as mold temperature, melt temperature, injection velocity, and cooling time for different molding materials. Other parameter such as injection pressure and packing pressure needed to be adjusted significantly from the predicted parameters to ensure proper replication of the microfeatures. Cooling time was a significantly important factor to ensure the created patterns were demolded sufficiently. Molding material had a notable effect on the amount of distortions that were shown on the molded pillars during demolding. Material with higher tensile strength (PS=3.1 GPa, and COC=3.2 GPA) showed higher frictional interaction between the molded pillars and the mold. TPU, LDPE, and HDPE showed signs of stretching during pillars demolding. It was found that the sprue gate area was the last

region to solidify. As a result, reducing the sprue diameter was done to reduce the cooling time and material waste.

It was observed in this research that the cooling time had a significant effect on replication quality in terms of final dimensions and the ability to remove the parts from the mold successfully. The cooling time was affected by the choice of molding materials as well. PS and COC micro-pillars showed signs of distortion due to strong interaction between the Si mold and material during demolding stage. Micro-pillars fabricated from TPU, LDPE, HDPE experienced pillars stretch with lower cooling times due to material relaxation time that is needed before demolding. Molding of micro pillars without antistiction coating was performed using Texin 985. At slower cooling times with signs of pillars adhesion to the mold was observed, while faster cooling times led to silicon mold breakage during the experiments due to high frictional forces during demolding.

Dimensional cost analysis is a beneficial tool that used to find the cost of injection molded unit. Cost of molded parts was significantly affected by the operational cost and the number of cycles that the mold lasts. Silicon mold inserts showed a higher cost of the molded unit compared to BMG mold inserts.

## **8.2 Impact of Dissertation Research**

This dissertation would provide the reader a better understanding of the science of the micro-molding process and guidelines for fabricating micro and nano structures with high quality. Moldflow<sup>®</sup> is a promise approach to confirm the filling of microscale cavities. It also showed another method to reduce the cycle time 35% by reducing the sprue size. It

was conducted that polymeric substrate with micro topography can enhance cell growth and offer strategies to design textured substrates for specific biomedical applications and could expand the usage of micro/nano injection molded parts. The fabrication of substrates with micro features utilizing the strategy described in this research will enhance the replication rate. It was shown that preliminary processing parameters accumulated from Moldflow simulations are a better alternative to trial and error type experiments.

This research has impacted the author in many aspects. When I first started my PhD project, I had an overall idea of what I was going to investigate and how I would progress. As I started the project, I realized many skills would be required of me for this academic research. I have gained multiple skills during my PhD work including:

- Creative and independent thinking
- Research Project development
- How to write research publications
- How to present my research clearly and concisely during conference presentations
- Working with 3D design software (Solidworks)
- Working with Numerical simulation tools (Autodesk Moldflow, Ansys)
- Manufacturing and Mold fabrication techniques
  1. Operating micro-injection molding machine
  2. Operating vacuum hot press furnace for BMG mold fabrication
  3. Photolithography (positive and negative photoresists)
  4. Deep Reactive Ion Etching (DRIE)
  5. Scanning Electron Microscope (SEM)
  6. Atomic Force Microscopy (AFM)

### 8.3 Future Recommendations

- Research on Coatings on Silicon Molds

Si molds with low fabrication cost lead to an economically viable solution for these micro molded parts if a proper coating is deposited onto the Si molds. A thin coating of material such as diamond like carbon coating[119] or Gallium nitride with low frictional force coefficients (0.02 - 0.15), and high wear resistance of  $10^{-7}$ - $10^{-9}$  ( $\text{mm}^3/\text{Nm}$ ) (nearly like a diamond) could potentially increase the number of cycles of Si molds by reducing the surface roughness of Si molds and decreasing the friction between the mold wall and the polymer [120]. The research can be extended using different coating described here to improve the life of the Si mold.

Another major issue that may occur during demolding at the micro/nanoscale is adhesion of the material to the cavities, and the friction occurs between the sidewalls and the material. As experimented in this work, antistiction layer ( $\text{C}_4\text{F}_8$ ) that is applied at the end of the DRIE etching for 20 second. It showed a huge influence of minimizing the effect of material adhesion and friction forces during demolding. Increasing the sputtering time of  $\text{C}_4\text{F}_8$  in the final step and experimentally study the Si tool life as a function of the antistiction thickness layer could increase the number of cycles that mold can last.

- **Choice of Mold Materials**

It was observed in this research that the bulk metallic glass (BMG) could be an excellent mold choice with controlling the thermoplastic forming process.

Initial load that was applied in vacuum hot press experiments in Chapter#4 should be eliminated during heating, which might prevent the edges crystallization and uniform the

process of transferring the pattern to the BMG. Heat distribution through the sample was not uniform using the hot press described in this research. Sample edges tend to acquire higher temperature quicker than the middle of the sample, which results in higher crystallinity at the edges. Pressure also promotes crystal nucleation on the edges during heating thus leads to higher crystallinity compare to the core of the sample. As a result, imprinting of the micro pillars become poor at the edges due to the increase of crystallinity.

- **Fabrication Strategies**

A focused ion beam (FIB) instrument could be used to fabricate the micro features. As the name suggests this instrument utilizes a focused gallium ion beam to ablate small amounts materials in a controlled manner. This could potentially prevent the crystallization of BMG during fabrication. The unintended crystallization of the BMG was observed to be a major issue for the thermo-forming of the BMG molds utilizing sacrificial textured silicon substrates. FIB machining of an area spanning several square millimeters would be a time consuming process, but will be a single step process to fabricate the molds. After the FIB machining the molds will be ready for use. However, it is not clear if this process would be more efficient and/or economical as compared to the conventional processing. The conventional processing a multi-step process involving creating a silicon master to imprint the features onto BMG molds at an elevated temperature and pressure followed by dissolving off the silicon in potassium hydroxide exposing the micro-features. The FIB machining will be a simpler alternative to the conventional fabrication route, but further research is required to understand the interaction between the ion beam and bulk metallic glasses and the efficacy of the process.

- **Molding Strategy**

Hot runner system could possibly be one of the best solutions available to overcome high cycle time when molding micro/nanoscale features since it is runner less process with multiple hot drops that have the ability to produce parts in large quantities. The injection velocity and packing pressure needed a proper examination to ensure such cavities is totally filled.

## REFERENCES:

- [1] What's so BIG about nanotechnology? | Science Buzz, (n.d). <http://www.sciencebuzz.org/nano>.
- [2] Surface allows self-cleaning: sacred lotus - AskNature, (n.d). <http://www.asknature.org/strategy/714e970954253ace485abf1cee376ad8>.
- [3] Evidence for self-cleaning in gecko setae, (n.d). <http://www.pnas.org/content/102/2/385/F1.expansion.html>.
- [4] A.H. Slocum, P. Willoughby, J. Werkmeister, Mechanical Components: Silicon Insert Molded Plastic (SIMP), (n.d.).
- [5] Makuta Micro Injection Molding | High-precision micro injection molding services, (n.d.). <http://makuta.com/> .
- [6] Parasite-Inspired Microneedles | The Karp Lab, (n.d). <http://www.karplab.net/portfolio-item/parasite-inspired-microneedles>.
- [7] Global injection molding plastics market expected to reach \$277.78 billion by 2020 | PlasticsToday.com, (n.d.). <http://www.plasticstoday.com/articles/global-injection-molding-plastics-market-expected-reach-27778-billion-2020>.
- [8] C. Frantz, K.M. Stewart, V.M. Weaver, The extracellular matrix at a glance, *Journal of Cell Science*. 123 (2010) 4195–4200. doi:10.1242/jcs.023820.
- [9] S. He, Y. Su, B. Ji, H. Gao, Some basic questions on mechanosensing in cell–substrate interaction, *Journal of the Mechanics and Physics of Solids*. 70 (2014) 116–135. doi:10.1016/j.jmps.2014.05.016.
- [10] P.A. Janmey, R.T. Miller, Mechanisms of mechanical signaling in development and disease, *Journal of Cell Science*. 124 (2011) 9–18. doi:10.1242/jcs.071001.
- [11] Microinjection molding of thermoplastic polymers: a review - IOPscience, (n.d.). <https://iopscience.iop.org/article/10.1088/0960-1317/17/6/R02>.
- [12] plastic injection, moulding machines - how they work, (n.d.). [http://www.rutlandplastics.co.uk/advice/moulding\\_machine.html](http://www.rutlandplastics.co.uk/advice/moulding_machine.html).
- [13] G. Tosello, H.N. Hansen, Micro-Injection-Molding, in: *Micro-Manufacturing Engineering and Technology*, Elsevier, 2010: pp. 90–113. doi:10.1016/B978-0-8155-1545-6.00006-5.
- [14] U.M. Attia, Micro-injection moulding of three-dimensional integrated microfluidic devices, (2009). <https://dspace.lib.cranfield.ac.uk/handle/1826/4478>.
- [15] N. Zhang, D.J. Browne, M.D. Gilchrist, Characterization of Micro Injection Molding Process for the Replication of Micro/Nano Features Using Bulk Metallic Glass Insert, *International Journal of Engineering and Technology*. (2013) 198–201. doi:10.7763/IJET.2013.V5.541.

- [16] M. Khan, S.K. Afaq, N.U. Khan, S. Ahmad, Cycle Time Reduction in Injection Molding Process by Selection of Robust Cooling Channel Design, *ISRN Mechanical Engineering*. 2014 (2014) 1–8. doi:10.1155/2014/968484.
- [17] Why Conformal Cooling Makes Sense: *Plastics Technology*, (n.d.). <http://www.ptonline.com/articles/why-conformal-cooling-makes-ense>.
- [18] K. Maghsoudi, R. Jafari, G. Momen, M. Farzaneh, Micro-nanostructured polymer surfaces using injection molding: A review, *Materials Today Communications*. 13 (2017) 126–143. doi:10.1016/j.mtcomm.2017.09.013.
- [19] M.H. Naitove, ‘Passive Variotherm’ Cooling Cuts Cycle Time at Low Cost, (n.d.). <https://www.ptonline.com/articles/passive-variotherm-cooling-cuts-cycle-time-at-low-cost>.
- [20] Y.K. Demir, Z. Akan, O. Kerimoglu, Characterization of Polymeric Microneedle Arrays for Transdermal Drug Delivery, *PLOS ONE*. 8 (2013) e77289. doi:10.1371/journal.pone.0077289.
- [21] Bulk Metallic Glass Multiscale Tooling for Molding of Polymers with Micro to Nano Features: A Review - Springer, (n.d.). <http://link.springer.com/article/10.1007%2Fs11661-012-1427-7#page-2>.
- [22] V. Saile, U. Wallrabe, O. Tabata, J.G. Korvink, eds., *LIGA and Its Applications*, Wiley-VCH Verlag GmbH & Co. KGaA, Weinheim, Germany, 2008. <http://doi.wiley.com/10.1002/9783527622573>.
- [23] S. Prakash, J. Yeom, *Advanced Fabrication Methods and Techniques*, in: *Nanofluidics and Microfluidics*, Elsevier, 2014: pp. 87–170. <http://linkinghub.elsevier.com/retrieve/pii/B9781437744699000044>.
- [24] B. Ziaie, A. Baldi, M.Z. Atashbar, *Introduction to micro-/nanofabrication*, in: *Springer Handbook of Nanotechnology*, Springer, 2010: pp. 231–269. [http://link.springer.com/10.1007/978-3-642-02525-9\\_8](http://link.springer.com/10.1007/978-3-642-02525-9_8).
- [25] R. Zhou, H. Zhang, Y. Hao, Y. Wang, Simulation of the Bosch process with a string–cell hybrid method, *Journal of Micromechanics and Microengineering*. 14 (2004) 851–858. doi:10.1088/0960-1317/14/7/003.
- [26] Wafer level silicon mould fabrication and imprinting of high density microstructures, (n.d.). <http://www.sciencedirect.com/science/article/pii/S0167931712005825>.
- [27] U. of Sheffield, Overview - EBL Patterning - Electron Beam Lithography - The University of Sheffield, (n.d.). <https://www.sheffield.ac.uk/eb/patterning>.
- [28] B. Berčič, *Introduction to Electron Beam Lithography*, (n.d.) 11.
- [29] Nanoporous anodic aluminium oxide: Advances in surface engineering and emerging applications, (n.d.). <http://www.sciencedirect.com/science/article/pii/S0079642513000030>.

- [30] Progress in Nano-Engineered Anodic Aluminum Oxide Membrane Development, (n.d.). [https://www.researchgate.net/publication/49966166\\_Progress\\_in\\_Nano-Engineered\\_Anodic\\_Aluminum\\_Oxide\\_Membrane\\_Development](https://www.researchgate.net/publication/49966166_Progress_in_Nano-Engineered_Anodic_Aluminum_Oxide_Membrane_Development).
- [31] NANOPOROUS AAO: A PLATFORM FOR REGULAR HETEROGENEOUS NANOSTRUCTURES AND ENERGY STORAGE DEVICES, (n.d.). <http://drum.lib.umd.edu/handle/1903/9828>.
- [32] Towards nano-injection molding, (n.d.). <http://www.sciencedirect.com/science/article/pii/S1369702112700925>.
- [33] Laser Micro Drilling, Oxford Lasers. (n.d.). <https://www.oxfordlasers.com/laser-micromachining/laser-micro-drilling/>.
- [34] Ultraprecision micromachining of hardened steel by applying ultrasonic elliptical vibration cutting (PDF Download Available), (n.d.). [https://www.researchgate.net/publication/4047332\\_Ultraprecision\\_micromachining\\_of\\_hardened\\_steel\\_by\\_applying\\_ultrasonic\\_elliptical\\_vibration\\_cutting](https://www.researchgate.net/publication/4047332_Ultraprecision_micromachining_of_hardened_steel_by_applying_ultrasonic_elliptical_vibration_cutting).
- [35] C.-C. Hu, Electrodeposition of Nickel-Phosphorus Deposits with a Variable Magnetic Property, (n.d.). <http://www.electrochem.org/dl/ma/198/pdfs/0636.pdf>.
- [36] <http://www.osti.gov/scitech/servlets/purl/6487211-EargfC/>, (n.d.). <http://www.osti.gov/scitech/servlets/purl/6487211-EargfC/>.
- [37] Microstructure evolution and hardening mechanisms of Ni–P electrodeposits, (n.d.). <http://www.sciencedirect.com/science/article/pii/S0257897210007723>.
- [38] A.M. Pillai, A. Rajendra, A.K. Sharma, Electrodeposited nickel–phosphorous (Ni–P) alloy coating: an in-depth study of its preparation, properties, and structural transitions, *Journal of Coatings Technology and Research*. 9 (2012) 785–797. doi:10.1007/s11998-012-9411-0.
- [39] R. Phatthanakun, S. Promwikorn, W. Pummara, C. Sriphung, B. Sutapun, N. Chomnawang, Fabrication of low-cost plastic micromolds for microfluidic systems using X-ray LIGA, in: 2014 11th International Conference on Electrical Engineering/Electronics, Computer, Telecommunications and Information Technology (ECTI-CON), IEEE, Nakhon Ratchasima, Thailand, 2014: pp. 1–5. doi:10.1109/ECTICon.2014.6839746.
- [40] F. Hybrii, 1. Patterning of silicon wafer, (n.d.) 23.
- [41] Nanoscale Research Letters | Full text | A review of roll-to-roll nanoimprint lithography, (n.d.). <http://www.nanoscalereslett.com/content/9/1/320>.
- [42] S.-H. Yoon, N.-G. Cha, J.S. Lee, J.-G. Park, D.J. Carter, J.L. Mead, C.M.F. Barry, Effect of processing parameters, antistiction coatings, and polymer type when injection molding microfeatures, *Polymer Engineering & Science*. 50 (2010) 411–419. doi:10.1002/pen.21541.
- [43] T.A. Osswald, ed., *Injection molding handbook*, Hanser, Munich, 2001.

- [44] Slip velocity model | Moldflow Insight | Autodesk Knowledge Network, (n.d.). <https://knowledge.autodesk.com/support/moldflow-insight/learn-explore/caas/CloudHelp/cloudhelp/2017/ENU/MoldflowInsight/files/GUID-7DF8DD90-EB8F-42C0-B3A1-0829A50ABF5F-htm.html>.
- [45] D. Masato, M. Sorgato, M. Babenko, B. Whiteside, G. Lucchetta, Thin-wall injection molding of polystyrene parts with coated and uncoated cavities, *Materials & Design*. 141 (2018) 286–295. doi:10.1016/j.matdes.2017.12.048.
- [46] An investigation of micro-scale fabrication using the injection molding process - ProQuest, (n.d.). <http://search.proquest.com/docview/304846068>.
- [47] Numerical and experimental studies in development of polymer injection micro molding - ProQuest, (n.d.). <http://search.proquest.com/docview/304553436>.
- [48] An Investigation of Mechanically Tunable and Nanostructured Polymer Scaffolds fo, (n.d.). <http://adsabs.harvard.edu/abs/2010PhDT.....93J>.
- [49] J.W. Rodgers, An Investigation of Micro and Nanomanufactured Polymer Substrates to Direct Stem Cell Response for Biomedical Applications, Lehigh University, 2014. <http://search.proquest.com/openview/2ee2b906a64decb1e454a939961bce69/1?pq-origsite=gscholar&cbl=18750&diss=y>.
- [50] Xiang and LaVan - 2007 - Analysis of soft cantilevers as force transducers.pdf, (n.d.).
- [51] J.W. Rodgers, M.E. Casey, S.S. Jedlicka, J.P. Coulter, Effect of Micro-Injection Molding Processing Conditions on the Replication and Consistency of a Dense Network of High Aspect Ratio Microstructures, *Journal of Micro and Nano-Manufacturing*. 2 (2014) 011006. doi:10.1115/1.4026606.
- [52] M.D.J. Vega, J. Mead, C. Barry, Injection molding microstructured substrates from rubber-containing polymers, in: Graz, Austria, 2016: p. 020012. doi:10.1063/1.4965463.
- [53] T.R. Tofteberg, H. Amédro, F. Grytten, E. Andreassen, Effects of Injection Molding Holding Pressure on the Replication of Surface Microfeatures, *International Polymer Processing*. 25 (2010) 236–241. doi:10.3139/217.2340.
- [54] Y. Qin, *Micro-manufacturing engineering and technology*, 1st ed, William Andrew [u.a.], Oxford, 2010.
- [55] SEM & Imaging: The Applications and Practical Uses of Scanning Electron Microscopes, ATA Scientific. (2017). <https://www.atascientific.com.au/sem-imaging-applications-practical-uses-scanning-electron-microscopes/>.
- [56] Acceleration voltage vs. specimen type | MyScope, (n.d.). <https://myscope.training/legacy/sem/practice/principles/voltagevstyp.php>.
- [57] Low-voltage scanning electron microscopy of polymers, *Polymer*. 36 (1995) 1781–1790. doi:10.1016/0032-3861(95)90924-Q.

- [58] Y. Yuan, T.R. Lee, Contact Angle and Wetting Properties, in: G. Bracco, B. Holst (Eds.), *Surface Science Techniques*, Springer Berlin Heidelberg, Berlin, Heidelberg, 2013: pp. 3–34. doi:10.1007/978-3-642-34243-1\_1.
- [59] Z. Yoshimitsu, A. Nakajima, T. Watanabe, K. Hashimoto, Effects of surface structure on the hydrophobicity and sliding behavior of water droplets, *Langmuir*. 18 (2002) 5818–5822.
- [60] Atomic Force Microscopy, Nanoscience Instruments. (n.d.). <https://www.nanoscience.com/techniques/atomic-force-microscopy/>.
- [61] Peak Force Tapping - Learn more, Bruker.Com. (n.d.). <https://www.bruker.com/products/surface-and-dimensional-analysis/atomic-force-microscopes/modes/modes/imaging-modes/peakforce-tapping/learn-more.html>.
- [62] M. Utlaut, Focused ion beams for nano-machining and imaging, in: *Nanolithography*, Elsevier, 2014: pp. 116–157. doi:10.1533/9780857098757.116.
- [63] K. Metavarayuth, P. Sitasuwan, X. Zhao, Y. Lin, Q. Wang, Influence of Surface Topographical Cues on the Differentiation of Mesenchymal Stem Cells in Vitro, *ACS Biomaterials Science & Engineering*. 2 (2016) 142–151. doi:10.1021/acsbiomaterials.5b00377.
- [64] B. Chen, P. Goldberg Oppenheimer, T.A.V. Shean, C.T. Wirth, S. Hofmann, J. Robertson, Adhesive Properties of Gecko-Inspired Mimetic via Micropatterned Carbon Nanotube Forests, *The Journal of Physical Chemistry C*. 116 (2012) 20047–20053. doi:10.1021/jp304650s.
- [65] Y. Xiang, D.A. LaVan, Analysis of soft cantilevers as force transducers, *Applied Physics Letters*. 90 (2007) 133901. doi:10.1063/1.2716376.
- [66] K. Kim, R. Taylor, J.Y. Sim, S.-J. Park, J. Norman, G. Fajardo, D. Bernstein, B.L. Pruitt, Calibrated micropost arrays for biomechanical characterisation of cardiomyocytes, *Micro & Nano Letters*. 6 (2011) 317. doi:10.1049/mnl.2011.0031.
- [67] G.R. Cowper, The shear coefficient in Timoshenko's beam theory, in: *ASME*, 1966.
- [68] M.N. Shahbazi, A. Jedrusik, S. Vuoristo, G. Recher, A. Hupalowska, V. Bolton, N.M.E. Fogarty, A. Campbell, L.G. Devito, D. Ilic, Y. Khalaf, K.K. Niakan, S. Fishel, M. Zernicka-Goetz, Self-organization of the human embryo in the absence of maternal tissues, *Nature Cell Biology*. 18 (2016) 700–708. doi:10.1038/ncb3347.
- [69] A.A. Blancas, C.-S. Chen, S. Stolberg, K.E. McCloskey, Adhesive forces in embryonic stem cell cultures, *Cell Adhesion & Migration*. 5 (2011) 472–479.
- [70] Photolithography - Semiconductor Technology from A to Z - Halbleiter.org, (n.d.). <https://www.halbleiter.org/en/photolithography/>.
- [71] Preparation of high aspect ratio surface microstructures out of a Zr-based bulk metallic glass, (n.d.). <http://www.sciencedirect.com/science/article/pii/S0167931703000960>.

- [72] A.A. Kündig, A. Dommann, W.L. Johnson, P.J. Uggowitzer, High aspect ratio micro mechanical structures made of bulk metallic glass, *Materials Science and Engineering: A*. 375–377 (2004) 327–331. doi:10.1016/j.msea.2003.10.269.
- [73] R. Martinez-Duarte, M.J. Madou, G. Kumar, J. Schroers, A novel method for amorphous metal micromolding using carbon MEMS, in: *Solid-State Sensors, Actuators and Microsystems Conference, 2009. TRANSDUCERS 2009. International*, IEEE, 2009: pp. 188–191. [http://ieeexplore.ieee.org/xpls/abs\\_all.jsp?arnumber=5285533](http://ieeexplore.ieee.org/xpls/abs_all.jsp?arnumber=5285533).
- [74] X. Zhang, J. Ma, G. Fang, B. Sun, J. Li, Q. Li, Polymer micro molding with bulk metallic glass mold, *Microsystem Technologies*. 21 (2015) 1453–1457. doi:10.1007/s00542-014-2221-9.
- [75] N. Zhang, J.S. Chu, C.J. Byrne, D.J. Browne, M.D. Gilchrist, Replication of micro/nano-scale features by micro injection molding with a bulk metallic glass mold insert, *Journal of Micromechanics and Microengineering*. 22 (2012) 065019. doi:10.1088/0960-1317/22/6/065019.
- [76] D.J. Browne, D. Stratton, M.D. Gilchrist, C.J. Byrne, Bulk Metallic Glass Multiscale Tooling for Molding of Polymers with Micro to Nano Features: A Review, *Metallurgical and Materials Transactions A*. 44 (2013) 2021–2030. doi:10.1007/s11661-012-1427-7.
- [77] Thermoplastic Forming (TPF) | Schroers Lab, (n.d.). <http://www.schroerslab.com/research/processing-of-bmgs/tpf>.
- [78] L.-C. Zhang, Crystallization Behavior and Control of Amorphous Alloys, in: Y. Mastai (Ed.), *Advances in Crystallization Processes*, InTech, 2012. doi:10.5772/36304.
- [79] E.E. Vidal, J.A. Yurko, C. Pokross, R.S. Beals, L.H. Ryczek, T.A. Waniuk, J.C. Poole, C.D. Prest, D.J. Stratton, Bulk metallic glasses with low concentration of beryllium, US20140261898A1, 2014. <https://patents.google.com/patent/US20140261898/en>.
- [80] G.N. Yang, Y. Shao, K.F. Yao, S.Q. Chen, A study of cooling process in bulk metallic glasses fabrication, *AIP Advances*. 5 (2015) 117111. doi:10.1063/1.4935440.
- [81] X. Xiao, F. Shoushi, W. Guoming, H. Qin, D. Yuanda, Influence of beryllium on thermal stability and glass-forming ability of Zr–Al–Ni–Cu bulk amorphous alloys, *Journal of Alloys and Compounds*. 376 (2004) 145–148. doi:10.1016/j.jallcom.2004.01.014.
- [82] C.C. Hays, C.P. Kim, W.L. Johnson, Large supercooled liquid region and phase separation in the Zr–Ti–Ni–Cu–Be bulk metallic glasses, *Applied Physics Letters*. 75 (1999) 1089–1091. doi:10.1063/1.124606.

- [83] Q. Zheng, J. Du, Low beryllium content Zr-based bulk metallic glass composite with plasticity and work hardenability, *Journal of Applied Physics*. 115 (2014) 043519. doi:10.1063/1.4863454.
- [84] G. Fu, N.H. Loh, S.B. Tor, B.Y. Tay, Y. Murakoshi, R. Maeda, Analysis of demolding in micro metal injection molding, *Microsystem Technologies*. 12 (2006) 554–564. doi:10.1007/s00542-005-0071-1.
- [85] Material databases | Moldflow Adviser | Autodesk Knowledge Network, (n.d.). <https://knowledge.autodesk.com/support/moldflow-adviser/learn-explore/caas/CloudHelp/cloudhelp/2014/ENU/MoldflowAdvisor/files/GUID-9C852155-1ECC-4A68-A45D-F3FC5E79E057-htm.html>.
- [86] S. Agarwal, D. Patidar, N.S. Saxena, Study on glass transition temperature and mechanical properties of cadmium sulfide/polystyrene nanocomposites, *Polymer Engineering & Science*. 53 (2013) 1223–1229. doi:10.1002/pen.23382.
- [87] Z. Xu, Z. Lv, L. Wang, K. Jiang, Z. Ji, C. Liu, J. Liu, Research on impact behaviour and silicon insert fracture phenomenon in microinjection moulding, *AIP Advances*. 5 (2015) 041317. doi:10.1063/1.4905950.
- [88] C. Osgood, All machine and structural designs are problems in fatigue because the forces of Nature are always at work and each object must respond in some fashion., (2004) 58.
- [89] R. Browell, Calculating and Displaying Fatigue Results, (n.d.) 42.
- [90] A. Varvani-Farahani, Fatigue-life assessment of silicon MEMS components, in: A. Varvani-Farahani (Ed.), *WIT Transactions on State of the Art in Science and Engineering*, 1st ed., WIT Press, 2005: pp. 485–502. doi:10.2495/1-85312-836-8/14.
- [91] Z. Parlar, M. Bakkal, A.J. Shih, Sliding tribological characteristics of Zr-based bulk metallic glass, *Intermetallics*. 16 (2008) 34–41. doi:10.1016/j.intermet.2007.07.011.
- [92] M.L. Morrison, R.A. Buchanan, P.K. Liaw, B.A. Green, G.Y. Wang, C.T. Liu, J.A. Horton, Four-point-bending-fatigue behavior of the Zr-based Vitreloy 105 bulk metallic glass, *Materials Science and Engineering: A*. 467 (2007) 190–197. doi:10.1016/j.msea.2007.05.066.
- [93] X.D. Wang, R.T. Qu, S.J. Wu, Q.Q. Duan, Z.Q. Liu, Z.W. Zhu, H.F. Zhang, Z.F. Zhang, Notch fatigue behavior: Metallic glass versus ultra-high strength steel, *Scientific Reports*. 6 (2016). doi:10.1038/srep35557.
- [94] S. Yoon, C. Srirojpinyo, J.S. Lee, J.L. Mead, S. Matsui, C.M.F. Barry, Evaluation of novel tooling for nanoscale injection molding, in: V.K. Varadan (Ed.), 2005: p. 107. doi:10.1117/12.599959.
- [95] M.-H. Tsai, K.-L. Ou, C.-F. Huang, H.-C. Cheng, Y.-K. Shen, C.-Y. Chang, C.-H. Wu, J.-H. Chen, P.-J. Guan, Study on micro-injection molding of light guiding plate by numerical simulation, *International Communications in Heat and Mass Transfer*. 35 (2008) 1097–1100. doi:10.1016/j.icheatmasstransfer.2008.05.013.

- [96] Y.-K. Shen, C.-Y. Chang, Y.-S. Shen, S.-C. Hsu, M.-W. Wu, Analysis for microstructure of microlens arrays on micro-injection molding by numerical simulation, *International Communications in Heat and Mass Transfer*. 35 (2008) 723–727. doi:10.1016/j.icheatmasstransfer.2008.01.013.
- [97] Injection Molding | Reducing Mold Cycle Time | Autodesk, (n.d.). <https://www.autodesk.com/industry/manufacturing/injection-molding/reducing-mold-cycle-time/overview>.
- [98] D. Yao, B. Kim, Simulation of the filling process in micro channels for polymeric materials, *Journal of Micromechanics and Microengineering*. 12 (2002) 604.
- [99] Polystyrene | chemical compound, *Encyclopedia Britannica*. (n.d.). <https://www.britannica.com/science/polystyrene>.
- [100] A. Rho, How Is General Purpose Polystyrene (GPPS) Different from High Impact Polystyrene (HIPS)?, (n.d.). <https://marketing.alpharho.com/blog/how-is-general-purpose-polystyrene-gpps-different-from-high-impact-polystyrene-hips>.
- [101] Americas Styrenics, (n.d.). [http://primeresinas.com/index.php?option=com\\_content&view=article&id=63&Itemid=61&lang=](http://primeresinas.com/index.php?option=com_content&view=article&id=63&Itemid=61&lang=).
- [102] Elastollan material properties : BASF Polyurethanes, (n.d.). [http://www.polyurethanes.basf.de/pu/Elastollan/Elastollan\\_Materialeigenschaften](http://www.polyurethanes.basf.de/pu/Elastollan/Elastollan_Materialeigenschaften).
- [103] Covestro Texin® 985 Urethane Thermoplastic Elastomer, (n.d.). <http://www.matweb.com/search/datasheet.aspx?MatGUID=f1632d86389a41e1bf1088a8fcf234a0>.
- [104] LDPE Plastic Injection Molding - Low Density Polyethylene Injection Molds, Texas Injection Molding. (n.d.). <https://texasinjectionmolding.com/low-density-polyethylene-ldpe-injection-molding/>.
- [105] Polyethylene - New World Encyclopedia, (n.d.). <http://www.newworldencyclopedia.org/entry/Polyethylene>.
- [106] A. Schulman CP851 High Flow, Injection Molding Grade, (n.d.). <http://www.matweb.com/search/datasheet.aspx?MatGUID=58fbf75065824f589621d351a02d7883>.
- [107] ExxonMobil HD 6733.17 Injection Molding Resin, (n.d.). <http://www.matweb.com/search/datasheet.aspx?MatGUID=23172243811d43f3842b2e40810628d8>.
- [108] TOPAS COC Polymers | TOPAS, (n.d.). <https://topas.com/products/topas-coc-polymers>.
- [109] H.-Y. Lin, W.-B. Young, Analysis of the filling capability to the microstructures in micro-injection molding, *Applied Mathematical Modelling*. 33 (2009) 3746–3755. doi:10.1016/j.apm.2008.12.012.

- [110] L. Xie, G. Ziegmann, B. Jiang, Numerical simulation method for weld line development in micro injection molding process, *Journal of Central South University of Technology*. 16 (2009) 774–780. doi:10.1007/s11771-009-0129-9.
- [111] Molding Window analysis (Concept) | Moldflow Insight | Autodesk Knowledge Network, (n.d.).
- [112] J. Shoemaker, ed., *Moldflow design guide: a resource for plastics engineers*, Hanser ; Hanser Gardner Publications, Munich : Cincinnati, 2006.
- [113] Moldflow: What theory are the flow solvers based on | Moldflow Adviser | Autodesk Knowledge Network, (n.d.). <https://knowledge.autodesk.com/support/moldflow-adviser/troubleshooting/caas/sfdcarticles/sfdcarticles/Moldflow-What-theory-are-the-flow-solvers-based-on.html>.
- [114] A.A. Rajhi, I.H. Jaafar, S.S. Jedlicka, J.P. Coulter, Numerical and Experimental Investigation in Replicating a Micro-Featured Surface with the Injection Molding Process, *TechConnect Briefs*. 1 (2017) 387–390.
- [115] A.A. Rajhi, S.S. Jedlicka, J.P. Coulter, MOLDFLOW OPTIMIZATION OF MICRO-CAVITIES FILLING DURING INJECTION MOLDING PROCESS, (n.d.) 6, ANTEC 2018.
- [116] G. Menges, W. Michaeli, P. Mohren, *How to Make Injection Molds*, Third Edition, Carl Hanser Verlag GmbH & Co. KG, München, 2001. doi:10.3139/9783446401808.
- [117] Global market for micro injection polymer molding expected to cross US\$897 mln by 2020, (n.d.). [http://www.plastemart.com/Plastic-Technical-Article.asp?LiteratureID=2094&Paper=Global-market-microinjection-polymer-molding-to-cross-US\\$897-million-by-2020](http://www.plastemart.com/Plastic-Technical-Article.asp?LiteratureID=2094&Paper=Global-market-microinjection-polymer-molding-to-cross-US$897-million-by-2020).
- [118] Polymer Microinjection Molding Market Analysis By Application And Segment Forecasts To 2020, (n.d.). <https://www.grandviewresearch.com/industry-analysis/polymer-microinjection-molding-industry>.
- [119] B. Saha, E. Liu, S.B. Tor, N.W. Khun, D.E. Hardt, J.H. Chun, Anti-sticking behavior of DLC-coated silicon micro-molds, *Journal of Micromechanics and Microengineering*. 19 (2009) 105025. doi:10.1088/0960-1317/19/10/105025.
- [120] Gallium nitride has wear resistance that approaches that of diamond, *The American Ceramic Society*. (2016). <https://ceramics.org/ceramic-tech-today/gallium-nitride-has-wear-resistance-that-approaches-that-of-diamond>.

## **VITA**

Ali A. Rajhi was born on March 22<sup>nd</sup> in Jazan, Saudi Arabia. He received his B.S in mechanical engineering from King Khalid University, Saudi Arabia in 2007 and a M.S from New Haven University, USA in 2012. He also has held an academic position at King Khalid University at Abha, Saudi Arabia in 2007, where he served as Teaching Assistance before he promoted to lecturer in 2012.

His main area of interest is polymer processing technologies including micro and nano injection molding, additive manufacturing, nanoimprinted lithography, material characterizations, and silicon fabrication.

During his academic career, Ali has written numerus conference papers and journal papers during his studies at Lehigh University. He has also been achieved multiple awards from The Society of Plastics Engineers, Lehigh Valley Chapter. He has presented his research at both professional conferences and in university lectures.